Finite Element Formulations for Biological Soft Hydrated Tissues under Finite Deformation

by

Edgard Sant'Anna de Almeida Neto

A Thesis Submitted to the Graduate

Faculty of Rensselaer Polytechnic Institute

in Partial Fulfillment of the

Requirements for the Degree of

DOCTOR OF PHILOSOPHY

Major Subject: Mechanical Engineering

Approved by the
Examining Committee:

_____
Robert L. Spilker, Thesis Adviser

_____
Mark H. Holmes, Member

_____
Ting-Leung Sham, Member

_____
Mark S. Shephard, Member

Rensselaer Polytechnic Institute
Troy, New York

July 1995
(For Graduation August 1995)

Table of Contents

List of Tables

List of Tables

List of Tables

List of Figures

Acknowledgments

I wish to express my gratitude to my adviser, Prof. Robert L. Spilker, for his support and encouragement during the course of this study. His constant enthusiasm and ability to work in an interdisciplinary environment much has contributed to my interest in the field of Biomechanics. I hope this is the beginning of a long-lasting collaboration.

I would like to thank Prof. Mark H. Holmes for his invaluable ideas and suggestions that enriched the presentation of the biphasic theory in this thesis. I am grateful to Professors Mark S. Shephard and Ting-Leung Sham for their attention as examining committee members. I am also grateful to Prof. Shephard for his insights into the finite element formulations, and for making the computational resources at SCOREC available for me.

I owe special thanks to friends and colleagues who have motivated me with their knowledge and friendship. Peter Donzelli for sharing his computational expertise; and Brea Barthel and Mark Zotto for everything they have taught me.

My stay in the USA would have not been possible without the support of great friends in the "Escola Politécnica da Universidade de São Paulo". In particular, Mario E. S. Soares, João C. André and Carlos N. Mazzilli have encouraged and followed closely the course of this study.

I would like to acknowledge the sponsors that have made this thesis a reality: "Escola Politécnica da Universidade de São Paulo", and FAPESP ("Fundação de Amparo à Pesquisa do Estado de São Paulo"). The support of the National Science Foundation (Grant ASC-9318184) and Surdna Foundation is also gratefully acknowledged.

My family has been specially valuable to me during my stay in the USA. I thank my parents and my sister Cecília for all their attention, interest, and patience.

GLOSSARY OF CONVENTIONS AND NOTATIONS

CONVENTIONS:

The following conventions are used to distinguish different entities in the text:

(a) sets and spaces – Zapf Chancery font: $\mathcal{B}$, $\mathcal{S}$;

(b) scalars – lightface italic: W, ρ;

(c) vectors and second order tensors – boldface italic: $\boldsymbol{v}$, $\boldsymbol{F}$, $\boldsymbol{\sigma}$;

(d) higher-order tensors – boldface Helvetica font: $\mathbf{C}$;

(e) arrays – boldface italic: $\boldsymbol{Y}_2^{\mathrm{e}}$, $\boldsymbol{v}^{\mathrm{s}}$;

(f) sub-arrays using the same name – boldface italic between square brackets or braces, with indices specifying the partition: $[\boldsymbol{Y}_2^{\mathrm{e}}]^{ab}$, $\{\boldsymbol{v}^{\mathrm{e}}\}^{a}$;

(g) array elements – lightface italic between square brackets or braces: $[\boldsymbol{Y}_2^{\mathrm{e}}]^{ab}_{ij}$, $\{\boldsymbol{v}^{\mathrm{e}}\}^{a}_{i}$;

(h) material quantities, reference configuration – upper case, or 0 as subscript: $\boldsymbol{X}$, $\boldsymbol{n}_0$;

(i) spatial quantities, current configuration – lower case: $\boldsymbol{x}$, $\boldsymbol{n}$;

Throughout the text, the convention of *summation over repeated indices* applies only to subscripts and superscripts in *italic* (superscripts and subscripts in roman letters are considered part of the variable name). The *comma convention*, where a comma in the subscript denotes partial differentiation, is often used to shorten the equations.

NOTATIONS:

Auxiliary Notation

$(\,)^{\alpha}$ superscript denoting the αth constituent;

$(\,)^{\alpha\beta}$ superscript with two greek letters denoting a relative quantity: $(\,)^{\alpha\beta} = (\,)^{\alpha} - (\,)^{\beta}$;

$(\bar{\ })$ prescribed value;

$(\underset{\sim}{\ })$ condensed form of a tensor: $\underset{\sim}{S}$;

$(\hat{\ })$ assembled counterparts of the element vectors, or supply quantities in the theory of mixtures: $\hat{\boldsymbol{v}}$, $\hat{c}^{\alpha}$;

$(\,)_0$ reference configuration: $\boldsymbol{n}_0$;

$(\,)^{\mathrm{e}}$ array defined at element level;

$()^{f}$ superscript denoting the fluid phase;

$()^{s}$ superscript denoting the solid phase;

$()^{sym}$ symmetric part of a tensor;

$\mathcal{L}()$ linearized form: $\mathcal{L}(C^{s})$;

:= sign meaning that the right-hand-side defines the left-hand-side (used to introduce intermediate matrices in the finite element formulations).

Boundary Value Problems

i, j indices referring to the current configuration;

K, L indices referring to the reference configuration;

$\mathbb{R}$ set of real numbers;

$\mathbb{R}^{n_{sd}}$ Euclidean n_{sd}-space;

Ω domain in $\mathbb{R}^{n_{sd}}$;

$\overline{\Omega}$ closure of Ω;

Γ boundary of Ω;

Γ_g part of the boundary where Dirichlet conditions are prescribed;

Γ_t part of the boundary where Neumann conditions are prescribed;

$\mathcal{S} \equiv \overline{\Omega}$ current configuration of the body;

$\mathcal{B} \equiv \overline{\Omega}_0$ reference configuration of the body;

$\boldsymbol{x}$ position in $\mathcal{S}$;

$\boldsymbol{X}$ position in $\mathcal{B}$.

Functional Spaces

$\mathcal{S}^{\alpha}$ space of trial solutions for the αth constituent;

$\mathcal{S}^{p}$ space of trial solutions for the pressure;

$\mathcal{V}^{\alpha}$ space of weighting functions for the αth constituent;

$\mathcal{V}^{p}$ space of weighting functions for the pressure.

Tensor and Matrix Notation

$\mathbf{1}$ second order identity tensor: $[\mathbf{1}]^{i}_{j} = \delta^{i}_{j}$;

$\boldsymbol{a} \otimes \boldsymbol{b}$ tensor product of two vectors, which has the property $(\boldsymbol{a} \otimes \boldsymbol{b})\, \boldsymbol{v} = \boldsymbol{a}\,(\boldsymbol{b} \cdot \boldsymbol{v})$ for arbitrary $\boldsymbol{v}$: $[\boldsymbol{a} \otimes \boldsymbol{b}]^{ij} = a^{i} b^{j}$;

$\boldsymbol{w} \cdot \boldsymbol{t}$ contraction of tensors: $\boldsymbol{w} \cdot \boldsymbol{t} = w^{i} t_{i}$;

$\boldsymbol{\sigma n}$ contraction of tensors (omitting the dot): $(\boldsymbol{\sigma n})^{i} = \sigma^{ij} n_{j}$;

$\boldsymbol{E} : \boldsymbol{S}$ double contraction of tensors: $\boldsymbol{E} : \boldsymbol{S} = \mathrm{tr}(\boldsymbol{E}^{\mathrm{T}} \boldsymbol{S}) = E_{KL} S^{KL}$;

$\mathrm{cof}(\boldsymbol{A})$ cofactor of $\boldsymbol{A}$: $\mathrm{cof}(\boldsymbol{A}) = \det(\boldsymbol{A}) \boldsymbol{A}^{-\mathrm{T}}$;

$\mathrm{tr}(\boldsymbol{A})$ trace of $\boldsymbol{A}$.

Calculus

$\dfrac{D}{Dt}$ material time derivative with respect to the center of mass of the mixture;

$\dfrac{D^{\alpha}}{Dt}$ material time derivative with respect to the αth constituent;

$\dot{(\,)}$ time derivative;

$(\,)_{,i}$ partial derivative with respect to x^{s}_{i};

$(\,)_{,K}$ partial derivative with respect to X^{s}_{K};

$\delta(\,)$ variation: $\delta \boldsymbol{u}^{s}$;

$\nabla(\,)$ gradient with respect to $\boldsymbol{x}$;

$\nabla_{X}(\,)$ gradient with respect to $\boldsymbol{X}$;

$\nabla(\,)^{\mathrm{sym}}$ symmetric part of the gradient tensor: $(\nabla \boldsymbol{v})^{sym} = \dfrac{1}{2}(\nabla \boldsymbol{v} + (\nabla \boldsymbol{v})^{\mathrm{T}})$

$\nabla \cdot (\,)$ divergence with respect to $\boldsymbol{x}$: $(\nabla \cdot \boldsymbol{T}) \cdot \boldsymbol{a} = \nabla \cdot (\boldsymbol{T}^{\mathrm{T}} \boldsymbol{a})$;

$\nabla_{X} \cdot (\,)$ divergence with respect to $\boldsymbol{X}$.

Latin letters

A area;

$\boldsymbol{A}^{\alpha}$ material description of the acceleration;

$\boldsymbol{b}$ body forces;

$\boldsymbol{B}$ left Cauchy-Green deformation tensor;

C_1, C_2 machine-dependent parameters;

C_p, C_{v^s}, C_{v^f} convergence rates for pressure, solid velocity and fluid velocity, respectively.

$\boldsymbol{C}$ right Cauchy-Green deformation tensor;

$\mathbf{C}$ elasticity tensor;

$\boldsymbol{D}$ rate of deformation tensor;

$e(p)$, $e(v^s)$, $e(v^f)$ error norm for pressure, solid velocity and fluid velocity, respectively;

E Young's Modulus;

$\boldsymbol{E}$ Lagrangian or Green-Lagrange strain tensor;

f forces;

$\boldsymbol{F}$ deformation gradient;

$\bar{g}^{\alpha}$, $\frac{D^{\alpha}\bar{g}^{\alpha}}{Dt}$ prescribed displacement and prescribed velocity;

$\boldsymbol{g}^s$ nonlinear elasticity vector of the solid phase;

G shear modulus;

H_A aggregate modulus;

I_1, I_2, I_3 principal invariants of $\boldsymbol{C}$;

I_4, I_5 fourth and fifth invariants of $\boldsymbol{C}$ and $\boldsymbol{M}$;

J^{α} Jacobian determinant of the deformation;

$\boldsymbol{L}$ velocity gradient;

$\boldsymbol{m}$ vector of preferred orientation in the current configuration;

$\boldsymbol{m}_0$ vector of preferred orientation in the reference configuration;

$\boldsymbol{M} = \boldsymbol{m} \otimes \boldsymbol{m}$ structural tensor in the current configuration;

$\boldsymbol{M}_0 = \boldsymbol{m}_0 \otimes \boldsymbol{m}_0$ structural tensor in the reference configuration;

n_{et} number of elements;

n_{npe} number of nodes per element;

n_{pc} number of pressure coefficients per element;

n_{pn} number of pressure nodes per element;

n_{sd} number of space dimensions;

$\boldsymbol{n}$ unit outward normal vector to the boundary;

N^a shape function (a refers to a node number);

$\mathcal{N}^a$ pressure shape function (a refers to a vertex number or to a pressure coefficient);

$\boldsymbol{P}$ first Piola-Kirchhoff stress tensor;

p pressure;

q weighting function;

Q fluid flow;

$\boldsymbol{Q}$ proper orthogonal tensor ($\boldsymbol{Q} \in \mathrm{Orth}^+$);

$\boldsymbol{R}$ rotation tensor;

$\boldsymbol{S}$ second Piola-Kirchhoff stress tensor;

$\boldsymbol{S}_{\mathrm{E}}$ elastic part of the second Piola-Kirchhoff stress tensor;

t time;

t_{d} diffusion time;

$\boldsymbol{t}$ Cauchy stress vector;

$\bar{\boldsymbol{t}}$ prescribed tractions on the boundary;

$\boldsymbol{T}$ first Piola-Kirchhoff stress tensor;

$\boldsymbol{U}$ right stretch tensor;

$\boldsymbol{u}$ displacement;

V volume;

$\boldsymbol{V}$ left stretch tensor;

$\boldsymbol{V}^{\alpha}$ material description of the velocity;

$\boldsymbol{v}$ velocity;

$\tilde{\boldsymbol{v}}^{\alpha}$ diffusion velocity of the αth constituent;

$\boldsymbol{X}$ position vector in $\mathcal{B}$;

$\boldsymbol{x}$ position vector in $\mathcal{S}$;

W strain energy function per unit of undeformed volume;

$\boldsymbol{W}$ spin tensor;

$\boldsymbol{w}$ weighting function.

Greek letters

β penalty parameter;

ζ diffusive drag coefficient;

$\boldsymbol{\zeta}$ diffusive drag tensor;

η entropy density;

θ, Θ angle (polar cylindrical coordinates);

θ_0 absolute temperature of an isothermal mixture;

κ intrinsic permeability;

$\boldsymbol{\kappa}$ intrinsic permeability tensor;

λ stretch; $\lambda_i,\ i = 1, 2, 3$, principal stretches;

λ, μ Lamé constants;

ν Poissons's ratio;

$\boldsymbol{\xi}$ parent coordinates;

π linear momentum supply;

ρ mass density;

ρ^α apparent mass density of the αth constituent in the current configuration;

ρ_0^α apparent mass density of the αth constituent in the reference configuration;

ρ_T^α mass density of the αth constituent (true density);

$\boldsymbol{\sigma}$ Cauchy stress tensor;

$\boldsymbol{\sigma}_E$ elastic part of the Cauchy stress tensor;

τ normalized time;

$\boldsymbol{\tau}$ Kirchhoff stress tensor;

ϕ^α volume fraction of the αth constituent;

$\boldsymbol{\chi}$ deformation function;

ψ Helmholtz free energy function;

$\psi_{,a} = \dfrac{\partial \psi}{\partial I_a}$ partial derivative of Ψ with respect to I_a, $a = 1 \ldots 5$;

$\psi_{,ab} = \dfrac{\partial^2 \psi}{\partial I_a \partial I_b}$ second partial derivative of ψ with respect to I_a, $a, b = 1 \ldots 5$;

ω finite difference parameter.

Abstract

This thesis addresses finite element based computational models for the 3-D nonlinear analysis of soft hydrated tissues such as articular cartilage in diarthrodial joints under physiologically relevant loading conditions. A biphasic continuum description is used to represent the soft tissue as a two-phase mixture of incompressible inviscid fluid and a hyperelastic, transversely isotropic solid. The theoretical foundations of this theory are reviewed with emphasis on constitutive modeling. Alternate mixed-penalty and velocity-pressure finite element formulations are used to solve the nonlinear biphasic governing equations, including the effects of a strain-dependent permeability and a hyperelastic solid phase under finite deformation. The resulting first-order nonlinear system of equations are discretized in time using an implicit finite difference scheme, and solved using the Newton-Raphson method. Both formulations are used to develop quadrilateral and triangular elements in 2-D and hexahedral and tetrahedral elements in 3-D. Numerical examples, including those representative of soft tissue material testing and simple human joints, are used to validate the formulations and to illustrate their applications. While not the central objective of this work, important insights have been gained from selected linear biphasic analyses. A focus of this work is the comparison of the alternate formulations for nonlinear problems. While it is demonstrated that both formulations produce a range of converging elements, the velocity-pressure formulation is found to be more efficient computationally.

A significant contribution of this work is the implementation and testing of a biphasic description with a transversely isotropic hyperelastic solid phase. This description considers a Helmholtz free energy function of five invariants of the Cauchy-Green deformation tensor and the preferred direction of the material, allowing for asymmetric behavior in tension and compression. An exponential form is suggested, and a set of material parameters is identified to represent the response of soft tissues in ranges of deformation and stress observed experimentally. After demonstrating the behavior of this constitutive model in simple tension and compression, a sample problem of unconfined compression is used to further validate the finite element implementation.

CHAPTER 1

Introduction and Historical Review

I am sure that the greatest contribution of biomechanics to mechanics lies in its youthfulness. It brings mechanics back to a new formative stage, and asks it to be young again.

Y.- C. FUNG [33, p.14]

In the last fifteen years, an impressive body of work related to articular cartilage and other biological soft hydrated tissues has contributed to expand the "biphasic theory" based on the biphasic model presented by Mow *et al.* [70]. In that seminal work, and in subsequent experimental and theoretical studies extending it, the biphasic model represents biological soft hydrated tissues as a binary continuum mixture composed by a solid matrix immersed in interstitial fluid, and its strength lies in general assumptions and constitutive laws validated experimentally.

The biphasic model has many practical applications in biomechanics. Direct applications include: (a) the correlation between failure mechanisms in biological tissues and degenerative diseases; (b) the determination of tissue degradation based on mechanical and biochemical properties; (c) the comparison and evaluation of surgical procedures to replace damaged tissues, using biological or synthetic grafts; and (d) the development of synthetic material replacement for biological soft hydrated tissues. Applications aimed at understanding mechanisms fundamental to joint mechanics also exist. The representation of fluid flow within articular cartilage, for instance, is a prerequisite for understanding the mechanisms of lubrication, friction and wear that occur in diarthrodial joints. Such knowledge is necessary for modelling the deformational behavior of joints, and is essential for the development and evaluation of less invasive surgical procedures and prosthetic devices.

Virtually any physiological application of the biphasic continuum description implies the use of nonlinear and anisotropic constitutive models, irregular three-dimensional geometries, and complicated boundary conditions, characteristics that can only be simulated numerically. Even the investigation of constitutive laws for biological tissues, which depend on experiments performed

on small, inhomogeneous specimens, often requires solutions of corresponding continuum problems that are intractable analytically. Therefore, applications of the biphasic model require effective and reliable numerical methods, such as the finite element method, that can cope with all the characteristics mentioned above. The purpose of this investigation is to develop and evaluate finite element formulations to simulate the biphasic, anisotropic and nonlinear behavior of biological soft hydrated tissues, in particular articular cartilage. The work involves the development of alternate finite element formulations of the biphasic theory, and the computational implementation of a hyperelastic, transversely isotropic constitutive model.

1.1 Articular Cartilage

In this section articular cartilage and its constituents are briefly described, and structural features relevant to the finite element representation are reviewed. For complete discussions of this area and extensive lists of related references, see review papers by Woo *et al.* [117], Mow *et al.* [72, 73] and Setton and Mow [89].

The human musculoskeletal system contains a number of freely articulating joints called diarthrodial, or synovial, joints. Some examples are the ankle, knee, hip, shoulder, and elbow. Diarthrodial joints provide anatomical congruity and stability for a large range of loads and relative motions. They constitute excellent mechanisms for shock absorption and load transmission between the bones.

To illustrate the characteristics of articular cartilage in diarthrodial joints we will look at the knee. Figure 1.1 shows a schematic cross-section of the human knee, where contacts between the femoral condyle (lower base of the femur) and the tibial plateau (upper end of the tibia), and between the femoral condyle and the patella are emphasized. Thin layers of cartilage cover the articulating surfaces of the bones and, together with the meniscus, are enclosed in a fibrous capsule. A vascular membrane lines the inner surface of the fibrous capsule and is responsible for the production of synovial fluid that fills the joint cavity (the region surrounded by the cartilage surfaces and the fibrous capsule). Ligaments and tendons, together with the meniscus interposed

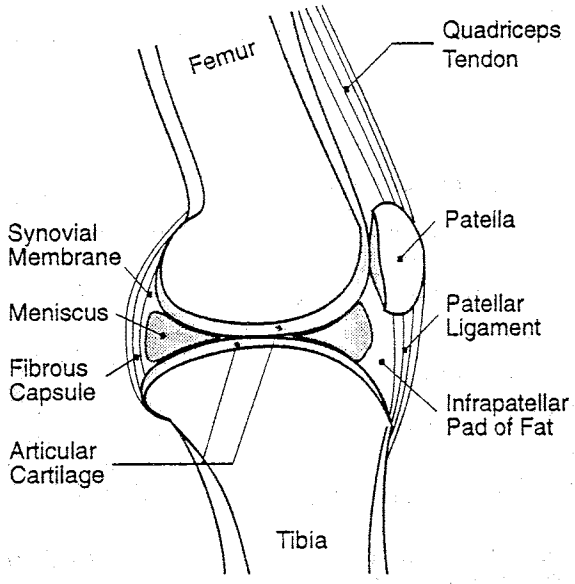

Figure 1.1 Schematic representation of the human knee joint.

between cartilage layers, contribute to the alignment of the bones and to the overall stability of the joint.

Articular cartilage works as a bearing element in the joint and consists of an avascular and aneural layer of soft tissue. It is composed of a solid matrix of collagen fibrils and proteoglycan aggregates saturated with interstitial fluid (Fig. 1.2). Articular cartilage exhibits anisotropic properties that reflect the orientation of collagen fibrils in planes parallel and perpendicular to the articular surface. The fibril orientation follows certain patterns according to the cartilage zone. As shown in Fig. 1.2 (a), fibrils are organized parallel to the surface on the superficial tangential zone, becoming thicker and more randomly oriented in the middle zone. In the deep zone fibrils form bundles which are inserted into the calcified cartilage, providing support for the tissue on the subchondral bone.

Interstitial fluid, basically water and electrolytes, is the major constituent of articular cartilage (with 60 to 85% of the total weight), followed by collagen (15 to 22%), proteoglycan (4 to 7%), and other constituents [72, 89]. The distribution of the constituents is inhomogeneous

throughout the thickness. The water content and collagen content decrease with depth, being higher in the superficial tangential zone. The opposite occurs with proteoglycans, with higher contents in the deeper zones.

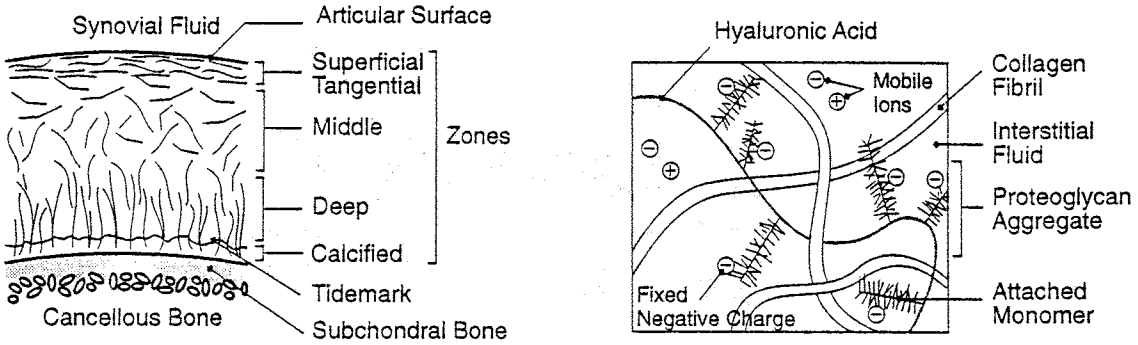

Figure 1.2 Structural features of articular cartilage: (a) orientation of the collagen network in different zones of the cartilage layer; (b) schematic representation of the molecular organization. Figures based on drawings presented in Mow *et al.* [72].

Proteoglycan monomers, being negatively charged and restrained within the tissue, are associated with the swelling pressure of articular cartilage. First, the high density of the fixed charges within the tissue induces repulsive forces between charged groups and between proteoglycan monomers. Second, the fixed charges give rise to concentrations of counter-ions, whose imbalance is responsible for the Donnan osmotic pressure in the tissue. The electro- and physicochemical properties and the stiffness of the collagen-proteoglycan network determine the overall compressive stiffness of the tissue. On the other hand, the tensile stiffness depends mainly on the collagen fibrils, with the entanglement with proteoglycans aggregates contributing indirectly through the pre-stretching of the collagen network.

1.2 Constitutive Model

Articular cartilage was first modelled as a single-phase elastic material and solutions to the associated continuum representations were obtained using the theory of elasticity. Poor correlation

with experimental results, however, indicated the need to incorporate viscous effects in order to explain the time-dependent response and incomplete recovery after unloading. The viscoelastic models that followed were able to represent the creep and stress-relaxation phenomena. Nevertheless, they were inadequate for articular cartilage because they cannot represent the transient stresses caused by the fluid flow within the tissue.

In order to include flow-dependent effects in the constitutive model, Mow *et al.* [70] developed the biphasic model for soft hydrated tissues based on the theory of mixtures of Truesdell and Toupin [109]. The biphasic model describes articular cartilage as a mixture of two immiscible and intrinsically incompressible constituents: a porous and permeable solid matrix of collagen and proteoglycans saturated with interstitial fluid. It is assumed that the interaction between solid and fluid phases is the major factor responsible for the apparent viscoelastic behavior in compression. The biphasic theory has been validated experimentally for articular cartilage under various loading conditions [2, 65, 69]. Its current form considers strain-dependent permeability [42-44, 61], finite deformation and hyperelasticity [43, 44, 57, 58, 71, 105], including anisotropic hyperelastic materials [24]. A triphasic model has also been developed based on the theory of mixtures [59]. This model has an additional ion phase representing the dissolved solute concentration, and can predict the Donnan osmotic pressure and the chemical-expansion stress responsible for the swelling of the cartilage.

1.3 Finite Element Formulations

Some background on types and titles of finite element formulations for biphasic continua may help. For purposes of this discussion we refer to biphasic or poroelastic models as "dynamic" if the inertial terms are included in the momentum equations. Quasistatic models are those for which the inertial effects can be neglected. On the other hand, quasistatic formulations for biphasic continua with intrinsically incompressible constituents can be classified in three broad groups:

a) *penalty* and *mixed-penalty* formulations, where the continuity condition is imposed using a penalty parameter;

b) *mixed* $\boldsymbol{u}$-p formulations, where the linear momentum equation for the fluid is used to eliminate the fluid velocity, and the pressure is continuously interpolated between elements;

c) *hybrid* formulations, where the momentum equation for the mixture is satisfied exactly and equilibrated stress/pressure are interpolated.

To our knowledge, nonlinear hybrid formulations for biphasic continuum have not been developed. Readers interested in linear hybrid formulations can consult the papers of Vermilyea and Spilker [112, 113]. Formulations considering compressible constituents are common in soil mechanics and can be specialized for incompressible constituents. The resulting formulations admit one of the following classifications: mixed $\boldsymbol{u}$-p, if the pressure appears as unknown, and penalty with reduced integration, if it does not. In the discussions which follow, formulations are identified using the following designations: p (or π) denotes the pressure, $\boldsymbol{u}$ and $\boldsymbol{U}$ denotes solid and fluid kinematic unknowns (displacements, velocities, accelerations, or corresponding increments), and $\boldsymbol{w}$ denotes a kinematic unknown that describes the relative motion of the fluid phase with respect to the solid phase.

Finite element formulations based on the poroelastic theory of Biot [10, 11] were first developed in soil mechanics. The linear $\boldsymbol{u}$-p formulation of Sandhu and Wilson was presented in 1969 [88], followed by the dynamic $\boldsymbol{u}$-$\boldsymbol{w}$ formulation of Ghaboussi and Wilson in 1972 [37]. Zienkiewicz *et al.* [119] and Carter *et al.* [22] presented elastoplastic formulations considering large deformations. Prevost used the framework of the theory of mixtures to derive constitutive models for elastoplastic and path-dependent soils [81]. He developed nonlinear $\boldsymbol{u}$-p and $\boldsymbol{u}$-$\boldsymbol{U}$ formulations to investigate consolidation [83] and the dynamic response of saturated soils [82, 84].

In biomechanics, Oomens *et al.* [79, 80] presented a nonlinear $\boldsymbol{u}$-p formulation based on the theory of mixtures to study porcine skin. In their theory, a simplified form of Fung's exponential strain energy function [34] was used to represent the solid matrix. A similar formulation was presented for articular cartilage by Wayne *et al.* [115], who adopted one of the Helmholtz free

energy functions proposed by Kwan *et al.* [57]. Simon and Gaballa [92], and Yuan and Simon [118] presented nonlinear ***u-p*** and ***u-w*** formulations based on the poroelastic theory of Biot to study arterial walls.

Spilker and Suh [100] presented a penalty finite element formulation of the linear biphasic mixture equations for soft tissues, and used that formulation to develop a 4-node, axisymmetric biphasic element. This formulation was extended later to include the nonlinearity due to strain-dependent permeability, finite deformation and a hyperelastic solid phase [105]. The mixed-penalty formulation for the linear biphasic model was presented by Spilker and Maxian [99]. For a six-node triangle, it was found that the linear mixed-penalty approach was superior to the standard penalty formulation, justifying the extension of this formulation to contact problems and to nonlinear problems. Donzelli [27, 28] used the mixed-penalty triangle to implement the contact condition for biphasic materials derived by Hou *et al.* [46]. As for nonlinear problems, initial results of this thesis have already been presented [97, 98], confirming the accuracy of the mixed-penalty triangle in numerical simulations of nonlinear confined compression problems.

Studies comparing finite element formulations for biphasic continua exist in the literature of soil mechanics and biomechanics. Formulations for soil dynamics are discussed by Zienkiewicz and Shiomi [120]. Higher-order one-dimensional elements were evaluated by Simon *et al.* [93], who also compared the ***u-p*** and ***u-w*** formulations using various time-integration schemes [94]. Insights into the ***u-p*** and ***u-U*** formulations were presented by Mish *et al.* [68]. There is an agreement upon the use of the ***u-p*** formulation in consolidation problems (quasistatic), and the use of the ***u-U*** and the ***u-w*** formulations in dynamic problems. However, issues concerning the loss of accuracy at early times [85], hyperelastic materials and strain-dependent permeability were not covered. In biomechanics, Spilker *et al.* [101] discussed the differences between penalty, mixed-penalty and hybrid finite formulations for biphasic continua.

While a number of studies of biphasic and poroelastic models have been performed, there is still relatively little known about the relative merits of the finite element formulations when applied to the 3-D, nonlinear, hyperelastic problems with strain-dependent permeability. This the-

sis addresses two alternate formulations, a mixed-penalty and a velocity-pressure formulations, for such problems and considers a number of 2-D and 3-D elements with each formulation. The intention is to provide guidelines toward identifying a superior formulation and element for such analyses. A relevant part of this work is the inclusion of a transversely isotropic hyperelastic solid phase in the biphasic finite element model. Within this development, a particular free energy function is suggested and evaluated. Example problems related to material testing configurations and simple, clinically-relevant problems are used to evaluated the methods.

1.4 Layout of this Thesis

A brief summary of the main contents in each chapter of this thesis is given below.

In the next chapter, the kinematics and axioms of the theory of mixtures are reviewed. Basic concepts, notation and definitions are introduced for later reference in the derivation of general forms of constitutive equations. At the end, the main assumptions of the biphasic theory are employed to derive balance equations and the entropy inequality.

Chapter 3 covers the theory necessary for the implementation of anisotropic materials. The general framework used to study constitutive equations is reviewed, including possible restrictions upon these equations. Experimental assumptions simplifying the form of constitutive equations are discussed, followed by examples of Helmholtz free energy functions for soft hydrated tissues found in the literature. The theory is then used to derive the elasticity tensor for transversely isotropic materials. The chapter ends with a summary of the governing equations for biphasic problems.

The extension of the biphasic mixed-penalty (MP) formulation to nonlinear problems is a major contribution of this study. The complete derivation plus the algorithm used to solve the nonlinear system of equations are presented in Chapter 4. In a manner parallel to incompressible media formulations, the use of a discrete divergence operator in the nonlinear penalty formulation leads to the equivalence with the MP formulation, a result that is shown here for the first time. A

variant of the $\boldsymbol{u}$-p formulation, called $\boldsymbol{v}$-p to emphasize that increments of velocity are used as unknowns, is also reviewed taking advantage of the development for the MP formulation.

Chapter 5 is dedicated to the finite elements used in the MP and $\boldsymbol{v}$-p formulations. The linear version of the confined compression creep problem is used to access element behavior and performance. In Chapter 6, several nonlinear problems are solved using two- and three-dimensional elements to demonstrate their capabilities.

The computational implementation of transversely isotropic materials is validated in Chapter 7. In this process an exponential Helmholtz free energy function is tested in its ability to represent the asymmetric behavior in tension and compression characteristic of biological tissues.

Concluding remarks and suggestions for future studies are found in Chapter 8.

CHAPTER 2

Field Equations for a Biphasic Mixture

"... To develop the general theory the notation alone can be overwhelming as it usually involves several alphabets and multiple layers of subscripts."

M. H. HOLMES [45, P. II.1]

This chapter introduces the field equations of a biphasic mixture based on the theory of mixtures of Truesdell and Toupin [109]. First the kinematics and axioms of the theory of mixtures for an arbitrary number of constituents are presented. The assumptions enunciated by Mow *et al.* [70] are then used to derive the field equations for a biphasic mixture under finite deformation. As in Mow *et al.* [70], we adopt a notation and a nomenclature that is almost standard in the continuum mechanics of a single-phase continuum [40, 66, 67].

The current framework of the theory of mixtures was developed by, among others, Bowen [18], Atkin and Craine [3, 4], and Bedford [8]. The papers by Bowen, and Atkin and Craine greatly contributed to resolving the uncertainties about the entropy inequality of a mixture, a polemic subject that "survived" the 1960's without general acceptance. Each of the above references is a thorough and updated review of the original theory proposed by Truesdell [107] and, together with a paper by Bowen [19], constitute the main references for the next two sections. The outline of this chapter is similar to that used by Kwan [58], Mow *et al.* [71], Holmes *et al.* [43], Suh [103], and Cohen [24]; the main difference is the emphasis on issues related to the finite element implementation.

2.1 Kinematics of a Mixture

A *mixture* can be seen as a superposition of deformable continua, or constituents, that occupy the same domain Ω in three-dimensional (3-D) space at the current time t. In order to represent the motion of the mixture, quantities associated with the motions of the constituents and the mixture as a whole must be defined. Let $\mathcal{B}^\alpha$ denote the *current configuration* of the αth continuum, or *constituent*, whose domain Ω^α and boundary Γ^α are shared with other constituents at

time t (Fig. 2.1). Each constituent follows an independent motion and has a fixed but otherwise arbitrary *reference configuration* $\mathcal{B}_0^\alpha$ occupying a domain Ω_0^α at time t_0.

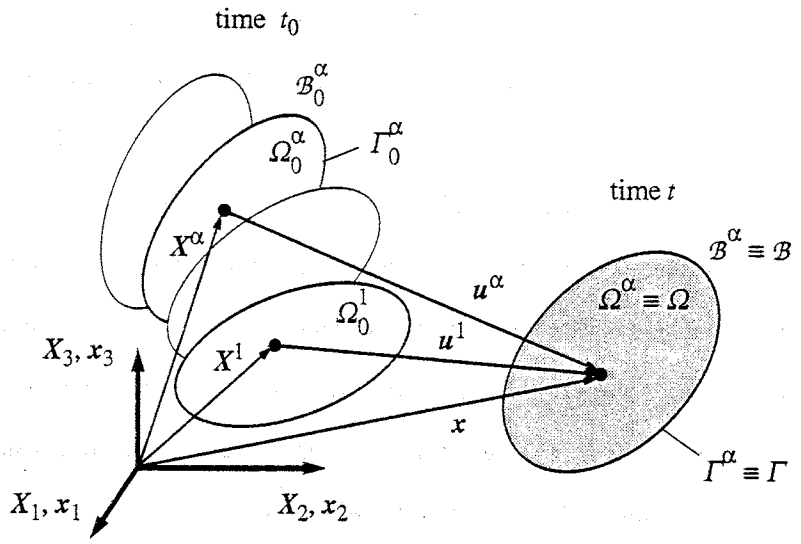

Figure 2.1 The kinematics of a mixture.

Let X^α denote the position of a particle of the αth constituent in its reference configuration. In the current configuration, the position of this particle is given by

$$x^\alpha = x = \chi^\alpha(X^\alpha, t)\,, \tag{2-1}$$

where χ^α is the *deformation function* of the αth constituent, which is assumed to be smooth and invertible such that $X^\alpha = (\chi^\alpha)^{-1}(x, t)$. The *velocity* and *acceleration* fields of each constituent are defined, respectively, as

$$V^\alpha(X^\alpha, t) = \frac{\partial}{\partial t}\chi^\alpha(X^\alpha, t)\bigg|_{X^\alpha}\,, \tag{2-2}$$

$$A^\alpha(X^\alpha, t) = \frac{\partial^2}{\partial t^2}\chi^\alpha(X^\alpha, t)\bigg|_{X^\alpha}\,. \tag{2-3}$$

Using the inverse of the deformation function, we can rewrite the velocity as a function v^{α} of the current position x:

$$v^{\alpha}(x, t) = V^{\alpha}((\chi^{\alpha})^{-1}(x, t), t), \tag{2-4}$$

where v^{α} is called the *spatial* or *current* description of the velocity, while V^{α} is called the *material* or *reference* description. When a common system of reference is used for the position vectors x^{α} and X^{α}, the *displacement* field is defined as $u^{\alpha}(X^{\alpha}, t) = x - X^{\alpha}$.

As in the continuum mechanics of a single-phase continuum [40, 66, 67], the *deformation gradient* F^{α} and the *velocity gradient* L^{α} of each constituent are linear transformations defined as

$$F^{\alpha} = \nabla_{X^{\alpha}} x = \frac{\partial x}{\partial X^{\alpha}}, \tag{2-5}$$

$$L^{\alpha} = \nabla v^{\alpha} = \frac{\partial v^{\alpha}}{\partial x}, \tag{2-6}$$

where ∇ is the gradient operator, and $\nabla_{X^{\alpha}}$ denotes the gradient operator with regard to reference coordinates. The *Jacobian determinant of the deformation* is given by

$$J^{\alpha} = \det(F^{\alpha}), \tag{2-7}$$

while the *right* and *left Cauchy-Green deformation tensors* are defined, respectively, as

$$C^{\alpha} = F^{\alpha T} F^{\alpha}, \qquad B^{\alpha} = F^{\alpha} F^{\alpha T}. \tag{2-8}$$

These two tensors have the same principal invariants given by

$$I_1^{\alpha} = \operatorname{tr} C^{\alpha}, \qquad I_2^{\alpha} = \frac{1}{2}\left[(\operatorname{tr} C^{\alpha})^2 - \operatorname{tr} C^{\alpha 2}\right], \qquad I_3^{\alpha} = \det C^{\alpha}. \tag{2-9}$$

The *rate of deformation tensor* D^{α} is the symmetric part of L^{α}, and is given by

$$D^{\alpha} = \frac{1}{2}\left[\nabla v^{\alpha} + (\nabla v^{\alpha})^{T}\right]. \tag{2-10}$$

In what follows we consider an *immiscible* mixture, for which both the mass m_e^α and the volume V_e^α of the αth constituent are well defined when an *element of volume* V_e of the mixture is given. The *apparent density* ρ^α and the *true density* ρ_T^α are then defined as

$$\rho^\alpha(x, t) = \lim_{V_e \to 0} \frac{m_e^\alpha}{V_e}, \tag{2-11}$$

$$\rho_T^\alpha(x, t) = \lim_{V_e^\alpha \to 0} \frac{m_e^\alpha}{V_e^\alpha}. \tag{2-12}$$

In reality, V_e and V_e^α must be such that the average material properties and mechanical interactions computed within elements of volume are representative of the mixture, not a separate constituent, around a position x. Note that if a constituent is assumed to be *intrinsically incompressible*, its true density remains constant during the process. The *volume fraction* ϕ^α of the αth constituent is defined as

$$\phi^\alpha(x, t) = \lim_{V_e \to 0} \frac{V_e^\alpha}{V_e} = \frac{\rho^\alpha}{\rho_T^\alpha}, \tag{2-13}$$

and, consequently,

$$\sum_\alpha \phi^\alpha = 1. \tag{2-14}$$

The previous definitions are associated with an arbitrary constituent. Let us now define functions associated with the mixture as a whole, starting with the *density of the mixture* defined as

$$\rho(x, t) = \sum_\alpha \rho^\alpha(x, t). \tag{2-15}$$

If the fields, say $f^\alpha(x, t)$, of all constituents are given, the *baricentric* or *mean* function $f(x, t)$ of the mixture is defined as a mass-weighted average given by

$$f(x,t) = \frac{1}{\rho}\sum_{\alpha}\rho^{\alpha} f^{\alpha}(x,t). \tag{2-16}$$

Thus, the *baricentric velocity*, which corresponds to the velocity of the center of mass of the mixture, is

$$v(x,t) = \frac{1}{\rho}\sum_{\alpha}\rho^{\alpha} v^{\alpha}. \tag{2-17}$$

Two kinds of *material derivatives* are defined in the theory of mixtures: one following the motion of the αth constituent,

$$\frac{D^{\alpha}\varphi^{\alpha}}{Dt} = \frac{\partial\varphi^{\alpha}}{\partial t} + v^{\alpha}\cdot\nabla\varphi^{\alpha}, \qquad \frac{D^{\alpha}w^{\alpha}}{Dt} = \frac{\partial w^{\alpha}}{\partial t} + (\nabla w^{\alpha})\,v^{\alpha}, \tag{2-18}$$

and another following the motion of the center of mass of the mixture,

$$\frac{D\varphi^{\alpha}}{Dt} = \frac{\partial\varphi^{\alpha}}{\partial t} + v\cdot\nabla\varphi^{\alpha}, \qquad \frac{Dw^{\alpha}}{Dt} = \frac{\partial w^{\alpha}}{\partial t} + (\nabla w^{\alpha})\,v, \tag{2-19}$$

where φ^{α} and w^{α} are spatially smooth scalar and vector valued fields, respectively. The material derivatives are related by

$$\frac{D^{\alpha}\varphi^{\alpha}}{Dt} = \frac{D\varphi^{\alpha}}{Dt} + \tilde{v}^{\alpha}\cdot\nabla\varphi^{\alpha}, \qquad \frac{D^{\alpha}w^{\alpha}}{Dt} = \frac{Dw^{\alpha}}{Dt} + (\nabla w^{\alpha})\,\tilde{v}^{\alpha}, \tag{2-20}$$

where $\tilde{v}^{\alpha}$ is the *diffusion velocity* of the αth constituent, and is defined as

$$\tilde{v}^{\alpha} = v^{\alpha} - v. \tag{2-21}$$

Finally, the material derivative of a baricentric function φ is related to the material derivatives of the corresponding functions φ^{α} of the constituents through the identity [18]:

$$\rho\frac{D\varphi}{Dt} = \sum_{\alpha}\left[\rho^{\alpha}\frac{D^{\alpha}\varphi^{\alpha}}{Dt} - \nabla\cdot(\rho^{\alpha}\varphi^{\alpha}\tilde{v}^{\alpha}) + \hat{c}^{\alpha}\rho^{\alpha}\right], \tag{2-22}$$

where $\hat{c}^{\alpha}$ represents the mass supply as will be defined in Subsection 2.2.1.

2.2 Field Equations for a Mixture

The thermodynamical processes of mixtures are embraced by the same axioms postulated for a single-phase continuum: the balance equations of mass, linear and angular momenta, the balance equation of energy, and the entropy inequality. The first three axioms correspond to the principles of mechanics while the last two correspond to the first and second laws of thermodynamics. In the theory of mixtures, the four balance axioms are stated for each constituent, and new terms are provided to account for the interactions among constituents. There are also four balance equations for the mixture as a whole. They are postulated based on the Principle of Mixtures, which states that the equations for the mixture should have the same form as those for a single constituent [4]. Alternative forms of these equations, directly restricting the interaction among constituents, are derived by enforcing compatibility between the equations for the mixture and the sums of the corresponding equations for the constituents. The entropy inequality, unlike the other axioms, is stated only for the mixture as a whole, and so it is essential for defining the admissible form of the constitutive equations, even for mechanical theories.

2.2.1 Balance of Mass

For a fixed domain Ω bounded by a surface Γ, the axiom of *balance of mass* for the αth constituent is expressed as

$$\frac{\partial}{\partial t}\int_{\Omega}\rho^{\alpha}d\Omega+\int_{\Gamma}\rho^{\alpha}\boldsymbol{v}^{\alpha}\cdot\boldsymbol{n}d\Gamma=\int_{\Omega}\hat{c}^{\alpha}d\Omega, \tag{2-23}$$

where $\hat{c}^{\alpha}$ is the *mass supply*, representing the rate of mass transferred per unit of volume from other constituents. With the use of the divergence theorem, the local form of Eq. (2-23) can be written as

$$\frac{\partial\rho^{\alpha}}{\partial t}+\nabla\cdot(\rho^{\alpha}\boldsymbol{v}^{\alpha})=\hat{c}^{\alpha}. \tag{2-24}$$

Since the total mass must be preserved, the axiom of *balance of mass for the mixture* is postulated as

$$\frac{\partial \rho}{\partial t} + \nabla \cdot (\rho \boldsymbol{v}) = 0. \tag{2-25}$$

From the comparison of Eq. (2-25) with the sum of the Eqs. (2-24) for all constituents, it follows that

$$\sum_{\alpha} \hat{c}^{\alpha} = 0. \tag{2-26}$$

In this work we are concerned with mixtures whose constituents are immiscible ($\rho^{\alpha} = \phi^{\alpha} \rho_{\mathrm{T}}^{\alpha}$) and intrinsically incompressible ($D^{\alpha} \rho_{\mathrm{T}}^{\alpha} / Dt = 0$). For these mixtures, it is convenient to eliminate the densities of the constituents in favor of their volume fractions and thus to replace Eq. (2-24) with

$$\frac{\partial \phi^{\alpha}}{\partial t} + \nabla \cdot (\phi^{\alpha} \boldsymbol{v}^{\alpha}) = \frac{\hat{c}^{\alpha}}{\rho_{\mathrm{T}}^{\alpha}}. \tag{2-27}$$

The sum of the Eqs. (2-27) for all constituents produces the *continuity equation for the mixture*:

$$\sum_{\alpha} \nabla \cdot (\phi^{\alpha} \boldsymbol{v}^{\alpha}) = \sum_{\alpha} \frac{\hat{c}^{\alpha}}{\rho_{\mathrm{T}}^{\alpha}}, \tag{2-28}$$

where use has been made of Eq. (2-14).

2.2.2 Balance of Linear Momentum

The axiom of *balance of linear momentum* for the αth constituent is expressed as

$$\frac{\partial}{\partial t} \int_{\Omega} \rho^{\alpha} \boldsymbol{v}^{\alpha} d\Omega + \int_{\Gamma} \rho^{\alpha} \boldsymbol{v}^{\alpha} (\boldsymbol{v}^{\alpha} \cdot \boldsymbol{n}) \, d\Gamma = \int_{\Gamma} \boldsymbol{t}^{\alpha} d\Gamma + \int_{\Omega} \left(\rho^{\alpha} \boldsymbol{b}^{\alpha} + \boldsymbol{\pi}^{\alpha} + \hat{c}^{\alpha} \boldsymbol{v}^{\alpha} \right) d\Omega, \tag{2-29}$$

where $\boldsymbol{b}^{\alpha}$ is the *external body force* per unit of mass, $\boldsymbol{\pi}^{\alpha}$ is the *momentum supply* per unit of volume (also called *local* or *internal* body force) and $\boldsymbol{t}^{\alpha}$ is the *external traction force*. The term $(\boldsymbol{\pi}^{\alpha} + \hat{c}^{\alpha} \boldsymbol{v}^{\alpha})$ results from the interaction with other constituents. The tetrahedron argument

[109], also known as Cauchy's fundamental lemma [62], is employed to establish the existence of the partial stress tensor $\boldsymbol{\sigma}^{\alpha}$ such that

$$\boldsymbol{\sigma}^{\alpha}\boldsymbol{n} = \boldsymbol{t}^{\alpha}. \tag{2-30}$$

Introducing this equation into Eq. (2-29), and applying the divergence theorem to obtain the local form, yields

$$\rho^{\alpha}\frac{D^{\alpha}\boldsymbol{v}^{\alpha}}{Dt} = \nabla\cdot\boldsymbol{\sigma}^{\alpha} + \rho^{\alpha}\boldsymbol{b}^{\alpha} + \boldsymbol{\pi}^{\alpha}. \tag{2-31}$$

The axiom of *balance of linear momentum for the mixture* is postulated as

$$\rho\frac{D\boldsymbol{v}}{Dt} = \nabla\cdot\boldsymbol{\sigma} + \rho\boldsymbol{b}, \tag{2-32}$$

where $\boldsymbol{b} = (1/\rho)\sum_{\alpha}\rho^{\alpha}\boldsymbol{b}^{\alpha}$ is the *external body force* per unit of mass, and the stress tensor for the mixture is defined as [109]

$$\boldsymbol{\sigma} = \sum_{\alpha}(\boldsymbol{\sigma}^{\alpha} - \rho^{\alpha}(\tilde{\boldsymbol{v}}^{\alpha}\otimes\tilde{\boldsymbol{v}}^{\alpha})). \tag{2-33}$$

The requirement that the sum of the linear momentum equations for the constituents is equal to Eq. (2-32) produces the following condition for the mixture:

$$\sum_{\alpha}(\boldsymbol{\pi}^{\alpha} + \hat{\boldsymbol{c}}^{\alpha}\tilde{\boldsymbol{v}}^{\alpha}) = \boldsymbol{0}. \tag{2-34}$$

2.2.3 Balance of Angular Momentum

The axiom of *balance of angular momentum* (or *moment of momentum*) for the αth constituent is expressed as

$$\begin{aligned}&\frac{\partial}{\partial t}\int_{\Omega}\rho^{\alpha}\boldsymbol{x}\times\boldsymbol{v}^{\alpha}\,d\Omega + \int_{\Gamma}\rho^{\alpha}\boldsymbol{x}\times\boldsymbol{v}^{\alpha}(\boldsymbol{v}^{\alpha}\cdot\boldsymbol{n})\,d\Gamma = \\ &\int_{\Gamma}\boldsymbol{x}\times(\boldsymbol{\sigma}^{\alpha}\boldsymbol{n})\,d\Gamma + \int_{\Omega}\left[\boldsymbol{x}\times\left(\rho^{\alpha}\boldsymbol{b}^{\alpha} + \boldsymbol{\pi}^{\alpha} + \hat{\boldsymbol{c}}^{\alpha}\boldsymbol{v}^{\alpha}\right) + \hat{\boldsymbol{m}}^{\alpha}\right]d\Omega,\end{aligned} \tag{2-35}$$

where $\hat{m}^{\alpha}$ is the angular momentum supply, and the last integral, except for the external body forces, is due to the interaction with other constituents. The local form of Eq. (2-35) can be written as

$$\hat{M}^{\alpha} = \sigma^{\alpha} - \sigma^{\alpha T}, \tag{2-36}$$

where $\hat{M}^{\alpha}$ is the skew-symmetric tensor associated with the vector $\hat{m}^{\alpha}$:

$$\hat{M}^{\alpha} = \begin{bmatrix} 0 & m_3^{\alpha} & -m_2^{\alpha} \\ -m_3^{\alpha} & 0 & m_1^{\alpha} \\ m_2^{\alpha} & -m_1^{\alpha} & 0 \end{bmatrix}. \tag{2-37}$$

It is clear from Eq. (2-36) that the stress tensor σ^{α} is symmetric in the absence of angular momentum supplies.

The *axiom of angular momentum for the mixture* is postulated as

$$\rho \frac{D}{Dt}\left(x \times \frac{Dv}{Dt} \right) = \nabla \cdot (x \times \sigma) + \rho\, x \times b, \tag{2-38}$$

from which results the symmetry of the total stress tensor ($\sigma = \sigma^{T}$). Adding Eqs. (2-36) for all constituents, and making use of the symmetry of σ, yields the following equation for the mixture

$$\sum_{\alpha} \hat{m}^{\alpha} = 0. \tag{2-39}$$

2.2.4 Balance of Energy

The axiom of *balance of energy* (or *first axiom of thermodynamics)* for the αth constituent is expressed as

$$\begin{aligned} &\frac{\partial}{\partial t}\int_{\Omega} \rho^{\alpha}\left(\varepsilon^{\alpha} + \frac{1}{2} v^{\alpha 2} \right) d\Omega + \int_{\Gamma} \rho^{\alpha}\left(\varepsilon^{\alpha} + \frac{1}{2} v^{\alpha 2} \right) v^{\alpha} \cdot n\, d\Gamma = \\ &\int_{\Gamma}\left(\sigma^{\alpha T} v^{\alpha} - q^{\alpha} \right) \cdot n\, d\Gamma + \int_{\Omega}\left[\rho^{\alpha} r^{\alpha} + \left(\rho^{\alpha} b^{\alpha} + \pi^{\alpha} \right) \cdot v^{\alpha} + \hat{\varepsilon}^{\alpha} + \hat{c}^{\alpha}\left(\varepsilon^{\alpha} + \frac{1}{2} v^{\alpha 2} \right) \right] d\Omega, \end{aligned} \tag{2-40}$$

where $v^{\alpha 2} = v^{\alpha} \cdot v^{\alpha}$, ε^{α} is the *internal energy density* (or specific internal energy [45]) of the αth constituent, q^{α} is the *heat flux vector*, r^{α} is the *external heat supply density* per unit of mass, and $\hat{\varepsilon}^{\alpha}$ is the *energy supply* to the αth constituent, which accounts for the energy interactions, just as π^{α} accounts for the linear momentum interactions. The left-hand side of Eq. (2-40) corresponds to the rate of change in the internal and kinetic energies within a fixed domain Ω plus the rate of change in energy associated with mass influx. With the use of the divergence theorem, the local form of the above equation is obtained:

$$\rho^{\alpha} \frac{D^{\alpha} \varepsilon^{\alpha}}{Dt} = \sigma^{\alpha} : L^{\alpha} - \nabla \cdot q^{\alpha} + \rho^{\alpha} r^{\alpha} + \hat{\varepsilon}^{\alpha}, \tag{2-41}$$

where L^{α} denotes the gradient of velocity of the αth constituent.

The axiom of *balance of energy for the mixture* can be written as

$$\rho \frac{D\varepsilon}{Dt} = \sigma : L - \nabla \cdot q + \rho r + \sum_{\alpha} \rho^{\alpha} \tilde{v}^{\alpha} \cdot b^{\alpha}, \tag{2-42}$$

where r is the *external heat supply density* for the mixture,

$$r = \frac{1}{\rho} \sum_{\alpha} \rho^{\alpha} r^{\alpha}, \tag{2-43}$$

ε is the *internal energy density* for the mixture,

$$\varepsilon = \varepsilon_{\mathrm{I}} + \frac{1}{2\rho} \sum_{\alpha} \rho^{\alpha} \tilde{v}^{\alpha} \cdot \tilde{v}^{\alpha}, \qquad \varepsilon_{\mathrm{I}} = \frac{1}{\rho} \sum_{\alpha} \rho^{\alpha} \varepsilon^{\alpha}, \tag{2-44}$$

and q is the *heat flux vector* for the mixture,

$$q = q_{\mathrm{I}} + \frac{1}{2} \sum_{\alpha} \rho^{\alpha} (\tilde{v}^{\alpha} \cdot \tilde{v}^{\alpha}) \tilde{v}^{\alpha}, \qquad q_{\mathrm{I}} = \sum_{\alpha} \left(q^{\alpha} - \sigma^{\alpha \mathrm{T}} \tilde{v}^{\alpha} + \rho^{\alpha} \varepsilon^{\alpha} \tilde{v}^{\alpha} \right), \tag{2-45}$$

with ε_{I} being the *inner part of the internal energy density,* and q_{I} being the *inner part of the heat flux vector.*

The derivation of the condition that enforces compatibility between the balance equations for the constituents, Eq. (2-41), and for the mixture, Eq. (2-42), can be found in Bowen [18]; the resulting equation is:

$$\sum_{\alpha}\left[\hat{\varepsilon}^{\alpha}+\hat{c}^{\alpha}\left(\varepsilon^{\alpha}+\frac{1}{2}\tilde{v}^{\alpha}\cdot\tilde{v}^{\alpha}\right)+\pi^{\alpha}\cdot\tilde{v}^{\alpha}\right]=0. \tag{2-46}$$

2.2.5 The Second Axiom of Thermodynamics

The *entropy inequality* for the mixture (or *second axiom of thermodynamics*), is postulated as [18]

$$\frac{\partial}{\partial t}\int_{\Omega}\rho\eta d\Omega+\int_{\Gamma}\rho\eta v^{\alpha}\cdot n d\Gamma\geq-\int_{\Gamma}\sum_{\alpha}\frac{\boldsymbol{h}^{\alpha}}{\theta^{\alpha}}\cdot n d\Gamma+\int_{\Omega}\sum_{\alpha}\frac{\rho^{\alpha}r^{\alpha}}{\theta^{\alpha}}d\Omega, \tag{2-47}$$

where $\boldsymbol{h}^{\alpha}$ is the *influx vector*, and θ^{α} is the absolute temperature for the αth constituent. The equal sign holds for reversible processes, and the symbol η denotes the *entropy density for the mixture*, which is defined as

$$\eta=\frac{1}{\rho}\sum_{\alpha}\rho^{\alpha}\eta^{\alpha}(x,t), \tag{2-48}$$

with η^{α} being the *entropy density* assigned to each constituent. Following Bowen [18], the following relationship is assumed between the influx vector and the heat flux vector:

$$\boldsymbol{h}^{\alpha}=\boldsymbol{q}^{\alpha}+\theta^{\alpha}\rho^{\alpha}\eta^{\alpha}\tilde{v}^{\alpha}. \tag{2-49}$$

With this assumption, the local form of Eq. (2-47) becomes

$$\rho\frac{D\eta}{Dt}+\nabla\cdot\sum_{\alpha}\left(\frac{\boldsymbol{q}^{\alpha}}{\theta^{\alpha}}+\rho^{\alpha}\eta^{\alpha}\tilde{v}^{\alpha}\right)-\sum_{\alpha}\frac{\rho^{\alpha}r^{\alpha}}{\theta^{\alpha}}\geq 0. \tag{2-50}$$

Equation (2-22) can be used to eliminate the entropy density for the mixture, yielding

$$\sum_{\alpha}\left[\rho^{\alpha}\frac{D^{\alpha}\eta^{\alpha}}{Dt}+\nabla\cdot\left(\frac{\boldsymbol{q}^{\alpha}}{\theta^{\alpha}}\right)-\frac{\rho^{\alpha}r^{\alpha}}{\theta^{\alpha}}+\hat{c}^{\alpha}\eta^{\alpha}\right]\geq 0. \tag{2-51}$$

Using Eq. (2-41) to eliminate the term $\rho^\alpha r^\alpha$, produces

$$\sum_\alpha \frac{1}{\theta^\alpha}\left[\rho^\alpha\left(\theta^\alpha\frac{D^\alpha\eta^\alpha}{Dt}-\frac{D^\alpha\varepsilon^\alpha}{Dt}\right)+\boldsymbol{\sigma}^\alpha:\boldsymbol{L}^\alpha-\left(\frac{\nabla\theta^\alpha}{\theta^\alpha}\right)\cdot\boldsymbol{q}^\alpha+\hat{\varepsilon}^\alpha+\hat{c}^\alpha\theta^\alpha\eta^\alpha\right]\geq 0. \tag{2-52}$$

As a matter of convenience, the internal energy in the total derivative can be replaced by the *Helmholtz free energy function,* defined as

$$\psi^\alpha = \varepsilon^\alpha - \eta^\alpha\theta^\alpha. \tag{2-53}$$

Using this definition and the balance of energy for the mixture, Eq. (2-46), yields

$$\begin{aligned}\sum_\alpha \frac{1}{\theta^\alpha}\Bigg[-\rho^\alpha\left(\frac{D^\alpha\psi^\alpha}{Dt}+\frac{D^\alpha\theta^\alpha}{Dt}\eta^\alpha\right)+\boldsymbol{\sigma}^\alpha:\boldsymbol{L}^\alpha-\frac{\nabla\theta^\alpha\cdot\boldsymbol{q}^\alpha}{\theta^\alpha}-\boldsymbol{\pi}^\alpha\cdot\tilde{\boldsymbol{v}}^\alpha\\ -\hat{c}^\alpha\left(\psi^\alpha+\frac{1}{2}\tilde{\boldsymbol{v}}^\alpha\cdot\tilde{\boldsymbol{v}}^\alpha\right)\Bigg]\geq 0.\end{aligned} \tag{2-54}$$

Notice that the above form of the entropy inequality can be readily simplified in the case of an isothermal mixture without mass exchange.

2.3 Balance Equations and Entropy Inequality for a Biphasic Mixture

In what follows the name *biphasic mixture* designates a binary mixture composed of a porous solid matrix saturated with fluid. The constituents, or *phases*, are assumed to be immiscible, intrinsically incompressible and chemically inert. It is further assumed that the mixture is isothermal and has a constant temperature θ_0.

The above assumptions considerably simplify the balance equations and the entropy inequality for a biphasic mixture. Thus, it is worthwhile to specialize the previous equations before proceeding with the constitutive equations in the next chapter. Superscripts "s" and "f" are used to identify quantities associated with the solid and fluid phases, respectively (Fig. 2.2).

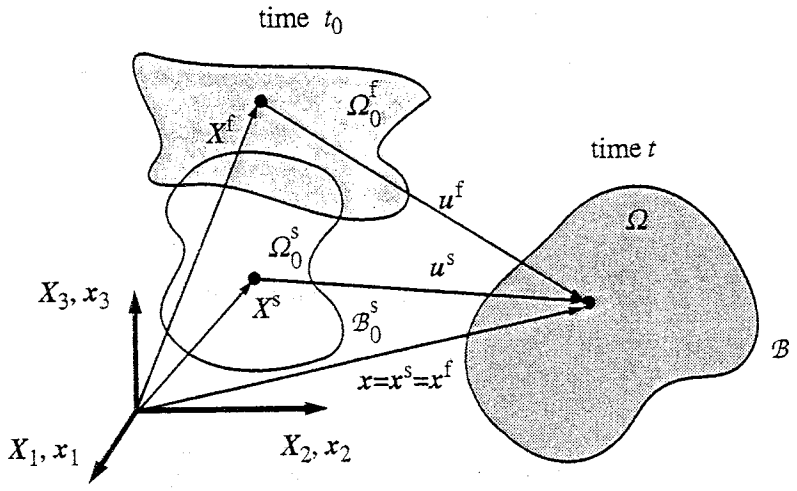

Figure 2.2 The kinematics of a biphasic mixture.

2.3.1 Balance of Mass for a Biphasic Mixture

The equations of balance of mass for the constituents, Eq. (2-27), and for the mixture, Eq. (2-28), can be replaced by two simpler equations

$$\phi^s + \phi^f = 1, \tag{2-55}$$

$$\nabla \cdot (\phi^s v^s + \phi^f v^f) = 0. \tag{2-56}$$

The last equation is the *continuity equation for a biphasic mixture*, and the volume fractions ϕ^s and ϕ^f are called the *solidity* [43] and *porosity* [19] of the mixture, respectively. Note that when one of the volume fractions vanishes, Eq. (2-56) becomes the incompressibility condition for a single-phase continuum.

The change in the solidity that occurs from the reference configuration to the current configuration can be obtained from the deformation of the solid phase. The true density must remain constant for an intrinsically incompressible solid phase, and therefore

$$\rho_T^s = \frac{\rho^s}{\phi^s} = \frac{\rho_0^s}{\phi_0^s}, \tag{2-57}$$

where the subscript "0" denotes quantities in the reference configuration. For a control volume following the solid phase, the density in the current configuration is given by

$$\rho^s = \frac{\rho_0^s}{J^s}, \tag{2-58}$$

where J^s is the Jacobian determinant of the deformation of the solid phase, Eq. (2-7). From Eqs. (2-57), (2-58) and (2-55),

$$\phi^s = \frac{\phi_0^s}{J^s}, \qquad \phi^f = 1 - \frac{\phi_0^s}{J^s}, \tag{2-59}$$

which shows that the changes in both volume fractions are completely determined by the deformation of the solid phase.

2.3.2 Balance of Linear Momentum for a Biphasic Mixture

Due to the low permeability of biological soft hydrated tissues, inertial terms and external body forces are usually negligible when compared to the linear momentum supplies (or *diffusive drag forces)* for frequencies and rates of deformation which occur physiologically [43, 70]. For this reason we replace Eq. (2-31) by the following quasistatic linear momentum equations:

$$\nabla \cdot \boldsymbol{\sigma}^s + \boldsymbol{\pi}^s = \mathbf{0}, \qquad \nabla \cdot \boldsymbol{\sigma}^f + \boldsymbol{\pi}^f = \mathbf{0}. \tag{2-60}$$

The symmetry of the partial stress tensors for the solid and fluid phases ($\boldsymbol{\sigma}^s = \boldsymbol{\sigma}^{sT}$, $\boldsymbol{\sigma}^f = \boldsymbol{\sigma}^{fT}$), which results from the angular momentum equations, has been incorporated into Eqs. 2-60. The linear momentum equation for the mixture, Eq. (2-34), provides an action-reaction relationship for the momentum supplies,

$$\boldsymbol{\pi}^s = -\boldsymbol{\pi}^f. \tag{2-61}$$

2.3.3 The Second Axiom of Thermodynamics for a Biphasic Mixture

Under the assumptions expressed at the beginning of this section, the entropy inequality of a biphasic mixture, Eq. (2-54), becomes

$$-\rho^{s}\frac{D^{s}\psi^{s}}{Dt}-\rho^{f}\frac{D^{f}\psi^{f}}{Dt}+\boldsymbol{\sigma}^{s}:\boldsymbol{L}^{s}+\boldsymbol{\sigma}^{f}:\boldsymbol{L}^{f}+\boldsymbol{\pi}^{s}\cdot(\boldsymbol{v}^{f}-\boldsymbol{v}^{s})\geq 0, \tag{2-62}$$

where, in reaching Eq. (2-62), the linear momentum equation for the mixture, Eq. (2-61), and the definition of diffusion velocity, Eq. (2-21), were used. For a mixture of incompressible constituents, the continuity equation for the mixture, Eq. (2-56), is a constraint in the thermodynamical process and, therefore, must be introduced into Eq. (2-62) in association with a Lagrange multiplier p, yielding

$$\begin{aligned}\Big[-\rho^{s}\frac{D^{s}\psi^{s}}{Dt}-\rho^{f}\frac{D^{f}\psi^{f}}{Dt}+\boldsymbol{\sigma}^{s}:\boldsymbol{L}^{s}+\boldsymbol{\sigma}^{f}:\boldsymbol{L}^{f}+\boldsymbol{\pi}^{s}\cdot(\boldsymbol{v}^{f}-\boldsymbol{v}^{s})\\ +p\,\nabla\cdot(\phi^{s}\boldsymbol{v}^{s}+\phi^{f}\boldsymbol{v}^{f})\Big]\geq 0.\end{aligned} \tag{2-63}$$

Recalling that $\nabla\phi^{f}=-\nabla\phi^{s}$ and $\nabla\cdot\boldsymbol{v}^{\alpha}=\mathbf{1}:\boldsymbol{L}^{\alpha}$, produces

$$\begin{aligned}\Big[-\rho^{s}\frac{D^{s}\psi^{s}}{Dt}-\rho^{f}\frac{D^{f}\psi^{f}}{Dt}+(\boldsymbol{\sigma}^{s}+\phi^{s}p\mathbf{1}):\boldsymbol{L}^{s}+(\boldsymbol{\sigma}^{f}+\phi^{f}p\mathbf{1}):\boldsymbol{L}^{f}\\ +(\boldsymbol{\pi}^{s}-p\nabla\phi^{s})\cdot(\boldsymbol{v}^{f}-\boldsymbol{v}^{s})\Big]\geq 0,\end{aligned} \tag{2-64}$$

which is called the *reduced entropy inequality* [45]. This inequality will be used in the next chapter to establish the general form of the constitutive equations for a biphasic mixture with incompressible constituents.

CHAPTER 3

Constitutive Equations and Summary of the Governing Equations

"The beginning is half of the whole."

PLATO

In the last chapter the kinematics and balance equations of the theory of mixtures have been reviewed and later simplified into the equations of the biphasic theory. It is now time to characterize the response of the constituents as individual materials and to consider the nature of the interactions between constituents. This is a fundamental step to complete the set of equations of the initial/boundary value problem that will be treated numerically using the finite element method.

A preliminary count of the number of equations and unknowns is summarized in Table 3.1 for the three-dimensional biphasic problem. The deformation functions χ^s and χ^f are chosen as independent kinematic variables. These functions are not arbitrary, as they must satisfy the boundary conditions and the continuity equation for the mixture imposed on velocity and volume fraction fields. Volume fractions, on the other hand, must obey the equation for a saturated mixture, $\phi^s + \phi^f = 1$. The continuity constraint does not affect the difference between the number of equations and unknowns, since it is introduced in the problem with the additional Lagrangian multiplier function (see Section 2.3.3). Therefore neither the continuity equation nor the Lagrange multiplier are listed in the table. There is also no need to list quantities derivable from the deformation, such as displacements, velocities, changes in volume fractions etc., if the corresponding equations are also omitted. In doing so, only the linear momentum equations remain on the left side, and the table can then be completed with the kinetic unknowns, that is stress tensors and momentum supply, which are the dependent variables in these equations. In three-dimensions, each symmetric stress tensor is associated with six scalar components, while each vector unknown is associated with three, yielding a total of 21 scalar unknowns.

Table 3.1 Preliminary count of the number of equations and unknowns for a biphasic mixture in three-dimensional space.

Equations	Num.	Unknowns	Num.
Balance of linear momentum:		Deformation functions; χ^s, χ^f	6
$\nabla \cdot \sigma^s + \pi^s = 0$	3	Stress tensors; σ^s, σ^f	12
$\nabla \cdot \sigma^f - \pi^s = 0$	3	Linear momentum supply; π^s	3
	6		21

This brief count shows the need for fifteen additional equations to solve the initial/boundary value problem in three-dimensions. The missing equations relate the kinetic unknowns to the kinematic variables and are termed the *constitutive equations*. They describe the material and its constituents through macroscopic relationships of cause and effect, and must be determined experimentally. Although the axioms of continuum mechanics can not be used to determine the material response, they can identify the form of the constitutive equations and their arguments. This will be illustrated in the next sections, where the axiom of material frame indifference, the entropy inequality, and restrictions imposed by material symmetry will be applied to a biphasic mixture.

The review sections in this chapter have various sources. The axiom of material frame indifference follows the presentation in Bowen [18]. The discussion of the entropy inequality for a biphasic mixture is based on the approach proposed by Holmes [43]. The discussion about material symmetry uses concepts presented in Truesdell and Noll [108], and Ogden [78]. These two references and the books by Marsden and Hughes [67], and Ciarlet [23] are the main references for the restrictions imposed on the constitutive equations.

3.1 Axiom of Material Frame Indifference

The axiom of *material frame indifference*, also called the axiom of *objectivity* or the axiom of *invariance under change of observer*, states that the constitutive equations must be invariant under changes of frames of reference [108]. A *change of frame* is a mapping that, given

a deformation function χ^{α}, yields a new deformation $\chi^{\alpha^*} = b(t) + Q(t)\chi^{\alpha}$, where b represents a translation and Q an orthogonal transformation (rigid rotation). A possible interpretation is to consider χ^{α^*} as the deformation seen by another observer. The concept of *objectivity*, or more precisely Eulerian objectivity [78], is associated with the following transformation rules under a change of frame:

$$\begin{aligned} \varphi^{\alpha^*} &= \varphi^{\alpha}, \\ w^{\alpha^*} &= Q w^{\alpha}, \\ \kappa^{\alpha^*} &= Q \kappa^{\alpha} Q^{\mathrm{T}}, \end{aligned} \tag{3-1}$$

where φ^{α}, w^{α} and κ^{α} represent, respectively, scalar, vector and second order tensor valued functions and fields. And an asterisk denotes quantities referred to the new frame. The Helmholtz free energy function ψ^{α}, the velocity v^{α}, the deformation gradient F^{α}, the right and left Cauchy-Green deformation tensors, C^{α} and B^{α}, and the velocity gradient L^{α} can be shown to obey the following transformation rules:

$$\begin{aligned} \psi^{\alpha^*} &= \psi^{\alpha}, & C^{\alpha^*} &= C^{\alpha}, \\ v^{\alpha^*} &= (\dot{b} + \dot{Q}x) + Q v^{\alpha}, & B^{\alpha^*} &= Q B^{\alpha} Q^{\mathrm{T}}, \\ F^{\alpha^*} &= Q F^{\alpha}, & L^{\alpha^*} &= Q L^{\alpha} Q^{\mathrm{T}} + \dot{Q} Q^{\mathrm{T}}, \end{aligned} \tag{3-2}$$

where the dot denotes time derivative. Therefore, only ψ^{α} and B^{α} are objective according to Eq. (3-1). Because the traction force on a surface and the normal vector to this surface are objective, the partial stress tensor, defined by $\sigma^{\alpha} n = t^{\alpha}$, is also objective. The transformation rules for the *relative velocity*, $v^{\alpha\beta} = v^{\alpha} - v^{\beta}$, and for the *relative velocity gradient*, $L^{\alpha\beta} = L^{\alpha} - L^{\beta}$, are obtained directly from Eq. (3-2)

$$\begin{aligned} v^{\alpha\beta^*} &= Q v^{\alpha\beta}, \\ L^{\alpha\beta^*} &= Q L^{\alpha\beta} Q^{\mathrm{T}}, \end{aligned} \tag{3-3}$$

showing that both fields are objective.

There are two ways of enforcing the axiom of material frame indifference. In the first, all functions and their arguments are required to be objective, and thus transform according to Eq. (3-1). Although this is preferred for simple constitutive equations, the correct choice of the objective arguments demands a considerable understanding of continuum mechanics in order not to introduce undesirable constraints. A good example is when the left Cauchy-Green deformation tensor, $\boldsymbol{B}^{\alpha}$, is chosen as the only deformation argument, instead of $\boldsymbol{F}^{\alpha}$. This choice implicitly incorporates the assumption of isotropic constituents into the constitutive equations [23].

The second way is illustrated here and has the advantage of providing important insights that would otherwise remain hidden. It starts with a very general constitutive statement that is later modified and restricted in order to satisfy the principle of material frame indifference. Let us express the dependence of the free energy functions, the linear momentum supplies, and the stress tensors in terms of the history of the deformation gradients, velocity gradients, and velocities. Using the concise notation of Bowen [18], this can be written as

$$\begin{aligned} [\psi^{\alpha}, \boldsymbol{\pi}^{\alpha}, \boldsymbol{\sigma}^{\alpha}] &= f(\boldsymbol{F}^{\mathrm{s}}, \boldsymbol{F}^{\mathrm{f}}, \boldsymbol{L}^{\mathrm{s}}, \boldsymbol{L}^{\mathrm{f}}, \boldsymbol{v}^{\mathrm{s}}, \boldsymbol{v}^{\mathrm{f}}) \\ &= f(\boldsymbol{F}^{\beta}, \boldsymbol{L}^{\beta}, \boldsymbol{v}^{\beta}), \qquad \text{with } \beta = \mathrm{s,f}, \end{aligned} \tag{3-4}$$

where each term on the left-hand-side is a function of the arguments on the right-hand-side, which are abbreviated in the second line. This is a rather general constitutive assumption that includes mixtures of viscoelastic constituents, although it may be insufficient to represent non-Newtonian fluids. The axiom of material frame indifference requires that the function f is independent of the transformation, yielding

$$[\psi^{\alpha*}, \boldsymbol{\pi}^{\alpha*}, \boldsymbol{\sigma}^{\alpha*}] = f(\boldsymbol{Q}\boldsymbol{F}^{\beta}, (\boldsymbol{Q}\boldsymbol{L}^{\beta}\boldsymbol{Q}^{\mathrm{T}} + \dot{\boldsymbol{Q}}\boldsymbol{Q}^{\mathrm{T}}), (\dot{\boldsymbol{b}} + \dot{\boldsymbol{Q}}\boldsymbol{x} + \boldsymbol{Q}\boldsymbol{v}^{\beta})), \tag{3-5}$$

whose left side can be rewritten to provide

$$[\psi^{\alpha}, \boldsymbol{Q}\boldsymbol{\pi}^{\alpha}, \boldsymbol{Q}\boldsymbol{\sigma}^{\alpha}\boldsymbol{Q}^{\mathrm{T}}] = f(\boldsymbol{Q}\boldsymbol{F}^{\beta}, (\boldsymbol{Q}\boldsymbol{L}^{\beta}\boldsymbol{Q}^{\mathrm{T}} + \dot{\boldsymbol{Q}}\boldsymbol{Q}^{\mathrm{T}}), (\dot{\boldsymbol{b}} + \dot{\boldsymbol{Q}}\boldsymbol{x} + \boldsymbol{Q}\boldsymbol{v}^{\beta})). \tag{3-6}$$

Eqs. (3-4) and (3-6) must hold for all vectors $\boldsymbol{b}(t)$ and orthogonal linear transformations $\boldsymbol{Q}(t)$. In particular, for $\boldsymbol{Q} = \mathbf{1}$, $\dot{\boldsymbol{Q}} = 0$ and $\dot{\boldsymbol{b}} = -\boldsymbol{v}^{\mathrm{s}}$, these two equations produce

$$f(\boldsymbol{F}^{\beta}, \boldsymbol{L}^{\beta}, \boldsymbol{v}^{\beta}) = f(\boldsymbol{F}^{\beta}, \boldsymbol{L}^{\beta}, \boldsymbol{v}^{f} - \boldsymbol{v}^{s}). \tag{3-7}$$

Eq. (3-7) shows that the dependence on $\boldsymbol{v}^{\beta}$ must occur through the relative velocity $\boldsymbol{v}^{fs}$, an objective quantity. The dependence on $\boldsymbol{L}^{\beta}$ is not arbitrary. Choosing $\boldsymbol{Q} = \boldsymbol{1}$ and $\dot{\boldsymbol{Q}} = -\boldsymbol{W}^{s}$, where $\boldsymbol{W}^{s}$ is the skew-symmetric tensor from the additive decomposition $\boldsymbol{L}^{s} = \boldsymbol{D}^{s} + \boldsymbol{W}^{s}$, yields

$$\begin{aligned} f(\boldsymbol{F}^{\beta}, \boldsymbol{L}^{\beta}, \boldsymbol{v}^{\beta}) &= f(\boldsymbol{F}^{\beta}, (\boldsymbol{D}^{\beta} + \boldsymbol{W}^{\beta} - \boldsymbol{W}^{s}), \boldsymbol{v}^{f} - \boldsymbol{v}^{s}) \\ &= f(\boldsymbol{F}^{\beta}, \boldsymbol{D}^{\beta}, \boldsymbol{W}^{f} - \boldsymbol{W}^{s}, \boldsymbol{v}^{f} - \boldsymbol{v}^{s}). \end{aligned} \tag{3-8}$$

This equation shows that the dependence on the velocity gradient must occur through the rate of deformation tensor $\boldsymbol{D}^{\beta}$ and the difference of spin tensors $\boldsymbol{W}^{fs}$, which are both objective quantities.

An additional assumption, motivated by the study of constitutive equations for single phase fluids, consists of replacing $\boldsymbol{F}^{f}$ by the apparent density of the fluid [3, 18, 19]. Since the fluid is assumed incompressible in the biphasic theory, the porosity ϕ^{f} can be used instead of the density, yielding

$$[\psi^{\alpha}, \boldsymbol{\pi}^{\alpha}, \boldsymbol{\sigma}^{\alpha}] = f(\boldsymbol{F}^{s}, \phi^{f}, \boldsymbol{D}^{s}, \boldsymbol{D}^{f}, \boldsymbol{W}^{f} - \boldsymbol{W}^{s}, \boldsymbol{v}^{f} - \boldsymbol{v}^{s}). \tag{3-9}$$

Although it is not apparent, at least not from the number of arguments, Eq. (3-9) is considerably more tractable than Eq. (3-4). Moreover, $\boldsymbol{F}^{s}$ is now the only non-objective argument in Eq. (3-9).

3.2 Restrictions Imposed by the Entropy Inequality

In order to establish the constitutive models for articular cartilage, Mow and co-workers [43, 57, 58, 70] introduced additional assumptions associated with the mechanical behavior of the constituents. They realized that the effects of the fluid viscosity were negligible compared with the diffusive drag forces and assumed that the fluid phase was inviscid. Their constitutive model for finite deformation also considered the solid phase as a hyperelastic material (Green-elastic material), with the frictional interaction between solid and fluid phases being responsible for the "apparent" viscous behavior of the tissue.

These assumptions considerably simplify the arguments in the Helmholtz free energy functions. For a hyperelastic solid phase, the corresponding function becomes $\psi^{\mathrm{s}} = \tilde{\psi}^{\mathrm{s}}(\boldsymbol{F}^{\mathrm{s}})$, where $\boldsymbol{F}^{\mathrm{s}}$ is the deformation gradient at the current time. Invariance of the scalar ψ^{s} requires that the dependence on $\boldsymbol{F}^{\mathrm{s}}$ occurs through $\boldsymbol{C}^{\mathrm{s}}$, or

$$\psi^{\mathrm{s}} = \hat{\psi}^{\mathrm{s}}(\boldsymbol{C}^{\mathrm{s}}). \tag{3-10}$$

This is proved by choosing $\boldsymbol{Q} = \sqrt{\boldsymbol{C}^{\mathrm{s}}}\,(\boldsymbol{F}^{\mathrm{s}})^{-1}$, a rotation motivated by the polar decomposition of the deformation gradient.

The assumption of an inviscid fluid implies that the free energy function for the fluid phase is independent of its rate of deformation tensor. Since the fluid phase is also incompressible, Holmes [43] assumed that its Helmholtz free energy function is independent of the deformation,

$$\psi^{\mathrm{f}} = \text{const.}, \tag{3-11}$$

which implies the consideration of small relative velocities [3]. Rewriting the reduced entropy inequality, Eq. (2-64), taking into account Eqs. (3-10) and (3-11) produces

$$\left(\boldsymbol{\sigma}^{\mathrm{s}} + \phi^{\mathrm{s}} p\mathbf{1} - 2\rho^{\mathrm{s}}\boldsymbol{F}^{\mathrm{s}}\frac{\partial\hat{\psi}^{\mathrm{s}}}{\partial\boldsymbol{C}^{\mathrm{s}}}\boldsymbol{F}^{\mathrm{s}\mathrm{T}}\right) : \boldsymbol{L}^{\mathrm{s}} + (\boldsymbol{\sigma}^{\mathrm{f}} + \phi^{\mathrm{f}} p\mathbf{1}) : \boldsymbol{L}^{\mathrm{f}} + (\boldsymbol{\pi}^{\mathrm{s}} - p\nabla\phi^{\mathrm{s}}) \cdot (\boldsymbol{v}^{\mathrm{f}} - \boldsymbol{v}^{\mathrm{s}}) \geq 0, \tag{3-12}$$

where use was made of the identity

$$\frac{D\hat{\psi}^{\mathrm{s}}(\boldsymbol{C}^{\mathrm{s}})}{Dt} = \left(2\boldsymbol{F}^{\mathrm{s}}\frac{\partial\hat{\psi}^{\mathrm{s}}}{\partial\boldsymbol{C}^{\mathrm{s}}}\boldsymbol{F}^{\mathrm{s}\mathrm{T}}\right) : \boldsymbol{L}^{\mathrm{s}}. \tag{3-13}$$

Eq. (3-12) must hold for all motions described by $\boldsymbol{L}^{\mathrm{s}}$, $\boldsymbol{L}^{\mathrm{f}}$ and $(\boldsymbol{v}^{\mathrm{f}} - \boldsymbol{v}^{\mathrm{s}})$, yielding

$$\boldsymbol{\sigma}^{\mathrm{s}} = -\phi^{\mathrm{s}} p\mathbf{1} + \boldsymbol{\sigma}^{\mathrm{s}}_{\mathrm{E}}, \qquad \text{with } \boldsymbol{\sigma}^{\mathrm{s}}_{\mathrm{E}} = 2\rho^{\mathrm{s}}\boldsymbol{F}^{\mathrm{s}}\frac{\partial\hat{\psi}^{\mathrm{s}}}{\partial\boldsymbol{C}^{\mathrm{s}}}\boldsymbol{F}^{\mathrm{s}\mathrm{T}}, \tag{3-14}$$

$$\boldsymbol{\sigma}^{\mathrm{f}} = -\phi^{\mathrm{f}} p\mathbf{1}, \tag{3-15}$$

$$(\boldsymbol{v}^{\mathrm{f}} - \boldsymbol{v}^{\mathrm{s}}) \cdot (\boldsymbol{\pi}^{\mathrm{s}} - p\nabla\phi^{\mathrm{s}}) \geq 0. \tag{3-16}$$

Eq. (3-14) shows that the solid stress can be decomposed into two parts. The *extra Cauchy stress* $\boldsymbol{\sigma}_{\mathrm{E}}^{\mathrm{s}}$ (also known as *elastic* or *effective* stress), which is completely determined when the deformation is known, and a hydrostatic stress that depends on the *pressure p*. The pressure, also called *true* or *pore pressure*, contributes to the stresses of the solid and fluid phases according to the volume fractions and is determined by equilibrium. In the finite element formulation, it will be convenient to use the second Piola-Kirchhoff stress tensor defined as [67]:

$$\boldsymbol{S}_{\mathrm{E}}^{\mathrm{s}} = J^{\mathrm{s}} \boldsymbol{F}^{\mathrm{s}-1} \boldsymbol{\sigma}_{\mathrm{E}}^{\mathrm{s}} \boldsymbol{F}^{\mathrm{s}-\mathrm{T}} . \tag{3-17}$$

From the expression of $\boldsymbol{\sigma}_{\mathrm{E}}^{\mathrm{s}}$ in Eq. $(3\text{-}14)_2$, results

$$\boldsymbol{S}_{\mathrm{E}}^{\mathrm{s}} = 2\rho_0^{\mathrm{s}} \frac{\partial \hat{\psi}^{\mathrm{s}}}{\partial \boldsymbol{C}^{\mathrm{s}}}, \qquad \text{and} \qquad \boldsymbol{\sigma}_{\mathrm{E}}^{\mathrm{s}} = \frac{1}{J^{\mathrm{s}}} \boldsymbol{F}^{\mathrm{s}} \boldsymbol{S}_{\mathrm{E}}^{\mathrm{s}} \boldsymbol{F}^{\mathrm{s}\mathrm{T}} . \tag{3-18}$$

As for the linear momentum supply, the following constitutive equation is assumed based on Eq. (3-16)

$$\boldsymbol{\pi}^{\mathrm{s}} = -\boldsymbol{\pi}^{\mathrm{f}} = p \, \nabla \phi^{\mathrm{s}} + \boldsymbol{\zeta} (\boldsymbol{v}^{\mathrm{f}} - \boldsymbol{v}^{\mathrm{s}}) . \tag{3-19}$$

The first term corresponds to a buoyancy force arising from the volume fraction gradient. The second term represents the diffusive drag due to the interaction between phases and is assumed proportional to the relative velocity. The *diffusive drag* $\boldsymbol{\zeta}$ is a second order tensor that measures the frictional resistance against fluid flow through the solid matrix.

Introducing Eqs. (3-15) and (3-19) into the linear momentum equation for the fluid phase, Eq. $(2\text{-}60)_2$, and recalling that $\nabla \phi^{\mathrm{f}} = -\nabla \phi^{\mathrm{s}}$, yields

$$\nabla p = -\frac{1}{\phi^{\mathrm{f}}} \boldsymbol{\zeta} (\boldsymbol{v}^{\mathrm{f}} - \boldsymbol{v}^{\mathrm{s}}) . \tag{3-20}$$

If $\boldsymbol{\zeta}$ is assumed invertible, we can then write

$$\boldsymbol{\kappa} \, \nabla p = -\phi^{\mathrm{f}} (\boldsymbol{v}^{\mathrm{f}} - \boldsymbol{v}^{\mathrm{s}}) , \tag{3-21}$$

where $\boldsymbol{\kappa} = \phi^{f2}\boldsymbol{\zeta}^{-1}$ is the *permeability tensor.* Except for the omission of the body force potential, Eq. (3-21) is the classical Darcy's law. A slightly different definition of permeability is used in the poroelastic theory of Biot [11]. In the case of a porous medium with an incompressible fluid phase, these two definitions are related by $\boldsymbol{\kappa}_{\text{Biot}} = \eta_{\text{v}}\boldsymbol{\kappa}$, where η_{v} is the fluid viscosity.

There are two types of permeability in the biphasic theory: the *intrinsic permeability* $\boldsymbol{\kappa}$ defined locally, and the *apparent permeability* measured in the permeation experiments. The distinction is necessary because the strain field varies considerably under finite deformation, and the apparent permeability, averaged through the entire thickness of the tissue, becomes inadequate to assess the dependence of the permeability on the deformation [43, 61].

3.3 Restrictions Imposed by Material Symmetry

In the previous subsection, the solid phase has been assumed hyperelastic in order to derive general forms of the constitutive equations for stresses and linear momentum supply using the entropy inequality for the mixture. The resulting equation for the solid stress, however, is still too general and must be further simplified. The simplification is pursued in this subsection, where the material symmetry of the solid phase, a property inferred experimentally, is incorporated into the equations.

Let $\boldsymbol{F}^{s\prime}$ and $\boldsymbol{F}^{s}$ denote the deformation gradients with respect to the configurations $\mathcal{B}_0^{s\prime}$ and $\mathcal{B}_0^{s}$, respectively (Fig. 3.1). The only difference between these configurations is the orthogonal transformation $\boldsymbol{K}$ of the material in the neighborhood of a point $\boldsymbol{X}$, given by

$$\boldsymbol{F}^{s\prime}(\boldsymbol{X}^{s}, t) = \boldsymbol{F}^{s}(\boldsymbol{X}^{s}, t)\boldsymbol{K}. \tag{3-22}$$

If the corresponding stress responses $\tilde{\boldsymbol{\sigma}}^{s\prime}(\boldsymbol{F}^{s\prime})$ and $\tilde{\boldsymbol{\sigma}}^{s}(\boldsymbol{F}^{s})$ coincide for any mechanical experiment, the material is said to be *indistinguishable in its response* after being subject to the transformation $\boldsymbol{K}$ [108]. In this case, we can write

$$\tilde{\boldsymbol{\sigma}}^{s}(\boldsymbol{F}^{s}) = \tilde{\boldsymbol{\sigma}}^{s}(\boldsymbol{F}^{s}\boldsymbol{K}). \tag{3-23}$$

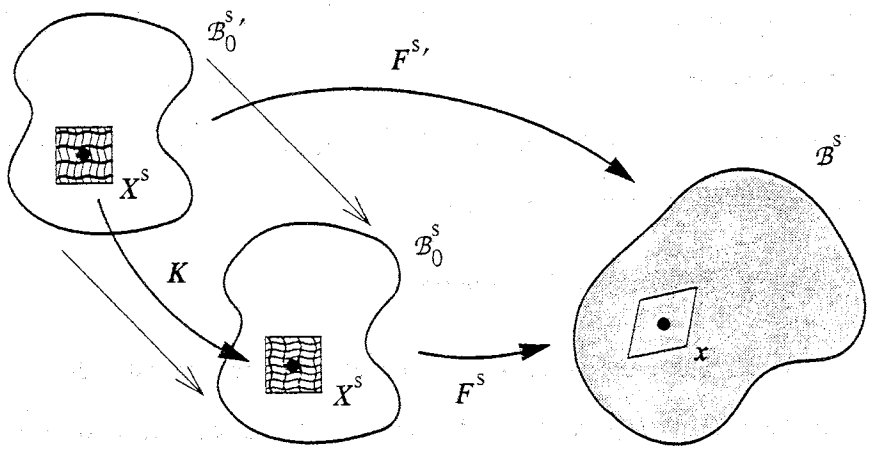

Figure 3.1 Orthogonal transformation of the material at a point X^s followed by a deformation.

The set of all invertible tensors $\boldsymbol{K}$ for which Eq. (3-23) is valid constitutes a group[1], called the symmetry group $\mathcal{G}$, and describes the symmetry of a Cauchy-elastic material. For a hyperelastic material, on the other hand, the symmetry group $\mathcal{G}_\psi$ is formed by the orthogonal transformations $\boldsymbol{K}$ for which the Helmholtz free energy function is unaffected:

$$\tilde{\psi}(\boldsymbol{F}^s) = \tilde{\psi}(\boldsymbol{F}^s\boldsymbol{K}), \tag{3-24}$$

and the free energy function is said to be form-invariant under the group $\mathcal{G}_\psi$. Equivalently, Eq. (3-24) can be expressed in terms of the right Cauchy-Green deformation tensor [78],

$$\hat{\psi}(\boldsymbol{K}^T\boldsymbol{C}^s\boldsymbol{K}) = \hat{\psi}(\boldsymbol{C}^s), \tag{3-25}$$

which is the form usually adopted since $\boldsymbol{C}$ is symmetric.

The problem of representing scalar functions such as $\hat{\psi}(\boldsymbol{C}^s)$ under the constraint imposed by Eq. (3-25) is a subject covered by the *representation theorems of scalar functions*. In broad terms, these theorems state that the dependence on a set of vectors and second-order symmetric tensors can be replaced by the dependence on a finite number of polynomial *invariants*

1. A set $\mathcal{G}$ is said to be a *group* with respect to the composition of functions $\boldsymbol{K}$ when: (a) $\mathbf{1} \in \mathcal{G}$; (b) if $\boldsymbol{K}_1, \boldsymbol{K}_2 \in \mathcal{G}$ then $\boldsymbol{K}_1\boldsymbol{K}_2 \in \mathcal{G}$; and (c) if there exist $\boldsymbol{K}^{-1}$ with $\boldsymbol{K} \in \mathcal{G}$, then $\boldsymbol{K}^{-1} \in \mathcal{G}$.

$I_1, I_2, \ldots, I_n$, that constitute an *irreducible integrity basis* (see [12, 13], and references therein). The term irreducible means that: (a) an invariant I_j is not expressible as a polynomial function of the others; and (b) any scalar function that is invariant under the transformations in $\mathcal{G}_\psi$ can be expressed as a function of the invariants.

3.3.1 Isotropic Scalar Functions

By definition, the symmetry group of an isotropic material is the set of all orthogonal tensors. In this case, the representation theorem states that a scalar function $\hat{\psi}^S(\boldsymbol{C}^S)$ is isotropic if and only if there exists a function $\psi^S(I_j(\boldsymbol{C}^S))$ such that

$$\hat{\psi}^S(\boldsymbol{C}^S) = \psi^S(I_1, I_2, I_3), \tag{3-26}$$

where I_j, $j = 1, 2, 3$, represent scalar invariants of $\boldsymbol{C}^S$ [40].

3.3.2 Transversely Isotropic Scalar Functions

A material is called a *transversely isotropic material* if there exists a plane such that every plane perpendicular to it is a plane of material symmetry [63]. Transverse isotropy is characterized by a symmetry group $\mathcal{G}$ that contains: (a) the unit tensor **1**; (b) the central inversion **-1**; (c) all rotations $\boldsymbol{R}_{\boldsymbol{m}}^{\varphi}$, $0 < \varphi < 2\pi$, about the axis $\boldsymbol{m}$ that determines the preferred direction of the material in the current configuration; and (d) one reflection $-\boldsymbol{R}_{\boldsymbol{m}}^{\varphi}$ about a plane containing $\boldsymbol{m}$. If the type of anisotropy is characterized by a proper subgroup $\mathcal{G}_+ \subset \mathcal{G}$, as in Truesdell and Noll [108], only the transformations (a) and (c) are taken into account.

The representation theorem for transversely isotropic scalar functions states that a scalar function $\hat{\psi}^S(\boldsymbol{C}^S)$ is transversely isotropic if and only if there exists a function $\psi^S(I_j(\boldsymbol{C}^S))$ such that

$$\hat{\psi}^S(\boldsymbol{C}^S) = \psi^S(I_1, I_2, I_3, I_4, I_5), \tag{3-27}$$

where I_j, $j = 1, \ldots, 5$, are invariants of $\boldsymbol{C}^S$ and the preferred direction expressed in the reference configuration, $\boldsymbol{m}_0$ [30]. The members of the integrity basis adopted in this study are the

three principal invariants of C^s and two additional invariants proposed by Ericksen and Rivlin [30]:

$$I_1 = \text{tr}\, C^s, \qquad I_2 = \frac{1}{2}\left[(\text{tr}\, C^s)^2 - \text{tr}\, C^{s2} \right], \qquad I_3 = \det C^s,$$
$$I_4 = M_0 : C^s, \qquad I_5 = M_0 : C^{s2}, \tag{3-28}$$

where M_0 is the structural tensor in the reference configuration defined by $M_0 = m_0 \otimes m_0$ (see also Appendix A).

Geometrical interpretations of the invariants I_4 and I_5 are useful in obtaining the form of the free energy function for transverse isotropy. Humphrey *et al.* [49, 50], for instance, used the interpretation of the invariant I_4 to propose structurally motivated strain energy functions for passive cardiac tissues. The association between this invariant and the deformation along the preferred direction is shown as

$$I_4 = M_0 : C^s = \text{tr}\,[m_0 \cdot (C^s m_0)] = (\lambda_{m_0})^2, \tag{3-29}$$

where λ_{m_0} denotes the stretch associated with the direction m_0. The invariant $I_5 = M_0 : C^{s2}$ is usually omitted from the constitutive equations because it does not have an easy geometrical interpretation. More recently, Achcar [1] used the following invariant to study the behavior of transversely isotropic materials:

$$I_{5A} = \left\| \pi(C^s m_0) \right\|^2 = \pi(C^s m_0) \cdot \pi(C^s m_0), \tag{3-30}$$

where $\pi(\ )$ denotes the orthogonal projection of a vector onto a plane whose normal is m_0, and is given by $\pi(w) = w - (m_0 \cdot w)\, m_0$ for an arbitrary vector w. The invariant I_{5A} is associated with the deformation perpendicular to the preferred direction and is thus more convenient than I_5 to express the constitutive equations. The development of Eq. (3-30) yields the identity

$$I_{5A} = I_5 - I_4^2, \tag{3-31}$$

which confirms that I_{5A} is an invariant.

3.4 The Cauchy Stress Tensor and the Elasticity Tensor

In hyperelasticity, the Cauchy stress tensor is typically computed from the second Piola-Kirchhoff stress tensor, which depends on the Helmholtz free energy function. Using Eq. (3-18)$_1$ and the chain rule of differentiation, the elastic part of the second Piola-Kirchhoff stress tensor can be written as

$$\boldsymbol{S}_{\mathrm{E}}^{\mathrm{s}} = 2\rho_0^{\mathrm{s}} \frac{\partial \hat{\psi}^{\mathrm{s}}}{\partial \boldsymbol{C}^{\mathrm{s}}} = 2\rho_0^{\mathrm{s}} \, \psi_{,j}^{\mathrm{s}} \, \frac{\partial I_j}{\partial \boldsymbol{C}^{\mathrm{s}}}, \qquad j = 1, \ldots, n, \tag{3-32}$$

where $\psi_{,j}^{\mathrm{s}} = \partial \psi^{\mathrm{s}} / \partial I_j$, and n is the total number of invariants in the integrity basis. Using Eq. (3-18)$_2$ and the partial derivatives of the invariants presented in Table A.1, the expression of the elastic Cauchy stress for a transversely isotropic material is obtained as

$$\begin{aligned} \boldsymbol{\sigma}_{\mathrm{E}}^{\mathrm{s}} = 2\rho^{\mathrm{s}} \Big[& \Big(I_2 \psi_{,2}^{\mathrm{s}} + I_3 \psi_{,3}^{\mathrm{s}} \Big) \mathbf{1} + \psi_{,1}^{\mathrm{s}} \boldsymbol{B}^{\mathrm{s}} - I_3 \psi_{,2}^{\mathrm{s}} \boldsymbol{B}^{\mathrm{s}^{-1}} + I_4 \psi_{,4}^{\mathrm{s}} \boldsymbol{M} \\ & + I_4 \psi_{,5}^{\mathrm{s}} \left(\boldsymbol{B}^{\mathrm{s}} \boldsymbol{M} + \boldsymbol{M} \boldsymbol{B}^{\mathrm{s}} \right) \Big], \end{aligned} \tag{3-33}$$

where $\boldsymbol{B}^{\mathrm{s}} = \boldsymbol{F}^{\mathrm{s}} \boldsymbol{F}^{\mathrm{s}^{\mathrm{T}}}$ is the left Cauchy-Green deformation tensor, and $\boldsymbol{M}$ is the structural tensor in the current configuration.

In the finite element formulation, the linearization of the nonlinear elasticity vector of the solid matrix produces the elasticity tensor $\mathbf{C}$, a fourth-order tensor with major and minor symmetries. This tensor relates the variation of stress $\delta \boldsymbol{S}_{\mathrm{E}}^{\mathrm{s}}$ and the corresponding variation of deformation $\delta \boldsymbol{C}^{\mathrm{s}}$

$$\delta \boldsymbol{S}_{\mathrm{E}}^{\mathrm{s}} = \frac{1}{2} \mathbf{C} : \delta \boldsymbol{C}^{\mathrm{s}}, \qquad \mathbf{C} = 4\rho_0^{\mathrm{s}} \frac{\partial}{\partial \boldsymbol{C}^{\mathrm{s}}} \left(\frac{\partial \hat{\psi}^{\mathrm{s}}}{\partial \boldsymbol{C}^{\mathrm{s}}} \right). \tag{3-34}$$

This is the same definition adopted by Simo and Pister [90], but differs from the one by Marsden and Hughes [67] due to the presence of the coefficient one-half. The general expression of the second derivative of $\hat{\psi}^{\mathrm{s}}$ for transversely isotropic materials is given by Eq. (A-7) in Appendix A, and its derivation and computational implementation constitutes one of the contributions of this thesis.

3.5 Restrictions Imposed on the Constitutive Equations

The search for suitable stored energy functions for single phase materials has been an important and active area of investigation (see Truesdell and Noll [108]; Marsden and Hughes [67]; Ogden [78]; Ciarlet [23], and references therein). As a result, many restrictions that limit the choice of the stored energy function have been proposed and studied in detail. Under the assumption of a hyperelastic solid phase, the same restrictions can be applied to the free energy function, since the function $\Psi^s = \rho_0^s \psi^s$ corresponds to the *stored energy function*, or *strain energy function*, in the case of an isothermal process at a uniform temperature. For infinitesimal deformation, ψ^s is reduced to a quadratic function of the strain components, and its form is completely determined after considering the existence of a natural state. For finite deformation, a quadratic function is just one possibility, unfortunately not very well behaved for large strains. In this case, restrictions are typically applied in order to obtain functions that are capable of representing the known, or hypothesized, behavior of the material.

It is common to distinguish between two types of restrictions: *mathematical restrictions*, proposed to ensure the existence of the solution of the boundary/initial value problem, and *physical restrictions*, proposed based on generalizations of experimental observations. In contrast with the former, most physical restrictions cover ranges of deformation that often overlap and, when extended to transverse isotropy, are limited in validity to states of pure stretch. Equivalences among physical restrictions are presented by Truesdell and Noll [108] for isotropic materials. See Marsden and Hughes [67], Ogden [78] and Ciarlet [23] for comprehensive discussions about mathematical restrictions such as ellipticity and polyconvexity.

In what follows, we list some of the restrictions and corresponding inequalities that have been used to evaluate the adequacy of the stored energy functions [108]. To express these inequalities, let us consider two configurations of a rectangular brick, $\mathcal{B}_0$ and $\mathcal{B}_0^*$, subjected to three orthogonal pairs of distributed forces normal to the faces. The asterisk denotes a quantity in the configuration $\mathcal{B}_0^*$, and subscripts i and j denote distinct principal directions perpendicular to the

faces. For a transversely isotropic material, we further assume that the preferred direction is along a principal direction, so that the configurations always differ by a state of pure stretch.

Pressure-Compression Condition (P-C). The volume of a compressible material should decrease when the solid is subjected to a hydrostatic compression, and increase when subjected to a hydrostatic tension.

"Invertibility" of the Force-Stretch Condition (IFS). The force-stretch relationship should be uniquely invertible.

Extension-Tension (E-T) and Tension-Extension (T-E) Conditions. When the length of the brick changes in one principal direction, while the faces parallel to this direction are held, the principal stress in this direction should increase with elongation and decrease with shortening. Conversely, when the magnitudes of one pair of opposing forces changes, with the remaining pairs of forces kept fixed, the brick should elongate with increasing magnitudes, and shorten with decreasing ones. This can be expressed by

$$(T_i^* - T_i)\,(\lambda_i^* - \lambda_i) > 0, \qquad \text{for } \lambda_i^* \neq \lambda_i, \text{ and } \begin{cases} \text{(E-T)} & \lambda_j = 1,\ j \neq i, \\ \text{(T-E)} & T_j^* = T_j, \end{cases} \tag{3-35}$$

where T_i is the distributed force per undeformed area, and λ_i is the corresponding stretch.

Ordered Forces Condition (O-F). For isotropic materials, the greater stretch should occur in the direction of the greater force. This condition can be expressed as

$$(T_i - T_j)\,(\lambda_i - \lambda_j) > 0, \qquad \text{for } \lambda_i \neq \lambda_j. \tag{3-36}$$

GCN_0 Inequality. For isotropic materials the GCN_0 inequality implies the conditions (P-C, IFS, E-T, T-E, and O-F) [108], and is expressed as

$$\sum_{i=1}^{3} (T_i^* - T_i)\,(\lambda_i^* - \lambda_i) > 0. \tag{3-37}$$

It is equivalent to the requirement that the incremental work is always positive.

Coleman-Noll (C-N) and Generalized Coleman-Noll (GCN). Coleman and Noll proposed the following inequality for the free energy function:

$$\tilde{\psi}(F^*) - \tilde{\psi}(F) - (F^* - F) : \frac{\partial}{\partial F}(\tilde{\psi}(F)) > 0\,, \tag{3-38}$$

where F^* and F correspond to deformations differing by a state of pure stretch. Interchanging the order of F^* and F above and adding to Eq. (3-38), produces

$$(F^* - F) : (T^* - T) > 0, \qquad \text{for } F^* \neq F\,, \tag{3-39}$$

where the definition of the first Piola-Kirchhoff stress tensor, $T = \rho_0 \partial \tilde{\psi}(F)/\partial F$ was used. Eqs. (3-38) and (3-39) are known as Coleman-Noll (C-N) and Generalized Coleman-Noll (GCN) inequalities and imply strict convexity of the free energy function in the case of isotropic hyperelastic materials [77].

Baker-Ericksen Inequalities (B-E). The Baker-Ericksen inequalities require that the greater principal stress occurs in the direction of the greater stretch,

$$(\sigma_i - \sigma_j)\,(\lambda_i - \lambda_j) > 0, \qquad \text{for } \lambda_i \neq \lambda_j\,, \tag{3-40}$$

where σ_i and σ_j are principal Cauchy stresses on the faces of the brick. The B-E inequalities constitute an important set of restrictions in Continuum Mechanics, but they do not hold for anisotropic materials.

Hill's Inequalities. Hill [41] proposed inequalities that consist of the scalar product of a strain-rate with an associated stress-rate. Different inequalities can be stated in this way, including the GCN inequality, by changing the strain-rate tensor. However, only the inequality with the logarithmic strain (logarithms of the principal stretches) allows incompressibility, the other inequalities being too strong for this type of material. For hyperelastic materials, this inequality is equivalent to the requirement that the strain energy be a convex function of the logarithmic strain [77].

Coerciveness Condition. This condition states that "infinite stress must accompany extreme strains" [23], requiring that the free energy function must approach $+\infty$ if any of the eigenvalues of $\boldsymbol{C}$ approach 0 or $+\infty$. This is equivalent to

$$\lim_{J \to 0^+} \hat{\psi}(\boldsymbol{F}) = +\infty, \qquad \text{and} \qquad \lim_{J \to +\infty} \hat{\psi}(\boldsymbol{F}) = +\infty. \tag{3-41}$$

This condition can also be expressed as an inequality, which is essential to demonstrate the existence theorems of hyperelasticity associated with the concept of polyconvexity [6].

Reduction to the Linear Theory. The free energy function must reduce to the quadratic function of the linear theory in the case of infinitesimal deformation.

Existence of a Natural State. The body must have a natural state associated with an undistorted configuration. For transverse isotropy, the natural state has one of the principal axes coinciding with the preferred direction $\boldsymbol{m}$ ($\boldsymbol{\sigma} = -p\mathbf{1} + q\ \boldsymbol{m} \otimes \boldsymbol{m}$), and includes the case of hydrostatic pressures, which is the natural state for isotropic materials [26].

The above list of restrictions is far from complete, but contributes to the idea that undesirable features of the constitutive model can be eliminated during its formulation. Some of the restrictions are considered too restrictive, as it is the case of the GCN condition that implies convexity of the free energy function. A convex function would make it easier to demonstrate the existence of a solution for problems in finite elasticity. However, convexity is unacceptable because it is in conflict with experimental evidences [23, 67]. First, it implies uniqueness of the solution and, therefore, contradicts examples showing the existence of multiple solutions in elasticity. It is also incompatible with the axiom of material frame indifference. A convex and frame-indifferent free energy function would produce a state of stress where the sum of any two principal Cauchy stresses is always positive. Finally, the convexity property is incompatible with the first part of the coerciveness condition, since it prevents $\tilde{\psi}(\boldsymbol{F})$ from approaching $+\infty$ when J approaches 0.

A way of circumventing this problem is to weaken the convexity condition using the concept of *polyconvexity* of Ball [6]. A function $\tilde{\psi}(\boldsymbol{F})$ is said to be polyconvex if there exists a convex function $\psi^{*}(\boldsymbol{F}, \operatorname{cof}\boldsymbol{F}, J)$ such that $\tilde{\psi}(\boldsymbol{F}) = \psi^{*}(\boldsymbol{F}, \operatorname{cof}\boldsymbol{F}, J)$ for all $\boldsymbol{F}$. Not only was this concept introduced to prove the theorem of existence, but it also became the basis of important constitutive laws in rubber elasticity, as described by Ogden in [78].

3.6 Restriction on the Volume Fraction and the Permeability Function

The restrictions listed above and associated with the solid phase are insufficient for a biphasic mixture, so an additional condition is necessary to guarantee that the solid volume fraction ϕ^{s} remains between zero and one. As a matter of fact, only the upper limit is a problem since a Helmholtz free energy function satisfying the coerciveness condition already prevents a negative ϕ^{s}. One way of imposing the upper limit is through a singular point incorporated into the energy function at $\phi^{s} = 1$ (or $J^{s} = \phi_0^{s}$), as done for the function proposed by Holmes [43]. This solution, however, modifies the original energy function of a fully drained solid phase and should be avoided if possible. A better alternative that leaves the function intact was devised by Holmes and Mow [44]. Considering that the permeability function must approach zero when ϕ^{s} approaches one, they concluded that even when the free energy function allows compressions with $\phi^{s} > 1$, the permeability function would prevent this from occurring since it would take an infinite time to reach a deformation with $\phi^{s} = 1$. Based on experimental data for articular cartilage, they proposed the following isotropic exponential function for the permeability:

$$\kappa = \kappa_0 \left(\frac{\phi_0^{s} \phi^{f}}{(1-\phi_0^{s})\,\phi^{s}} \right)^{L} e^{M(I_3 - 1)/2}, \tag{3-42}$$

where the exponents L and M are material parameters, and κ_0 is the intrinsic permeability associated with the undeformed configuration. Eq. (3-42) has the equivalent forms

$$\kappa = \kappa_0 \left(\frac{\phi_0^s \phi^f}{\phi^s \phi_0^f} \right)^L e^{M(I_3 - 1)/2} = \kappa_0 \left(\frac{J^s - \phi_0^s}{1 - \phi_0^s} \right)^L e^{M(J^{s2} - 1)/2}, \tag{3-43}$$

where the latter expresses the permeability as a function of the volumetric deformation. Notice from Eq. (3-43) that this function satisfies the conditions

$$\lim_{J^s \to \phi_0^s} \kappa = 0, \qquad \lim_{\phi^s \to 0} \kappa = \infty. \tag{3-44}$$

Eq. (3-42) represents a significant contribution of the biphasic theory to the study of soft hydrated tissues under finite deformation. It can be reduced to the permeability function obtained by Lai and Mow [60], as shown by Holmes and Mow [44], and it has been demonstrated to correlate well with permeation and confined compression experiments of articular cartilage [43, 44].

The importance of Eq. (3-42) is apparent when examining permeability functions used to describe other biological soft tissues. For skin under finite deformation, Oomens *et al.* [79, 80] use the function

$$\kappa = \kappa_0 e^{M(I_3 - 1)} \tag{3-45}$$

based on the expression suggested by Mow *et al.* [70]. Van Campen *et al.* [110] improved upon the model developed by the Huyghe *et al.* [51], and adopted the following function to represent the redistribution of intracoronary blood in the ventricular wall:

$$\kappa = \kappa_0 \left(\frac{J^s - \phi_0^s}{1 - \phi_0^s} \right)^2 = \kappa_0 \left(\frac{J^s - 1}{\phi_0^f} + 1 \right)^2. \tag{3-46}$$

This expression can be obtained from Eq. (3-42) by setting $L = 2$ and $M = 0$. The reader is referred to Mow *et al.* [70], Lai and Mow [60], Lai *et al.* [61], Holmes [42, 43], and Holmes and Mow [44] for comprehensive presentations of this subject, including the description of the experiments.

3.7 Examples of Helmholtz Free Energy Functions

Several free energy functions have been proposed to study biological soft hydrated tissues under finite deformation. Kwan [58] and Kwan *et al.* [57] investigated polynomial and exponential functions suitable for uniaxial compression of articular cartilage. They recommended the following "modified-quadratic" free energy function that correlated well data from confined compression tests:

$$\rho_0^s \psi^s = \frac{1}{8I_3}\left[(3\lambda^s + 2\mu^s) I_1 + (\lambda^s + 2\mu^s) I_1^2 - (9\lambda^s + 10\mu^s) I_2 \right], \tag{3-47}$$

where I_1, I_2 and I_3 are the principal invariants of C^s. This function has only two material parameters, λ^s and μ^s, which coincide with the Lamé constants of the fully drained solid phase under infinitesimal deformation. Although it is acceptable for compression tests, and has been implemented by Wayne in a finite element program [115], this function has some drawbacks when modelling multiaxial deformation. According to Suh [103], the resulting state of stress can become nonphysical when the tissue is elongated beyond a certain limit.

Oomens *et al.* [79] used a variant of the exponential form suggested by Fung [34] to represent porcine skin. They rewrote the free energy function, originally for incompressible materials, as

$$\rho_0^s \psi^s = \frac{1}{2}\alpha_{IJKL} E_{IJ} E_{KL} + \frac{1}{2} C\, e^{a_{IJKL} E_{IJ} E_{KL}} + g(I_3), \tag{3-48}$$

where α_{IJKL}, C, and a_{IJKL} denote material parameters, and E_{IJ} are the components of the Green-Lagrange strain tensor. Since a good fit to uniaxial experiments was obtained using only the exponential part of the function, a simplified 2-D version of Eq. (3-48) was adopted in their finite element implementation:

$$\rho_0^s \psi^s = C\, e^{(a_1 E_{11}^2 + a_2 E_{22}^2 + a_3 E_{12}^2 + 2a_4 E_{11} E_{22})}, \tag{3-49}$$

with the equality $a_1 = a_2$ valid for isotropic materials.

Simon and Gaballa [92] also based their constitutive model on Fung's exponential function. They used the following form to study rabbit aorta undergoing finite deformation:

$$\rho_0^s \psi^s = \frac{1}{2} C_0 e^{B_{IJKL} E_{IJ} E_{KL}}. \tag{3-50}$$

Holmes [43] proposed the following exponential free energy function to study the uniaxial behavior of articular cartilage:

$$\psi^s = \frac{\gamma}{\left(I_3 - \phi_0^{s\,2} \right)^n} e^{\beta (I_1 - 3)}, \tag{3-51}$$

where $n = \beta \left(1 - \phi_0^{s\,2} \right)$; and β and γ are material parameters. Note that the above function has a singularity at $\phi^s = 1$, which was later found to be an unnecessary restriction (see Section 3.6). Holmes and Mow [44], and Suh *et al.* [105] modified Eq. (3-51) to account for multiaxial deformation, and suggested the isotropic function

$$\rho_0^s \psi^s = \alpha_0 \frac{e^{\alpha_1 (I_1 - 3) + \alpha_2 (I_2 - 3)}}{I_3^{\,n}}, \tag{3-52}$$

where $n = \alpha_1 + 2\alpha_2$; and α_0, α_1 and α_2 are positive material parameters. Holmes and Mow [44] have shown that the above function satisfies the Baker-Ericksen inequalities, and have obtained material parameters for human and bovine articular cartilage via curve-fitting. Furthermore, Suh and co-workers [103, 104] have used the penalty finite element formulation to verify that this function provides physically acceptable responses for configurations other than the confined compression test.

Cohen [24] extended the form expressed in Eq. (3-52) to anisotropic materials. He proposed the general form

$$\rho_0^s \psi^s = \frac{\gamma}{\alpha} \left[e^{\alpha Q (I_1, I_2, \ldots, I_m)} - 1 \right], \tag{3-53}$$

where α and γ are material parameters and Q is a function of the integrity basis $(I_1, I_2, \ldots, I_m)$, which depends on the symmetry group of the material. Cohen also suggested a transversely isotropic free energy function, for which the function Q is given by

$$Q(I_1, I_2, \ldots, I_m) = \beta_1 (I_1 - 3) + \beta_2 (I_2 - 3) + \beta_3 (I_1 - 3)(I_4 - 1) + \beta_4 (I_4 - 1) + \beta_5 (I_5 - 1) + \beta_6 (I_4 - 1)^2 - \ln(I_3). \tag{3-54}$$

If the multiplicative coefficient α is not counted in Eq. (3-53), only five independent coefficients remain after imposing a natural state as a reference configuration. This is the minimum number required to reproduce the stress-strain relationships of linear transverse isotropy. We shall return to this constitutive model in Chapter 7, where a transversely isotropic Helmholtz free energy function will be examined to validate the finite element implementation.

3.8 Governing Equations of a Biphasic Mixture

We can now resume the count of the number of equations and unknowns left incomplete in the introduction of this chapter. To do so, it is convenient to rewrite the linear momentum equations in Table 3.1 to minimize the number of unknowns. Replacing the solid and fluid stresses using Eqs. (3-14) and (3-15), and introducing the expressions of the linear momentum supplies, Eq. (3-19), we finally obtain Eqs. (a) and (b) in Table 3.2. These equations are explicitly written in terms of the elastic stress tensor, the pressure, and the solid and fluid velocity fields, which are the unknowns of the problem. To complete the set of equations, we add the expression of the elastic stress tensor and the continuity equation for the mixture. Moreover, we recall that the diffusive drag ζ and the Helmholtz free energy are functions of C^s, which, together with the changes of ϕ^s and ϕ^f (where $\phi^s + \phi^f = 1$), are computed from the solid displacement field $\boldsymbol{u}^s$.

The equations shown in Table 3.2 are similar to the equations obtained in the quasistatic version of the nonlinear consolidation theory of Biot [11], in the case of incompressible and inviscid solid and fluid phases. However, Mow and co-workers opted to use the theory of mixtures to derive these equations because it offers a consistent framework to incorporate the assumptions

Table 3.2 Final count of the number of equations and unknowns for a biphasic mixture in three-dimensional space.

Equations	Num.	Unknowns	Num.
Balance of linear momentum:			
$\nabla \cdot \boldsymbol{\sigma}_{\mathrm{E}}^{\mathrm{s}} - \phi^{\mathrm{s}} \nabla p - \boldsymbol{\zeta}(\boldsymbol{C}^{\mathrm{s}})\,(\boldsymbol{v}^{\mathrm{s}} - \boldsymbol{v}^{\mathrm{f}}) = \mathbf{0}$ (a)	3	Velocities; $\boldsymbol{v}^{\mathrm{s}}, \boldsymbol{v}^{\mathrm{f}}$	6
$-\phi^{\mathrm{f}} \nabla p + \boldsymbol{\zeta}(\boldsymbol{C}^{\mathrm{s}})\,(\boldsymbol{v}^{\mathrm{s}} - \boldsymbol{v}^{\mathrm{f}}) = \mathbf{0}$ (b)	3		
Elastic stress tensor:			
$\boldsymbol{\sigma}_{\mathrm{E}}^{\mathrm{s}} = 2\rho^{\mathrm{s}} \boldsymbol{F}^{\mathrm{s}} \dfrac{\partial \hat{\psi}^{\mathrm{s}}(\boldsymbol{C}^{\mathrm{s}})}{\partial \boldsymbol{C}^{\mathrm{s}}} \boldsymbol{F}^{\mathrm{s}\mathrm{T}}$	6	Stress; $\boldsymbol{\sigma}_{\mathrm{E}}^{\mathrm{s}}$	6
Continuity equation for the mixture:			
$\nabla \cdot (\phi^{\mathrm{s}} \boldsymbol{v}^{\mathrm{s}} + \phi^{\mathrm{f}} \boldsymbol{v}^{\mathrm{f}}) = 0$	1	Pressure; p	1
	13		13

regarding soft hydrated tissues. The versatility of the theory of mixtures is clearly demonstrated by the triphasic theory of Lai *et al.* [59], where an additional ion phase is introduced.

3.8.1 Boundary Conditions

With the governing equations established, it is possible to introduce the time-dependent boundary conditions that makes the initial/boundary problem well-posed. Fig. 3.2 shows the boundary conditions on the solid and fluid domains in the current configuration. The following kinematic boundary conditions applies:

$$\boldsymbol{u}^{\mathrm{s}}(\boldsymbol{x}, t) = \bar{\boldsymbol{g}}^{\mathrm{s}}, \qquad \text{for } \boldsymbol{x} \in \Gamma_{g^{\mathrm{s}}}; \tag{3-55}$$

$$\boldsymbol{v}^{\mathrm{f}}(\boldsymbol{x}, t) = \frac{D\bar{\boldsymbol{g}}^{\mathrm{f}}}{Dt} = \dot{\bar{\boldsymbol{g}}}^{\mathrm{f}}, \qquad \text{for } \boldsymbol{x} \in \Gamma_{g^{\mathrm{f}}}, \tag{3-56}$$

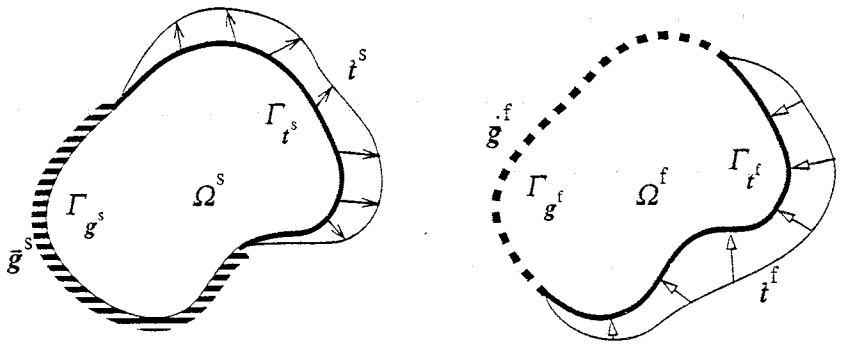

Figure 3.2 Schematic representation of the boundary conditions.

where the over-bar ($\bar{}$) denotes a prescribed value, and Γ_{g^s} and Γ_{g^f} are portions of the boundary on which solid displacement and fluid velocity, respectively, are prescribed. The boundary conditions imposed on the kinetic fields are

$$\boldsymbol{\sigma}^s(\boldsymbol{x}, t)\, \boldsymbol{n} = \bar{\boldsymbol{t}}^s, \qquad \text{for } \boldsymbol{x} \in \Gamma_{t^s}; \tag{3-57}$$

$$\boldsymbol{\sigma}^f(\boldsymbol{x}, t)\, \boldsymbol{n} = \bar{\boldsymbol{t}}^f, \qquad \text{for } \boldsymbol{x} \in \Gamma_{t^f}, \tag{3-58}$$

where $\boldsymbol{n}$ is the outward normal vector; and Γ_{t^s} and Γ_{t^f} are portions of the boundary on which solid and fluid tractions are prescribed. In the case of an inviscid fluid, Eq. (3-58) is simplified to $\boldsymbol{\sigma}^f(\boldsymbol{x}, t) = -\phi^f \bar{p}\, \mathbf{1}$, for $\boldsymbol{x} \in \Gamma_{t^f}$. The partition of the boundary Γ is such that

$$\begin{aligned} \overline{\Gamma_{g^s} \cup \Gamma_{t^s}} &= \overline{\Gamma_{g^f} \cup \Gamma_{t^f}} = \Gamma, \\ \Gamma_{g^s} \cap \Gamma_{t^s} &= \Gamma_{g^f} \cap \Gamma_{t^f} = \varnothing, \end{aligned} \tag{3-59}$$

where the superimposed bar denotes a set closure. The boundary partitions in Fig. 3.2 and Eq. (3-59) have illustrative purposes only since different partitions are possible according to the component of the external traction forces.

3.8.2 Initial Conditions

Initial conditions are specified with respect to the reference configuration of the solid phase in terms of initial velocity fields:

$$v^s(X^s, 0) = \dot{g}^s, \qquad \text{for} \quad X^s \in \Omega_0^s, \tag{3-60}$$

$$v^f(X^s, 0) = \dot{g}^f, \qquad \text{for} \quad X^s \in \Omega_0^s, \tag{3-61}$$

where $\dot{g}^s$ and $\dot{g}^f$ must satisfy the continuity equation for the mixture. In the finite element implementation it will be assumed that the reference configuration corresponds to a natural state and that the initial velocities are zero, trivially satisfying the continuity equation.

3.9 Summary

In this chapter the theoretical foundations of the biphasic theory have been reviewed with emphasis on the constitutive modeling. Restrictions imposed by the axiom of material frame indifference, the entropy inequality for a biphasic mixture, and symmetry of the material have been examined, together with restrictions intrinsic to a biphasic mixture. The Cauchy stress tensor and the elasticity tensor for hyperelastic transverse isotropy have been derived for use in the finite element formulations, for which the governing equations and initial/boundary are stated at the end of this chapter.

CHAPTER 4

Nonlinear Finite Element Formulations

"Although in some exact solutions to problems in finite elasticity the assumption of an incompressible material leads to certain simplifications in the analysis, such is not the case in finite element applications",

J. T. ODEN [76, p. 236]

In this chapter three nonlinear finite element formulations for biphasic continua are discussed. First, the linear mixed-penalty formulation presented by Spilker and Maxian [99] is extended to nonlinear problems in order to consider an anisotropic, hyperelastic material under finite deformation, and a strain-dependent permeability. Second, the nonlinear penalty formulation of Suh *et al.* [105] is reviewed and updated using the discrete divergence operator to allow the use of higher-order interpolation elements. With this update, the equivalence between penalty and mixed-penalty formulations is demonstrated, a result that reduces the number of candidate elements to be investigated. Third, a nonlinear version of the mixed $\boldsymbol{u}$-p formulation, called $\boldsymbol{v}$-p to distinguish from previous versions, is examined for comparison with the mixed-penalty formulation.

All three formulations incorporate nonlinearities that are essential to represent soft hydrated tissues under finite deformation: anisotropic hyperelasticity, strain-dependent permeability and geometric nonlinearity. A semidiscretization procedure, involving the spatial discretization in finite elements followed by a temporal discretization using a finite difference scheme, is adopted to solve the quasistatic biphasic equations [9]. This is accomplished by using the Galerkin weighted residual method to derive finite element weak forms for each formulation, and a trapezoidal rule to obtain recursive expressions in time for the resulting systems of ordinary, first-order, differential equations [47]. A total Lagrangian approach is adopted in constructing the nonlinear systems of equations, whose incremental forms are solved iteratively using the Newton-Raphson method [7].

A common characteristic of the mixed-penalty and penalty formulations considered here for biphasic problems is that they employ a penalized form of the continuity equation for the mixture. In the mixed-penalty formulation, based on the consistent penalty method of Engelman *et al.* [29] for single-phase incompressible media, the pressure is retained as an independent field variable. Thus, the penalized continuity equation is introduced, along with the momentum equations and natural boundary conditions for each phase, into the weighted residual statement. Since the derivative of the pressure does not appear in the finite element weak form, a pressure field which is discontinuous between elements can be used, and the pressure unknowns can subsequently be eliminated through static condensation.

In the penalty method of Suh *et al.* [105], the penalized continuity equation is used to eliminate the pressure as a field variable, so that the development is analogous to a displacement-based formulation. Thus, only the linear momentum equations and the natural boundary conditions, expressed in terms of velocities, enter in the weighted residual statement. Selective/reduced integration is used for the penalty terms. As a result, there is little control over the pressure interpolation, and other alternatives must be considered for the implementation of elements in nonlinear analysis. In the present study, the concept of a discrete divergence operator used by Simo *et al.* [91] is adopted to extend the nonlinear penalty formulation to elements with higher-order interpolation.

Historically, penalty finite elements have also been derived by considering limiting cases of finite element formulations that address mixtures with compressible constituents (a common practice in soil mechanics). When such an approach is used, the penalty form of the continuity equation plays a secondary role since it becomes a 'simplification' at the end. This secondary role has prevented further development of the corresponding finite elements, which have been restricted to 4-node quadrilaterals with selective/reduced integration.

The v-p formulation is a mixed formulation where the quasistatic linear momentum equation for the fluid is used to eliminate the fluid velocity from the governing equations. The weak form is obtained by introducing the momentum equation for the mixture, a modified form of the

continuity equation, and boundary conditions for flux and total traction into the weighted residual statement. Different versions of this formulation have been implemented both in soil mechanics [15, 38, 56, 68, 83, 88, 94] and biomechanics [79, 80, 115]. The version of the ***u-p*** formulation presented here is called ***v-p*** in order to emphasize that the solid velocity is used as a primary variable, and to distinguish it from other versions with distinct assumptions with regard to the nonlinearities.

In limiting conditions, the biphasic equations presented in Table 3.2 represent either single-phase incompressible elasticity ($\kappa \to 0$ with $v^s \sim v^f$) or permeation through a porous, rigid medium ($v^s \sim 0$). Even in conditions far from these extremes, the short term response of a mixture initially at rest resembles the response of a single phase incompressible solid (with the fluid phase being trapped within the solid matrix). Due to these considerations, biphasic finite elements are required to satisfy the LBB (or inf-sup) condition for single phase continua in order to avoid problems such as spurious pressure modes and 'locking' normally associated with the enforcement of the compressibility constraint. The LBB condition poses restrictions on the use of arbitrary interpolations for primary and secondary variables in order to guarantee the stability and convergence of the solution. It was derived independently by Babuska [5] and Brezzi [20], with a similar condition previously obtained by Ladyszhenskaya for the case of Stoke's flow. In the next chapter important results from analytical studies with mixed finite elements are used to select biphasic finite elements. For a complete discussion about mixed finite element methods and the enforcement of constraints see Brezzi and Fortin [21] and references therein.

4.1 Penalty Form of the Continuity Equation

The continuity equation for a biphasic mixture, Eq. (2-56), is a kinematic constraint that expresses the intrinsic incompressibility of the solid and fluid phases. A similar equation is used to enforce the incompressibility constraint in Stokes flow (divergence-free condition), but for incompressible elasticity the constraint is normally written using the Jacobian determinant of the deformation [35, 36, 106]. This is done to avoid the accumulation of residual volumetric deformations,

taking advantage of the fact that the volumetric deformation has to be zero everywhere. For biphasic continua, however, an expression in terms of Jacobian determinants does not improve accuracy since the current volume is unknown. For this reason, the divergence form is adopted in the finite element formulations.

In the mixed-penalty and penalty formulations, the continuity equation for the mixture, Eq. (2-56), is replaced by the following penalty form:

$$\nabla \cdot (\phi^{s} \boldsymbol{v}^{s} + \phi^{f} \boldsymbol{v}^{f}) + \frac{p}{\beta} = 0, \tag{4-1}$$

where the additional term corresponds to an arbitrarily small perturbation, and β is a user-specified penalty parameter. Notice that as β approaches infinity, the continuity equation is correctly enforced. There is a strong resemblance between this equation and the continuity equation for a *mixture with a compressible fluid phase* [84], suggesting that β allows a small compressibility. However, further analogy between β and the bulk modulus can be misleading since the material time derivative of the pressure, instead of the pressure itself, appears in the continuity equation in the compressible case.

To enforce continuity, the penalty parameter must be a large number, but not so large that it would make the system of equations ill-conditioned. Determining a suitable range for β depends mainly on numerical experiments. Suh *et al.* [105] verified that β can range over four orders of magnitude, and derived the following expression based on one-dimensional problems:

$$\beta \approx C_1 \frac{\|\nabla \boldsymbol{u}\|}{\|\nabla \boldsymbol{v}\|} \frac{H_A}{\phi^{f}} \approx C_1 \, t_0 \frac{H_A}{\phi^{f}}, \tag{4-2}$$

where $\|\nabla \boldsymbol{u}\|$ and $\|\nabla \boldsymbol{v}\|$ are Euclidean norms of the displacement and velocity gradients, respectively; $H_A = \lambda^{s} + 2\mu^{s}$ is the aggregate modulus of the linear biphasic theory [70]; ϕ^{f} is the porosity; and t_0 is a representative time. The coefficient C_1 is a machine-dependent parameter, and a value of $C_1 = 10^{6}$ is recommended for 64-bit, double-precision calculations. Since the gradient

norms are not known *a priori*, the usual procedure is to obtain β from simple analyses that can represent the class of problems being studied.

Note that Eq. (4-2) is similar to the second part of the relation provided by Prevost for soils [84] which, converted to the notation of this work, reads:

$$\beta \approx C_2 \max\left(\frac{\phi^{\mathrm{f}}}{\kappa}, \frac{\Delta t H_A}{2\phi^{\mathrm{f}}}\right), \tag{4-3}$$

where κ is the permeability coefficient, Δt is the increment of time, and a value $C_2 = 10^7$ is suggested for the machine-dependent parameter. Penalty parameters obtained using the first part of Eq. (4-3), however, may lead to a ill-conditioned system of equations for permeability values typical of articular cartilage ($\kappa \sim 1\times10^{-14}$ m^4/Ns).

4.2 Function Spaces for the Mixed-Penalty and Penalty Formulations

Appropriate function spaces must be defined in order to obtain the weak form using the weighted residual method [47, 53]. To this end, the space of square-integrable functions in Ω is required:

$$L_2(\Omega) = \{ w \mid \int_{\Omega} w(x)^2 d\Omega < \infty, \quad x \in \Omega \}, \tag{4-4}$$

as is the Sobolev space with square-integrable first derivatives:

$$H^1(\Omega) = \{ w \mid w \in L_2, \ (D_i w \in L_2, i=1,..,n_{sd}) \}, \tag{4-5}$$

where $D_i w$ denotes the first derivative with respect to x_i, and n_{sd} is the number of space dimensions.

Let $\mathcal{S}^{\mathrm{s}}$ and $\mathcal{S}^{\mathrm{f}}$ denote *spaces of trial solutions* for the solid and fluid phase velocities, respectively, which have square-integrable first derivatives over the domain Ω and satisfy the essential boundary conditions

$$\mathcal{S}^{\mathrm{s}} = \{ v^{\mathrm{s}}(\bullet, t) \,|\, v^{\mathrm{s}}(\bullet, t) \in [H^1(\Omega)]^{n_{sd}},\ v^{\mathrm{s}}(x, t) = \dot{g}^{\mathrm{s}} \text{ on } \Gamma_{g^{\mathrm{s}}} \},$$
$$\mathcal{S}^{\mathrm{f}} = \{ v^{\mathrm{f}}(\bullet, t) \,|\, v^{\mathrm{f}}(\bullet, t) \in [H^1(\Omega)]^{n_{sd}},\ v^{\mathrm{f}}(x, t) = \dot{g}^{\mathrm{f}} \text{ on } \Gamma_{g^{\mathrm{f}}} \}, \tag{4-6}$$

where $\dot{g}^{\mathrm{s}}$ and $\dot{g}^{\mathrm{f}}$ are prescribed solid and fluid velocities (Fig. 4.1). Let $\mathcal{V}^{\mathrm{s}}$ and $\mathcal{V}^{\mathrm{f}}$ be *spaces of arbitrary weighting functions* for the solid and fluid phases, w^{s} and w^{f} respectively, which satisfy the homogeneous form of the essential boundary conditions

$$\mathcal{V}^{\mathrm{s}} = \{ w^{\mathrm{s}} \,|\, w^{\mathrm{s}} \in [H^1(\Omega)]^{n_{sd}},\ w^{\mathrm{s}}(x) = 0 \text{ on } \Gamma_{g^{\mathrm{s}}} \},$$
$$\mathcal{V}^{\mathrm{f}} = \{ w^{\mathrm{f}} \,|\, w^{\mathrm{f}} \in [H^1(\Omega)]^{n_{sd}},\ w^{\mathrm{f}}(x) = 0 \text{ on } \Gamma_{g^{\mathrm{f}}} \}. \tag{4-7}$$

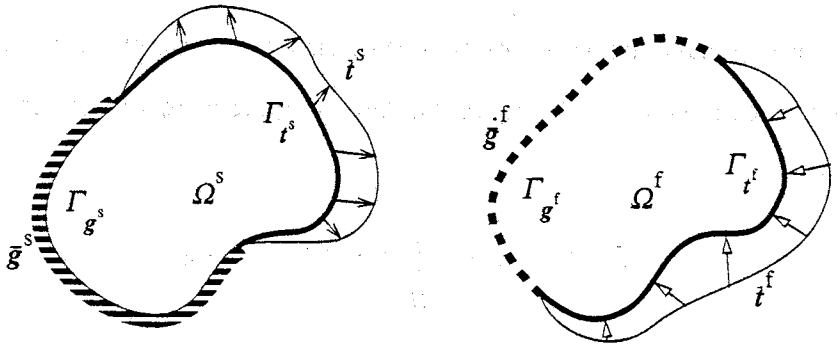

$\Gamma_{t^{\mathrm{s}}}$: t^{s} prescribed solid traction

$\Gamma_{g^{\mathrm{s}}}$: $\bar{g}^{\mathrm{s}}$ prescribed solid displacement

$\Gamma_{t^{\mathrm{f}}}$: t^{f} prescribed fluid traction

$\Gamma_{g^{\mathrm{f}}}$: $\dot{g}^{\mathrm{f}}$ prescribed fluid velocity

Figure 4.1 Boundary surfaces for the mixed-penalty (MP) and penalty (PE) formulations.

Additional spaces are necessary for the mixed-penalty formulation. The space $\mathcal{S}^{\mathrm{p}}_{\mathrm{MP}}$ of trial solutions p is defined as

$$\mathcal{S}^{\mathrm{p}}_{\mathrm{MP}} = \{ p(\bullet, t) \;|\; p(\bullet, t) \in L^2(\Omega) \}, \tag{4-8}$$

which reflects the fact that no inter-element continuity is required for the pressure field. And the space $\mathcal{V}_{\mathrm{MP}}^{\mathrm{p}}$ of arbitrary weighting functions q is

$$\mathcal{V}_{\mathrm{MP}}^{\mathrm{p}} = \{ q \mid q \in L^2(\Omega) \} . \tag{4-9}$$

The portions of the boundaries Γ_{g^s}, Γ_{g^f}, Γ_{t^s} and Γ_{t^f} are specified in the current configuration $\mathcal{B}$, which is shared at time t by the solid and fluid phases. It is assumed that the corresponding surfaces in the reference configuration $\mathcal{B}_0^{\mathrm{s}}$ are well defined through the deformation of the solid phase. Note that functions in $\mathcal{V}^{\mathrm{s}}$, $\mathcal{V}^{\mathrm{f}}$ and $\mathcal{V}_{MP}^{\mathrm{p}}$ do not depend on time, while the functions in $\mathcal{S}^{\mathrm{s}}$, $\mathcal{S}^{\mathrm{f}}$ and $\mathcal{S}_{MP}^{\mathrm{p}}$ vary with t due to the essential boundary conditions.

In the finite element method, the spaces defined by Eqs. (4-6) to (4-9) are approximated by discrete, or finite-dimensional, subspaces. These subspaces are associated with a discretization of the domain Ω (*finite element mesh*), identified with a subscript "h". The approximated trial solutions are restricted to the subspaces

$$v_{\mathrm{h}}^{\alpha} \in \mathcal{S}_{\mathrm{h}}^{\alpha} \subset \mathcal{S}^{\alpha}, \qquad p_{\mathrm{h}} \in \mathcal{S}_{\mathrm{MP\,h}}^{\mathrm{p}} \subset \mathcal{S}_{\mathrm{MP}}^{\mathrm{p}}, \tag{4-10}$$

and analogously for the weighting functions,

$$w_{\mathrm{h}}^{\alpha} \in \mathcal{V}_{\mathrm{h}}^{\alpha} \subset \mathcal{V}^{\alpha}, \qquad q_{\mathrm{h}} \in \mathcal{V}_{\mathrm{MP\,h}}^{\mathrm{p}} \subset \mathcal{V}_{\mathrm{MP}}^{\mathrm{p}}. \tag{4-11}$$

4.3 The Mixed-Penalty Formulation (MP)

In order to obtain the weak form in the mixed-penalty formulation (MP), the linear momentum equations (a) and (b) in Table 3.2, the penalty form of the continuity equation (Eq. (4-1)), and the natural boundary conditions (Eqs. (3-57) and (3-58)) are multiplied by weighting functions and introduced into the weighted residual statement:

$$\int_{\Omega} \{ w^s \cdot [\nabla \cdot \sigma_E^s - \phi^s \nabla p - \zeta (v^s - v^f)] + w^f \cdot [-\phi^f \nabla p + \zeta (v^s - v^f)] + q\left[\nabla \cdot (\phi^s v^s + \phi^f v^f) + \frac{p}{\beta}\right] \} d\Omega + \int_{\Gamma_{t^s}} w^s \cdot (\bar{t}^s - \sigma^s n)\, d\Gamma - \int_{\Gamma_{t^f}} w^f \cdot n\, \phi^f (\bar{p} - p)\, d\Gamma = 0. \tag{4-12}$$

To reduce the order of differentiation of the field variables, and thus the order of continuity required subsequently in the finite element interpolations, the divergence theorem is applied to Eq. (4-12). In particular, it is worthwhile to show the intermediate steps:

$$\int_{\Omega} w^s \cdot (\nabla \cdot \sigma_E^s)\, d\Omega = \int_{\Gamma_{t^s}} w^s \cdot (\sigma_E^s n)\, d\Gamma - \int_{\Omega} \mathrm{tr}((\nabla w^s)^T \sigma_E^s) d\Omega\,, \tag{4-13}$$

$$\int_{\Omega} w^\alpha \cdot (\phi^\alpha \nabla p)\, d\Omega = \int_{\Gamma_{t^\alpha}} w^\alpha \cdot n\; p \phi^\alpha d\Gamma - \int_{\Omega} \nabla \cdot (\phi^\alpha w^\alpha)\, p d\Omega, \qquad \alpha = \text{s,f (no summation)}, \tag{4-14}$$

where the definitions of the spaces for w^α, Eq. (4-7), have been used to reduce the domain of integration on the boundary. After cancelling boundary terms we obtain

$$\int_{\Omega} \{ \mathrm{tr}((\nabla w^s)^T \sigma_E^s) - \nabla \cdot (\phi^s w^s + \phi^f w^f)\, p + (w^s - w^f) \cdot \zeta (v^s - v^f) - q\left[\nabla \cdot (\phi^s v^s + \phi^f v^f) + \frac{p}{\beta}\right] \} d\Omega = \int_{\Gamma_{t^s}} w^s \cdot \bar{t}^s d\Gamma - \int_{\Gamma_{t^f}} w^f \cdot n\; \bar{p} \phi^f d\Gamma. \tag{4-15}$$

In the total Lagrangian approach, the above equation must be rewritten in the reference configuration [7]. Recall that the elements of volume $d\Omega$ and area $d\Gamma$ refer to the current configuration, and are related to the corresponding reference values $d\Omega_0$ and $d\Gamma_0$ by

$$d\Omega = J^s d\Omega_0\,, \tag{4-16}$$

$$\boldsymbol{n}d\Gamma = J^{s}\boldsymbol{n}_0 \cdot \boldsymbol{F}^{s^{-1}} d\Gamma_0, \tag{4-17}$$

where $\boldsymbol{F}^{s}$ is the deformation gradient of the solid phase, J^{s} is its determinant, and $\boldsymbol{n}_0$ is the outward unit normal to $d\Gamma_0$ [66, 67]. The last equation can also be presented in a ratio form using the right Cauchy-Green deformation tensor $\boldsymbol{C}^{s}$

$$J_{\Gamma}^{s} = \frac{d\Gamma}{d\Gamma_0} = J^{s}\sqrt{\boldsymbol{n}_0 \cdot \boldsymbol{C}^{s^{-1}}\boldsymbol{n}_0}. \tag{4-18}$$

For hyperelastic materials it is customary to introduce the *Lagrangian strain tensor* $\boldsymbol{E}^{s}$ (*Green-Lagrange strain tensor*) and the *elastic part of the second Piola-Kirchhoff stress tensor* $\boldsymbol{S}_{E}^{s}$ defined, respectively, as

$$\boldsymbol{E}^{s} = \frac{1}{2}(\boldsymbol{C}^{s} - \boldsymbol{1}), \tag{4-19}$$

$$\boldsymbol{S}_{E}^{s} = J^{s}\boldsymbol{F}^{s^{-1}}\boldsymbol{\sigma}_{E}^{s}\,\boldsymbol{F}^{s^{-T}}, \tag{4-20}$$

$\boldsymbol{\sigma}_{E}^{s}$ being the elastic Cauchy stress tensor, Eq. (3-17). For a hyperelastic solid phase, $\boldsymbol{S}_{E}^{s}$ is derived from the Helmholtz free energy function as

$$\boldsymbol{S}_{E}^{s} = \rho_0^{s}\frac{\partial\tilde{\psi}^{s}}{\partial\boldsymbol{E}^{s}} = 2\rho_0^{s}\frac{\partial\hat{\psi}^{s}}{\partial\boldsymbol{C}^{s}}. \tag{4-21}$$

Introducing Eqs. (4-16) to (4-18) and (4-20) into Eq. (4-15) yields the weak form of the boundary/ initial value problem:

$$\begin{aligned}
&\int_{\Omega_0} \mathrm{tr}\Big((\nabla_X \boldsymbol{w}^{s})^{T}\,\boldsymbol{F}^{s}\boldsymbol{S}_{E}^{s}\Big) d\Omega_0 \\
&+ \int_{\Omega_0} \{ (\boldsymbol{w}^{s} - \boldsymbol{w}^{f}) \cdot \boldsymbol{\zeta}(\boldsymbol{v}^{s} - \boldsymbol{v}^{f}) - \nabla \cdot (\phi^{s}\boldsymbol{w}^{s} + \phi^{f}\boldsymbol{w}^{f})\, p - q\Big[\nabla \cdot (\phi^{s}\boldsymbol{v}^{s} + \phi^{f}\boldsymbol{v}^{f}) + \frac{p}{\beta}\Big]\} J^{s} d\Omega_0 \\
&= \int_{\Gamma_{t_0^{s}}} \boldsymbol{w}^{s} \cdot \boldsymbol{t}^{s} J_{\Gamma}^{s}\, d\Gamma_0 - \int_{\Gamma_{t_0^{f}}} \boldsymbol{w}^{f} \cdot \Big(\boldsymbol{n}_0 \cdot \boldsymbol{F}^{s^{-1}}\Big) \bar{p}\phi^{f} J^{s} d\Gamma_0.
\end{aligned} \tag{4-22}$$

In order to solve the problem numerically, the finite element method is used to approximate Eq. (4-22) in terms of a finite number of unknowns. The basic idea consists of replacing the spaces $\mathcal{S}^{\alpha}$, $\mathcal{S}^{\mathrm{p}}_{\mathrm{MP}}$, $\mathcal{V}^{\alpha}$ and $\mathcal{V}^{\mathrm{p}}_{\mathrm{MP}}$ with finite-dimensional subspaces $\mathcal{S}^{\alpha}_{\mathrm{h}}$, $\mathcal{S}^{\mathrm{p}}_{\mathrm{MP\,h}}$, $\mathcal{V}^{\alpha}_{\mathrm{h}}$ and $\mathcal{V}^{\mathrm{p}}_{\mathrm{MP\,h}}$. The discrete analogue of Eq. (4-22), called the *finite element weak form*, is obtained by subdividing the continuum into n_{et} elements of domain Ω_{e} and boundary Γ_{e}. Within element "e", solid displacement, and solid and fluid velocity fields are interpolated in terms of nodal values as

$$\boldsymbol{u}^{\mathrm{s}}_{\mathrm{h}} = N^{sa}\boldsymbol{u}^{sa}, \qquad \boldsymbol{v}^{\mathrm{s}}_{\mathrm{h}} = N^{sa}\boldsymbol{v}^{sa}, \qquad \boldsymbol{v}^{\mathrm{f}}_{\mathrm{h}} = N^{fa}\boldsymbol{v}^{fa}, \qquad a = 1,...,n_{npe}, \tag{4-23}$$

where N^{sa} and N^{fa} are local C^0 interpolation functions, with the property $N^{\alpha a}(\boldsymbol{x}^b) = \delta^{ab}$, $\boldsymbol{x}^b$ being the coordinates of node b, and $\boldsymbol{u}^{sa}$, $\boldsymbol{v}^{sa}$ and $\boldsymbol{v}^{fa}$ are nodal displacement and velocities associated with element node a. According to Eq. (4-23), the components of a vector are independently interpolated by the same scalar function. The summation convention only applies to the index a, which varies from one to the number of nodes per element, n_{npe}. The pressure field is interpolated in terms of pressure coefficients, with n_{pc} being the number of coefficients per element:

$$p_{\mathrm{h}} = \mathcal{N}^{c}\, p^{c}, \qquad c = 1,...,n_{pc}. \tag{4-24}$$

Since spatial derivatives of pressure do not occur in the weak form, the interpolation function $\mathcal{N}^{c}$ can be of class C^{-1}. The pressure interpolation can not be arbitrarily selected in a constrained problem, and typically a polynomial of lower order than the ones used for the velocity fields is chosen.

In the *Galerkin approximation* of the weighted residual statement, the weighting functions share the same interpolation functions used for the trial solutions, yielding

$$\boldsymbol{w}^{\mathrm{s}}_{\mathrm{h}} = N^{sa}\boldsymbol{w}^{sa}, \qquad \boldsymbol{w}^{\mathrm{f}}_{\mathrm{h}} = N^{fa}\boldsymbol{w}^{fa}, \qquad a = 1,...,n_{npe}; \tag{4-25}$$

$$q_{\mathrm{h}} = \mathcal{N}^{c}\, q^{c}, \qquad c = 1,...,n_{pc}. \tag{4-26}$$

While different interpolations could be used for the solid and fluid phases, there is no apparent reason to do so. Therefore, in what follows the same interpolation functions are used for both phases, $N^{sa} = N^{fa} = N^a$. By introducing Eqs. (4-23) to (4-26) into Eq. (4-22), the finite element weak form is obtained:

$$\begin{aligned}
&\sum_{e=1}^{n_{et}} \Bigg(\int_{\Omega_0^e} \mathrm{tr}\Big((\nabla_X w^s)^T F^s S_E^s \Big) d\Omega_0 \\
&+ \int_{\Omega_0^e} \Big[w^{sa} \cdot N^a \zeta N^b (v^{sb} - v^{fb}) - \nabla \cdot (\phi^s N^a w^{sa}) \mathcal{N}^d p^d \Big] J^s d\Omega_0 \\
&+ \int_{\Omega_0^e} [w^{fa} \cdot N^a \zeta N^b (-v^{sb} + v^{fb}) - \nabla \cdot (\phi^f N^a w^{fa}) \mathcal{N}^d p^d] J^s d\Omega_0 \\
&- q^c \int_{\Omega_0^e} \mathcal{N}^c \Big[\nabla \cdot (\phi^s N^b v^{sb}) + \nabla \cdot (\phi^f N^b v^{fb}) + \frac{1}{\beta} \mathcal{N}^d p^d \Big] J^s d\Omega_0 \Bigg) \\
&= \sum_{e=1}^{n_{et}} \Bigg(w^{sa} \cdot \int_{\Gamma_{t_0^s}} N^a \bar{t}^s J_\Gamma^s d\Gamma_0 - w^{fa} \cdot \int_{\Gamma_{t_0^f}} N^a n_0 \cdot F^{s-1} \bar{p} \phi^f J^s d\Gamma_0 \Bigg),
\end{aligned} \tag{4-27}$$

with $a, b = 1,...,n_{npe}$, and $c, d = 1,...,n_{pc}$. Note that the summation convention and the ranges associated with the letters *a, b, c* and *d* will be consistently maintained throughout this chapter.

In Section 4.7 it will be shown that the first integral in the above equation can be written as a product of two vectors:

$$w^{se^T} g^{se} := \int_{\Omega_0^e} \mathrm{tr}\Big((\nabla_X w^s)^T F^s S_E^s \Big) d\Omega_0, \tag{4-28}$$

with w^{se} containing the nodal weighting values for the solid phase, and g^{se} representing the nonlinear elasticity of the solid phase (the assembled counterpart of g^{se} is called the *nonlinear elasticity*). Collecting coefficients of the vectors of nodal values, Eq. (4-27) can be rewritten in matrix form:

$$\sum_{e=1}^{n_{el}} \begin{bmatrix} w^{eT} & q^{eT} \end{bmatrix} \left(\begin{bmatrix} Y_2^e & -A^{eT} \\ -A^e & -\frac{1}{\beta} H^e \end{bmatrix} \begin{Bmatrix} v^e \\ p^e \end{Bmatrix} + \begin{Bmatrix} g^e \\ 0 \end{Bmatrix} \right) = \sum_{e=1}^{n_{el}} \begin{bmatrix} w^{eT} & q^{eT} \end{bmatrix} \begin{Bmatrix} f^e \\ 0 \end{Bmatrix}, \tag{4-29}$$

where, with regard to element "e", $v^{eT} = [\, v^{seT} \;\; v^{feT} \,]$ represents nodal velocities; p^e, pressure coefficients; $w^{eT} = [\, w^{seT} \;\; w^{feT} \,]$, nodal weighting values; and q^e pressure weighting function coefficients.

A convenient way of expressing matrix A^e is to use the partition $A^e = [\, A^s \; A^f \,]$, with the sub-matrices for the solid and fluid phases being given by

$$[A^\alpha]^{cb} \{v^\alpha\}^b = \int_{\Omega_0^e} \mathcal{N}^c \nabla \cdot (\phi^\alpha N^b v^{\alpha b}) J^s d\Omega_0, \tag{4-30}$$

where no summation is implied by α = s,f. Eq. (4-30) is abbreviated using intermediate vectors, which will be specialized for 3-D and axisymmetry in Appendix B, to represent the divergence terms:

$$\{h^{\alpha T}\}^b v^{\alpha b} := \nabla \cdot (\phi^\alpha N^b v^{\alpha b}), \tag{4-31}$$

yielding, for an arbitrary element of A^e,

$$[A^\alpha]_i^{cb} = \int_{\Omega_0^e} \mathcal{N}^c \{h^\alpha\}_i^b J^s d\Omega_0. \tag{4-32}$$

Note that $[A^\alpha]^{cb}$ represents a sub-array, while $[A^\alpha]_i^{cb}$, without bold text, represents a single element; the same applies to other arrays such as in $\{h^\alpha\}^b$ and $\{h^\alpha\}_i^b$.

The remaining arrays in Eq. (4-29) are obtained from the expressions of the corresponding sub-matrices and elements[1]:

1. See Appendices B and C for a complete development of the finite element matrices for 3-D and axisymmetric problems.

$$[Y_2^{\mathrm{e}}]^{ab} = \int_{\Omega_0^{\mathrm{e}}} N^a \zeta N^b J^{\mathrm{s}} d\Omega_0, \tag{4-33}$$

$$[H^{\mathrm{e}}]^{cd} = \int_{\Omega_0^{\mathrm{e}}} \mathcal{N}^c \mathcal{N}^d J^{\mathrm{s}} d\Omega_0, \tag{4-34}$$

$$g^{\mathrm{e}} = \left\{ \begin{array}{c} g^{\mathrm{se}} \\ \mathbf{0} \end{array} \right\}, \tag{4-35}$$

and, finally, the force vector is given by

$$\{f^{\mathrm{e}}\} = \left\{ \begin{array}{c} \{f^{\mathrm{se}}\}^a \\ \{f^{\mathrm{fe}}\}^a \end{array} \right\} = \left\{ \begin{array}{c} \displaystyle\int_{\Gamma_{t_0^{\mathrm{s}}}} N^a \bar{t}^{\mathrm{s}} J_{\Gamma}^{\mathrm{s}} d\Gamma_0 \\ \displaystyle -\int_{\Gamma_{t_0^{\mathrm{f}}}} N^a \boldsymbol{n}_0 \cdot \boldsymbol{F}^{\mathrm{s}-1} \bar{p} \phi^{\mathrm{f}} J^{\mathrm{s}} d\Gamma_0 \end{array} \right\}. \tag{4-36}$$

Because pressure is discontinuous between elements, and pressure coefficients are independent from element to element, p^{e} can be eliminated at the element level by using the equations for the pressure in Eq. (4-29):

$$p^{\mathrm{e}} = -\beta (H^{\mathrm{e}})^{-1} A^{\mathrm{e}} v^{\mathrm{e}}. \tag{4-37}$$

Substituting Eq. (4-37) into the velocity equations in Eq. (4-29) produces the matrix equation for the nonlinear mixed-penalty formulation:

$$\sum_{\mathrm{e}=1}^{n_{el}} w^{\mathrm{e}\mathrm{T}} [\, (\beta\, Y_1^{\mathrm{e}} + Y_2^{\mathrm{e}}) v^{\mathrm{e}} + g^{\mathrm{e}}] = \sum_{\mathrm{e}=1}^{n_{el}} w^{\mathrm{e}\mathrm{T}} f^{\mathrm{e}}, \tag{4-38}$$

where

$$Y_1^{\mathrm{e}} = A^{\mathrm{e}\mathrm{T}} (H^{\mathrm{e}})^{-1} A^{\mathrm{e}}. \tag{4-39}$$

Global matrices are obtained through standard assembly operations over the elements. That is, element degrees of freedom and weighting function nodal values are related to their global counterparts, and contributions of each element are summed to produce the global system of equations. A caret ($\hat{}$) is used to indicate the assembled form of an element nodal vector. For arbitrary nonzero $\hat{w}$ the following assembled system of nonlinear equations is obtained:

$$Y_{\mathrm{MP}}\,\hat{v} + \hat{g} = \hat{f}, \tag{4-40}$$

where $Y_{\mathrm{MP}} = [\beta\, Y_1 + Y_2]$; and Y_1, Y_2, $\hat{g}$ and $\hat{f}$ are the assembled counterparts of the element matrices.

4.4 The Equivalence of the Penalty and Mixed-Penalty Formulations

The weak form of the penalty formulation of Suh *et al.* [105] is developed in a similar fashion, the only difference being the absence of the penalty form of the continuity equation from the weighted residual statement

$$\begin{aligned}\int_{\Omega} \{ w^{\mathrm{s}} \cdot [\nabla \cdot \sigma_{\mathrm{E}}^{\mathrm{s}} - \phi^{\mathrm{s}} \nabla p - \zeta (v^{\mathrm{s}} - v^{\mathrm{f}})] + w^{\mathrm{f}} \cdot [-\phi^{\mathrm{f}} \nabla p + \zeta (v^{\mathrm{s}} - v^{\mathrm{f}})] \}\, d\Omega \\ + \int_{\Gamma_{t^{\mathrm{s}}}} w^{\mathrm{s}} \cdot (t^{\mathrm{s}} - \sigma^{\mathrm{s}} n)\, d\Gamma - \int_{\Gamma_{t^{\mathrm{f}}}} w^{\mathrm{f}} \cdot n\, \phi^{\mathrm{f}} (\bar{p} - p)\, d\Gamma = 0.\end{aligned} \tag{4-41}$$

The continuity equation, instead, is solved for the pressure, which is then substituted into Eq. (4-41), yielding,

$$\begin{aligned}\int_{\Omega} \{ \mathrm{tr}((\nabla w^{\mathrm{s}})^{\mathrm{T}} \sigma_{\mathrm{E}}^{\mathrm{s}}) + \beta\, \nabla \cdot (\phi^{\mathrm{s}} w^{\mathrm{s}} + \phi^{\mathrm{f}} w^{f})\ \nabla \cdot (\phi^{\mathrm{s}} v^{\mathrm{s}} + \phi^{\mathrm{f}} v^{f}) \\ + (w^{\mathrm{s}} - w^{\mathrm{f}}) \cdot \zeta (v^{\mathrm{s}} - v^{\mathrm{f}})\ \}\, d\Omega \\ = \int_{\Gamma_{t^{\mathrm{s}}}} w^{\mathrm{s}} \cdot t^{\mathrm{s}}\, d\Gamma - \int_{\Gamma_{t^{\mathrm{f}}}} w^{\mathrm{f}} \cdot n\, \bar{p} \phi^{\mathrm{f}}\, d\Gamma.\end{aligned} \tag{4-42}$$

Using Eqs. (4-16) to (4-18) and (4-20) to write the above equation in the reference configuration produces the weak form

$$\int_{\Omega_0} \mathrm{tr}\Big((\nabla_X w^{\mathrm{s}})^{\mathrm{T}} F^{\mathrm{s}} S_{\mathrm{E}}^{\mathrm{s}} \Big) d\Omega_0$$

$$+ \int_{\Omega_0} [\beta \nabla \cdot (\phi^{\mathrm{s}} w^{\mathrm{s}} + \phi^{\mathrm{f}} w^{f}) \ \nabla \cdot (\phi^{\mathrm{s}} v^{\mathrm{s}} + \phi^{\mathrm{f}} v^{f}) + (w^{\mathrm{s}} - w^{\mathrm{f}}) \cdot \zeta (v^{\mathrm{s}} - v^{\mathrm{f}})] J^{\mathrm{s}} d\Omega_0 \tag{4-43}$$

$$= \int_{\Gamma_{t_0^{\mathrm{s}}}} w^{\mathrm{s}} \cdot \bar{t}^{\mathrm{s}} J_{\Gamma}^{\mathrm{s}} \, d\Gamma_0 - \int_{\Gamma_{t_0^{\mathrm{f}}}} w^{\mathrm{f}} \cdot \Big(n_0 \cdot F^{\mathrm{s}-1} \Big) \bar{p} \phi^{\mathrm{f}} J^{\mathrm{s}} d\Gamma_0 .$$

As before, the finite element weak form is obtained by subdividing the continuum into finite elements, and interpolating the trial solution and the weighting functions within each element. Adopting the same interpolation function for the velocity components of both phases, and introducing Eqs. (4-23) to (4-25) into Eq. (4-43), gives

$$\sum_{\mathrm{e}=1}^{n_{el}} \Bigg(\int_{\Omega_0^{\mathrm{e}}} \mathrm{tr}\Big((\nabla_X w^{\mathrm{s}})^{\mathrm{T}} F^{\mathrm{s}} S_{\mathrm{E}}^{\mathrm{s}} \Big) d\Omega_0$$

$$\int_{\Omega_0^{\mathrm{e}}} \{\beta \nabla \cdot (\phi^{\mathrm{s}} N^a w^{sa}) [\nabla \cdot (\phi^{\mathrm{s}} N^b v^{sb}) + \nabla \cdot (\phi^{\mathrm{f}} N^b v^{fb})]$$

$$+ w^{sa} \cdot N^a \zeta N^b (v^{sb} - v^{fb}) \} J^{\mathrm{s}} d\Omega_0$$

$$\int_{\Omega_0^{\mathrm{e}}} \{\beta \nabla \cdot (\phi^{\mathrm{f}} N^a w^{fa}) [\nabla \cdot (\phi^{\mathrm{s}} N^b v^{sb}) + \nabla \cdot (\phi^{\mathrm{f}} N^b v^{fb})] \tag{4-44}$$

$$+ w^{fa} \cdot N^a \zeta N^b (-v^{sb} + v^{fb}) \} J^{\mathrm{s}} d\Omega_0 \Bigg)$$

$$= \sum_{\mathrm{e}=1}^{n_{el}} \Bigg(w^{sa} \cdot \int_{\Gamma_{t_0^{\mathrm{s}}}} N^a \bar{t}^{\mathrm{s}} J_{\Gamma}^{\mathrm{s}} \, d\Gamma_0 - w^{fa} \cdot \int_{\Gamma_{t_0^{\mathrm{f}}}} N^a n_0 \cdot F^{\mathrm{s}-1} \bar{p} \phi^{\mathrm{f}} J^{\mathrm{s}} d\Gamma_0 \Bigg),$$

$$a, b = 1, \ldots, n_{npe}.$$

By collecting vectors of nodal values, and making use of Eq. (4-28), Eq. (4-44) can be rewritten in matrix form as

$$\sum_{e=1}^{n_{el}} w^{eT} [\,(\beta\, Y_3^e + Y_2^e)\, v^e + g^e] \;=\; \sum_{e=1}^{n_{el}} w^{eT} f^e \,. \tag{4-45}$$

Matrix Y_2 and vectors g^e and f^e are the same arrays shown for the mixed-penalty formulation (Eqs. (4-33), (4-35) and (4-36)). While matrix Y_3 is given by

$$[Y_3^e] \;=\; \begin{bmatrix} Y_3^{ss} & Y_3^{sf} \\ Y_3^{fs} & Y_3^{ff} \end{bmatrix}, \tag{4-46}$$

where the sub-matrices are defined by

$$\left[w^{\alpha T}\right]^a [Y_3^{\alpha\gamma}]^{ab} \{v^\gamma\}^b := \int \nabla\cdot(\phi^\alpha N^a w^{\alpha a})\, \nabla\cdot(\phi^\gamma N^b v^{\gamma b})\, J^s d\Omega_0, \qquad \text{with no summation on } \alpha, \gamma = \text{s,f.} \tag{4-47}$$

If the intermediate vector h^α, defined in Eq. (4-31), were to be used to replace the divergence terms, the sub-matrices $[Y_3^{\alpha\gamma}]^{ab}$ above would be computed as

$$[Y_3^{\alpha\gamma}]^{ab} \;=\; \int_{\Omega_0^e} \{h^{\alpha T}\}^a \{h^\gamma\}^b J^s d\Omega_0 \,. \tag{4-48}$$

However, the computation of Y_3 requires special treatment to avoid problems such as locking (overconstrained solution) or rank deficiency (spurious zero energy modes). When dealing with bilinear quadrilaterals, selective/reduced integration can be employed, leading to a standard penalty formulation. A more general approach, valid for higher-order interpolation elements, uses the following *discrete divergence operator* [91]:

$$\begin{aligned} \nabla^h\cdot(\phi^\alpha w) \;&=\; \mathcal{N}^c [H^e]^{cd} \int_{\Omega^e} \mathcal{N}^d \nabla\cdot(\phi^\alpha w)\, d\Omega \\ &=\; \mathcal{N}^c [H^e]^{cd} [A^\alpha]^{db} \{w\}^b, \end{aligned} \tag{4-49}$$

where $[A^{\alpha}]^{db}$ and $[H^{e}]^{cd}$ are given by Eqs. (4-32) and (4-34), respectively. Replacing the divergence operators in Eq. (4-47) by their discrete counterparts, yields

$$
\begin{aligned}
[Y_3^{\alpha\gamma}]^{ab} &= \int_{\Omega_0^e} \left[A^{\alpha T}\right]^{ac} \left[H^{e-T}\right]^{cd} \mathcal{N}^d \mathcal{N}^f \left[H^{e-1}\right]^{fg} [A^{\gamma}]^{gb} J^s d\Omega_0 \\
&= \left[A^{\alpha T}\right]^{ac} \left[H^{e-1}\right]^{cd} [A^{\gamma}]^{db},
\end{aligned}
\tag{4-50}
$$

with $a, b = 1, \ldots, n_{npe}$, and $c, d, f, g = 1, \ldots, n_{pc}$.

The comparison between Eqs. (4-50) and (4-39), and Eqs. (4-45) and (4-38) is sufficient to demonstrate the equivalence between the nonlinear penalty and mixed-penalty formulations when the discrete divergence is adopted. For bi-linear quadrilaterals, Eq. (4-49) is considerably simplified due to the constant pressure interpolation, leading to an efficient mean-dilatation penalty formulation [100, 105]. For elements with higher-order interpolation, however, there is no apparent computational advantage in using the penalty formulation, and preference should be given to the mixed-penalty formulation.

4.5 Mixed Solid Velocity - Pressure Formulation (v-p)

The use of the linear momentum equation for the fluid phase to eliminate the fluid velocity from the governing equations characterizes the mixed velocity-pressure (v-p) formulation. The weak form, obtained using the momentum equation for the mixture and a modified form of the continuity equation, contains the gradient of the pressure and thus requires an inter-element continuous interpolation for the pressure, which is a now a primary variable. The corresponding discrete form produces systems with smaller number of equations than in the previous methods. And, because of this advantage, different variants of the velocity-pressure or displacement-pressure formulations (both linear and nonlinear) have been investigated in the fields of soil mechanics [15, 38, 56, 68, 83, 88, 94] and biomechanics [79, 80, 115]. In this section, a nonlinear version of the v-p formulation is developed adopting as unknowns increments of velocity and pressure. The load-

ing terms of the *v-p* formulation, though rarely addressed in the above references, are presented here for completeness.

The process of eliminating the fluid velocity starts by rewriting the linear momentum equation for the fluid phase (Eq. (b) in Table 3.2) as

$$\phi^{\mathrm{f}}(v^{\mathrm{f}} - v^{\mathrm{s}}) = -\phi^{\mathrm{f}\,2}\zeta^{-1}\nabla p = -\kappa\nabla p, \tag{4-51}$$

where $\kappa = (\phi^{\mathrm{f}})^{2}\zeta^{-1}$ is the *permeability tensor.* Except for the omission of the conservative body forces, Eq. (4-51) is the classical Darcy's law. For a saturated mixture, the continuity equation can be expressed as

$$\nabla \cdot [v^{\mathrm{s}} + \phi^{\mathrm{f}}(v^{\mathrm{f}} - v^{\mathrm{s}})] = 0. \tag{4-52}$$

Adding the linear momentum equations in Table 3.2, and introducing Eq. (4-51) into Eq. (4-52), produces the following system of equations:

$$\nabla \cdot (\sigma_{\mathrm{E}}^{\mathrm{s}} - p\mathbf{1}) = \mathbf{0}, \tag{4-53}$$

$$\nabla \cdot (v^{\mathrm{s}} - \kappa\nabla p) = 0, \tag{4-54}$$

where the first equation is the momentum equation for the mixture. The elimination of the fluid velocity from the governing equations leads to a mixed finite element formulation in which the pressure and solid velocity/displacement are interpolated. Consequently, the prescribed fluid flux that leaves the domain Ω through the boundary Γ_{Q} replaces the prescribed fluid traction as a natural boundary condition. Using Darcy's law, the prescribed fluid flux is defined as

$$\bar{Q} = -(\kappa\nabla p) \cdot \boldsymbol{n} = \phi^{\mathrm{f}}(v^{\mathrm{f}} - v^{\mathrm{s}}) \cdot \boldsymbol{n}. \tag{4-55}$$

Therefore, the boundary conditions associated with the governing equations are

$$\boldsymbol{u}^{\mathrm{s}}(\boldsymbol{x}, t) = \bar{\boldsymbol{g}}^{\mathrm{s}}, \qquad \text{for } \boldsymbol{x} \in \Gamma_{\boldsymbol{g}^{\mathrm{s}}}; \tag{4-56}$$

$$p(\boldsymbol{x}, t) = \bar{p}, \qquad \text{for } \boldsymbol{x} \in \Gamma_{p}; \tag{4-57}$$

$$\sigma(x, t)\, n = \hat{t}, \qquad \text{for } x \in \Gamma_{t^s}; \tag{4-58}$$

$$-(\kappa \nabla p) \cdot n = \bar{Q}, \qquad \text{for } x \in \Gamma_Q, \tag{4-59}$$

where the surfaces Γ_{g^s} and Γ_{t^s} are complementary subsets of the boundary Γ, and so are Γ_p and Γ_Q, as shown in Fig. 4.2.

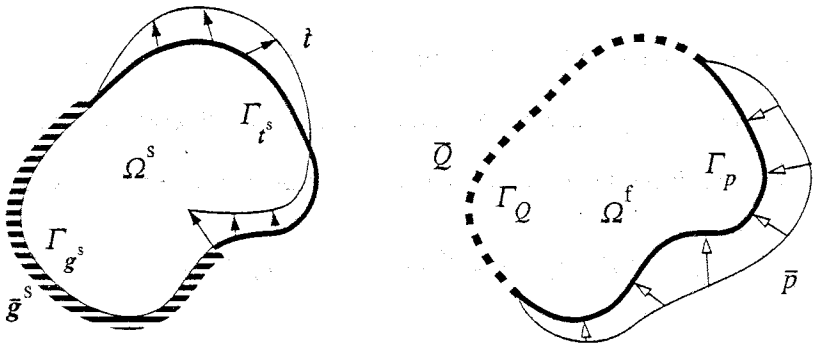

Γ_{t^s}: $\hat{t}$ prescribed total traction

Γ_{g^s}: $\bar{g}^s$ prescribed solid displacement

Γ_p: $\bar{p}$ prescribed pressure

Γ_Q: $\bar{Q}$ prescribed fluid flow

Figure 4.2 Boundary surfaces for the *v-p* formulation.

The function spaces defined for the pressure in Section 4.2 are inadequate for the *v-p* formulation, so new spaces must be defined. Let $\mathcal{S}_{vp}^{\mathrm{p}}$ denote the space of trial solutions for the pressure, which have square-integrable first derivatives over the domain Ω, and satisfy the boundary condition for the pressure:

$$\mathcal{S}_{vp}^{\mathrm{p}} = \{ p(\bullet, t) \mid p(\bullet, t) \in H^1(\Omega),\ p(x, t) = \bar{p} \text{ on } \Gamma_p \}, \tag{4-60}$$

and let $\mathcal{V}_{vp}^{\mathrm{p}}$ be the space of weighting functions q, which satisfy the homogeneous form of the essential boundary condition,

$$\mathcal{V}_{vp}^{\mathrm{p}} = \{ q \mid q \in H^1(\Omega),\ q(x) = 0 \text{ on } \Gamma_p \}. \tag{4-61}$$

In the *v-p* formulation, Eqs. (4-53) and (4-54) and boundary conditions, Eqs. (4-58) and (4-59), are introduced into the weighted residual statement, yielding

$$\int_{\Omega} \{ w^{s} \cdot [\nabla \cdot (\sigma_{E}^{s} - p\mathbf{1})] + q[\nabla \cdot (v^{s} - \kappa \nabla p)] \} d\Omega + \int_{\Gamma_{t^{s}}} w^{s} \cdot (\bar{t} - \sigma n) d\Gamma - \int_{\Gamma_{Q}} q(\bar{Q} + (\kappa \nabla p) \cdot n) d\Gamma = 0, \tag{4-62}$$

where use has been made of Eqs. (4-7) and (4-61) to restrict the domains of integration on the boundary, explaining why $\bar{t}$ is considered only on $\Gamma_{t^{s}}$. The divergence theorem is then applied to reduce the order of differentiation, as is illustrated below for two of the integrals:

$$\int_{\Omega} w^{s} \cdot \nabla p d\Omega = \int_{\Gamma_{t^{s}}} p w^{s} \cdot n d\Gamma - \int_{\Omega} p \nabla \cdot w^{s} d\Omega, \tag{4-63}$$

$$\int_{\Omega} q \nabla \cdot (\kappa \nabla p) d\Omega = \int_{\Gamma_{Q}} q(\kappa \nabla p) \cdot n d\Gamma - \int_{\Omega} (\kappa \nabla p) \cdot \nabla q \, d\Omega. \tag{4-64}$$

After cancelling boundary terms, the weak form in the current configuration is obtained:

$$\int_{\Omega} \{ \mathrm{tr}((\nabla w^{s})^{\mathrm{T}} \sigma_{E}^{s}) - q \nabla \cdot v^{s} - p \nabla \cdot w^{s} - (\kappa \nabla p) \cdot \nabla q \} d\Omega = \int_{\Gamma_{t^{s}}} w^{s} \cdot \bar{t} d\Gamma + \int_{\Gamma_{Q}} q \bar{Q} d\Gamma. \tag{4-65}$$

In the total Lagrangian formulation, the integrals in Eq. (4-65) must be rewritten in the reference configuration, yielding

$$\int_{\Omega_{0}} \mathrm{tr}\left((\nabla_{X} w^{s})^{\mathrm{T}} F^{s} S_{E}^{s} \right) d\Omega_{0} - \int_{\Omega_{0}} [q \nabla \cdot v^{s} + p \nabla \cdot w^{s} + (\kappa \nabla p) \cdot \nabla q] J^{s} d\Omega_{0} = \int_{\Gamma_{t_{0}^{s}}} w^{s} \cdot \bar{t} J_{\Gamma}^{s} d\Gamma_{0} + \int_{\Gamma_{Q_{0}}} q \bar{Q} J_{\Gamma}^{s} d\Gamma_{0}, \tag{4-66}$$

where Eqs. (4-16) to (4-18) and (4-20) have been employed.

The finite element weak form is obtained by subdividing the continuum into n_{et} elements of domain Ω_e and boundary Γ_e. Within an element "e", pressure, solid displacement and solid velocity are interpolated in terms of nodal values as

$$p_h = \mathcal{N}^c \, p^c, \qquad c = 1,...,n_{pn}; \tag{4-67}$$

$$\boldsymbol{u}_h^s = N^a \boldsymbol{u}^{sa}, \qquad \boldsymbol{v}_h^s = N^a \boldsymbol{v}^{sa}, \qquad a = 1,...,n_{npe}, \tag{4-68}$$

where $\mathcal{N}^c$ and N^a are C^0 interpolation functions; n_{pn} is the number of *pressure nodes* per element, and n_{npe} is the number of kinematic nodes per element. The above interpolation functions are also used for the weighting functions:

$$q_h = \mathcal{N}^c \, q^c, \qquad c = 1,...,n_{pn}; \tag{4-69}$$

$$\boldsymbol{w}_h^s = N^a \boldsymbol{w}^{sa}, \qquad a = 1,...,n_{npe}. \tag{4-70}$$

By introducing Eqs. (4-67) to (4-70) into Eq. (4-66), the following finite element weak form is obtained:

$$\begin{aligned} \sum_{e=1}^{n_{et}} \Bigg(& \int_{\Omega_0^e} \mathrm{tr}\Big((\nabla_X \boldsymbol{w}^s)^{\mathrm{T}} \boldsymbol{F}^s \boldsymbol{S}_E^s \Big) d\Omega_0 - \int_{\Omega_0^e} \nabla \cdot (N^a \boldsymbol{w}^{sa}) \, \mathcal{N}^d p^d J^s \, d\Omega_0 \\ & - q^c \int_{\Omega_0^e} [\nabla \mathcal{N}^c \cdot \boldsymbol{\kappa} \nabla \mathcal{N}^d p^d + \mathcal{N}^c \nabla \cdot (N^b \boldsymbol{v}^{sb})] \, J^s \, d\Omega_0 \Bigg) \\ & = \sum_{e=1}^{n_{et}} \left(\boldsymbol{w}^{sa} \cdot \int_{\Gamma_{t_0}^e} N^a \hat{\boldsymbol{t}} J_\Gamma^s \, d\Gamma_0 + q^c \int_{\Gamma_{Q_0}^e} \mathcal{N}^c \bar{Q} J_\Gamma^s \, d\Gamma_0 \right), \end{aligned} \tag{4-71}$$

with $a, b = 1,..,n_{npe}$ and $c, d = 1,...,n_{pn}$. This expression is more compact than the penalty-based expressions presented earlier, having the advantage of avoiding the divergence term $\nabla \cdot (\phi^\alpha \boldsymbol{v}^\alpha)$. By collecting coefficients of the vectors of nodal values, Eq. (4-71) can be rewritten in the matrix form

$$\sum_{e=1}^{n_{et}} \begin{bmatrix} w^{se\mathrm{T}} & q^{e\mathrm{T}} \end{bmatrix} \left(\begin{bmatrix} 0 & -A_{vp}^{e\,\mathrm{T}} \\ -A_{vp}^{e} & -H_{vp}^{e} \end{bmatrix} \begin{Bmatrix} v^{se} \\ p^{e} \end{Bmatrix} + \begin{Bmatrix} g^{se} \\ 0 \end{Bmatrix} \right) = \sum_{e=1}^{n_{et}} \begin{bmatrix} w^{e\mathrm{T}} & q^{e\mathrm{T}} \end{bmatrix} \begin{Bmatrix} f^{te} \\ Q^{e} \end{Bmatrix}, \tag{4-72}$$

where v^{se}, p^{e}, w^{se} and q^{e} are nodal vectors of solid velocity, pressure, and weighting values for the solid phase and pressure, respectively, for element "e". Vector g^{se} is the nonlinear elasticity of the solid phase, Eq. (4-28), and f^{te} corresponds to the total traction. Matrices in Eq. (4-72) have the following sub-matrices[1]:

$$[A_{vp}^{e}]^{ca} \{v^{se}\}^{a} = \int_{\Omega_0^e} \mathcal{N}^{c} \nabla \cdot (N^{a} v^{sa}) J^{s} d\Omega_0, \tag{4-73}$$

$$[H_{vp}^{e}]^{cd} = \int_{\Omega_0^e} \nabla \mathcal{N}^{c} \cdot \kappa \nabla \mathcal{N}^{d} J^{s} d\Omega_0; \tag{4-74}$$

and the force vector is given by

$$\{f^{e}\} = \begin{Bmatrix} \{f^{te}\}^{a} \\ \{Q^{e}\}^{c} \end{Bmatrix} = \begin{Bmatrix} \int_{\Gamma_{t_0}^e} N^{a} \bar{t} J_{\Gamma}^{s} \, d\Gamma_0 \\ \int_{\Gamma_{Q_0}^e} \mathcal{N}^{c} \bar{Q} J_{\Gamma}^{s} \, d\Gamma_0 \end{Bmatrix}. \tag{4-75}$$

It is convenient to define an intermediate vector to represent the divergence (see Section B.5), such that

$$h^{\mathrm{T}} v^{s} := \nabla \cdot (N^{a} v^{s\,a}) . \tag{4-76}$$

Thus, the elements of matrix A_{vp}^{e} are given by

$$[A_{vp}^{e}]_{i}^{ca} = \int_{\Omega_0^e} \mathcal{N}^{c} \{h\}_{i}^{a} J^{s} d\Omega_0 . \tag{4-77}$$

---

1. See Appendix C for the complete development of the finite element matrices for 3-D and axisymmetric problems.

By defining the following vectors and matrix:

$$v^{e} = \left\{ \begin{array}{c} v^{se} \\ p^{e} \end{array} \right\}, \qquad w^{e} = \left\{ \begin{array}{c} w^{se} \\ q^{e} \end{array} \right\}, \qquad Y^{e}_{vp} = \begin{bmatrix} 0 & -A^{e\,T}_{vp} \\ -A^{e}_{vp} & -H^{e}_{vp} \end{bmatrix}, \tag{4-78}$$

Eq. (4-72) can be represented as

$$\sum_{e=1}^{n_{et}} w^{eT} [Y^{e}_{vp} v^{e} + g^{e}] = \sum_{e=1}^{n_{et}} w^{eT} f^{e}. \tag{4-79}$$

After assembling the element matrices, and assuming arbitrary nonzero weighting values, the system of nonlinear equations is obtained as

$$Y_{vp} \hat{v} + \hat{g} = \hat{f}, \tag{4-80}$$

where a caret ($\hat{}$) indicates the assembled counterpart of an element vector.

4.6 Solution of the Nonlinear System of Equations

Eqs. (4-40) and (4-80) constitute systems of ordinary first-order differential equations condensed into the form[1]

$$Y \dot{\hat{v}} + \hat{g} = \hat{f}, \tag{4-81}$$

where $\hat{v}$ is the vector of nodal unknowns (either velocities, or velocities and pressures); Y is the capacity matrix [47, 83]; $\hat{g}$ is the vector of nonlinear elasticity, which contains nodal forces corresponding to elastic stresses in the solid matrix; and $\hat{f}$ is the vector of external forces (see Sections 4.3, 4.4 and 4.5 for specific details).

The system of equations (4-81) is nonlinear and it is valid at any instant of time. To solve this system numerically, the time domain is subdivided into intervals called *time steps*, *i.e.*

1. Although the solution process is unified in this presentation, the reader should be aware that, in contrast to the penalty formulations, the coefficient matrix of the *v-p* formulation is not positive definite.

$\Delta t_{n+1} = t_{n+1} - t_n$, where $t_{n+1}, t_n, \ldots, t_0$ denote instants of time. A finite difference scheme is used to obtain approximations of the temporal response using a series of recursive solutions at successive time steps. For time t_{n+1}, Eq. (4-81) can be written as

$$Y_{n+1}\hat{v}_{n+1} + \hat{g}_{n+1} = \hat{f}_{n+1}, \tag{4-82}$$

where it is assumed that $\hat{v}_{n+1} \approx \hat{v}(t_{n+1})$ and $\hat{u}^s_{n+1} \approx \hat{u}^s(t_{n+1})$. The coefficient matrix Y_{n+1} and the nonlinear elasticity vector $\hat{g}_{n+1}$ depend on the current configuration, which is unknown at t_{n+1}. The external force vector is an explicit function of time and can depend on the current configuration, as occurs for a prescribed pressure or a solid-phase traction normal to the boundary. In order to solve this nonlinear system of equations, Eq. (4-82) must be linearized, and an appropriate finite difference rule and iterative scheme must be introduced within a time step to account for the approximation of vectors and coefficient matrices.

The approach adopted here expresses the solution in terms of increments of nodal velocities and, for the *v-p* formulation, increments of nodal pressure. This approach is similar to the one presented by Suh *et al.* [105]; it has also been employed by Prevost [82-84] and Borja [17] with elasto-plastic constitutive models. Another possible approach uses increments of displacements instead of velocities to solve the nonlinear equations [80, 115]. Because both approaches are related by a finite difference rule, their computational implementations are quite similar. Finally, it should be noted that only nodal vectors in assembled form are dealt with in what follows and, since there is no danger of confusion, the caret symbol ($\hat{}$) used to denote global nodal values is dropped.

In order to obtain a recursive relation for Eq. (4-82), a partial linearization that includes only the nonlinear elasticity g is performed. In this approach, due to the absence of linearized forms for the capacity matrix and the force vector, the arrays Y and f have to be updated throughout the iterations. The complete linearization of Eq. (4-82) and simplifications that lead to the approach adopted here are issues examined in the next section. The linearized form for g is derived

in Section 4.7.2 and has, in the context of the Newton-Raphson method, the following recursive form:

$$g_{n+1} = \begin{Bmatrix} g^{s}_{n+1} \\ 0 \end{Bmatrix}, \qquad g^{s(i)}_{n+1} = g^{s(i-1)}_{n+1} + K^{s(i-1)}_{n+1} \Delta u^{s(i)}_{n+1}, \tag{4-83}$$

where K^{s}_{n+1} is the tangent stiffness matrix of the solid phase. The zero vector above corresponds to either fluid velocity or pressure degrees of freedom, depending on the formulation being considered. The superscript within parentheses designates the iteration number, with $(i-1)$ referring to vectors and matrices that are known from the previous iteration:

$$g^{(i-1)}_{n+1} = g_{n+1}(x^{s(i-1)}_{n+1}), \qquad K^{(i-1)}_{n+1} = \begin{bmatrix} K^{s}_{n+1}(x^{s(i-1)}_{n+1}) & 0 \\ 0 & 0 \end{bmatrix}. \tag{4-84}$$

The above equations require a starting value for the vector of solid-phase displacements. To compute this value, a predictor vector obtained from the converged displacements and velocities at the previous time t_n is adopted [47]. The predictor phase is followed by multi-corrector phases, whose recursive relation is developed below.

Let us start by assuming that the displacement at t_{n+1} is given by

$$u^{s}_{n+1} = u^{s}_{n} + \Delta t \, v^{s}_{\omega}, \tag{4-85}$$

where v^{s}_{ω} denotes the vector containing the solid-phase components in v_{ω}, a velocity vector that occurs between t_n and t_{n+1}. A *trapezoidal,* one-step finite difference scheme is used to compute v_{ω}:

$$v_{\omega} = (1-\omega) v_{n} + \omega \, v_{n+1}, \tag{4-86}$$

with ω being a specified parameter $(0 \le \omega \le 1)$. Since the solid displacements are obtained iteratively, Eq. (4-85) is rewritten as

$$u^{s(i)}_{n+1} = u^{s}_{n} + (1-\omega) \Delta t \, v^{s}_{n} + \omega \, \Delta t \, v^{s(i)}_{n+1}, \tag{4-87}$$

which yields:

$$\Delta u_{n+1}^{s(i)} = u_{n+1}^{s(i)} - u_{n+1}^{s(i-1)} = \omega \, \Delta t \, \Delta v_{n+1}^{s(i)} . \tag{4-88}$$

The complete velocity vector in Eq. (4-82) is expressed in terms of the incremental velocity $\Delta v_{n+1}^{(i)}$ in order to obtain a recursive relation for that equation, resulting in:

$$v_{n+1}^{(i)} = v_{n+1}^{(i-1)} + \Delta v_{n+1}^{(i)} . \tag{4-89}$$

Introducing Eqs.(4-83), (4-88) and (4-89) into Eq. (4-82) leads to the expression

$$[Y_{n+1}^{(i-1)} + \omega \Delta t K_{n+1}^{(i-1)}] \Delta v_{n+1}^{(i)} = f_{n+1}^{(i-1)} - Y_{n+1}^{(i-1)} v_{n+1}^{(i-1)} - g_{n+1}^{(i-1)} . \tag{4-90}$$

In the case of an external force vector that does not depend on the current configuration, $f_{n+1}^{(i-1)}$ is replaced by f_{n+1}. For systems with weak nonlinearities, the iteration procedure can be performed without updating the coefficient matrix on the left-hand-side of Eq. (4-90). This corresponds to the *Modified Newton-Raphson Method*, in which the recursive equation is replaced by

$$[Y_{n+1}^{(0)} + \omega \Delta t K_{n+1}^{(0)}] \Delta v_{n+1}^{(i)} = f_{n+1}^{(i-1)} - Y_{n+1}^{(i-1)} v_{n+1}^{(i-1)} - g_{n+1}^{(i-1)} . \tag{4-91}$$

Note that the right-hand-side of this equation is the residual of Eq. (4-82), which is updated at each iteration. The complete flow chart of the iterative solution process is presented in Table 4.1.

Trapezoidal schemes are often used to solve ordinary differential equations, and some of them have special names as indicated in Table 4.2 [122]. From this table, it is clear that optimum accuracy and high frequency numerical dissipation cannot be achieved simultaneously with any of these schemes [48]. Stability and convergence analyses for the trapezoidal schemes applied to linear and nonlinear biphasic problems are presented by Booker and Small [14] and Prevost [83], respectively. The result is now well known: the solution is unconditionally stable for $\omega \geq 1/2$, a condition that is also valid for strictly increasing time steps. Although the stability analyses for nonlinear problems are based on linearized stability, numerical examples in the literature have

Table 4.1 Iterative solution flow chart

Description
FIRST ITERATION
Predictor phase
A.1 Initialize velocity and solid displacement vectors, where v_n and u_n^s are converged vectors from the previous time t_n $$v_{n+1}^{(0)} := v_n, \qquad u_{n+1}^{s(0)} := u_n^s + \Delta t v_n^s;$$
A.2 Set iteration counter to $i := 1$;
A.3 Use $u_{n+1}^{s(0)}$ to compute matrices and the residual vector in Eq. (4-90), yielding a system of linear equations that is solved for the first increment in nodal velocities $\Delta v_{n+1}^{(1)}$ $$[Y_{n+1}^{(0)} + \omega \Delta t K_{n+1}^{(0)}] \Delta v_{n+1}^{(1)} = f_{n+1}^{(0)} - Y_{n+1}^{(0)} v_{n+1}^{(0)} - g_{n+1}^{(0)}.$$
Corrector Phase
B.1 End the first iteration with a corrector phase, which updates velocity and displacement vectors: $$v_{n+1}^{(1)} := v_{n+1}^{(0)} + \Delta v_{n+1}^{(1)}, \qquad u_{n+1}^{(1)} := u_{n+1}^{(0)} + \omega \Delta t \Delta v_{n+1}^{(1)}.$$
REMAINING ITERATIONS
Multi-corrector Phase
C.1 Update the iteration counter to $i := i + 1$;
C.2 Update matrices and vectors using $u_{n+1}^{(i-1)}$;
C.3 Solve Eq. (4-90) for the increment of nodal velocities $\Delta v_{n+1}^{(i)}$, $$[Y_{n+1}^{(i-1)} + \omega \Delta t K_{n+1}^{(i-1)}] \Delta v_{n+1}^{(i)} = f_{n+1}^{(i-1)} - Y_{n+1}^{(i-1)} v_{n+1}^{(i-1)} - g_{n+1}^{(i-1)};$$
C.4 End the current iteration with a corrector phase, updating velocity and displacement vectors: $$v_{n+1}^{(i)} := v_{n+1}^{(i-1)} + \Delta v_{n+1}^{(i)}, \qquad u_{n+1}^{s(i)} := u_{n+1}^{s(i-1)} + \omega \Delta t \Delta v_{n+1}^{s(i)};$$
C.5 Return to step C.1 and proceed with a new iteration until the norm of the vector of incremental velocities $\Delta v_{n+1}^{(i)}$ satisfies the convergence criteria.

shown that it is strong enough for most practical problems in soil mechanics [15-17, 83] and biomechanics [105].

Table 4.2 Trapezoidal finite difference schemes [122]

ω	Trapezoidal Scheme	Characteristics
0	Euler, Forward difference	Explicit, but conditionally stable.
1/2	Crank-Nicolson	Higher order of accuracy, but response may have oscillations.
2/3	Galerkin	Good for damping high-frequency oscillations.
.878	Liniger	Developed to minimize the domain error.
1	Backward difference	Fully implicit.

The Galerkin scheme was used in most of the examples in this work; it is unconditionally stable and can damp nonphysical higher-order frequencies introduced by the finite element approximation. Systems of equations arising from soft hydrated tissue problems can be considered stiff [17], and, consequently, the forward difference scheme is generally discarded because it requires very small time steps in order to be stable.

In the present study, the following convergence criterion was used for iterations within a time step:

$$\frac{\left|\Delta v^{(i)}\right|}{\left|\Delta v^{(1)}\right|} < TOL, \tag{4-92}$$

where $TOL = 10^{-4}$. Because there may be oscillations during convergence, the criterion must be satisfied through m consecutive iterations (in this study $m = 3$ has been adopted).

4.7 Incremental Linearization

In the previous section a linearized form of the nonlinear elasticity, Eq. (4-83), was used to obtain the incremental form of the biphasic equations. The objective of this section is to derive that equation and, in a broader context, discuss the assumptions behind the partial linearization adopted at that time.

4.7.1 Linearization about a Reference Motion

The current position vector of a solid-phase particle is given by the deformation function $\boldsymbol{\chi}^{\mathrm{s}}(\boldsymbol{X}^{\mathrm{s}}, t)$, where $\boldsymbol{X}^{\mathrm{s}}$ is the position vector at $t = 0$. The deformation can be decomposed into a *reference motion* $\tilde{\boldsymbol{x}}^{\mathrm{s}}$ and a *superposed motion* $\delta\boldsymbol{u}^{\mathrm{s}}$:

$$\boldsymbol{x}^{\mathrm{s}} = \boldsymbol{\chi}^{\mathrm{s}}(\boldsymbol{X}^{\mathrm{s}}, t) = \tilde{\boldsymbol{x}}^{\mathrm{s}}(\boldsymbol{X}^{\mathrm{s}}, t) + \delta\boldsymbol{u}^{\mathrm{s}}(\boldsymbol{X}^{\mathrm{s}}, t). \tag{4-93}$$

The reference motion can be seen as a motion in the neighborhood of $\boldsymbol{x}^{\mathrm{s}}$, with $\delta\boldsymbol{u}^{\mathrm{s}}$ being an admissible increment (or variation) with respect to this motion. Note that as both motions $\boldsymbol{x}^{\mathrm{s}}$ and $\tilde{\boldsymbol{x}}^{\mathrm{s}}$ refer to the same time t, $\delta\boldsymbol{u}^{\mathrm{s}}$ is not the displacement vector $\boldsymbol{u}^{\mathrm{s}} = \boldsymbol{x}^{\mathrm{s}} - \boldsymbol{X}^{\mathrm{s}}$. The letter δ will also denote the first term of the expansion of a Taylor series in $\delta\boldsymbol{u}^{\mathrm{s}}$, for example:

$$\begin{aligned} A(\tilde{\boldsymbol{x}}^{\mathrm{s}} + \delta\boldsymbol{u}^{\mathrm{s}}) &= A(\tilde{\boldsymbol{x}}^{\mathrm{s}}) + DA\big|_{\tilde{\boldsymbol{x}}^{\mathrm{s}}} \cdot \delta\boldsymbol{u}^{\mathrm{s}} + O(\delta\boldsymbol{u}^{\mathrm{s}2}) \\ &= \tilde{A} + \delta A + O(\delta\boldsymbol{u}^{\mathrm{s}2}), \end{aligned} \tag{4-94}$$

where a tilde $(\tilde{\ })$ is used to represent a quantity associated with the reference motion. The *linearized form* of $\boldsymbol{A}$ is then defined as

$$\mathcal{L}A(\tilde{\boldsymbol{x}}^{\mathrm{s}} + \delta\boldsymbol{u}^{\mathrm{s}}) = \tilde{A} + \delta A, \tag{4-95}$$

where the letter $\mathcal{L}$ identifies the first-order approximation of $\boldsymbol{A}$.

4.7.2 Linearization of the Solid-Phase Elasticity

In the finite element weak form, the solid-phase elasticity arises from the integral

$$G_g^{\mathrm{s}} = \int_{\Omega_0^{\mathrm{e}}} \mathrm{tr}\Big((\nabla_X \boldsymbol{w}^{\mathrm{s}})^{\mathrm{T}} \boldsymbol{F}^{\mathrm{s}} \boldsymbol{S}_{\mathrm{E}}^{\mathrm{s}} \Big) d\Omega_0, \tag{4-96}$$

where F^s and S_E^s depend on the deformation $\chi^s(X^s, t)$. F^s is a linear function of the deformation and, assuming that it is continuous and has continuous first-order derivatives[1], $F(\tilde{x}^s + \delta u^s)$ coincides with the linearized form $\mathcal{L}F^s$,

$$F^s(\tilde{x}^s + \delta u^s) = \tilde{F}^s + \nabla_X(\delta u^s) . \tag{4-97}$$

Before dealing with the stress tensor, it is convenient to have the linearized form of the right Cauchy-Green deformation tensor, $C^s = F^{s^T} F^s$,

$$\begin{aligned} \mathcal{L}C^s(\tilde{x}^s + \delta u^s) &= \tilde{C}^s + \tilde{F}^{s^T} \nabla_X(\delta u^s) + [\nabla_X(\delta u^s)]^T \tilde{F}^s \\ &= \tilde{C}^s + \delta C^s . \end{aligned} \tag{4-98}$$

The stress tensor for a hyperelastic material depends only on the current deformation (see Eq. (4-21)). Therefore, by using the chain rule of differentiation, the following expression is obtained:

$$\mathcal{L}S_E^s = \tilde{S}_E^s + \left.\frac{\partial S_E^s}{\partial C^s}\right|_{\tilde{x}^s} : \left(DC^s\big|_{\tilde{x}^s} \cdot \delta u^s \right) = \tilde{S}_E^s + \frac{1}{2}\tilde{\mathbf{C}} : \delta C^s , \tag{4-99}$$

or, in a more familiar form,

$$\mathcal{L}S_E^s = \tilde{S}_E^s + \tilde{\mathbf{C}} : \delta E^s , \tag{4-100}$$

where the symbol (:) denotes a tensor product yielded by the double contraction [67], and $\tilde{\mathbf{C}} = \mathbf{C}|_{\tilde{x}^s}$ is the fourth-order *elasticity tensor* defined by [90]

$$\mathbf{C} = \frac{\partial S_E^s}{\partial E^s} = 2\frac{\partial S_E^s}{\partial C^s} \qquad \text{or,} \qquad \mathbf{C} = 4\rho_0^s \frac{\partial^2 W}{\partial C^s \partial C^s} . \tag{4-101}$$

The linearization of Eq. (4-96) is achieved by expansion in a Taylor series. In this case, the same result is obtained by introducing Eqs. (4-97) to (4-99) into Eq. (4-96), and then eliminating higher-order terms in δu^s:

---

1. In what follows, the appropriate differentiability is always assumed.

$$\mathcal{L}G_g^s = \tilde{G}_g^s + \int_{\Omega_0^e} \{ \frac{1}{2} \Big[(\nabla_X w^s)^T \tilde{F}^s \Big] : \tilde{\mathbf{C}} : \Big[\tilde{F}^{sT} \nabla_X (\delta u^s) + (\nabla_X (\delta u^s))^T \tilde{F}^s \Big] + \mathrm{tr}\Big((\nabla_X w^s)^T \nabla_X (\delta u^s) \tilde{S}_E^s \Big) \} \, d\Omega_0 . \tag{4-102}$$

The above equation can be simplified by using the symmetry of $\tilde{S}_E^s$ and $\tilde{\mathbf{C}}$, yielding

$$\mathcal{L}G_g^s = \tilde{G}_g^s + \int_{\Omega_0^e} \{ \Big[(\nabla_X w^s)^T \tilde{F}^s \Big]^{sym} : \tilde{\mathbf{C}} : \Big[\tilde{F}^{sT} \nabla_X (\delta u^s) \Big]^{sym} + \mathrm{tr}\Big((\nabla_X w^s)^{sym} \tilde{S}_E^s [\nabla_X (\delta u^s)]^{T\,sym} \Big) \} \, d\Omega_0 , \tag{4-103}$$

where the superscript "sym" designates the symmetric part of a tensor. Finally, approximating w^s and δu^s using interpolation functions within a finite element, and developing the gradient terms as shown in Appendix B, produces the matrix form

$$\mathcal{L}G_g^s = w^{seT} g^{se} = w^{seT} [\tilde{g}^{se} + K^{se} \delta u^s] . \tag{4-104}$$

Matrix K^{se} is the *tangent stiffness matrix* of nonlinear elasticity [7], which is usually decomposed in the *large deformation stiffness matrix*, K_L^{se}, and the *geometric stiffness matrix*, K_G^{se} (see Appendix C for the development of these matrices). Vector $\tilde{g}^{se}$ is the *nonlinear elasticity vector* of element "e", given by

$$\tilde{g}^{se} = \int_{\Omega_0^e} B_L^T \tilde{S}_E^s d\Omega_0 , \tag{4-105}$$

where $\tilde{S}_E^s$ is a condensed vector containing the components of the second Piola-Kirchhoff stress tensor and, together with the intermediate matrix B_L, is specialized in Appendix B.

4.7.3 Considerations about Full and Partial Linearizations

Let $G(x^s)$ be the residual of the biphasic equation, defined based on Eq. (4-81) as

$$G(x^s) = Y(x^s)\, v(x^s) + g(x^s) - f(x^s) , \tag{4-106}$$

where the dependence upon the current configuration has been made explicit by using the current position of the solid phase, $x^s = x$. The linearized form of Eq. (4-106) is expressed as

$$\mathcal{L}G(\tilde{x}^s + \delta u^s) = G(\tilde{x}^s) + \delta G, \tag{4-107}$$

with the first term of the Taylor expansion given by

$$\delta G = \delta Y\, v + Y\, \delta v + \delta g - \delta f. \tag{4-108}$$

Applying the chain rule of differentiation to δg and δf in Eq. (4-108), and introducing the result into Eq. (4-107), provides

$$\mathcal{L}G(\tilde{x}^s + \delta u^s) = \tilde{Y}\,\tilde{v} + \delta Y\,\tilde{v} + \tilde{Y}\,\delta v + \left(\tilde{g} + \frac{\partial g}{\partial u^s}\bigg|_{\tilde{x}^s} \delta u^s\right) - \left(\tilde{f} + \frac{\partial f}{\partial u^s}\bigg|_{\tilde{x}^s} \delta u^s\right). \tag{4-109}$$

This full linearization is an expensive alternative, and approximate forms of the above equation are normally used in the finite element implementation. For example, if changes in the matrix Y can be neglected during an iteration, Eq. (4-109) can be simplified to

$$\mathcal{L}G(\tilde{x}^s + \delta u^s) \approx Y(\tilde{x}^s)\; v(\tilde{x}^s + \delta u^s) + \left(g(\tilde{x}^s) + \frac{\partial g}{\partial u^s}\bigg|_{\tilde{x}^s} \delta u^s\right) - \left(f(\tilde{x}^s) + \frac{\partial f}{\partial u^s}\bigg|_{\tilde{x}^s} \delta u^s\right). \tag{4-110}$$

The linearization of the nonlinear elasticity vector is essential to obtain a non-singular system of equations, but the second linearization can be avoided when convergence is achieved just by updating the force vector. In this case, the above equation becomes

$$\mathcal{L}G(\tilde{x}^s + \delta u^s) \approx Y(\tilde{x}^s)\; v(\tilde{x}^s + \delta u^s) + \left(g(\tilde{x}^s) + \frac{\partial g}{\partial u^s}\bigg|_{\tilde{x}^s} \delta u^s\right) - f(\tilde{x}^s + \delta u^s). \tag{4-111}$$

In this thesis, this approximation was chosen instead of Eq. (4-110) for the following reasons: it is usually less expensive, and it produces a symmetric system of equations due to the absence of matrices arising from the linearization of the force term.

4.8 Summary

In this chapter, three nonlinear finite element formulations for biphasic mixtures of incompressible constituents have been derived using the Galerkin weighted residual method. The mixed-penalty biphasic formulation has been extended to nonlinear problems, and its equivalence with the penalty formulation has been demonstrated. A velocity-pressure formulation which considers the nonlinearities found in soft hydrated tissues, has been developed. And finally special attention has been dedicated to the incremental linearization of the system of equations, which is done in a form compatible with the weighted residual method, that is, without explicitly introducing the concept of virtual strain energy.

CHAPTER 5

Selected Element Results for the Linear Confined Compression Biphasic Problem

It is a standard practice to develop general finite element formulations which are dissociated from the element type. During the derivation, discrete spaces of functions are defined and issues such as element geometry, number of nodes per element, and interpolation functions are left for the implementation. In so doing, not only does the development of the formulation become more general and concise, but the computational implementation also becomes more flexible and systematic in the way element routines are managed. This dissociation between formulation and element implementation should not be misinterpreted as implying that all elements arising from a formulation will be robust. For example, the success of a formulation for constrained media still strongly depends on element-by-element numerical and theoretical analyses to find reliable and accurate sets of elements.

Most successful biphasic formulations and elements, taken to the limit of pure solid or fluid, have analogs that are used to represent single phase incompressible elasticity or Stokes flow [31, 32, 86]. With regard to formulations presented in this thesis, elements of the mixed velocity-pressure (v-p) formulation can be classified as members of the Taylor-Hood family of elements, which are characterized by continuous pressure interpolations one order lower than the velocity interpolations. Elements of the mixed-penalty (MP) formulation share the same combinations of inter-element, discontinuous-pressure and continuous-velocity interpolations employed for single phase incompressible media. This analogy with elements for single phase incompressible media has motivated the implementation of MP elements since a more accurate representation of the incompressibility constraint is expected for elements with discontinuous pressure.

The focus of this thesis is nonlinear analysis, and therefore it is important to put the presentations of this chapter in the proper perspective. In the process of developing and implementing alternate formulations for nonlinear analysis, it has been necessary to adopt what appear to be the most appropriate element shapes and interpolations, guided where possible by results for linear

biphasic analysis and/or linear or nonlinear single phase analysis. At various stages in this development, unexpected results in nonlinear analysis have led to re-examination of linear biphasic analysis. As the number of candidate elements is large, it is not the intention of this thesis, or more specifically this chapter, to present an exhaustive study and comparison of elements. Rather, the intention is to provide examples and information that provide insights and guide the choice of finite elements to be used in the nonlinear analysis.

Linear biphasic versions of both *v-p* and MP elements are used to illustrate how element type, mesh refinement and mesh distortion affect the numerical approximation of the confined compression creep (CC-creep) problem. New results are analyzed in the light of previous studies on element performance conducted by Sandhu [87], Reed [85], Spilker and co-workers [99, 100, 112, 113], and Murad and Loula [74, 75]. Although it is a one-dimensional problem (even when modeled by 2-D or 3-D elements), the CC-creep problem is adequate for diagnosing convergence problems, and showing that biphasic elements do not always have the same performance as their single-phase analogs. Furthermore, the CC-creep problem is an extreme test of the elements in that all of the load is suddenly placed on the solid phase. Examples in the next chapter will show that the performance can improve for problems where the load is distributed over both phases, as may be typical in realistic joint loading cases.

5.1 Types of Elements

Several plane-strain, axisymmetric and 3-D finite elements, both linear and nonlinear, have been implemented (see Figs. 5.1 and 5.2 in the next pages). All elements are characterized by a pressure interpolation which is of lower-order than the velocity interpolation. The Taylor-Hood elements use inter-element, continuous-pressure interpolations, in contrast with the MP elements which use inter-element, discontinuous-pressure interpolations. Isoparametric interpolation functions are adopted for velocity fields. Interpolation functions for these elements can be found in Bathe [7], Zienkiewicz and Taylor [121], Hughes [47] and Kardestuncer [54].

For this thesis, elements are identified by the number of nodes and element geometry (*e.g.* 8-node quadrilateral). However, because error-estimate analyses use a nomenclature based on the names of the velocity (displacement) and pressure interpolations, those names are also shown in the figures. In this context, P_k denotes the set of complete polynomials of degree k. Q_k denotes the set of functions that are polynomials of degree k along each coordinate, and a superscript in parentheses indicates the number of coefficients or nodal points. For example, in two dimensions Q_1 contains bilinear functions, while $Q_2^{(8)}$ and $Q_2^{(9)}$ contain incomplete and fully biquadratic functions, respectively. A plus sign as a superscript indicates an internal node or, more generically, the presence of bubble functions.

Table 5.1 presents the integration rules adopted to compute the finite element matrices of the MP and *v-p* formulations (with the order of the polynomial exactly integrated given within parentheses). As a matter of convenience, the same integration rule was used for all matrices of the *v-p* formulation. It should be noted that $\boldsymbol{H}_{vp}^{e}$ can utilize a lower order integration without affecting the result of integration. Numerical integration rules and their application are discussed by Strang and Fix [102], Bathe [7], Hughes [47] and Zienkiewicz [121]. Higher order integration rules for tetrahedra are provided by Jinyun [52] and Keast [55].

Table 5.1 Integration rules adopted to compute the finite element matrices

Element Geometry	Stiffness matrices $\boldsymbol{K}_{L}^{e}$ & $\boldsymbol{K}_{G}^{e}$	MP formulation $\boldsymbol{Y}_{2}^{e}$	MP formulation $\boldsymbol{A}^{e}$ & $\boldsymbol{H}^{e}$	*v-p* formulation $\boldsymbol{A}_{vp}^{e}$ & $\boldsymbol{H}_{vp}^{e}$
6-node triangle	6 points (4)	7 points (7)	6 points (4)	6 points (4)
9-node quadrilateral	3 x 3 (5)	4 x 4 (7)	3 x 3 (5)	3 x 3 (5)
20-node hexahedron	3 x 3 x 3 (5)	4 x 4 x 4 (7)	3 x 3 x 3 (5)	3 x 3 x 3 (5)
10-node tetrahedron	11 points (4)	---	---	11 points (4)

5.1.1 Mixed-Penalty (MP) Finite Elements

Figure 5.1 shows finite elements used with the MP formulation; solid circles represent fluid and solid velocity nodes, and crosses identify the pressure interpolation (one cross per pressure parameter, or coefficient). With respect to these elements, the 7-node triangle, the 9-node quadrilateral and the 27-node hexahedron satisfy the LBB condition for single-phase continuum [31, 47]. The six-node triangle was the first element to be implemented in the linear MP formulation [99], followed by the 10-node tetrahedron [112] not shown in the figure. The 10-node tetrahedron has not been included in part due to poor performance in problems with multiaxial deformation. Specifically, it has been noticed while solving nonlinear confined and unconfined compression problems that this element requires very fine meshes and can manifest locking. The remaining elements are based on standard elements for incompressible media, and were implemented for biphasic continua in this study.

The 5-node quadrilateral was the last element implemented in the program. According to Fortin [32], it does not satisfy the LBB condition, but the presence of a bubble function avoids the locking phenomenon. We shall present results showing good behavior and optimal rates of convergence for this element, making it competitive with quadratic elements for the confined compression problem. The lowest-order MP element is the 4-node quadrilateral with constant pressure (not shown), which does not satisfy the LBB condition. This element is equivalent to the penalty element investigated by Spilker and Suh [100] and Suh *et al.* [105] and thus will not be examined here.

In the MP formulation, the pressure can be expressed within the element in terms of either parent or global coordinates. For linear pressure interpolations, the function contains $n_{pc} = n_{sd} + 1$ pressure coefficients, and is expressed either as $p(\boldsymbol{\xi}) = a_0 + a_i \xi_i$ in parent, or $p(X) = b_0 + b_i X_i$ in global coordinates, with $i = 1, \ldots, n_{sd}$. Interpolations using parent coordinates are adopted in this study except where noted to the contrary in this chapter.

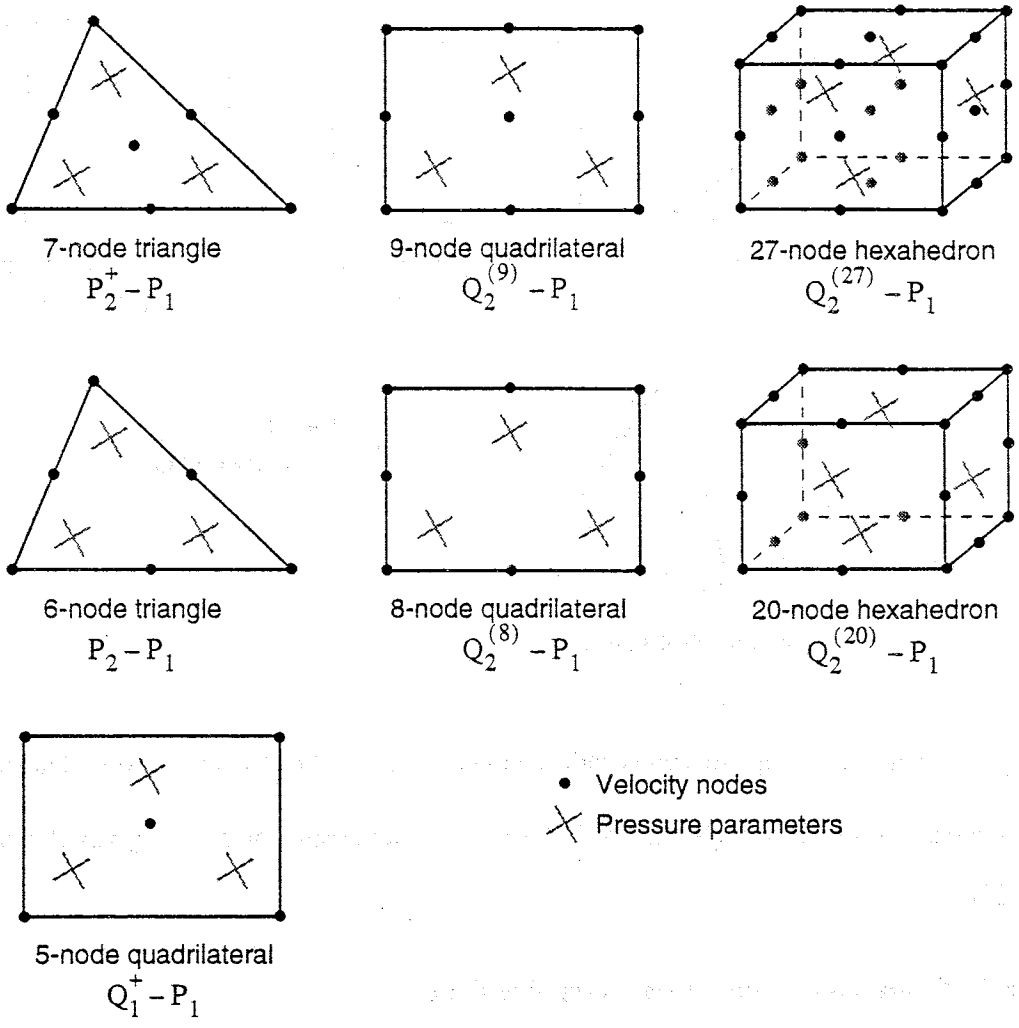

Figure 5.1 Finite elements with discontinuous pressure fields.

5.1.2 Mixed *v* - *p* Finite Elements

Figure 5.2 shows elements used with the *v*-*p* formulation; solid circles represent solid velocity nodes, and open circles around the vertices represent pressure degrees of freedom. The pressure field in the Taylor-Hood family is continuous between elements and is based on element vertices in the case of the quadratic elements considered in this study. The 6-node triangle and the 9-node quadrilateral satisfy the LBB condition for single-phase analysis [47]. It is interesting to

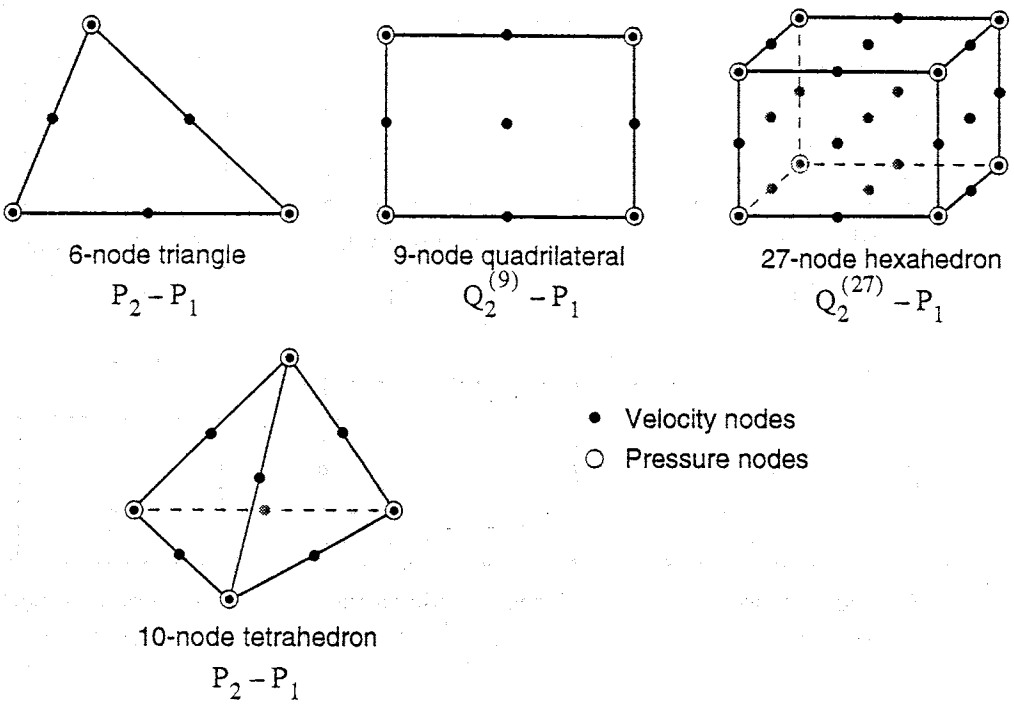

Figure 5.2 Finite elements with continuous pressure fields (Taylor-Hood elements).

note that the 6-node triangle was the first element used to model biphasic (or poroelastic) continua [88].

5.2 Confined Compression Creep Problem

The confined compression creep (CC-creep) problem has been chosen to test elements due to the existence of analytical solutions (see, for instance, Mow *et al.* [70]). In addition, independent solutions for the nonlinear case can be obtained using the finite difference method in space and time [44, 45]. Such solutions are used in the next chapter to demonstrate the accuracy of the nonlinear elements.

The CC-creep problem corresponds to the experimental test schematically represented in Fig. 5.3, which is performed in soft hydrated tissues to determine permeability and aggregate modulus. In this test a cylindrical sample of soft hydrated tissue is placed into a confining chamber and

its top surface is subjected to a step load applied through a rigid, porous and permeable platen. The sample is assumed to fit exactly inside the chamber, and the chamber walls are assumed to be frictionless, so that deformation and fluid flow occur only in the axial direction.

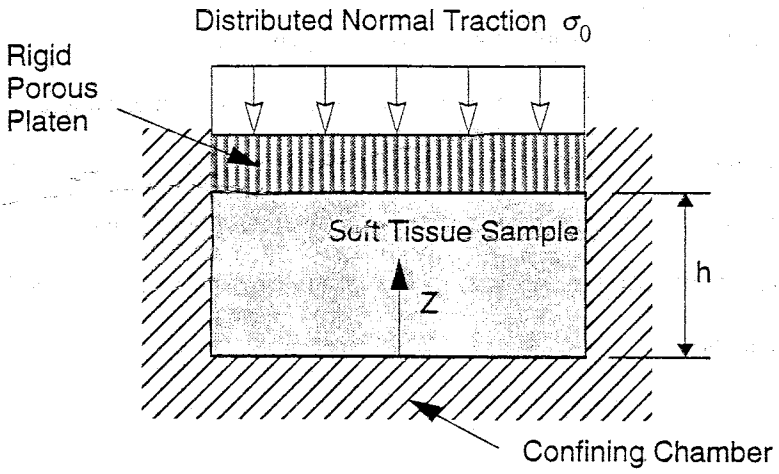

Figure 5.3 Schematic representation of the confined compression creep test of a cylindrical disk of soft hydrated tissue.

In the CC-creep problem, the load is applied entirely to the solid phase. A sudden change in load produces severe gradients in the response near the loaded surface and can create nonphysical spatial oscillations in the finite element approximation [85]. The oscillations are more intense immediately after the change in load, and diminish over several increments in time. Vermeer and Verruijt [111] have studied this problem in linear biphasic analyses and found that the oscillations can be avoided by choosing a time step greater than the lower bound:

$$\Delta t \geq \frac{1}{6} \frac{(\Delta h)^2}{\omega \, \kappa_0 \, H_A}, \tag{5-1}$$

where Δh is the element size in the direction of the flow, ω is the finite difference parameter, κ_0 is the permeability, and $H_A = \lambda^s + 2\mu^s$ is the aggregate modulus. This lower bound was derived by assuming continuous linear pressure interpolations and uniform mesh refinement. Thus there

are competing demands on the time increment; Δt must be small enough to accurately integrate the system of equations, but large enough to avoid oscillations. Alternatively, element size, Δh, can be reduced to avoid oscillations. Moreover, because of the strain-dependent permeability, Eq. (5-1) may not work in nonlinear analysis, where the oscillations can lead to large errors in the nonlinear contributions and subsequent non-convergent results.

Figure 5.4 shows the finite element meshes of 9-node quadrilaterals and 6-node triangles used to solve the CC-creep problem. Nonuniform meshes were chosen to capture the steep gradients that develop near the top surface (later in this chapter, the efficacy of these meshes will be compared to that of uniform meshes). Plane-strain elements are used to facilitate the comparison with 3-D elements.

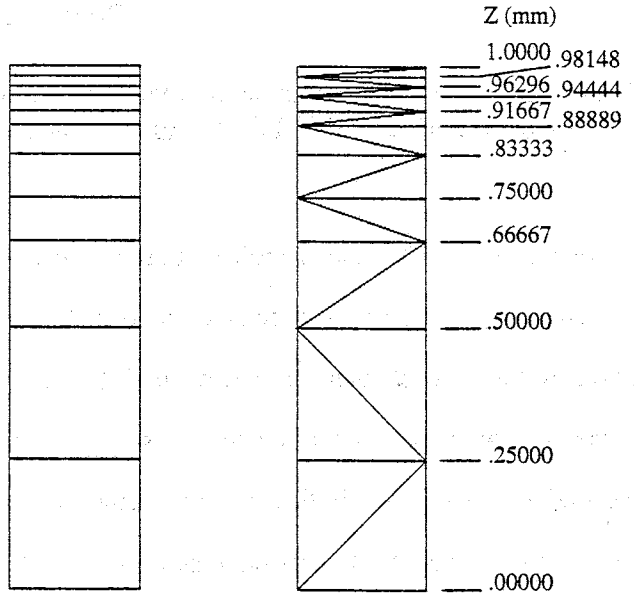

Figure 5.4 Nonuniform 2-D finite element meshes for the confined compression problem.

The linear material properties used in this chapter were obtained from nonlinear constitutive laws for bovine cartilage under the assumption of infinitesimal deformation [44]:

Aggregate Modulus: $H_A = 0.33$ MPa

Solidity: $\phi^s = 0.2$

Permeability: $\kappa_0 = 2.519\times10^{-15}\ \mathrm{m}^4/\mathrm{N\,s}$,

where the aggregate modulus of the solid phase is defined as $H_A = \partial\sigma_E^s/\partial\lambda_z\big|_{\lambda_z\sim 1}$, with σ_E^s and λ_z being the elastic stress and the stretch in the z direction. This definition yields $H_A = 4\alpha_0(\alpha_1 + 2\alpha_2)$ for the free energy function given in Eq. (3-52), and $H_A = \lambda^s + 2\mu^s$ in the case of infinitesimal deformation, with λ^s and μ^s being Lamé constants. As for Poisson's ratio, the expressions $\nu^s = \alpha_2/(\alpha_1 + 3\alpha_2)$ and $\nu^s = \lambda^s/[2(\lambda^s + \mu^s)]$ can be derived for finite deformation and infinitesimal deformation, respectively [105]. It is important to mention that the 'infinitesimal' constants determined in this fashion yield a material that is softer than the one obtained by curve-fitting the experimental data using the linear biphasic theory. So that such differences do not affect the observations made in these studies, a diffusion time scale is adopted; that is $\tau = t/t_d$, with $t_d = h^2/(\kappa H_A)$ being the *diffusion time*. All numerical analyses use the finite difference parameter $\omega = 0.667$, with time steps varying from $\Delta\tau = 5.0\times10^{-5}$ to 4.2×10^{-4}. A penalty parameter equal to 1×10^{13} is adopted in the MP formulation. A distributed force, $\sigma_0 = 0.1\ H_A$, is applied to the upper surface and kept constant during the analysis.

Distributions of pressure (Fig. 5.5), solid velocity (Fig. 5.6), and fluid velocity (Fig. 5.7) at several normalized times are representative of the response in the CC-creep problem. Nodal values obtained using the mesh of 6-node MP triangles agree well with the analytical solution represented by solid lines. Results for the 9-node MP quadrilateral coincide with results for the triangle and are not presented here.

Due to the variation in solid and fluid velocities, both in time and space, plots such as the above are not practical to evaluate the elements. Velocity values at $\tau = 1.0$, for instance, were omitted because they almost coincide with the horizontal axis. An alternative approach is the use of error norms, which reduces the comparison between analytical and numerical solutions at a particular time to a single scalar value.

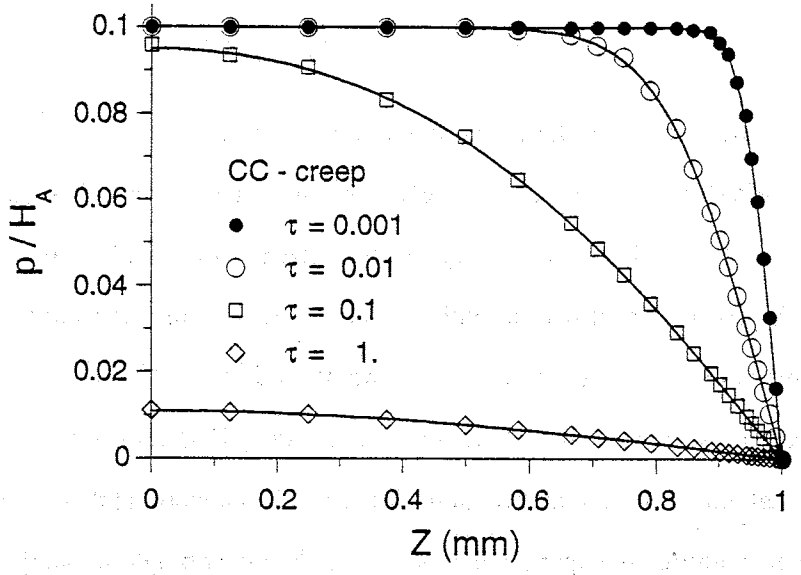

Figure 5.5 Normalized pressure versus height. Comparison between 6-node MP triangle results (symbols) and analytical solution (solid lines).

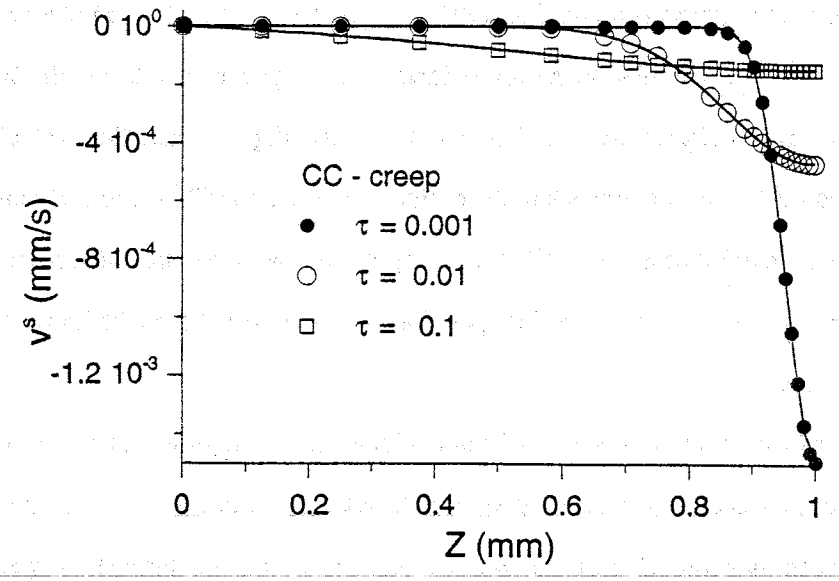

Figure 5.6 Solid velocity versus height. Comparison between 6-node MP triangle results (symbols) and analytical solution (solid lines).

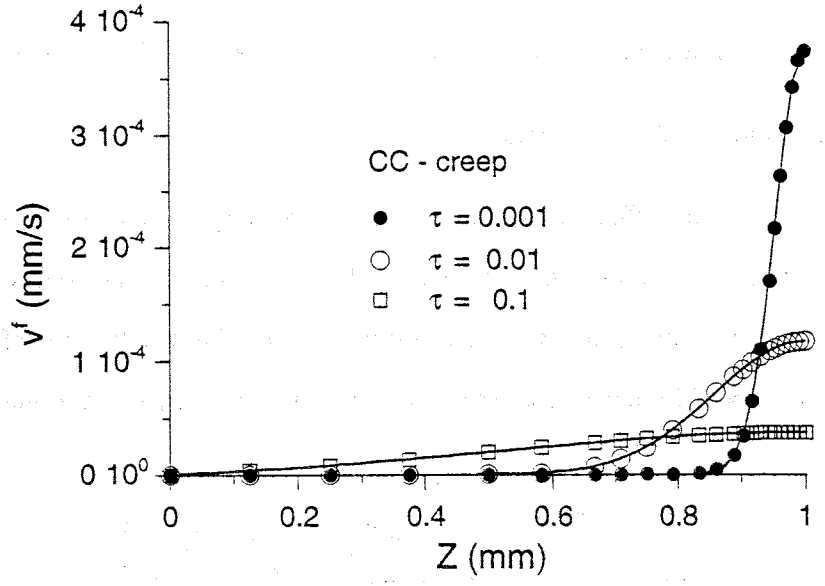

Figure 5.7 Fluid velocity versus height. Comparison between 6-node MP triangle results (symbols) and analytical solution (solid lines).

5.3 Error Norms for the Confined Compression Creep Problem

The velocity error norm at time t is defined here as the L_2-norm of the error divided by the L_2- norm of the velocity, or:

$$e\left(v(t)\right) = \frac{1}{\|v\|_0 V}\sqrt{\sum_{e=1}^{n_{el}}\int_{\Omega_e}\left(v_h - v_a\right)^2 d\Omega}, \qquad \text{with} \qquad \|v\|_0 = \frac{1}{V}\sqrt{\sum_{e=1}^{n_{el}}\int_{\Omega_e} v_a{}^2 d\Omega}, \qquad (5\text{-}2)$$

where v_h represents finite element results interpolated from nodal values, and v_a is the analytical solution. The error norm for the pressure, $e\left(p(t)\right)$, is similarly defined, with scalar pressure quantities replacing the velocity vectors. Nodal values for pressure in the MP formulation and for fluid velocity in the *v-p* formulation are obtained using nodal averaging; *i. e.* nodal values are computed at the element level and averaged at each node according to the number of adjacent elements. More accurate post-processing methods can be utilized to compute secondary fields, see for exam-

ple Zienkiewicz and Zhu [123]. In the next subsections, error norms are used to measure the effects of mesh refinement, nonuniformity and distortion on the finite element results.

5.3.1 Uniform Finite Element Meshes

To determine the effects of mesh refinement, a rectangular domain measuring 1.00 by 0.25mm was discretized with 8 layers of elements (Fig. 5.8), and then subdivided twice to yield meshes with 16 and 32 layers. Since the refinement is restricted to the direction of the flow, convergence rates obtained from the error norms are valid only for rectangular elements.

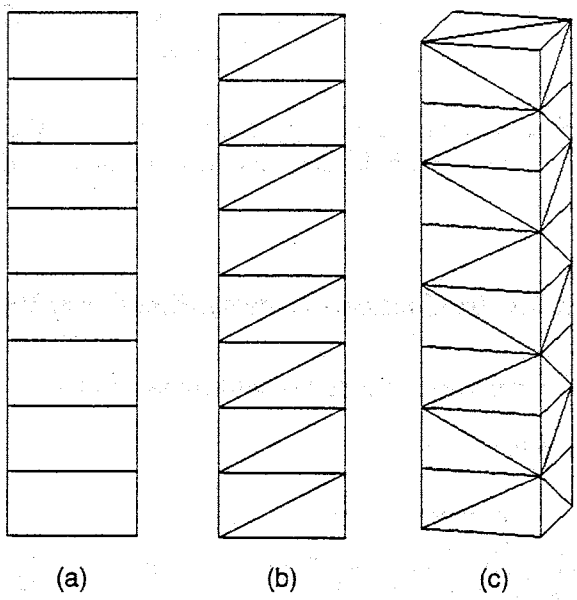

Figure 5.8 Uniform finite element meshes of (a) quadrilaterals, (b) triangles and (c) tetrahedra for the confined compression problem.

Error norms are plotted for the MP and *v-p* formulations considering 9-node quadrilaterals and 6-node triangles, Figs. 5.9 and 5.10, respectively. The disconnected symbols refer to the non-uniform meshes in Fig. 5.4 and are discussed later. The general trend observed in these plots confirms the higher accuracy of the MP elements. However, based on the number of degrees of freedom, this advantage is considerably reduced, particularly for quadrilaterals.

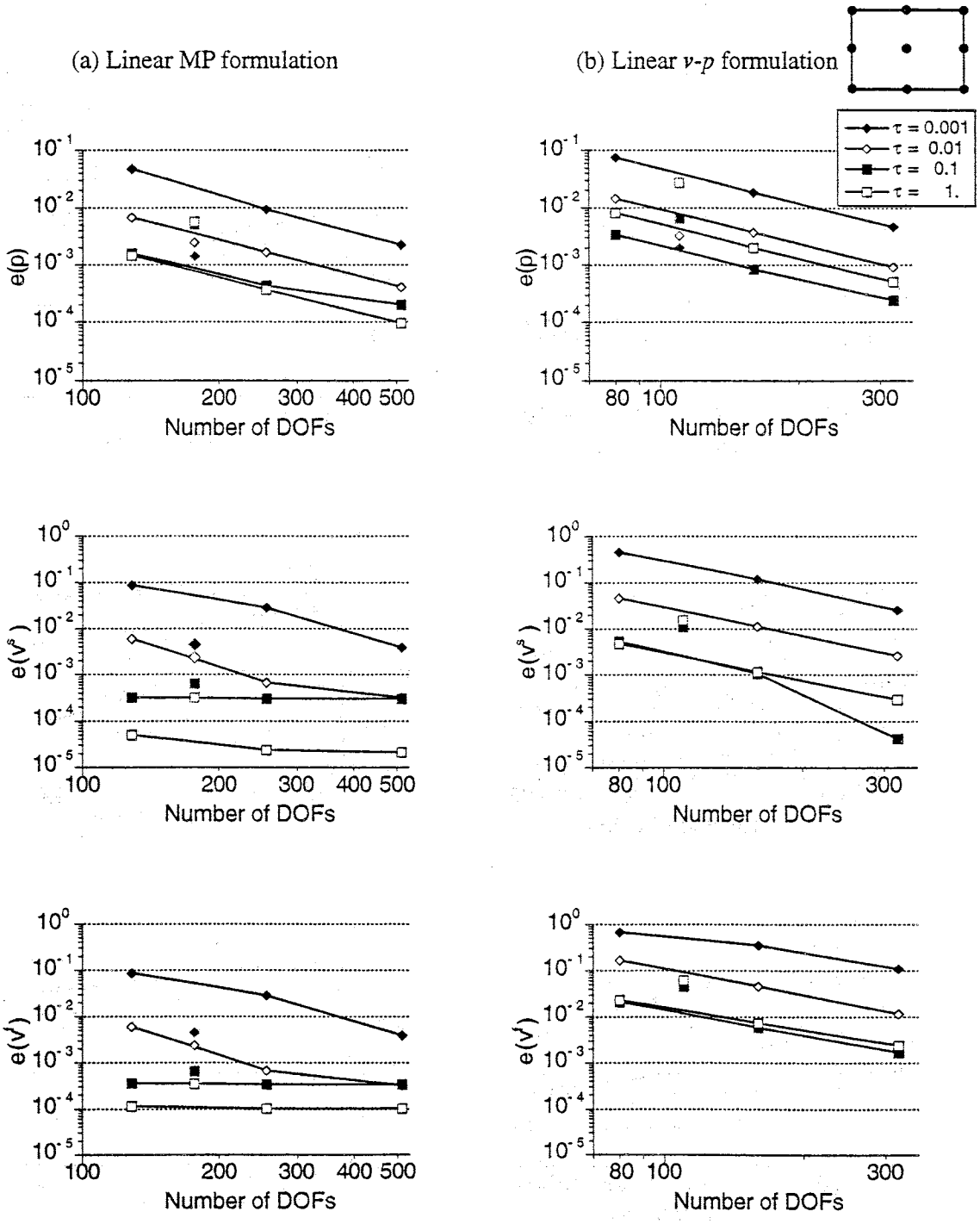

Figure 5.9 Error norms for 9-node quadrilaterals of the MP (a) and *v-p* (b) formulations. NOTES: Plots in each column refer to pressure, solid and fluid velocity fields. Solid lines connect error norms obtained using uniform meshes with 8, 16 and 32 elements(Fig. 5.8). Disconnected symbols refer to the nonuniform mesh with 11 elements (Fig. 5.4).

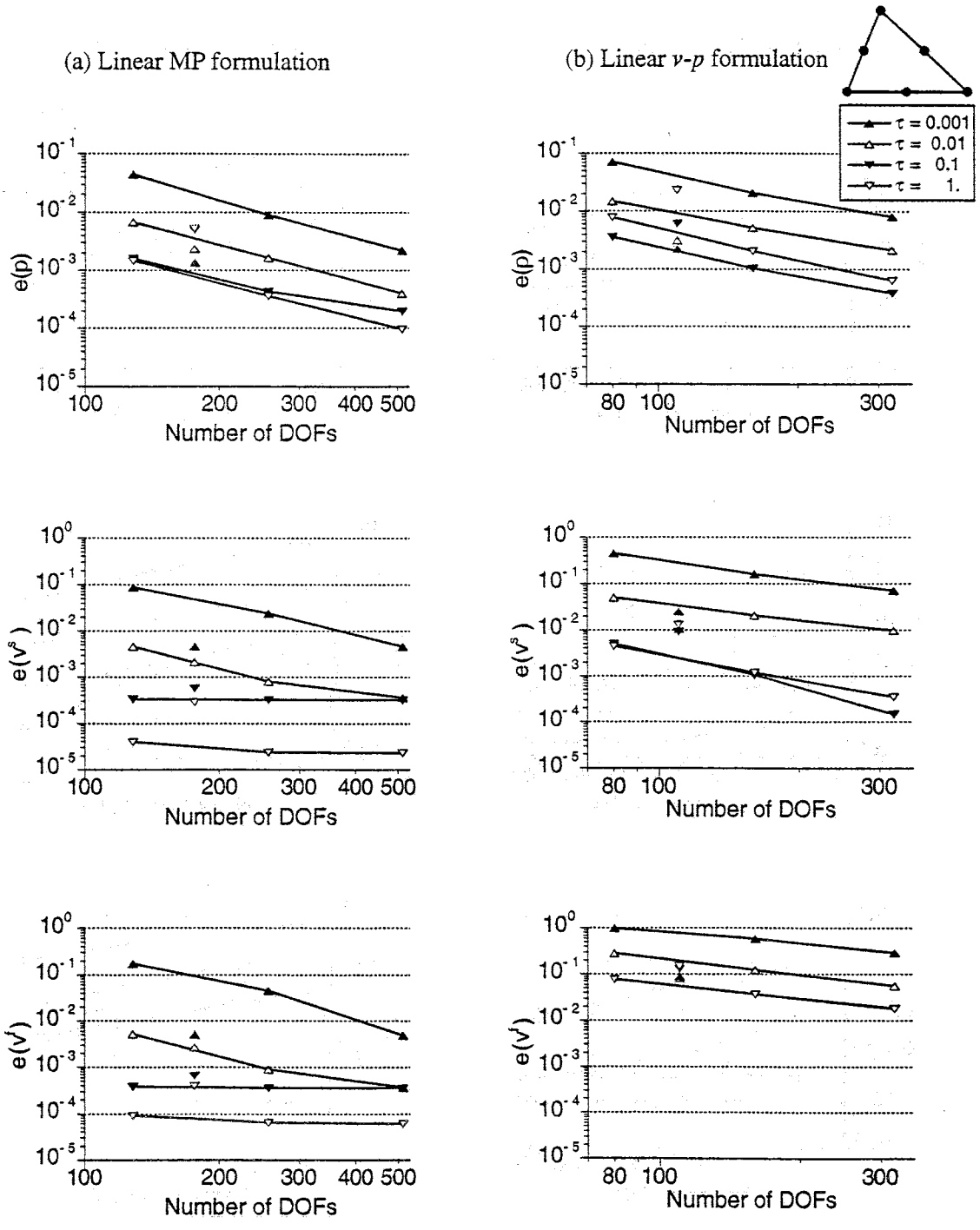

Figure 5.10 Error norms for 6-node triangles of the MP (a) and *v-p* (b) formulations. NOTES: Plots refer to pressure, solid and fluid velocity fields. Solid lines connect error norms obtained using uniform meshes with 8, 16 and 32 layers of elements (Fig. 5.8). Disconnected symbols refer to the nonuniform mesh with 11 layers of elements (Fig. 5.4).

5.3.1.1 Error Norms for the MP Elements

The errors plotted in Fig. 5.9 can be used to compute convergence rates for the 9-node MP rectangle. Intentionally, a small time step was used to minimize its effects on the finite element results ($\Delta\tau = 5.0\times10^{-5}$, $\omega = 0.667$). Convergence rates for pressure are quadratic (Fig. 5.9.a). At early times, the convergence rates for velocities are approximately -2.1, and thus suboptimal compared with the cubic convergence expected for this element. Little can be said about the rates at later times since the error is already in the range affected by the penalty parameter.

Errors for the 6-node MP triangle, Fig. 5.10, even though the aspect ratio of this element decreases with mesh refinement, are very close to those for the rectangle (Fig. 5.9.a). The 5-node quadrilateral is an appealing option due to its optimal rates of convergence (Fig. 5.11). Pressure and velocity errors obtained using rectangular meshes (Fig. 5.8) yield rates of $C_p = -2.06$, $C_{v^s} = -2.01$ and $C_{v^f} = -2.01$, at $\tau = 0.01$, an outcome that makes this element competitive with the quadratic elements for the CC-creep problem.

5.3.1.2 Error Norms for the *v* - *p* Elements

For the 9-node *v*-*p* rectangle, convergence rates are $C_p = -1.99$ and $C_{v^s} = -2.06$ for the pressure and solid velocity, respectively ($\tau = 0.01$). The rate for pressure is compatible with the error estimate derived by Murad and Loula [74], but for velocity the rate is sub-optimal compared to their estimate of quadratic convergence for solid strain. It is interesting to note, however, that the above values agree with an intermediate expression in their work (equation 68 on page 653), which yields a suboptimal convergence for strain with respect to the elliptical projection. Notice that nodal averaging improves the rate of convergence for fluid velocity. Rates of -1.9 and -1.6 at $\tau = 0.01$ and 1.0, respectively, were obtained instead of the value -1.0 expected for a quantity derived from the pressure field.

In the CC-creep problem, the response of the 6-node *v*-*p* triangle (Fig. 5.10.b) is consistently worse than the response of the 9-node *v*-*p* rectangle (Fig. 5.9.b). This poor performance is likely to be caused by the lateral constraint of confined compression and the nodal averaging pro-

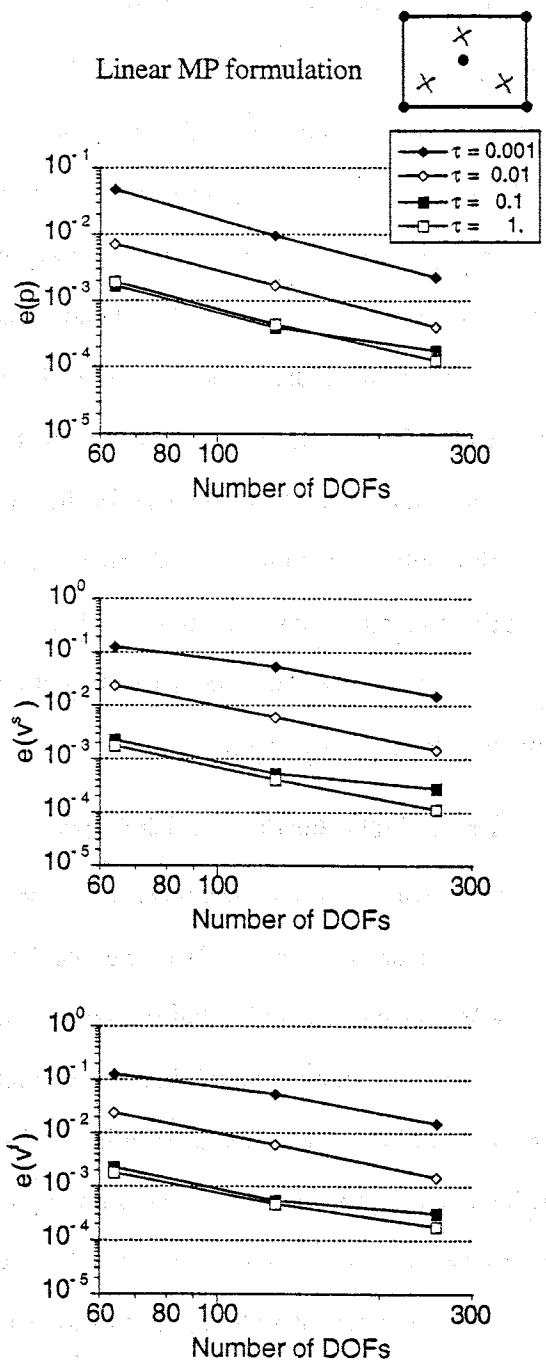

Figure 5.11 Error norms for the 5-node quadrilateral of the MP formulation. NOTES: Plots refer to pressure, solid and fluid velocity fields. Solid lines connect error norms obtained using uniform meshes with 8, 16 and 32 elements (Fig. 5.8).

cess. Sandhu *et al.* [87] also noticed this problem and were able to improve the response by averaging the results of two meshes of triangles, one being the reflection of the other. Note that the 10-node *v-p* tetrahedron (Fig. 5.12) is free from this problem, showing error norms similar to the quadrilateral.

5.3.2 Nonuniform Finite Element Meshes

Nonuniform meshes were used at the beginning of this chapter to illustrate the response of the CC-creep problem (Fig. 5.4). In order to evaluate their efficacy, the error norms were calculated and incorporated into Figs. 5.9 and 5.10 (disconnected symbols). The norms compare favorably at early times with interpolated values from uniform meshes, but show a small degradation at later times. The degradation is greater for the *v-p* formulation, in particular for the pressure field.

5.3.3 Distorted Finite Element Meshes

Mesh distortion has little effect upon the responses of the elements of the *v-p* formulation considered in this study, but can lead to unacceptable behavior for some elements of the MP formulation. This is illustrated using the distorted meshes in Fig. 5.13. Unlike the 6-node MP triangle

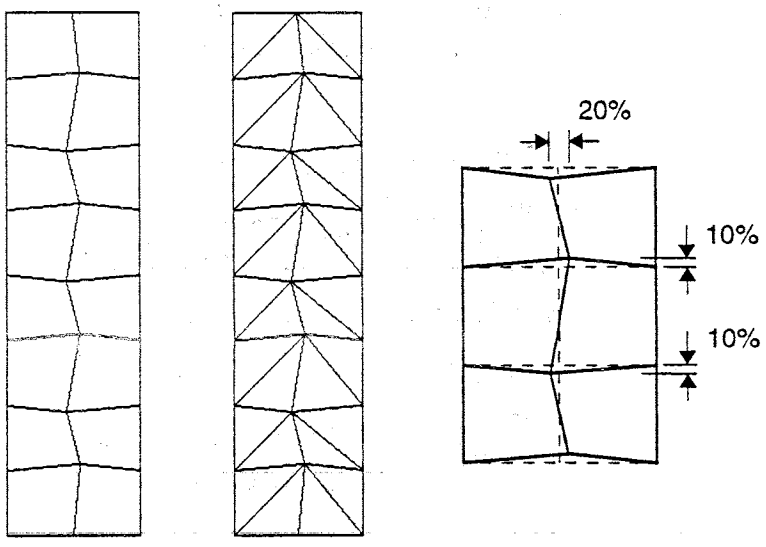

Figure 5.13 Finite element meshes for the CC-creep problem with distorted elements and detail of the distortion.

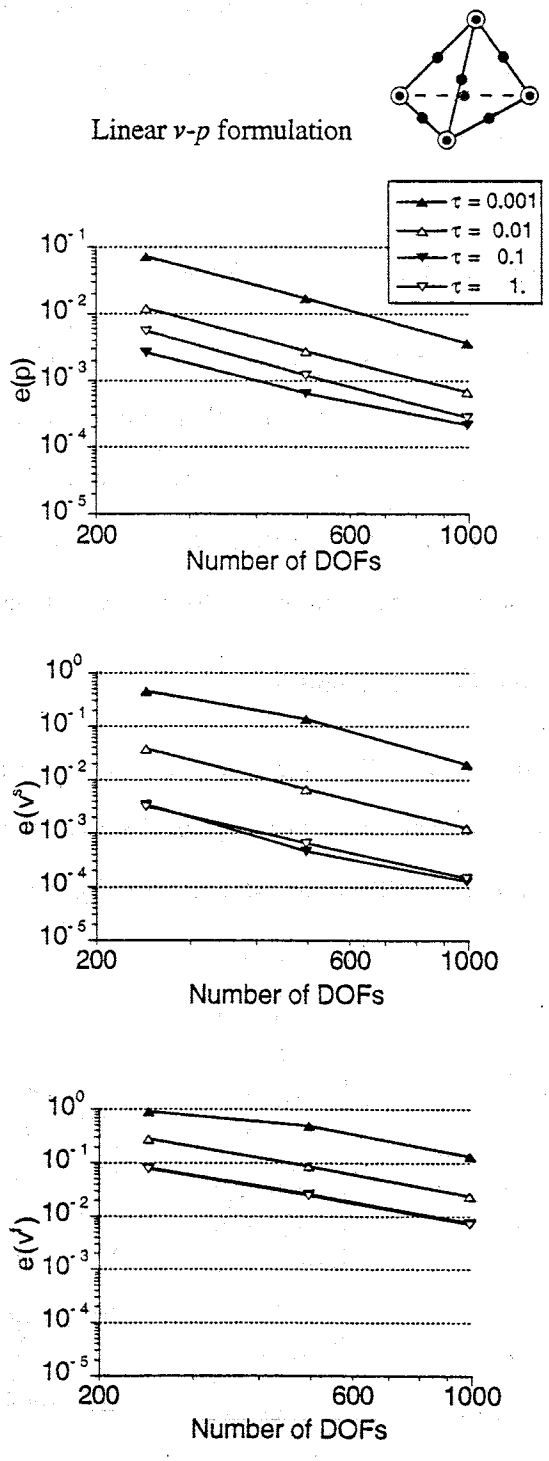

Figure 5.12 Error norms for the 10-node tetrahedron of the *v-p* formulation.
NOTES: Plots refer to pressure, solid and fluid velocity fields. Solid lines connect error norms obtained using uniform meshes with 8, 16 and 32 layers of elements (Fig. 5.8).

$(P_2 - P_1^{\xi})$ and 5-node MP quadrilateral $(Q_1^{+} - P_1^{\xi})$, for which the pressure and fluid velocity fields are fairly accurate, the distorted 9-node MP quadrilateral has difficulty representing these fields (Fig. 5.14). For this element we distinguish between pressure interpolations using parent

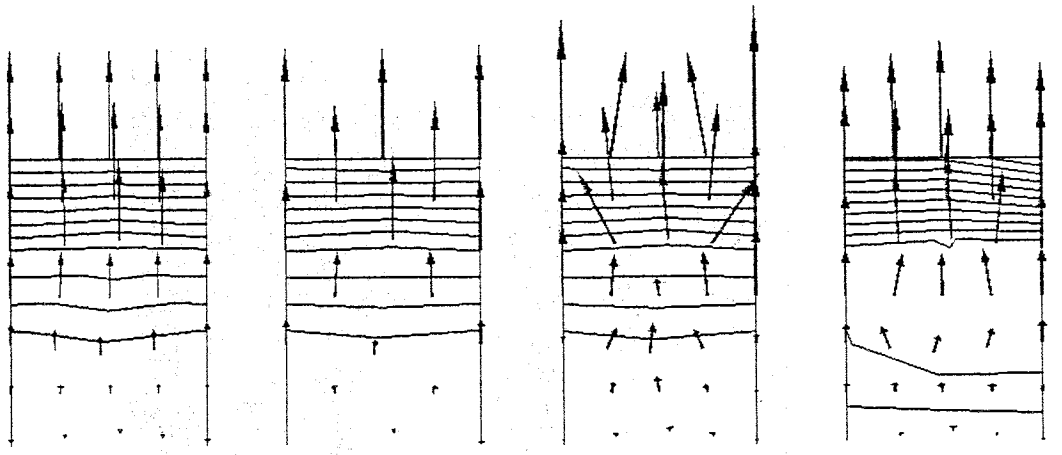

Figure 5.14 Fluid velocity at nodes and pressure isolines for distorted meshes of MP elements in the CC-creep problem ($\tau = 0.01$). ξ and X refer to parent and global coordinates, respectively.

$(Q_2 - P_1^{\xi})$ and global $(Q_2 - P_1^{X})$ coordinates. The first leads to unacceptable errors in fluid velocity, even though the errors in solid velocity are small ($e(v^{f}) = 0.25$ against $e(v^{s}) = 0.0067$, at $\tau = 0.01$). The second improves the fluid velocity, but has a negative effect on the pressure. Similar results occur for the 8-node MP quadrilateral, and are likely to occur for the 20- and 27-node MP hexahedra in similar conditions. Despite the seriousness of the problem, the accuracy in solid velocity leads us to believe that the distortion sensitivity can be solved at the element level.

5.3.4 Irregular Mesh of Tetrahedra

Since both triangle and tetrahedron have quadratic interpolations, the better accuracy of the latter in the CC-creep problem was not expected. This result cannot be attributed to the use of rectangular blocks of tetrahedra to compute the error norms since this element also works well

with irregular meshes. The mesh in Fig. 5.15, for instance, provides error norms that are close to the ones plotted in Fig. 5.12 for uniform meshes ($e(p) = 0.014$, $e(\boldsymbol{v}^s) = 0.044$ and $e(\boldsymbol{v}^f) = 0.29$, at $\tau = 0.01$).

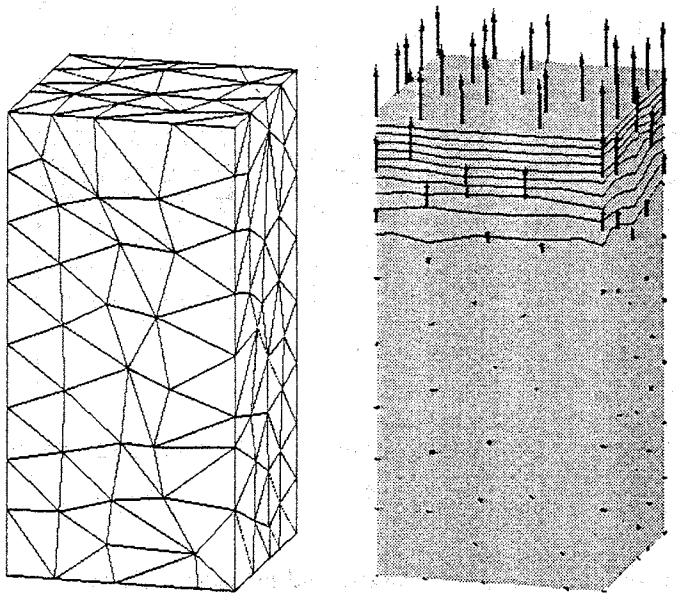

Figure 5.15 (a) Irregular mesh of 10-node tetrahedra for the CC-creep problem; (b) relative velocity at vertices and pressure isolines at $\tau = 0.01$ ($\boldsymbol{v}$-p formulation).

5.4 Closing Remarks

In the initial phase of this study, the 9-node MP quadrilateral seemed to be a promising nonlinear element, in part because it is considered one of the most effective quadrilaterals to deal with incompressible media [31, 47]. Excellent results obtained with meshes that were either rectangular, or that favored in some way the direction of the fluid flow, contributed to this opinion. It was therefore surprising to find its sensitivity to element distortion, which manifests primarily in the fluid velocity approximation. The same difficulties are expected for the 20- and 27-node MP hexahedra, analogs in three-dimensions of the 8- and 9-node quadrilaterals, when subjected to similar conditions. Additional studies are needed to determine if this sensitivity of fluid velocity

can be circumvented without drastically changing the formulation. If not, the 6- and 7-node triangles and the 5-node quadrilateral would be the only robust elements of the mixed-penalty formulation recommended from this study, and further research will be necessary to minimize the sensitivity of other MP elements.

Except for the triangle, the Taylor-Hood elements used in the *v-p* formulation were found to be robust elements in the CC-creep problem. The tetrahedron did not inherit the problems shown by the triangle, and the hexahedron should behave well under multiaxial deformation. One drawback of these elements is the large initial errors due to spatial oscillations. A problem that is more accentuated when sudden loads are applied directly to the solid phase, as in the CC-creep problem.

CHAPTER 6

Nonlinear Finite Element Examples

In contrast to linear biphasic formulations, for which example problems with closed form solutions are available, the nonlinear formulations must depend on other resources to validate their implementation. This validation process normally includes comparisons with linear solutions in the case of infinitesimal deformation, independent finite difference solutions, results from different finite element formulations and from distinct descriptions of the same problem (plane-strain, axi-symmetric and 3-D models). In the examples that follow, resources used to validate the mixed-penalty (MP) and mixed velocity-pressure (v-p) formulations are illustrated for selected elements that have shown a good performance in the previous chapter. Additional aspects concerning the nonlinear Helmholtz free energy function for transversely isotropic materials are examined in the next chapter.

6.1 The Nonlinear Confined Compression Problem

In the confined compression test, a cylindrical sample of tissue is laterally confined and subjected to either an applied load or a prescribed ramp displacement through a rigid porous platen (see Fig. 5.3 in Chapter 5). The diagrams in Fig. 6.1 describe the temporal variation of the loads adopted in the numerical simulations of the creep and stress-relaxation versions of this test, where t_r denotes an user-defined time which is small compared with the diffusion time. In the creep case, a force corresponding to a distributed normal traction σ_0 in the reference configuration is applied and held constant. In the stress-relaxation example there are two stages: first, prescribed velocities are used to represent a nearly-linear increase in displacement up to a maximum deformation ε_0 (equilibrium or fully drained deformation); second, the displacement at the top is held constant, corresponding to the stress-relaxation stage.

The Helmholtz free energy function given by Eq. (3-52) is used to represent the solid phase. Material properties used in the numerical models are $\alpha_0 = 0.1084$ MPa, $\alpha_1 = 0.592$ and

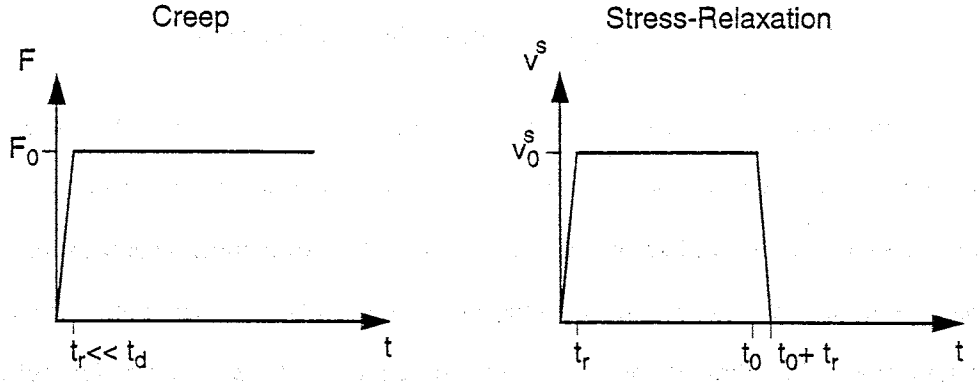

Figure 6.1 Creep and stress-relaxation load diagrams adopted in the numerical solutions of the confined compression examples.

$\alpha_2 = 0.0846$. They can be derived from $H_A = 0.330$ MPa and $n = 0.761$ obtained from non-linear regression curve-fitting of confined-compression experimental data for bovine cartilage [44] by assuming a Poisson's ratio of 0.1 under infinitesimal deformation. Parameters for the permeability function, Eq. (3-42), are $\phi_0^s = 0.2$, $\kappa_0 = 2.519\text{x}10^{-15}\,\text{m}^4/(\text{Ns})$, $L = 0.0848$ and $M = 4.638$. The tissue sample height is assumed to be 1 mm, yielding a diffusion time of approximately 1200 s.

The finite difference description makes use of the uniaxial equations presented by Holmes [43] and Holmes and Mow [44]. The corresponding program, though one-dimensional, had an important role in the verification of the nonlinear finite element formulations. For the material parameters above, a total of 801 points were necessary in order to obtain converged finite difference results for the CC-creep problem.

6.1.1 Creep Example

In the creep example, a normal traction of $\sigma_0 = 0.8\,H_A$ is applied in a ramp of $t_r = 0.24$ s and held constant. Time steps varying from 0.06 to 2.4 seconds are used in the finite element analysis. Finite element results are obtained using the nonuniform 11-layer mesh of 6-node MP triangles indicated in Fig. 5.4.

Figures 6.2 and 6.3 show the temporal variation of pressure and axial stretch, respectively, at different heights, and Fig. 6.4 shows the distribution of axial stress at different times. The response is smooth in time and space, and excellent agreement is obtained despite the high load applied, which causes deformations of 40% at the top of the sample. This is an indication that the CC-creep problem does not pose serious problems for the 6-node MP triangle. This is also true for the quadrilaterals and hexahedra of the MP formulation, whose responses are similar to the ones presented for the triangle.The finite element mesh, however, is coarse for this problem and is responsible for a slight increase in the creep rate, as noticeable in the curve for $\tau = 1$ in Fig. 6.4. This problem is readily solved by subdividing the elements in the lower region of the domain.

The nonlinear *v-p* formulation, on the other hand, is particularly sensitive to a sudden load applied on the solid phase. For the magnitude of load considered here, the 11-layer mesh of 9-node *v-p* quadrilaterals (Fig. 5.4) gives rise to oscillations in the solid stress response that compromise the convergence of the Newton-Raphson method. It is important to mention that the problem persists when the mesh is subdivided, but is absent when a uniform mesh with 32 elements along the height is used. Figure 6.5 presents results for this 32 element mesh showing excellent agreement with the long term response, but also showing some lack of accuracy at earlier times. Except for the CC-creep problem, the *v-p* elements have shown a reasonable tolerance to mesh gradation in other examples, including the case of stress-relaxation examined next.

6.1.2 Stress-Relaxation Example

In the stress-relaxation example, a displacement ramp corresponding to $\varepsilon_0 = 0.1$ is prescribed at the top in 60s ($t_r = 1.2\text{s}$). The ramp parameters are chosen to provide values for stresses and stretches close to the ones found in the previous example. A constant time step of 0.2s is used in the finite element analyses.

For this problem, a *diffusion rate parameter* defined by $R^2 = t_0/t_d$ can be used to access the level of interaction between solid and fluid phases that will lead to the maximum local compression [103]. Values $R > 1$ represent small rates, while values $R < 1$ represent fast rates of com-

pression. In this example, $R = 0.22$, which means that considerable effects due to finite deformation and strain-dependent permeability can be expected.

Again, the same mesh of 6-node MP triangles is used to obtain responses shown in the next three figures. Figures 6.6 and 6.7 present temporal variation of pressure and axial stretch, respectively, at different heights. Note that the fast compression rate causes the stretch to decrease far below its elastic equilibrium value. Figure 6.8 shows the distribution of pressure at different times. A very good agreement is obtained, with some loss of accuracy for τ around 0.05. This is particularly noticeable in the pressure distributions in Fig. 6.8. Note that the errors during and after the displacement ramp tend to compensate in this example, so that a better agreement is obtained at $\tau = 0.1$.

For this problem, the accuracy of the 9-node *v-p* quadrilateral is comparable to, if not better than, the accuracy of the MP triangle using the nonuniform mesh of 11 elements (Fig. 6.9). Note that the problems observed for the *v-p* quadrilateral in the CC-creep problem occurred for similar levels of stress and strain and, therefore, are attributed to the fast application of the load in the creep case.

For completeness, the CPU times (RS6000 IBM340) are reported. A total of 695 time steps for the CC-creep problem required 4.8 and 5.4 minutes in the MP and *v-p* formulations, respectively, with different meshes. The relative performance changed when the same mesh was used to analyze the CC-relaxation problem: 3.3 against 1.6 minutes for the *v-p* formulation to compute 600 time steps.

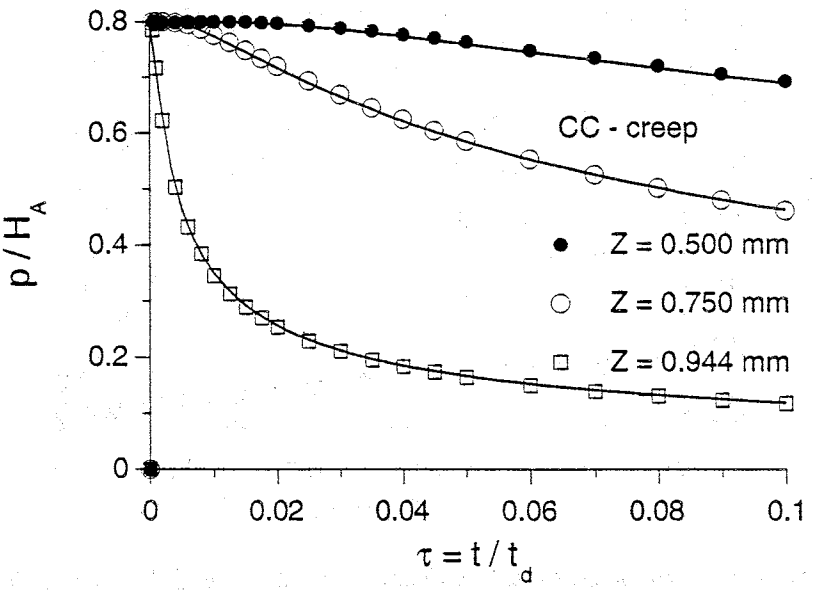

Figure 6.2 Pressure time history at various heights. Finite difference (solid lines) and 6-node MP triangle (symbols) results for the CC-creep problem.

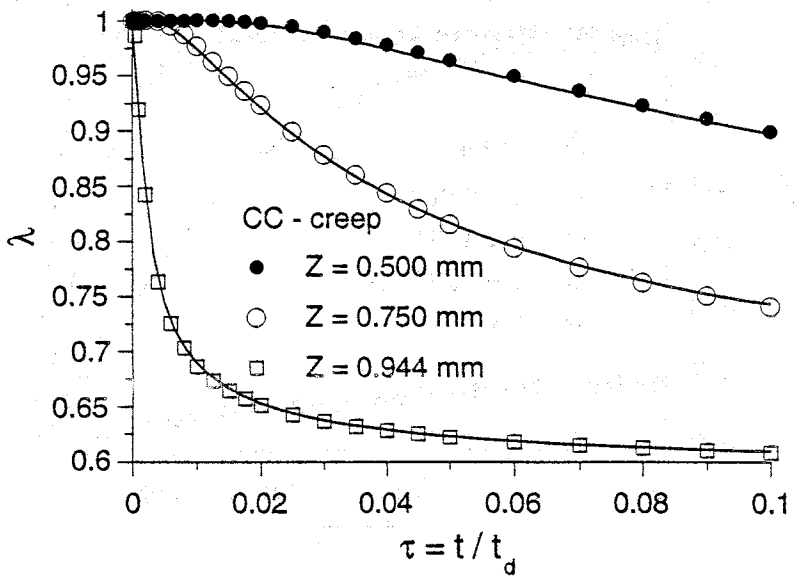

Figure 6.3 Stretch time history at various heights. Finite difference (solid lines) and 6-node MP triangle (symbols) results for the CC-creep problem.

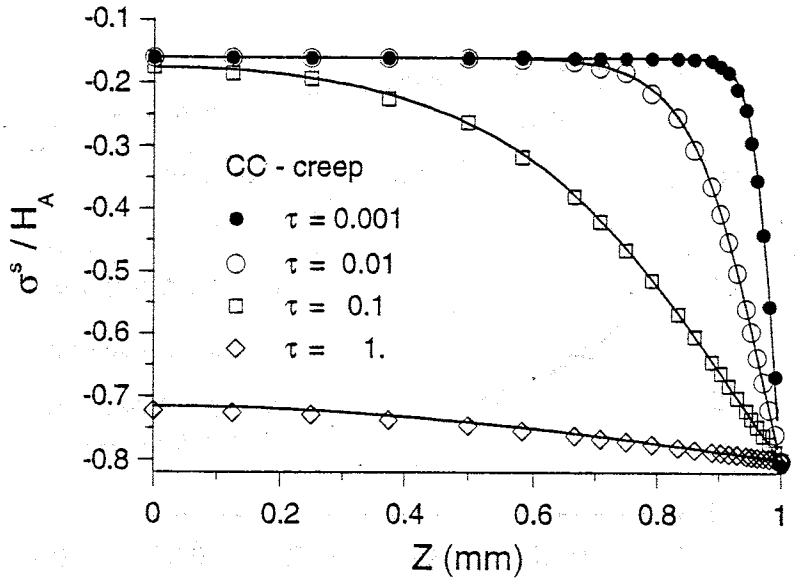

Figure 6.4 Normalized solid stress versus height. Finite difference (solid lines) and 6-node MP triangle (symbols) results for the CC-creep problem.

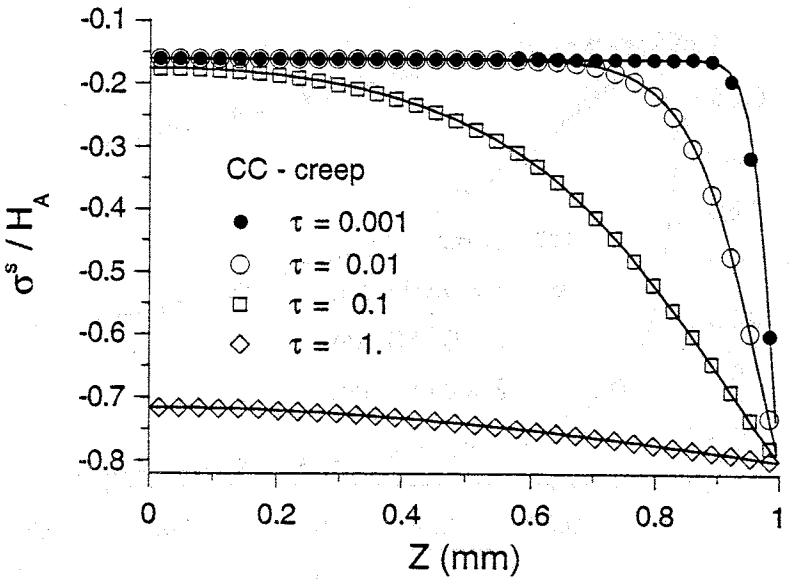

Figure 6.5 Normalized solid stress versus height. Finite difference (solid lines) and 9-node *v-p* quadrilateral (symbols) results for the CC-creep problem.

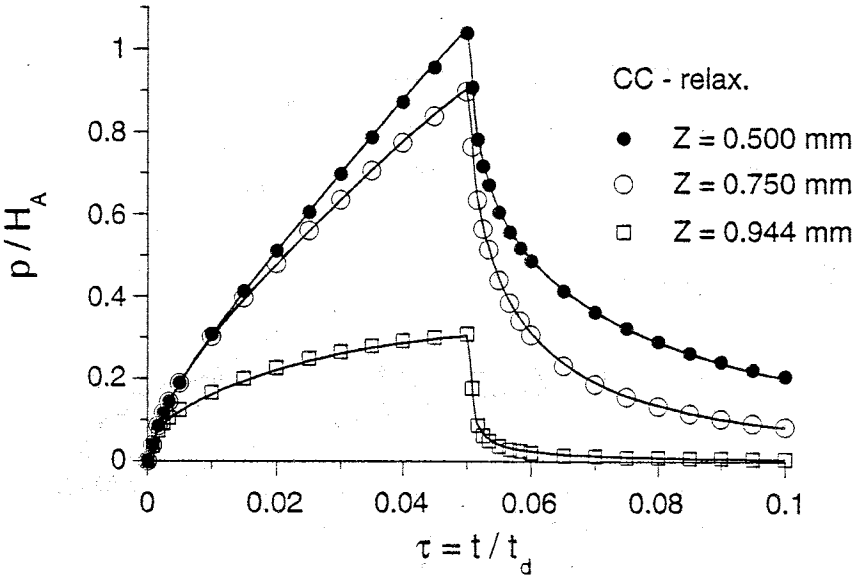

Figure 6.6 Pressure time history at various heights. Finite difference (solid lines) and 6-node MP triangle (symbols) results for the CC-relaxation problem.

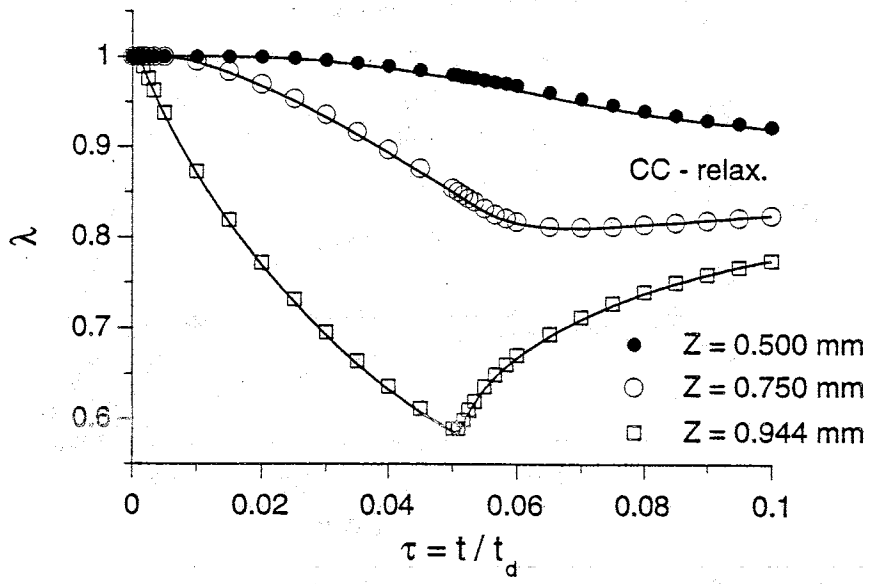

Figure 6.7 Stretch time history at various heights. Finite difference (solid lines) and 6-node MP triangle (symbols) results for the CC-relaxation problem.

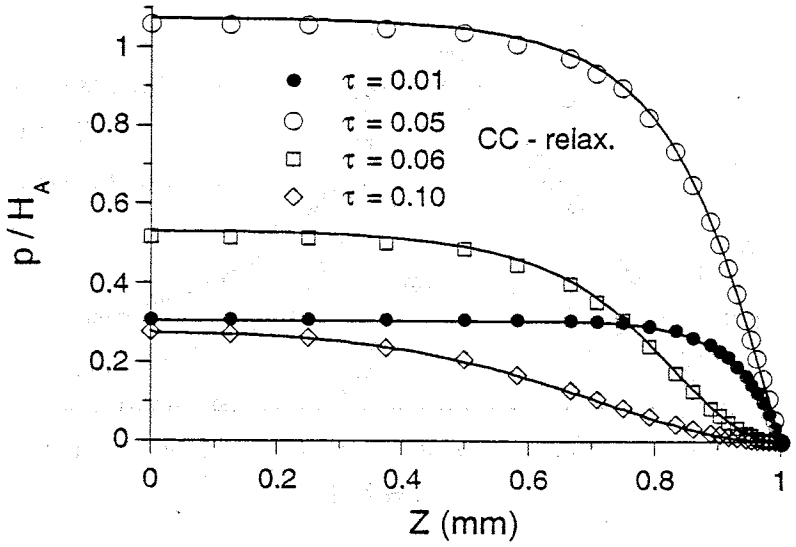

Figure 6.8 Normalized pressure versus height. Finite difference (solid lines) and 6-node MP triangle (symbols) results for the CC-relaxation problem.

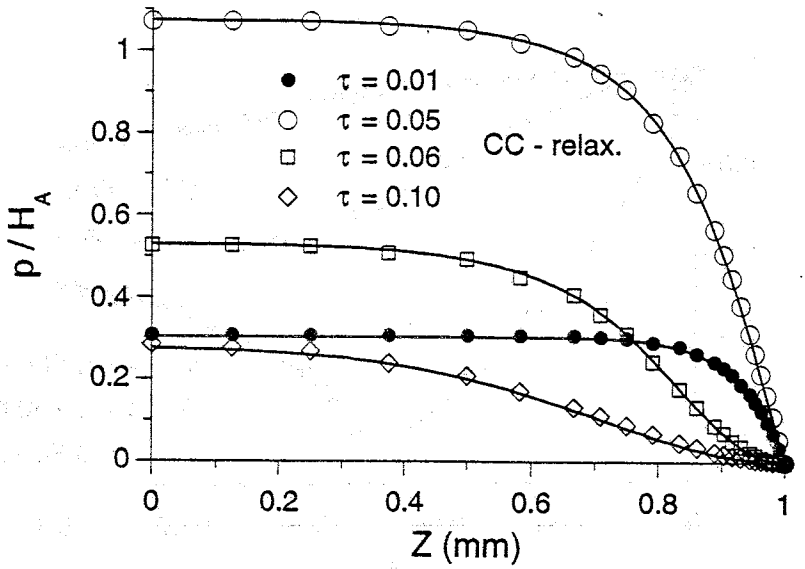

Figure 6.9 Normalized pressure versus height. Finite difference (solid lines) and 9-node *v-p* quadrilateral (symbols) results for the CC-relaxation problem.

6.2 Unconfined Compression with Adhesive Platen

In the unconfined compression test, a thin cylindrical disk of tissue is compressed between two rigid and impermeable platens (Fig. 6.10). Under these conditions, the axial compression produces radial expansion, which is accompanied by elastic radial stresses in the solid matrix. The lower platen is assumed fixed, and a prescribed ramp displacement is enforced through the upper platen. Loading parameters are selected as $\varepsilon_0 = 0.15$ and $t_0 = 50\text{s}$, and a cylindrical sample of $h_0 = 2\text{mm}$ and $d_0 = 6\text{mm}$ is considered.

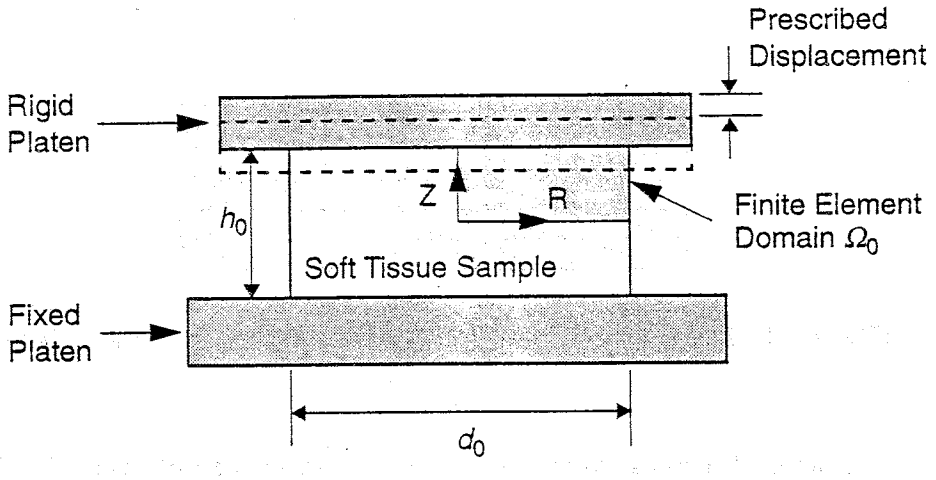

Figure 6.10 Schematic representation of the unconfined compression stress-relaxation test of a cylindrical disk of soft hydrated tissue.

This example focuses on the 'singularity' at the corner of the cylindrical wall in the case of perfectly adhesive contact between platen and tissue. It is known from numerical analyses conducted by Spilker and Suh [100] that this boundary condition considerably stiffens the sample, leading to a higher peak reaction force and a smaller relaxation time when compared to the case of perfectly lubricated platens. The singularity, however, has prevented the numerical solution under finite deformation in that study, and thus constitutes a good test for the biphasic elements.

Because of the symmetries with respect to the central axis and to the mid-height, only one quadrant is considered in the finite element representation. The contact with the upper platen is

modelled as perfectly adhesive ($v_r^s = 0$; $v_z^s = v_z^f = \bar{v}_0$) and, on the mid-height plane, nodes are fixed to the plane but free to move radially. For the *v-p* formulation, a zero pressure must be prescribed on the cylindrical surface. Figure 6.11 shows the finite element mesh used to represent this problem. A radial refinement around the corner is required to obtain convergence for the Newton-Raphson method using a relative coarse mesh (7 layers by 7 columns). The strategy of refining the region where large distortions are expected is justified by the exponential stiffening of the constitutive law for the solid phase. This accentuated stiffening restricts the region of large stresses and strains, and it is an important feature observed in soft biological tissues [33].

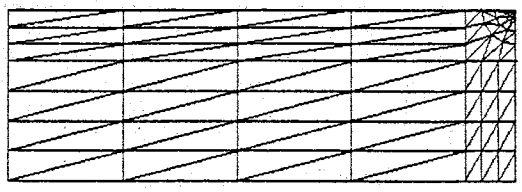

Figure 6.11 Finite element mesh for the adhesive unconfined compression problem.

Figure 6.12 shows solid velocity at nodes and pressure isolines at 50s. There is a very good agreement between the results for the MP and *v-p* formulations. Figure 6.13 presents almost identical isolines for maximum distortions which reach values up to 1 radian in this problem. Figure 6.14 constitutes a detail showing isolines for the maximum shear stress. This last figure illustrates the effect of the exponential stiffening provided by the constitutive model, which restricts the region of stress concentration to the neighborhood of the singularity.

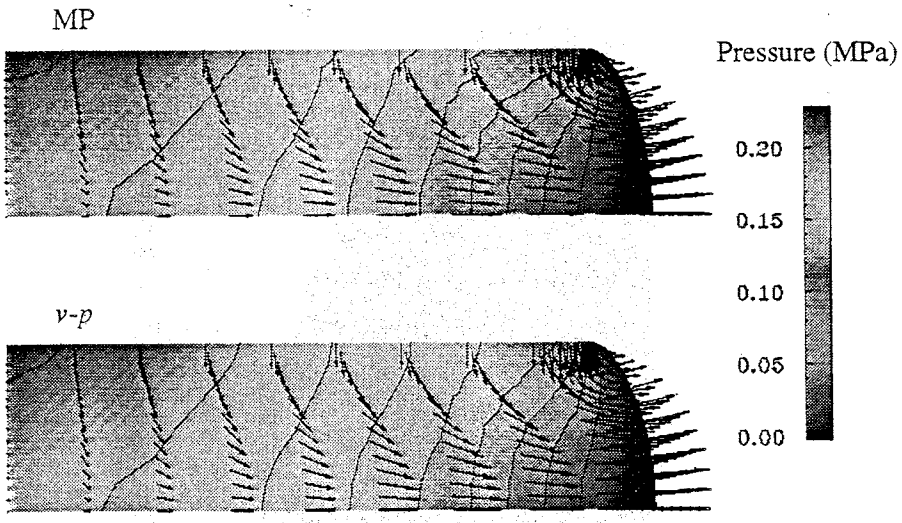

Figure 6.12 Solid velocity at nodes and pressure isolines at 50 s for the adhesive unconfined compression problem.

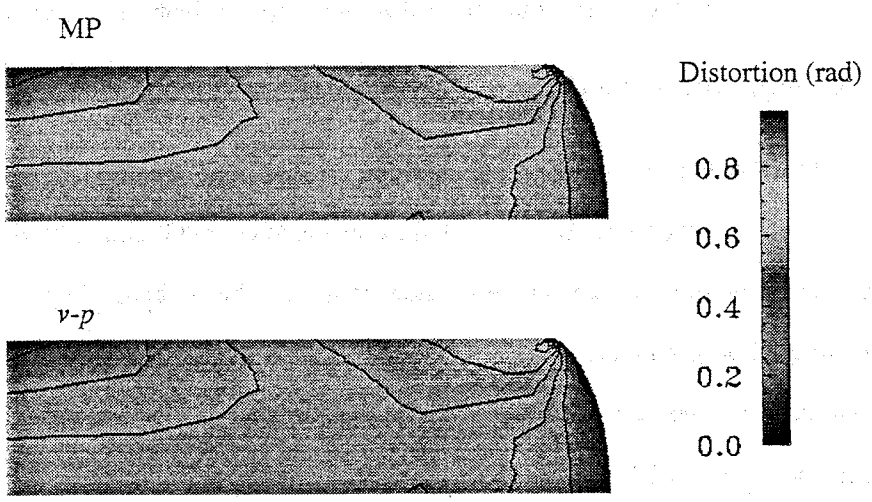

Figure 6.13 Maximum angle of distortion at 50 s for the adhesive unconfined compression problem.

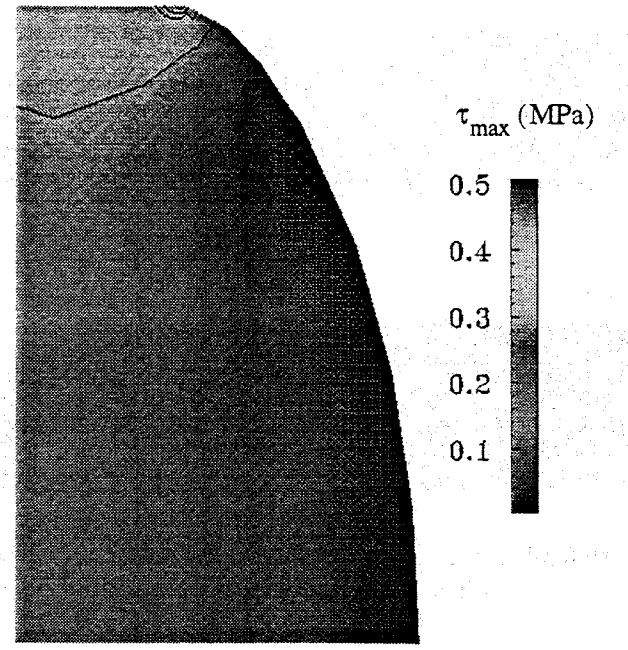

Figure 6.14 Detail of the free lateral surface showing maximum shear stress at 50 s for the adhesive unconfined compression problem (*v-p* formulation).

6.3 Example Using the Geometry of the Articular Cartilage of the Humeral Head

The shoulder is a close-fitting ball-and-socket joint, where the glenoid can be seen as a shallow cup covering approximately one third of the spherical humeral head [72]. Precise measures of the anatomic surfaces in the shoulder joint have been obtained by Soslowsky *et al.* [96] using stereophotogrammetry. For an average male specimen, the cartilage layer of the human humeral head can be described by an axisymmetric geometry of thickness $h_0 = 1.42$ mm and bone radius $R_b = 26.10$ mm, as illustrated in Fig. 6.15 [95].

The shoulder joint has recently being analyzed by Donzelli [27] using a biphasic mixed-penalty contact finite element formulation. At early times, it was found that the contact load is almost parabolic, with the contact surface being established soon after the load is applied. It was also confirmed that the load is shared by solid and fluid phases according to their volume fractions [46]. In this example, the contact surface is defined by $a = 7.5$ mm, and the corresponding load is adapted from contact forces determined by Donzelli in a linear contact analysis of similar prob-

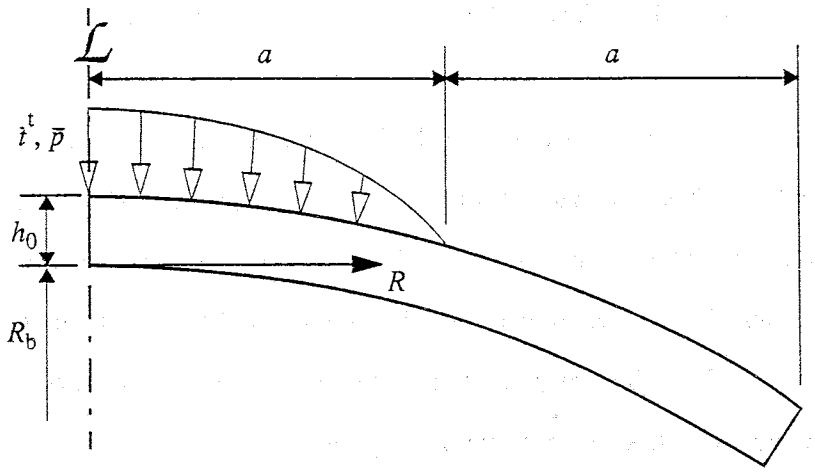

Figure 6.15 Schematic representation of the articular cartilage of the humeral head, and the applied pressure load.

lem. The prescribed total traction and pressure increase linearly in time, reaching the following maximum distributions after one second:

$$\begin{aligned} \bar{t} &= -573 + 42.3R + 5.13R^2\,(kPa), \\ \bar{p} &= 512 - 40.1R - 3.86R^2\,(kPa). \end{aligned} \tag{6-1}$$

Although nonlinear material parameters are not available for the humeral head, Soslowsky [95] provides linear biphasic material properties from which hypothetical permeability and free energy functions can be built for illustrative purposes. The exponential form in Eq. (3-52) is adopted for the Helmholtz free energy function. The corresponding parameters are selected so that the compressive secant stiffness coincides with the linear properties for a deformation of 15%. As far as the permeability function is concerned, the coefficient κ_0 in Eq. (3-42) coincides with the linear permeability, and the exponent is built based on material parameters of the previous examples. The average values for the linear material properties provided by Soslowsky [95] are $\phi_0^s = 0.25$, $\kappa_0 = 1.7\times10^{-15}\,\mathrm{m}^4/(\mathrm{Ns})$, $H_A = 0.56$ MPa and $\nu = 0.05$. The hypothetical parameters for the exponent of the permeability function are $L = 0.1$ and $M = 4$, and for the Helmholtz free energy function are $\alpha_0 = 0.09$MPa, $\alpha_1 = 0.98$ and $\alpha_2 = 0.06$, which correspond to $H_A = 4\alpha_0(\alpha_1 + 2\alpha_2) = 0.4$ MPa and $\nu = \alpha_2/(\alpha_1 + 3\alpha_2) = 0.05$ (see Holmes

and Mow [44] and Suh *et al.* [105] for relations between nonlinear parameters and elastic constants).

For this example, axisymmetric and 3-D descriptions are solved using the *v-p* formulation. Finite element meshes of 8-node quadrilaterals (288 elements, 937 nodes, 2040 equations) and 20-node hexahedra (144 elements, 941 nodes, 2208 equations) are presented in Fig. 6.16. The axisymmetric mesh is twice as refined, and it has a nonuniform distribution of elements along the thickness. The 3-D mesh corresponds to a sector of 30°, with constraint equations being used to prevent normal velocities on the skew vertical plane.

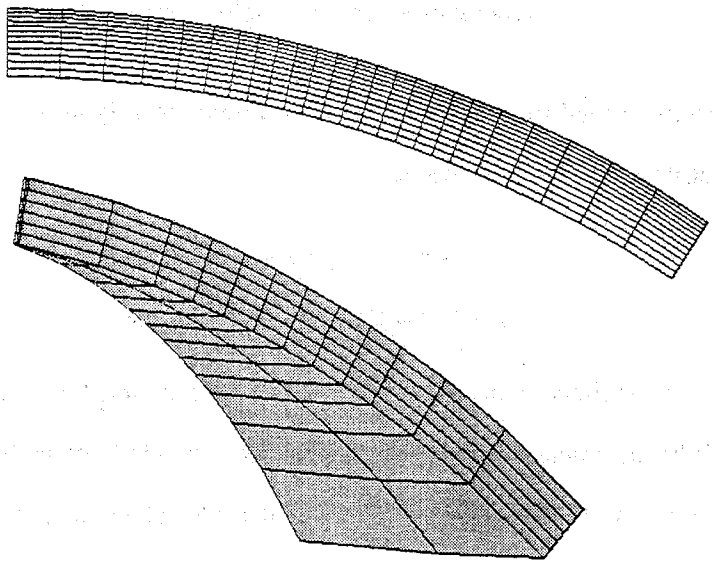

Figure 6.16 Axisymmetric and 3-D finite element meshes for the articular cartilage of the humeral head.

Pressure isosurfaces equally spaced by 0.1MPa are shown in Fig. 6.17 at 1s. Isosurfaces have the circumferential shapes expected for this problem, and are in agreement with axisymmetric pressure results shown in Fig. 6.18. The 3-D problem was also solved using the MP formulation, but since no discernible difference was observed in the pressure isosurfaces, the results are not shown here.

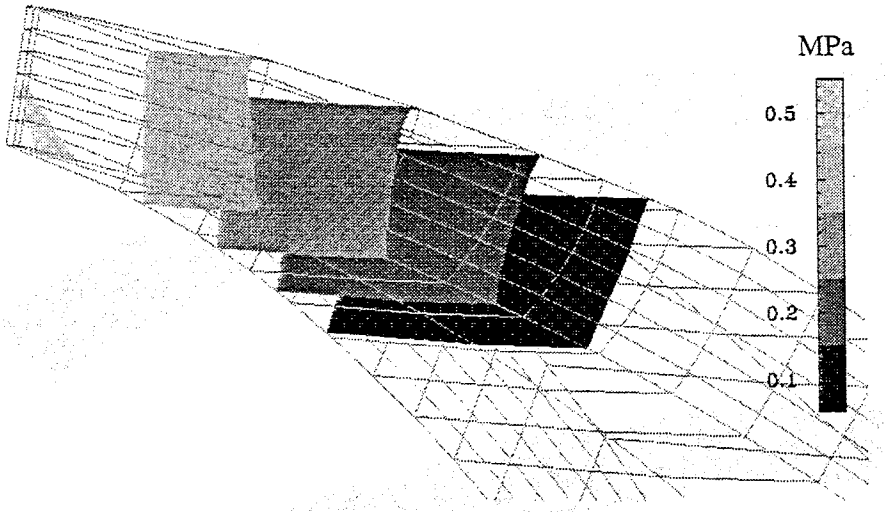

Figure 6.17 Pressure isosurfaces at 1s for the cartilage of the humeral head.

Figure 6.18 also shows isolines for the maximum stretch (λ_1) and maximum angle of distortion. Note the tensile strains under the load, and maximum stretches of 1.26 occurring on the bone interface. Maximum distortions up to 0.45 rad are also found close to the bone surface. These high values are caused by the use of an isotropic constitutive law curve-fitted to represent the compressive behavior of articular cartilage. Since the tensile behavior is also important here, it can be anticipated the need for more complex constitutive models. As seen in the next chapter, the tensile stiffness of articular cartilage in planes parallel to the surface is one order of magnitude greater than its compressive stiffness normal to the surface [25], a fact that cannot be ignored in future analyses of the humeral head.

CPU times in minutes, corresponding to the first 20 time steps, are 0.11 for the axisymmetric analysis, and 44.6 and 238.5 for the 3-D analysis using the *v-p* and MP formulations, respectively.

6.4 Final Remarks

In almost all problems examined here, a clear advantage has been noticed for the *v-p* formulation. The advantage reflects smaller number of equations per node and, in most cases, smaller number of iterations per increment of time required by the Newton-Raphson method. It is worth-

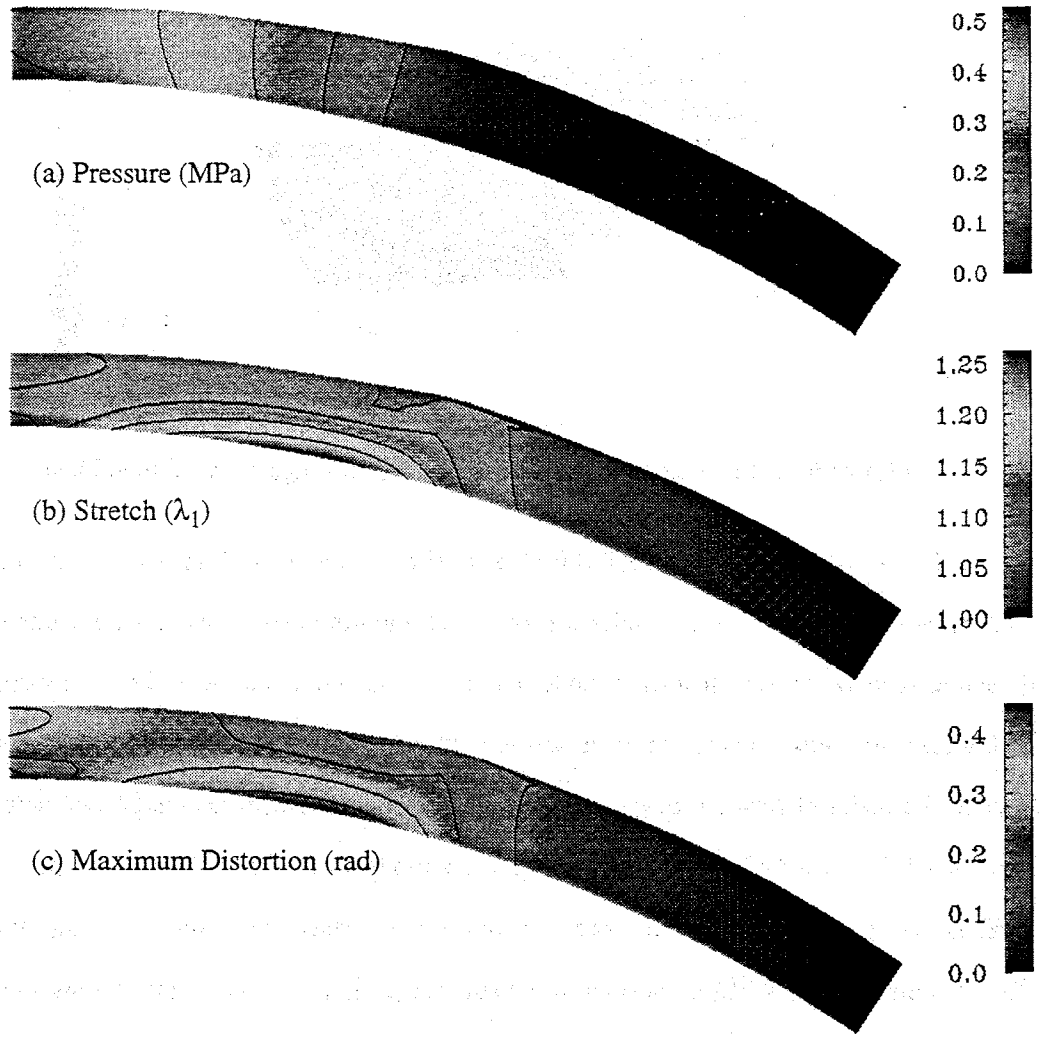

Figure 6.18 Axisymmetric results at 1s for the cartilage of the humeral head.

while to mention that both MP and *v-p* formulations may fail to converge with coarse meshes, although no pattern in mesh or problem type was observed which could predict this failure in advance. The MP formulation, however, will show more iterations per time-step before failing, where for the *v-p* formulation the failure to converge may occur suddenly without a change in the number of iterations. This fact confirms the distinct features of the corresponding nonlinear systems of equations, which should be studied independently to pursue more cost-efficient nonlinear solvers.

CHAPTER 7

Exponential Helmholtz Free Energy Function

"Thus far, investigators have used linear, isotropic theories. However, analysis of some of the more general problems requires tackling intractable mathematical difficulties and developing more complex computer codes."

MOW *et al.* [72, p.93]

In 1993, Cohen *et al.* [25] presented linear transversely isotropic material properties for articular cartilage of the human humeral head. These properties were obtained by matching finite element results with experimental data from creep indentation tests. Significantly different values were found for Young's moduli in planes parallel ($E_1 = 5.8$ MPa) and perpendicular to the cartilage surface ($E_2 = 0.46$ MPa). The use of a linear isotropic constitutive model, on the other hand, provided $E = 0.69$ MPa for the same experimental data. As for Poisson's ratios, the values were almost zero in all cases. Another important difference occurred in the permeability: 5.1×10^{-15} against 3.0×10^{-15} $m^4/(N\,s)$ obtained in the isotropic model. These results, showing the importance of cartilage anisotropy, have motivated the implementation of a nonlinear transversely isotropic model, whose validation is the subject of this chapter.

In order to pursue this objective, the Cauchy stress tensor and elasticity tensor derived for transverse isotropy in Chapter 3 have been implemented in the finite element program. Since there is no experimental transversely isotropic Helmholtz free energy function available yet, a hypothetical exponential function is proposed in the next section to represent articular cartilage. To this end, the orthotropic behavior of articular cartilage is approximated assuming that the solid matrix is a hyperelastic, transversely isotropic material. This model neglects the anisotropy of the tissue in planes parallel to the cartilage surface and considers a single preferred direction perpendicular to the surface. In the remaining sections of this chapter, the response of the proposed exponential function is investigated simultaneously with the validation of the program.

7.1 Transversely Isotropic Helmholtz Free Energy Function

The general form of the exponential, transversely isotropic Helmholtz free energy function considered here is given by

$$\rho_0^s \psi^s = \alpha_0 \frac{e^{\varphi(I_1, I_2, I_4, I_5)}}{I_3^n} = \alpha_0 e^{[\varphi(I_1, I_2, I_4, I_5) - n \ln(I_3)]}, \tag{7-1}$$

where the exponent φ is a polynomial function of the invariants, and includes terms up to forth order in the stretches:

$$\begin{aligned}\varphi(I_1, I_2, I_4, I_5) = {} & \alpha_1 (I_1 - 3) + \alpha_2 (I_2 - 3) + \alpha_3 (I_1 - 3)^2 + \alpha_4 (I_4 - 1) + \alpha_5 (I_4 - 1)^2 \\ & + \alpha_6 (I_1 - 3)(I_4 - 1) + \alpha_7 (I_5 - 1).\end{aligned} \tag{7-2}$$

where $\alpha_0, \ldots, \alpha_7$ and n are material parameters. The above equation is similar to Eq. (3-54) suggested by Cohen [24], except that the number of parameters has been increased. The term $\alpha_3 (I_1 - 3)^2$ in Eq. (7-2) is new, and the third invariant in the denominator of Eq. (7-1) now has an exponent n. These additional terms are necessary to control the exponential response of the tissue both in tension and compression. Only 7 parameters are independent, since the imposition of a natural state as a reference configuration reduces the number of parameters by two (see Appendix D). Note that Eq. (7-1) can be extended into a sum of exponentials in order to include, for example, the pseudo strain energy function proposed by Humphrey and Yin [50] for passive myocardium.

For completeness, the derivatives with respect to the invariants that appear in the elastic stress tensor and the elasticity tensor are presented. First derivatives are given by

$$\begin{gathered}\psi^s_{,1} = \vartheta_1 \psi^s, \qquad \psi^s_{,2} = \alpha_2 \psi^s, \qquad \psi^s_{,3} = -\frac{n}{I_3} \psi^s, \\ \psi^s_{,4} = \vartheta_4 \psi^s, \qquad \psi^s_{,5} = \alpha_7 \psi^s,\end{gathered} \tag{7-3}$$

where $\psi^s_{,j}$ denotes partial derivative with respect to the invariant I_j, and coefficients ϑ_1 and ϑ_4 abbreviate the following terms

$$\vartheta_1 = \alpha_1 + 2\alpha_3 (I_1 - 3) + \alpha_6 (I_4 - 1),$$
$$\vartheta_4 = \alpha_4 + 2\alpha_5 (I_4 - 1) + \alpha_6 (I_1 - 3). \tag{7-4}$$

Table 7.1 contains the second partial derivatives $\psi_{,ij}$ with respect to the invariants I_i and I_j, which are identified by column and row numbers.

Table 7.1 Second partial derivatives with respect to the invariants

	I_1	I_2	I_3	I_4	I_5
I_1	$(\vartheta_1^2 + 2\alpha_3)\,\psi^s$	$\alpha_2 \psi^s_{,1}$	$-\frac{n}{I_3}\psi^s_{,1}$	$(\vartheta_1\vartheta_4 + \alpha_6)\,\psi^s$	$\alpha_7 \psi^s_{,1}$
I_2		$\alpha_2 \psi^s_{,2}$	$-\frac{n}{I_3}\psi^s_{,2}$	$\vartheta_4 \psi^s_{,2}$	$\alpha_7 \psi^s_{,2}$
I_3			$-\frac{(n+1)}{I_3}\psi^s_{,3}$	$\vartheta_4 \psi^s_{,3}$	$\alpha_7 \psi^s_{,3}$
I_4	Symmetric			$(\vartheta_4^2 + 2\alpha_5)\,\psi^s$	$\alpha_7 \psi^s_{,4}$
I_5					$\alpha_7 \psi^s_{,5}$

To avoid problems associated with nonphysical responses which may result from the exponential function, basic issues are examined in Appendix D. These issues include the existence of a natural state, the stress-strain relations under infinitesimal deformation, and the extension-tension (E-T) condition for stretches in the principal directions of the material.

For correlation with experiments, the number of material parameters in Eq. (7-2) is certainly excessive. Nevertheless, the reduction in the number of parameters is more effectively done by relating some of them to the infinitesimal material properties, rather than by simply removing terms from the function. The following material parameters have been selected to illustrate the qualitative trends of the stress response produced by the exponential function: n = 0.6, α_0 = 0.08 MPa, α_1 = 7.733, α_2 = -3.567, α_3 = 1.905, α_4 = 3.958, α_5 = 0.8904, α_6 = -0.0111, α_7 = -1.979. For infinitesimal deformation they correspond to $E_m = E_1 = 0.7$ MPa, $E_2 = 1.4$ MPa,

$G_{12} = 0.35$ MPa and $\nu_{12} = \nu_{23} = 0.05$, where $\boldsymbol{m}$ denotes the preferred direction (in this example, perpendicular to the cartilage surface). Relationships between material parameters and engineering coefficients are developed in Appendix D.

7.2 Single-Phase Tests

The selection of the Helmholtz free energy function is a trial and error process, so that the elimination of functional forms that give rise to nonphysical responses is a crucial part of the investigation. This can be done by inspecting the general trends of the response from simulated tests, in particular single phase tests considering only the solid matrix. Although far from conclusive, these tests eliminate functions that, despite correlating well with uniaxial responses, are unable to represent multiaxial behavior. Finite element models are particularly suitable for this task; the implementation of various free energy functions represents a small effort when compared to the attainment of analytical solutions for each function. Furthermore, complex boundary conditions do not represent obstacles to the finite element method as they do for analytical methods. The results of such tests are also useful for subsequent mathematical investigations, which must be pursued to establish the range of deformation for which the model is adequate

7.2.1 Confined Compression of the Solid Matrix

The confined compression of the solid matrix is a straightforward way of examining the resulting response and also a good test for the implementation of the elasticity tensor computed from the Helmholtz free energy function. The analytical solution for prescribed stretches is found in Appendix D (Eqs. (D-11) - (D-15)) and can be used to verify numerical results as shown in Figs. 7.1 and 7.2. Subscripts λ, m and t are used to identify the direction of stretch, the preferred direction, and a transverse direction in the plane of isotropy, respectively. In those figures, analytical and finite element results practically coincide for the stretch prescribed along and perpendicular to the preferred direction of the material.

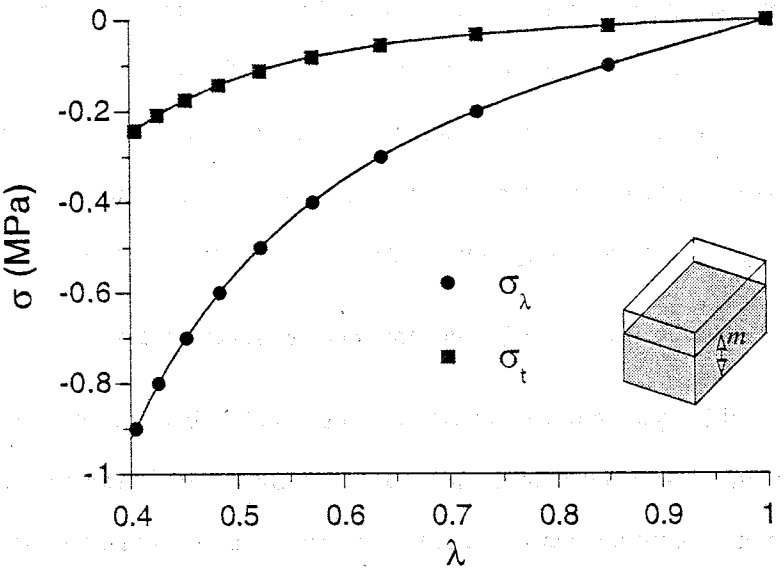

Figure 7.1 Principal stresses versus stretch (λ) prescribed along the preferred direction (m). Comparison between FE results (symbols) and analytical solution (solid lines) for the confined compression of the solid matrix.

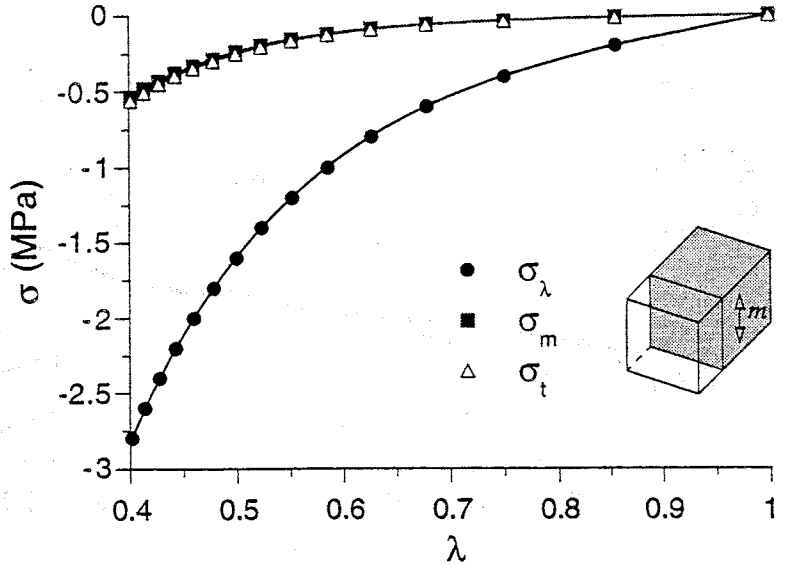

Figure 7.2 Principal stresses versus stretch (λ) prescribed perpendicularly to the preferred direction (m). Comparison between FE results (symbols) and analytical solution (solid lines) for the confined compression of the solid matrix.

This test has also been used to select the nonlinear material parameters α_0 and n so that the compressive response resembles the experimental curves for stress at equilibrium presented in Holmes [43] and Warden *et al.* [114]. It is important to mention that this test uncovered one limitation of the exponential function: when the material is stiffer in the plane of isotropy, larger Poisson's ratios can give rise to confining stresses greater than the applied stress.

7.2.2 Simple Tension and Compression of the Solid Matrix

Additional insights into the material response can be obtained from simple tension tests simulated using the finite element program. Figure 7.3 shows normal stress versus stretch for loads applied parallel and perpendicular to the preferred direction. Two important trends are shown in the figure: the asymmetric stiffening in tension and compression, and the differential increase in the Young's moduli. Both trends are desirable features since they allow distinct degrees of anisotropy depending on the stretch.

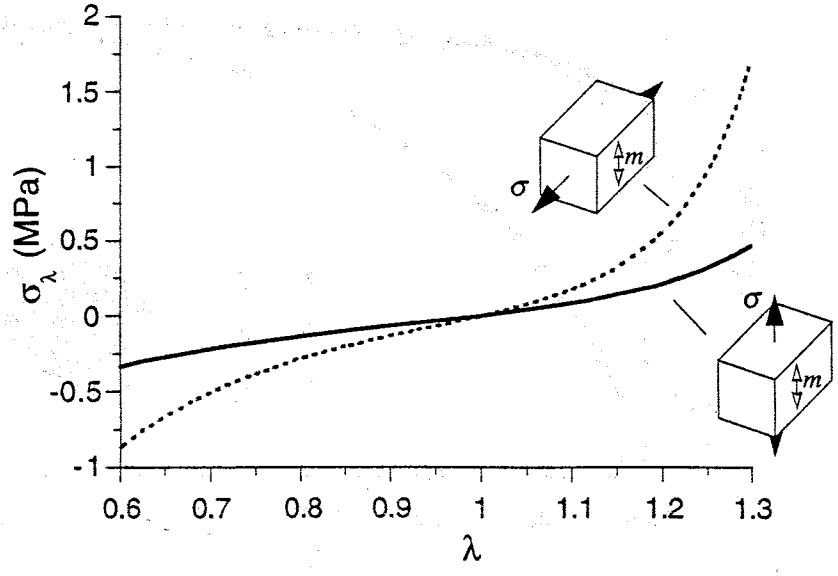

Figure 7.3 Normal stress versus stretch for loads applied perpendicularly and parallel to the preferred direction. FE results for simple tension/compression of the solid matrix.

Figure 7.4 shows transverse stretch versus prescribed stretch for loads applied parallel and normal to the preferred direction. Physically acceptable results are obtained for the entire range of deformation of interest for articular cartilage. Note that Poisson's ratios increase with stretch. The desirability of this result still has to be verified experimentally, but is likely to be inadequate for large stretches where fibers are supposed to be predominantly aligned in the direction of the largest stretch.

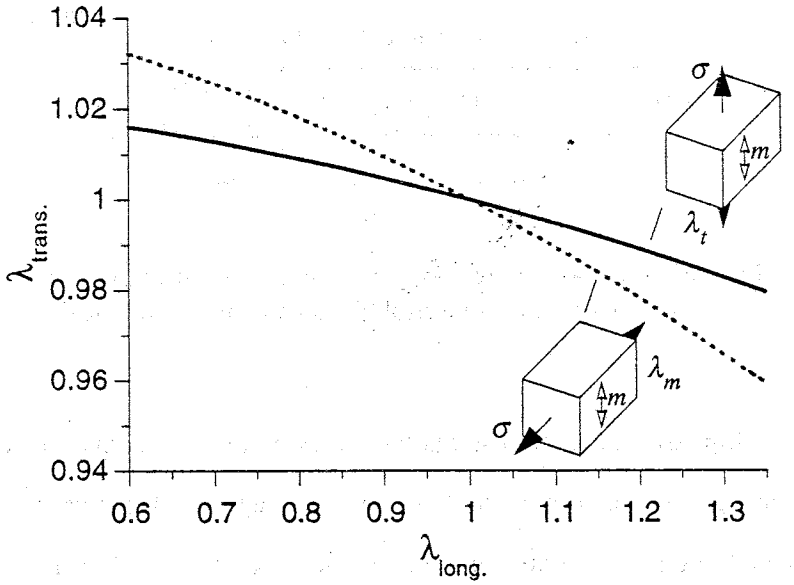

Figure 7.4 Transverse stretch versus longitudinal stretch produced by loads applied perpendicularly and parallel to the preferred direction of the material. FE results for simple tension/compression of the solid matrix.

7.3 Biphasic Unconfined Compression Example

In order to test the constitutive model in a biphasic problem, the previous material parameters are adopted for the solid phase, and used to simulate the biphasic unconfined compression creep test. This is the problem discussed in Chapter 6, except that the rigid platens are considered to be lubricated here. This simpler boundary condition will allow the comparison between 3-D

results of the *v-p* formulation and axisymmetric results of the MP formulation using a relatively small number of elements (Fig. 7.5).

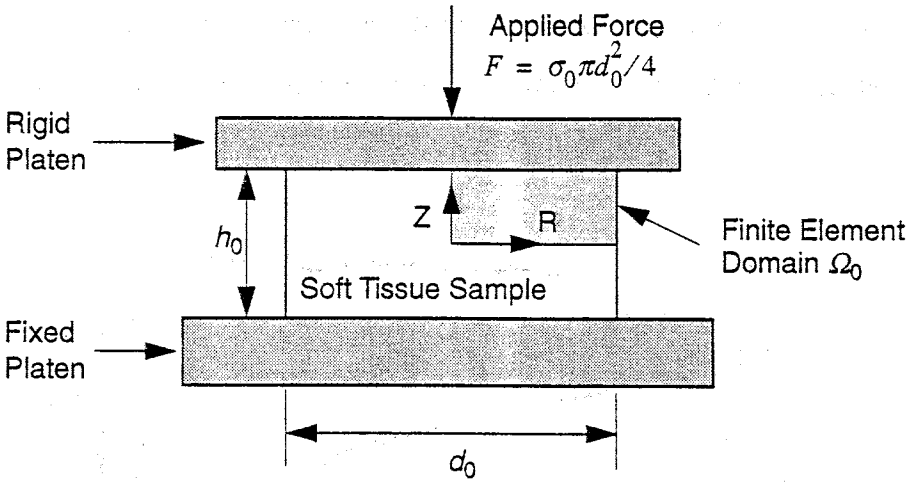

Figure 7.5 Schematic representation of the unconfined compression creep test of a cylindrical disk of soft hydrated tissue.

For this biphasic example, material properties of Section 7.1 are selected alone with the permeability function adopted in the first example of Chapter 6 [44], with $\phi_0^s = 0.2$. As for the loading, an axial force corresponding to a normal traction of $\sigma_0 = 1\text{MPa}$ in the reference configuration is applied in a 10-second ramp and held constant. The deformation imposed by the rigid platen is simulated by representing the vertical nodal velocities at the loaded surface as a single (unknown) degree of freedom.

The dimensions are $h_0 = 2\text{mm}$ and $d_0 = 6\text{mm}$. Finite element meshes are shown in Fig. 7.6; 9-node MP rectangles are used in the axisymmetric analysis and 10-node *v-p* tetrahedra are used in the 3-D analysis. The 3-D mesh has 328 tetrahedra, 757 nodes and 1776 degrees-of-freedom, either solid velocity or pressure. Time steps varying from 0.5 to 5 seconds are adopted in both analyses, with smaller times being used during the ramp stage and the beginning of the creep.

Figure 7.7 shows pressure isosurfaces at 20 and 500 seconds. The surfaces within the 3-D mesh have the cylindrical shapes which are expected for this axisymmetric problem. They are

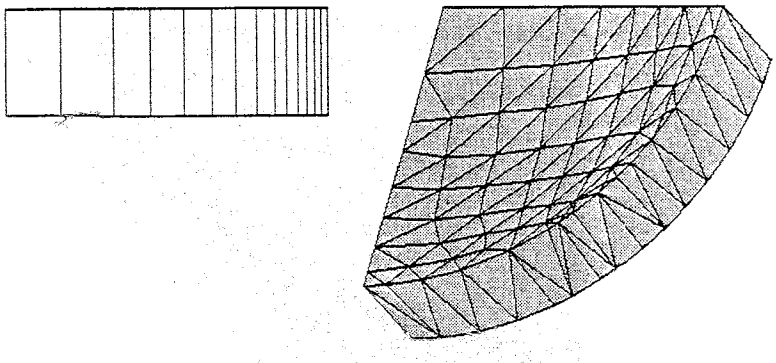

Figure 7.6 Axisymmetric and 3-D finite element meshes for the unconfined compression problem.

almost circumferential near the boundary, and perturbations occur only at 500 seconds in the region with the coarsest refinement. Relative velocities at 20 seconds are represented in Fig. 7.8. The maximum amplitude is 2.5×10^{-6} m/s, and the directions are radially oriented, once again demonstrating the good behavior of the *v-p* tetrahedra.

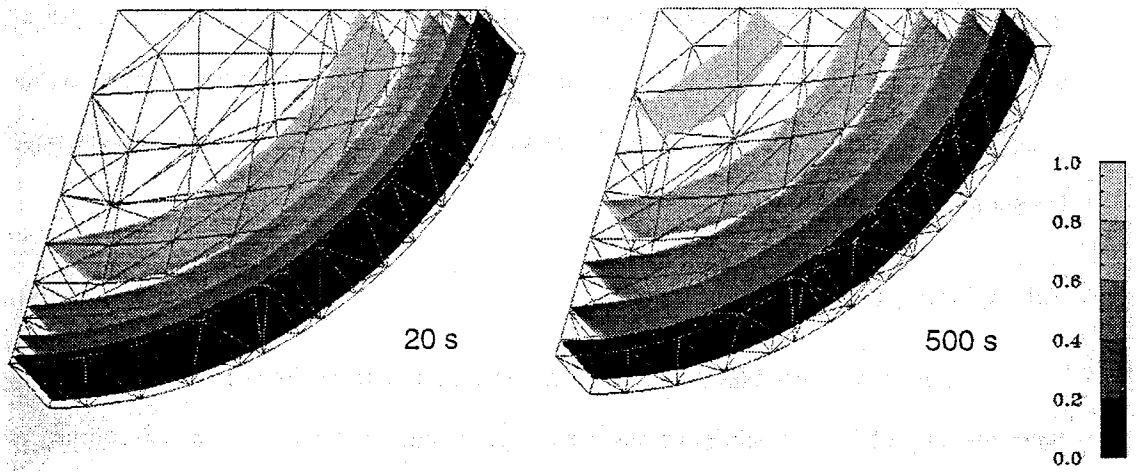

Figure 7.7 Pressure isosurfaces at 20 s and 500 s for the unconfined compression problem.

Since 3-D results do not vary with radial position, linear plots can be used in the comparison with the axisymmetric solution (Fig. 7.9). Excellent agreement exists in terms of pressure, elastic stresses and stretches. Note that values are plotted in the current configuration in order to

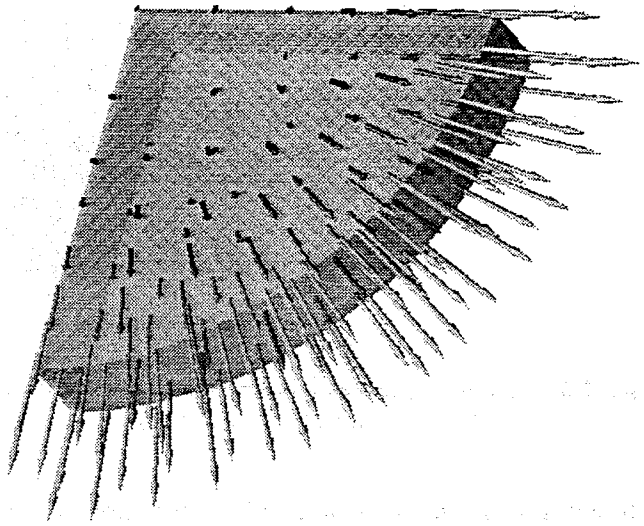

Figure 7.8 Relative velocities at 20 s for the unconfined compression problem.

allow the verification of equilibrium in the vertical direction. Moreover, the material anisotropy is noticeable from the radial and axial values of stresses and stretches: large magnitudes of stress in the radial direction are accompanied by smaller deformation when compared to the deformation in the axial direction. One characteristic that differentiates linear and nonlinear analyses is the increase in the radial stress σ_{Err} near the axis, which is a result of the considerable reduction of the sample's current height.

7.4 Closing Remarks

A three-dimensional constitutive model that considers the nonlinearity, anisotropy and heterogeneity of articular cartilage has been implemented in the finite element program. Simultaneously with the validation of the implementation, results of single-phase and biphasic examples have been used to assess the response obtained from an exponential Helmholtz free energy function. The results, although limited, demonstrate some of the capabilities and limitations of this functional form. The emphasis has been in computational mechanics and implementation aspects of the problem. This preliminary study precedes a more elaborate investigation which would

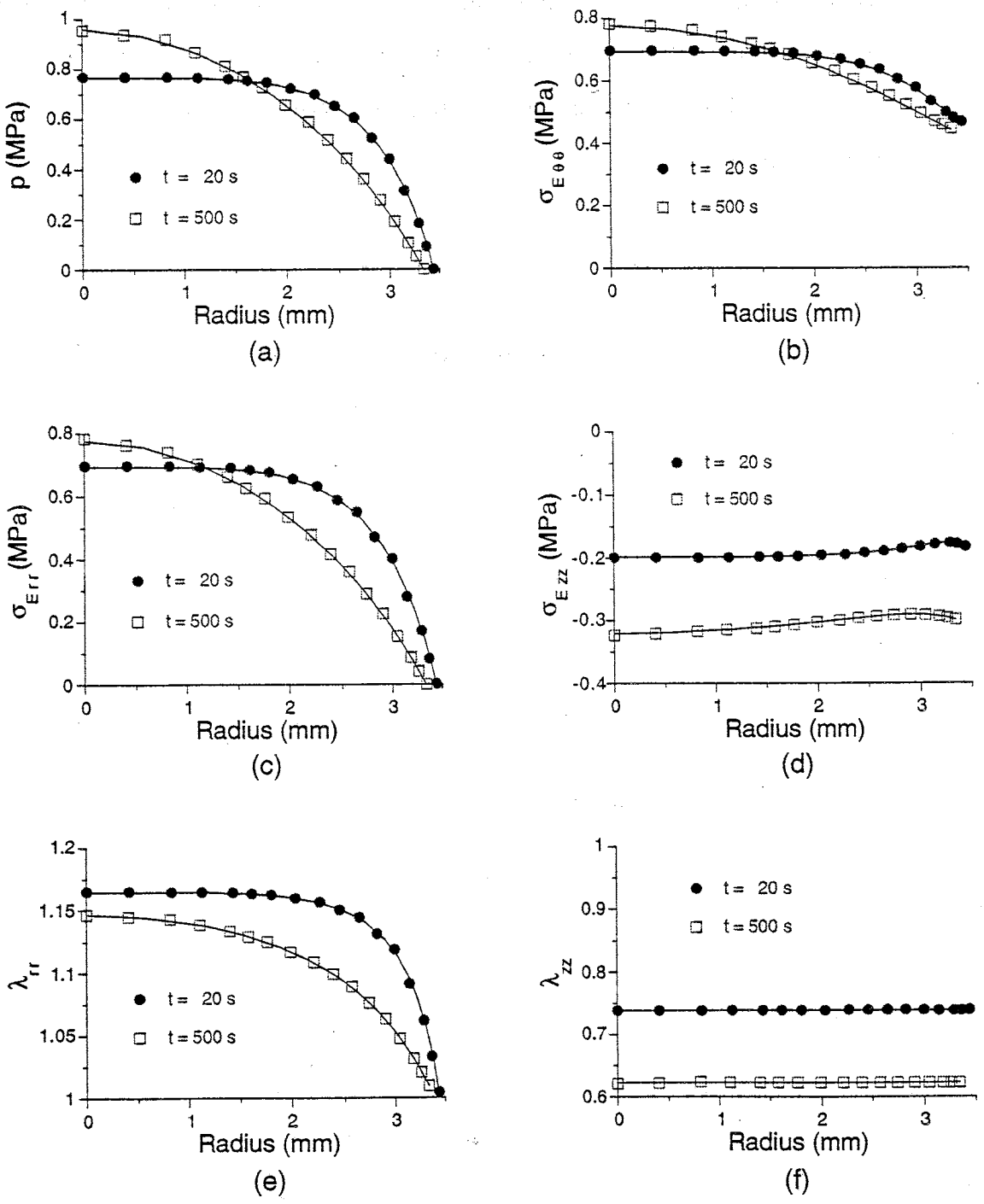

Figure 7.9 Pressure, elastic Cauchy stresses, and stretches versus deformed radius for the unconfined compression problem with a transversely isotropic material. NOTES: (a) pressure (b) circumferential stress, (c) radial stress, (d) axial stress, (e) radial stretch, and (f) axial stretch. Results obtained using 10-node *v-p* tetrahedra (symbols) and 9-node MP quadrilaterals (solid lines).

include experiments to determine material parameters and to validate the exponential form. Further studies must also examine physical and mathematical restrictions to determine the range of deformation for which this exponential form is adequate to model the three-dimensional behavior of articular cartilage.

CHAPTER 8

Summary, Conclusions and Suggestions for Future Studies

This thesis addresses computational models for the 3-D, nonlinear analysis of soft hydrated tissues such as articular cartilage. A biphasic continuum description has been used to represent the soft tissue as a two-phase mixture of an incompressible, inviscid fluid and a hyperelastic, transversely isotropic solid. The theoretical foundations of this theory have been reviewed with emphasis on constitutive modeling. Alternate mixed-penalty and velocity-pressure finite element formulations have been used to solve the nonlinear biphasic governing equations, including the effects of strain-dependent permeability and a hyperelastic solid phase under finite deformation. The resulting first-order nonlinear system of equations is discretized in time using an implicit finite difference scheme, and solved using the Newton-Raphson method.

The objective of developing the nonlinear formulations is to enable the 3-D analysis of tissue layers in diarthrodial joints under physiologically relevant loading conditions. The formulations are general and have been used to develop quadrilateral and triangular elements in 2-D and hexahedral and tetrahedral elements in 3-D. Numerical examples including those representative of soft tissue material testing and simple human joints have been used to validate the formulations and to illustrate their applications. Using these examples, the formulations have been compared for robustness, flexibility in interfacing with automatic and adaptive meshing, and computational efficiency. While not the central focus of this work, important insights have been gained from selected linear biphasic analyses.

The mixed-penalty finite element formulation has been extended to nonlinear problems in this thesis. The weak form is constructed via the weighted residual method from a penalized form of the continuity equation for the mixture, the linear momentum equations for the solid and fluid phases, and the traction boundary conditions for the two phases. Primary field variables correspond to solid and fluid velocities, interpolated with continuous functions, and pressure, which is

discontinuous between elements. Pressure coefficients are eliminated at the element level, resulting in a system of nonlinear first order equations for the time-dependent tissue response.

In the velocity-pressure formulation implemented in this thesis, the fluid phase velocity is eliminated from the governing equations through the fluid linear momentum equation. The weak form is obtained via the weighted residual method by introducing the linear momentum equation for the mixture, the continuity equation, and traction and fluid flux boundary conditions into the weighted residual statement. The primary field variables are solid velocity and pressure, each interpolated by continuous functions. With respect to this formulation, the contribution here in has been the evaluation of its performance compared with the mixed-penalty formulation. To this end, various 2-D and 3-D finite elements have been implemented and validated.

An important result that helped to make the discussion of the nonlinear formulations more concise is the equivalence between penalty and mixed-penalty formulations for biphasic continua. The equivalence is based on the concept of the discrete divergence operator, which, in this study, has been incorporated into the penalty formulation of Suh *et al.* [105]. The resulting approach is more general than the reduced/selective integration approach used in that reference, for which the equivalence can only be demonstrated for a few elements such as the bilinear quadrilateral.

A significant contribution of this work is the implementation and testing of a biphasic material model with a transversely isotropic hyperelastic solid phase. This model assumes a preferential material direction with properties that are distinct from those in planes perpendicular to the preferred direction, and allows for asymmetric behavior in tension and compression. The theoretical foundations for this model have been reviewed, and an exponential form has been suggested. Through trial and error, a set of material parameters has been identified to represent the response of soft tissues in ranges of deformation and stress previously observed experimentally. After demonstrating the behavior of this constitutive model in simple tension and compression, a sample problem of unconfined compression is used to further validate the finite element implementation and demonstrate the effects of this material model.

An important aspect of this thesis is the comparison of alternate formulations for nonlinear biphasic problems and alternate elements, particularly 3-D elements for which such studies have not been previously attempted. Over the course of this study, various example problems were considered to make these comparisons, ranging from material testing configurations, such as confined and unconfined compression, to first order approximations of joint problems such as the shoulder. Through these examples, observations of the alternate formulations and elements have been made. It has not been possible to draw final conclusions, but it is expected that these observations will guide the next set of studies and formulations. These observations are summarized in the paragraphs which follow.

In the confined compression problem, the two formulations have different performances in creep and stress relaxation and show different sensitivities to mesh refinement. For example, the creep response of the velocity-pressure formulation is poor compared with the mixed-penalty formulation if the comparison is done on a per-element basis. In contrast, for the stress relaxation problem, both formulations give accurate solutions using the same mesh. The difficulties found for the velocity-pressure formulation are associated with oscillations of the solid phase strain and stress at early times and near the loaded surface that prevent the convergence of the nonlinear solution.

For problems such as unconfined compression, with perfectly adhesive or lubricated platens, good accuracy is obtained using both formulations with relatively coarse meshes (for example, seven subdivisions/elements in each direction) and for both creep and stress relaxation problems. Despite the value of the confined compression creep problem to validate biphasic finite elements, it appears from the unconfined compression and shoulder examples that numerical difficulties observed in that problem are not representative of physiologically realistic problems where the load is typically distributed over the two phases. Therefore, performance evaluations of the finite element formulations should not be limited to the behavior shown in the confined compression creep problem.

A drawback of the velocity-pressure formulation is that it produces fluid and relative velocity fields that are not as accurate as in the mixed-penalty formulation. However, when computational time is considered, a significant advantage has been observed for the velocity-pressure formulation. This advantage is a result of the smaller number of degrees of freedom required to achieve comparable accuracy in the nonlinear analyses. Therefore, since analysis costs increase substantially for 3-D problems, preference has been given to this formulation in the examples. It should be noted that such computational comparisons may be premature and there are many other computational issues which may affect this comparison, such as the use of adaptivity, parallel methods and so on.

Dynamic problems constitute a good reason for continued consideration of the mixed-penalty formulation, despite the better performance of the velocity-pressure formulation for quasistatic problems. Dynamic problems, including wave propagation in tissues, arise in biomechanical studies such as the correlation between brain damage and the impact caused by car collisions. For dynamic problems, the extension of the velocity-pressure formulation would require that either the fluid inertial terms be neglected (in which the fluid velocity can be eliminated algebraically) or the fluid momentum equation be integrated in time. The former is an acceptable assumption in soil mechanics, where the porosity is around 0.3, but an impractical one for soft hydrated tissues, where the porosity is 0.75 or more. The introduction of inertial terms in the mixed-penalty formulation, on the other hand, is comparatively easier because the quasistatic linear momentum equation is not used to eliminate the fluid velocity field in the governing equations.

FUTURE STUDIES

Important issues can be addressed in future studies to improve the performance of the nonlinear finite elements, and thus make the simulation of large problems in joint biomechanics more tractable. Since these problems are complex and multi-disciplinary, the suggestions listed below cover different aspects of the computational implementation.

Augmented Lagrangian Formulation

The author has observed in numerical examples that the current version of mixed-penalty formulation has a negative impact on the Newton-Raphson method, preventing it from achieving its quadratic rate of convergence. This can be improved with the implementation of augmented Lagrangian methods in the mixed-penalty formulation. These methods, first developed for constrained optimization, have been applied successfully to finite element formulations in incompressible elasticity in order to reduce solution costs of large constrained problems [64]. The application of augmented Lagrangian methods implies rewriting the weak form so that the continuity condition can be approximated by linear constraints, which are then imposed by combining penalty and Lagrangian multiplier terms. In this way, the solution of the system of equations requires a sequence of solutions, which use increasing penalty parameters determined from the Lagrangian multipliers. This means that some compressibility is initially allowed in the iterative process, with penalty parameters gradually increased to enforce the constraint. Based on results reported for nonlinear incompressible elasticity, it is anticipated that the additional effort required for augmented Lagrangian methods will be compensated by faster rates of convergence when compared with the standard mixed-penalty formulation.

A New Variant of the Mixed-Penalty Formulation

A new variant of the mixed-penalty formulation was identified at the completion of this thesis research. In this variant, the fluid velocity unknown is replaced by the relative velocity associated with fluid flux within the tissue. The choice of this field as primary variable has the advantage of eliminating the need to calculate the gradients of the volume fractions and, therefore, the need to calculate the second derivatives of the interpolation functions. This represents a substantial economy for the computation of the finite element matrices and strongly motivates the implementation of this variant in the near future. Due to the relevance of this result for the present study, a brief derivation of this variant is presented in Appendix E.

Elements with Equal-Order Interpolation for the v-p Formulation

A result derived by Murad and Loula [74, 75] for the linear displacement-pressure (or velocity-pressure) formulation was left unexplored in this thesis: that elements not satisfying the

LBB condition can still have a convergent long term solution. Based on this result and the work of Reed [85], these authors suggested the use of elements with equal interpolation for pressure and velocity/displacement, followed by the smoothing of the pressure field. It remains to be investigated if equal-order interpolation is feasible in nonlinear analyses and, if so, which post-processing technique must be employed.

Adaptivity

For physiological problems the short-time response is important and substantial mesh refinement under and near the contact region is required. This suggests reallocating nodes to obtain the necessary element gradation, a procedure already developed for single phase materials using the Arbitrary Lagrangian-Eulerian (ALE) finite element formulation [39]. However, aspects such as small thickness of the cartilage layer and moving contact loads considerably restrict the ALE formulation, demanding other forms of adaptivity that allow the change of element interpolation (p-adaptivity) and element size (h-adaptivity).

The implementation of adaptivity is the reason behind tests with the 10-node velocity-pressure tetrahedron since most resources regarding automatic 3-D mesh generation and h-adaptivity favors tetrahedral elements. Furthermore, the velocity-pressure formulation is particularly attractive for adaptivity. Simple nonlinear finite element matrices, straightforward extension to higher-order interpolations, and absence of penalty terms are strong motivations offered by this formulation for the implementation of p-adaptivity.

Triphasic Theory

The cost-efficiency provided by the velocity-pressure formulation provides an opportunity for the implementation of the triphasic theory. This theory has an additional ion phase and is appropriate for modelling the swelling of articular cartilage. Results of this theory can also complement the biphasic theory providing mechanical properties under various physico-chemical conditions for articular cartilage.

References

1. Achcar, N., *Corpos Transversalmente Isotrópicos Não Ortotrópicos*, Thesis, Ph.D., Escola Politécnica da Universidade de São Paulo, 1990.

2. Armstrong, C. G., Lai, W. M. and Mow, V. C., An analysis of the unconfined compression of articular cartilage., *J. Biomech. Eng.*, **106**: 165-173, 1984.

3. Atkin, R. J. and Craine, R. E., Continuum theories of mixtures: Applications, *J. Inst. Maths. Applics.*, **17**: 153-207, 1976.

4. Atkin, R. J. and Craine, R. E., Continuum theories of mixtures: Basic theory and historical development, *Quart. J. Mech. Appl. Math.*, **29**: 209-244, 1976.

5. Babuska, I., The finite element method with Lagrangian multipliers, *Numer. Math.*, **20**: 179-192, 1973.

6. Ball, J. M., Convexity conditions and existence theorems in nonlinear elasticity, *Archives for Rational Mechanics Analysis,* **15**: 337-403, 1977.

7. Bathe, K. J., *Finite Element Procedures in Engineering Analysis*, Prentice-Hall, Englewood Cliffs, NJ, 1982.

8. Bedford, A. and Drumheller, D. S., Recent advances: Theories of immiscible and structured mixtures, *Int. J. Engng. Science,* **21**: 863-960, 1983.

9. Belytschko, T., An overview of semidiscretization and time integration procedures. In *Computational Methods for Transient Analysis* , T. Belytschko and t. J. R. Hughes Eds., pp. 1-65, Elsevier Science, New York, 1983.

10. Biot, M. A., General theory of three dimensional consolidation, *J. Appl. Phys.*, **12**: 155-164, 1941.

11. Biot, M. A., Theory of Finite Deformations of Porous Solids, *Indiana Univ. Math. J.*, **21**: 597-620, 1972.

12. Boehler, J. P., On irreducible representations for isotropic scalar functions, *ZAMM,* **57**: 323-327, 1977.

13. Boehler, J. P. Ed. *Applications of Tensor Functions in Solid Mechanics*, Springer-Verlag, Wien - New York, 1987.

14. Booker, J. R. and Small, J. C., An investigation of the stability of numerical solutions of Biot's equations of consolidation, *Int. J. Sol. Struct.*, **11**: 907-917, 1975.

15. Borja, R. I., Finite element formulation for transient pore pressure dissipation: A variational approach, *Int. J. Sol. Struct.*, **22**: 1201-1211, 1986.

16. Borja, R. I., Linearization of elasto-plastic consolidation equations, *Engng. Comput.*, **6**: 163-168, 1989.

17. Borja, R. I., One-step and linear multistep methods for nonlinear consolidation, *Comp. Meth. Appl. Mech. Eng.*, **85**: 239-272, 1991.

18. Bowen, R. M., Theory of mixtures. In *Continuum Physics*, A. C. Eringen Ed., Vol. 3, pp. 1-127, Academic Press, New York, 1976.

19. Bowen, R. M., Incompressible porous media models by use of the theory of mixtures, *Int. J. Engng. Science,* **18**: 1129-1148, 1980.

20. Brezzi, F., On the existence, uniqueness and approximation of saddle-point problems arising from Lagrange multipliers, *RAIRO,* **8**: 129-151, 1974.

21. Brezzi, F. and Fortin, M., *Mixed and Hybrid Finite Element Methods*, Vol. 15 - Springer Series in Computational Mathematics, Springer-Verlag, New York, NY, 1991.

22. Carter, J. P., Small, J. C. and Booker, J. R., A theory of finite elastic consolidation, *Int. J. Sol. Struct.*, **13**: 467-478, 1977.

23. Ciarlet, P. G., *Mathematical Elasticity. Volume I: Three Dimensional Elasticity*, North-Holland, Amsterdam, 1988.

24. Cohen, B., *Anisotropic Hydrated Soft Tissues in Finite Deformation and the Biomechanics of the Growth Plate*, Thesis, Ph.D., Columbia University, 1992.

25. Cohen, B., Gardner, T. R. and Ateshian, G. A., The influence of transverse isotropy on cartilage indentation behavior: A study of the human humeral head, *Trans. Orthop. Res. Soc.*, **18**: 185, 1993.

26. Coleman, B. D. and Noll, W., Material symmetry and thermostatic inequalities in finite elastic deformations, *Archives for Rational Mechanics Analysis,* **15**: 87-111, 1964.

27. Donzelli, P. S., *A Mixed-Penalty Contact Finite Element Formulation for Biphasic Soft Tissues*, Thesis, Ph.D., Rensselaer Polytechnic Institute, 1995.

28. Donzelli, P. S. and Spilker, R. L., A finite element formulation for contact of biphasic materials: evaluation for plane problems. In *1993 Advances in Bioengineering*, J. M. Tarbell Ed., pp. 47-50, ASME, New York, 1993.

29. Engelman, M. S., Sani, R. L., Gresho, P. M. and Bercovier, M., Consistent vs. reduced integration penalty methods for incompressible media using several old and new elements, *Int. J. Num. Meth. Fluids,* **2**: 25-42, 1982.

30. Ericksen, J. L. and Rivlin, R. S., Large elastic deformations of homogeneous anisotropic materials, *J. Rat. Mech. Anal.,* **3**: 281-301, 1954.

31. Fortin, M., Old and new finite elements for incompressible flows, *Int. J. Num. Meth. Fluids,* **1**: 347-364, 1981.

32. Fortin, M. and Fortin, A., Newer and newer elements for incompressible flow. In *Finite Elements in Fluids*, R. H. Gallagher, G. F. Carey, J. T. Oden and Zienkiewicz Eds., Vol. 6, pp. 171-187, John Wiley and Sons, 1985.

33. Fung, Y. C., *Biomechanics: Mechanical Properties of Living Tissues.*, 2nd ed., Springer-Verlag, New York, NY, 1993.

34. Fung, Y. C. B., Biorheology of Soft Tissues, *Biorheol.,* **10**: 139-155, 1973.

35. Gadala, M. S., Numerical solution of nonlinear problems of continua - II. Survey of incompressibility constraints and software aspects, *Comp. & Struct.,* **22**: 841-855, 1986.

36. Gadala, M. S., Alternative methods for the solution of hyperelastic problems with incompressiblity, *Comp. & Struct.,* **42**: 1-10, 1992.

37. Ghaboussi, J. and Wilson, E. L., Variational formulation of dynamics of fluid saturated porous elastic solids, *J. Eng. Mech. Div. ASCE,* **98(EM4)**: 947-963, 1972.

38. Ghaboussi, J. and Wilson, E. L., Flow of compressible fluid in porous elastic media, *Int. J. Num. Meth. Eng.,* **5**: 419-442, 1973.

39. Ghosh, S. and Kikuchi, N., An arbitrary Lagrangian-Eulerian finite element method for large deformation analysis of elastic-viscoplastic solids, *Comp. Meth. Appl. Mech. Eng.,* **86**: 127-188, 1991.

40. Gurtin, M. E., *An Introduction to Continuum Mechanics*, Academic Press, New York, NY, 1981.

41. Hill, R., Constitutive inequalities for isotropic elastic solids under finite strain, *Proc. Royal Soc. London, A*, **314**: 457-472, 1970.

42. Holmes, M. H., A theoretical analysis for determining the nonlinear hydraulic permeability of a soft tissue from a permeation experiment, *Bulletin of Mathematical Biology.*, **47**: 669-683, 1985.

43. Holmes, M. H., Finite deformation of soft tissue: Analysis of a mixture model in uni-axial compression, *J. Biomech. Eng.*, **108**: 372-381, 1986.

44. Holmes, M. H. and Mow, V. C., The nonlinear characteristics of soft gels and hydrated connective tissues in ultrafiltration, *J. Biomech.*, **23**: 1145-1156, 1990.

45. Holmes, M. H., Mow, V. C., Spilker, R. L. and Lai, W. M., *Mixture Theories for the Mechanics of Biological Tissues*, Book in preparation, 1993.

46. Hou, J. S., Holmes, M. H., Lai, W. M. and Mow, V. C., Boundary conditions at the cartilage-synovial fluid interface for joint lubrication and theoretical verifications, *J. Biomech. Eng.*, **111**: 78-87, 1989.

47. Hughes, T. J. R., *The Finite Element Method: Linear Static and Dynamic Finite Element Analysis*, Prentice-Hall, Englewood Cliffs, NJ, 1987.

48. Hughes, T. J. R. and Belytschko, T., *A précis* of developments in computational methods for transient analysis, *J. Appl. Mech.*, **50**: 1033-1041, 1983.

49. Humphrey, J. D., Determination of a constitutive relation for passive myocardium: I. A new functional form. II. Parameter estimation, *J. Biomech. Eng.*, **112**: 333-339, 340-346, 1990.

50. Humphrey, J. D. and Yin, F. C. P., On constitutive relations and finite deformations of passive cardiac tissue: I. A pseudostrain energy function, *J. Biomech. Eng.*, **109**: 298-304, 1987.

51. Huyghe, J. M., van Campen, D. H., Arts, T. and Heethaar, R. M., A two-phase finite element model of the diastolic left ventricle, *J. Biomech.*, **24**: 527-538, 1991.

52. Jinyun, Y., Symmetric Gaussian quadrature formulae for tetrahedronal regions, *Comp. Meth. Appl. Mech. Eng.*, **43**: 349-353, 1984.

53. Johnson, C., *Numerical Solution of Partial Differential Equations by the Finite Element Method*, Cambridge University Press, Cambridge, 1992.

54. Kardestuncer, H., Norrie, D. H. and Brezzi, F. Eds., *Finite Element Handbook*, McGraw-Hill, New York, NY, 1987.

55. Keast, P., Moderate-degree tetrahedral quadrature formulas, *Comp. Meth. Appl. Mech. Eng.*, **55**: 339-348, 1986.

56. Krause, G., Finite element schemes for porous elastic media, *J. Eng. Mech. Div.*, **104**: 605-620, 1978.

57. Kwan, M. K., Lai, W. M. and Mow, V. C., A finite deformation theory for cartilage and other soft hydrated connective tissues - I. Equilibrium results, *J. Biomech.*, **23**: 145-155, 1990.

58. Kwan, M. K.-W., *A Finite Deformation Theory for Nonlinearly Permeable Cartilage and Other Soft Hydrated Connective Tissues and Rheological Study of Cartilage Proteoglycans*, Thesis, Ph.D., Rensselaer Polytechnic Institute, 1985.

59. Lai, W. M., Hou, J. S. and Mow, V. C., A triphasic theory for the swelling and deformation behaviors of articular cartilage, *J. Biomech. Eng.*, **113**: 245-258, 1991.

60. Lai, W. M. and Mow, V. C., Drag induced compression of articular cartilage during a permeation experiment, *Biorheol.*, **103**: 111-123, 1980.

61. Lai, W. M., Mow, V. C. and Roth, V., The effects of the strain dependent permeability and rate of compression on the stress behavior of articular cartilage, *J. Biomech. Eng.*, **103**: 61-66, 1981.

62. Lai, W. M., Rubin, D. and Krempl, E., *Introduction to Continuum Mechanics*, Vol. 17 - Pergamon Unified Engineering Series, SI/Metric ed., Pergamon Press, Oxford, U.K., 1978.

63. Lai, W. M., Rubin, D. and Krempl, E., *Introduction to Continuum Mechanics*, 3rd ed., Pergamon Press, Oxford, England, 1993.

64. Le Tallec, P., Numerical Methods for Three-dimensional Elasticity. In *Handbook of Numerical Analysis: Techniques of Scientific Computing (Part 1); Numerical Methods for Solids (Part 1); Solution of Equations in R^n*, P. G. Ciarlet and J. L. Lions Eds., Vol. III, pp. 465-622, North-Holland, Amsterdam, 1994.

65. Mak, A. F., Lai, W. M. and Mow, V. C., Biphasic indentation of articular cartilage: I. Theoretical analysis, *J. Biomech.*, **20**: 703-714, 1987.

66. Malvern, L. E., *Introduction to the Mechanics of a Continuum Medium*, Prentice-Hall, Englewood Cliffs, NJ, 1969.

67. Marsden, J. E. and Hughes, T. J. R., *Mathematical Foundations of Elasticity*, Prentice-Hall, Englewood Cliffs, NJ, 1983.

68. Mish, K. D., Herrmann, L. R. and Muraleetharan, K., A comparison of Biot formulation finite element models for two- and three-dimensional transient soil problems, *Symposium on Computational Mechanics of Porous Materials and their Thermal Decomposition*, Tempe, Arizona. ASME, **AMD 136**: 69-79, 1992.

69. Mow, V. C., Holmes, M. H. and Lai, W. M., Fluid transport and mechanical properties of articular cartilage: a review, *J. Biomech.*, **17**: 377-394, 1984.

70. Mow, V. C., Kuei, S. C., Lai, W. M. and Armstrong, C. G., Biphasic creep and stress relaxation of articular cartilage in compression: Theory and experiments, *J. Biomech. Eng.*, **102**: 73-84, 1980.

71. Mow, V. C., Kwan, M. K., Lai, W. M. and Holmes, M. H., A finite deformation theory for nonlinearly permeable soft hydrated biological tissues. In *Frontiers in Biomechanics*, S. L.-Y. Woo, G. Schmid-Schonbein and B. Zweifach Eds., pp. 153-179, Springer-Verlag, New York, 1986.

72. Mow, V. C. and Ratcliffe, A. R., Cartilage and diarthrodial joints as paradigms for hierarchical materials and structures, *Biomat.*, **13**: 67-97, 1992.

73. Mow, V. C., Zhu, W. and Ratcliffe, A., Structure and function of articular cartilage and meniscus. In *Basic Orthopaedic Biomechanics*, V. C. Mow and W. C. Hayes Eds., Raven Press, New York, 1991.

74. Murad, M. and Loula, A. F. D., On stability and convergence of finite element approximations of Biot's consolidation problems, *Int. J. Num. Meth. Eng.*, **37**: 645-667, 1994.

75. Murad, M. A. and Loula, A. F. D., Improved accuracy in finite element analysis of Biot's consolidation problem., *Comp. Meth. Appl. Mech. Eng.*, **95**: 359-382, 1992.

76. Oden, J. T., *Finite Elements of Nonlinear Continua*, McGraw-Hill, 1972.

77. Ogden, R. W., Compressible isotropic elastic solids under finite strain - constitutive inequalities, *Quart. J. Mech. Appl. Math.*, **23**: 457-468, 1970.

78. Ogden, R. W., *Non-linear Elastic Deformations*, Ellis Horwood, Chichester, U.K., 1984.

79. Oomens, C. W. J., van Campen, D. H. and Grootenboer, H. J., *In vitro* compression of a soft tissue layer on a rigid foundation, *J. Biomech.*, **20**: 923-935, 1987.

80. Oomens, C. W. J., van Campen, D. H. and Grootenboer, H. J., A mixture approach to the mechanics of skin, *J. Biomech.*, **20**: 877-885, 1987.

81. Prevost, J. H., Mechanics of Continuous Porous Media, *Int. J. Engng. Science,* **18**: 787-800, 1980.

82. Prevost, J. H., Nonlinear transient phenomena in saturated porous media, *Comp. Meth. Appl. Mech. Eng.*, **20**: 3-18, 1982.

83. Prevost, J. H., Implicit-explicit schemes for nonlinear consolidation, *Comp. Meth. Appl. Mech. Eng.*, **39**: 225-239, 1983.

84. Prevost, J. H., Wave propagation in fluid-saturated porous media: An efficient finite element procedure, *Soil Dyn. Earth. Eng.*, **4**: 183-202, 1985.

85. Reed, M. B., An investigation of numerical errors in the analysis of consolidation by finite elements, *Int. J. Num. Anal. Meth. Geomech.*, **8**: 243-257, 1984.

86. Ruas, V., Finite element methods for three-dimensional incompressible viscous flow. In *Finite Elements in Fluids*, T. J. Chung Ed., Vol. 8, pp. 211-235, Hemisphere Publishing Company, 1992.

87. Sandhu, R. S., Liu, H. and Singh, K. J., Numerical performance of some finite element schemes for analysis of seepage in porous elastic media, *Int. J. Num. Anal. Meth. Geomech.*, **1**: 177-194, 1977.

88. Sandhu, R. S. and Wilson, E. L., Finite Element Analysis of Seepage in Elastic Media, *J. Eng. Mech. Div. ASCE,* **95(EM3)**: 641-651, 1969.

89. Setton, L. A. and Mow, V. C., The Tensile and Compressive Properties of Articular Cartilage. CRC Press (in Press), 1994.

90. Simo, J. C. and Pister, K. S., Remarks on rate constitutive equations for finite deformation problems: computational implications, *Comp. Meth. Appl. Mech. Eng.*, **46**: 201-215, 1984.

91. Simo, J. C., Taylor, R. L. and Pister, K. S., Variational and projection methods for the volume constraint in finite deformation elasto-plasticity, *Comp. Meth. Appl. Mech. Eng.*, **51**: 177-208, 1985.

92. Simon, B. R. and Gaballa, M. A., Finite strain, poroelastic finite element models for large arterial cross sections. In *Computational Methods in Bioengineering*, R. L. Spilker and B. R. Simon Eds., Vol. BED - 9, pp. 325-333, ASME, New York, 1988.

93. Simon, B. R., Wu, J. S.-S. and Zienkiewicz, O. C., Evaluation of higher order, mixed and Hermitean finite element procedures for the dynamic analysis of saturated porous media using one-dimensional models, *Int. J. Num. Anal. Meth. Geomech.*, **10**: 483-499, 1986.

94. Simon, B. R., Wu, J. S.-S., Zienkiewicz, O. C. and Paul, D. K., Evaluation of u-w and u-π finite element methods for the dynamic response of saturated porous media using one-dimensional models, *Int. J. Num. Anal. Meth. Geomech.*, **10**: 461-482, 1986.

95. Soslowsky, L. J., *Studies on Diarthrodial Joint Biomechanics with Special Reference to the Shoulder*, Thesis, Ph.D., Columbia University, 1991.

96. Soslowsky, L. J., Flatow, E. L., Bigliani, L. U., et al., Quantitation of in situ contact areas at the glenohumeral joint: A biomechanical study, *J. Orthop. Res.*, **10**: 524-534, 1992.

97. Spilker, R. L. and Almeida, E. S., A mixed-penalty finite element formulation for the finite deformation of a biphasic continuum with hyperelastic solid phase, *Symposium on Computational Mechanics of Porous Materials and their Thermal Decomposition*, Tempe, Arizona. ASME, **AMD 136**: 43-53, 1992.

98. Spilker, R. L., Almeida, E. S. and Donzelli, P. S., Finite element methods for the biomechanics of soft hydrated tissues: nonlinear analysis and adaptive control of meshes. In *High Performance Computing in Biomedical Research*, T. C. Pilkington, B. Loftis, J. F. Thompson, S. L.-Y. Woo, T. C. Palmer and T. F. Budinger Eds., pp. 227-261, CRC Press, Boca Raton, Florida, USA, 1993.

99. Spilker, R. L. and Maxian, T. A., A mixed-penalty finite element formulation of the linear biphasic theory for soft tissues, *Int. J. Num. Meth. Eng.*, **30**: 1063-1082, 1990.

100. Spilker, R. L. and Suh, J.-K., Formulation and evaluation of a finite element model for the biphasic model of hydrated soft tissues, *Comp. & Struct.*, **35**: 425-439, 1990.

101. Spilker, R. L., Suh, J.-K., Vermilyea, M. E. and Maxian, T. A., Alternate hybrid, mixed, and penalty finite element formulations for the biphasic model of soft hydrated tissues. In *Biomechanics of Diarthrodial Joints*, V. C. Mow, T. A. Ratcliffe and S. Y.-L. Woo Eds., Vol. I, pp. 401-435, Springer-Verlag, 1990.

102. Strang, G. and Fix, G. J., *An Analysis of the Finite Element Method*, Prentice-Hall, Englewood Cliffs, N.J., 1973.

103. Suh, J.-K., *A Finite Element Formulation for Nonlinear Behavior of Biphasic Hydrated Soft Tissue under Finite Deformation*, Thesis, Ph.D., Rensselaer Polytechnic Institute, 1989.

104. Suh, J.-K. and Spilker, R. L., Indentation analysis of biphasic articular cartilage: nonlinear phenomena under finite deformation, *J. Biomech. Eng.*, **116**: 1-9, 1993.

105. Suh, J.-K., Spilker, R. L. and Holmes, M. H., A penalty finite element analysis for nonlinear mechanics of biphasic hydrated soft tissue under large deformation, *Int. J. Num. Meth. Eng.*, **32**: 1411-1439, 1991.

106. Sussman, T. and Bathe, K.-J., A finite element formulation for nonlinear incompressible elastic and inelastic analysis, *Comp. & Struct.*, **26**: 357-409, 1987.

107. Truesdell, C., Sulle basi della thermomeccanica, *Rend. Accad. Lincei, Series 8*, pp. 33-38, 158-166, 1957.

108. Truesdell, C. and Noll, W., The non-linear field theories of mechanics. In *Handbuch der Physik*, S. Flugge Ed., Vol. III.3, Springer-Verlag, Berlin, 1965.

109. Truesdell, C. and Toupin, R. A., The classical field theories. In *Handbuch der Physik*, S. Flugge Ed., Vol. III.1, pp. 226-881, Springer-Verlag, Berlin, 1960.

110. Van Campen, D. H., Huyghe, J. M., Bovendeerd, P. H. M. and Arts, T., Biomechanics of heart muscle, *Eur. J. Mech. A/Sol.*, **13**: 19-41, 1994.

111. Vermeer, P. A. and Verruijt, A., An accuracy condition for consolidation by finite elements, *Int. J. Num. Anal. Meth. Geomech.*, **5**: 1-14, 1981.

112. Vermilyea, M. and Spilker, R. L., Hybrid and mixed-penalty finite elements for 3-D analysis of soft hydrated tissue, *Int. J. Num. Meth. Eng.*, **36**: 4223-4243, 1993.

113. Vermilyea, M. E. and Spilker, R. L., A hybrid finite element formulation of the linear biphasic equations for hydrated soft tissue, *Int. J. Num. Meth. Eng.*, **33**: 567-593, 1992.

114. Warden, W. H., Athesian, G. A., Grelsamer, R. P. and Mow, V. C., Biphasic finite deformation material properties of bovine articular cartilage. In *Transactions of the 40th Annual Meeting of the Orthopaedic Research Society*, A. L. Boskey Ed., Vol. 19 - Section 2, p. 413, Orthopaedic Research Society, New Orleans, LA, 1994.

115. Wayne, J. S., Woo, S. L.-Y. and Kwan, M. K., Application of the u-p finite element method to the study of articular cartilage, *J. Biomech. Eng.*, **113**: 397-403, 1991.

116. Weiss, J. A., *A Constitutive Model and Finite Element Representation for Transversely Isotropic Soft Tissues*, Thesis, Ph.D., University of Utah, 1994.

117. Woo, S. L.-Y., Mow, V. C. and Lai, M. W., Biomechanical Properties of Articular Cartilage. In *Handbook of Bioengineering*, R. Skalak and S. Chien Eds., pp. 4.1-4.44, McGraw-Hill, New York, 1987.

118. Yuan, Y. and Simon, B. R., Constraint relations for orthotropic porohyperelastic constitutive laws and finite element formulations for soft tissues. In *1992 Advances in Bioengineering*, M. W. Bidez Ed., Vol. BED-22, pp. 203-206, ASME, New York, 1992.

119. Zienkiewicz, O. C., Chang, C. T. and Hinton, E., Nonlinear seismic response and liquefaction, *Int. J. Num. Anal. Meth. Geomech.*, **2**: 381-404, 1978.

120. Zienkiewicz, O. C. and Shiomi, T., Dynamic behavior of saturated porous media - the generalized Biot formulation and its numerical solution, *Int. J. Num. Anal. Meth. Geomech.*, **8**: 71-96, 1984.

121. Zienkiewicz, O. C. and Taylor, R. L., *The Finite Element Method*, Vol. 1, 4th ed., McGraw-Hill, London, 1988.

122. Zienkiewicz, O. C. and Taylor, R. L., *The Finite Element Method*, Vol. 2, 4th ed., McGraw-Hill, Berkshire (UK), 1991.

123. Zienkiewicz, O. C. and Zhu, J. Z., The superconvergent patch recovery and *a posteriori* error estimates: I The recovery technique, *Int. J. Num. Meth. Eng.*, **33**: 1331-1364, 1992.

APPENDIX A

Derivatives of the Helmholtz Free Energy Function for Hyperelastic Transversely Isotropic Materials

This appendix contains the expressions of the first and second derivatives of the Helmholtz free energy function used to compute the elastic Cauchy stress tensor, Eq. (3-33), and the elasticity tensor, Eq. (3-34). Similar expressions have been independently developed by Weiss [116] for single-phase materials, adopting C^{s2} instead of C^{s-1} used here.

A.1 Invariants for Transverse Isotropy

Table A.1 lists the scalar invariants derived by Ericksen and Rivlin [30] for transversely isotropic materials in terms of the right Cauchy-Green deformation tensor $\boldsymbol{C}^s$, and the *structural tensor* in the reference configuration $\boldsymbol{M}_0 = \boldsymbol{m}_0 \otimes \boldsymbol{m}_0$, with $\boldsymbol{m}_0$ being the *vector of preferred direction* in the reference configuration. The right-hand-side of this table contains the derivatives of the invariants with respect to $\boldsymbol{C}^s$. The first three invariants, called principal invariants of $\boldsymbol{C}^s$, are the coefficients of the characteristic equation:

$$\det(\boldsymbol{C}^s - \lambda_j^2 \mathbf{1}) = (\lambda_j^2)^3 - I_1 (\lambda_j^2)^2 + I_2 (\lambda_j^2) - I_3 = 0, \tag{A-1}$$

where λ_j, j= 1,2,3, denotes the principal stretches. According to the Cayley-Hamilton theorem [40], every tensor must satisfy its own characteristic equation,

$$\boldsymbol{C}^{s3} - I_1 \boldsymbol{C}^{s2} + I_2 \boldsymbol{C}^s - I_3 \mathbf{1} = \mathbf{0}. \tag{A-2}$$

This equation allows us to obtain the following identity used to abbreviate the expressions of the derivatives:

$$\boldsymbol{C}^{s-1} = \frac{1}{I_3}\left(\boldsymbol{C}^{s2} - I_1 \boldsymbol{C}^s + I_2 \mathbf{1} \right). \tag{A-3}$$

Table A.1 Invariants and corresponding derivatives with respect to the right Cauchy-Green deformation tensor

Invariants	Derivatives with respect to C^s
$I_1 = \text{tr}\, C^s$	$\dfrac{\partial I_1}{\partial C^s} = \mathbf{1}$
$I_2 = \frac{1}{2}\left[(\text{tr}\, C^s)^2 - \text{tr}\, C^{s2} \right]$	$\dfrac{\partial I_1}{\partial C^s} = I_1 \mathbf{1} - C^s$
$I_3 = \det C^s$	$\dfrac{\partial I_3}{\partial C^s} = I_2 \mathbf{1} - I_1 C^s + C^{s2} = I_3 C^{s-1}$
$I_4 = M_0 : C^s$	$\dfrac{\partial I_4}{\partial C^s} = M_0$
$I_5 = M_0 : C^{s2}$	$\dfrac{\partial I_5}{\partial C^s} = M_0 C^s + C^s M_0$

A.2 First Derivative of the Helmholtz Free Energy Function

The derivatives of the invariants presented on Table A.1 are used to obtain the first derivative of the Helmholtz free energy function with respect to C^s:

$$\frac{\partial \hat{\psi}^s}{\partial C^s} = (\psi^s_{,1} + I_1 \psi^s_{,2})\,\mathbf{1} - \psi^s_{,2} C^s + I_3 \psi^s_{,3} C^{s-1} + \psi^s_{,4} M_0 + \psi^s_{,5} (M_0 C^s + C^s M_0)\,, \tag{A-4}$$

where $\psi^s_{,j}$ denotes the partial derivative with respect to the invariant I_j. In the case of isotropic materials, Eq. (A-4) reduces to a more familiar expression

$$\frac{\partial \hat{\psi}^s}{\partial C^s} = (\psi^s_{,1} + I_1 \psi^s_{,2})\,\mathbf{1} - \psi^s_{,2} C^s + I_3 \psi^s_{,3} C^{s-1}\,, \tag{A-5}$$

or making use of Eq. (A-3) to replace C^{s-1},

$$\frac{\partial \hat{\psi}^s}{\partial C^s} = (\psi^s_{,1} + I_1 \psi^s_{,2} + I_2 \psi^s_{,3})\,\mathbf{1} - (\psi^s_{,2} + I_1 \psi^s_{,3})\, C^s + \psi^s_{,3} C^{s2}\,. \tag{A-6}$$

A.3 Second Derivative of the Helmholtz Free Energy Function

The second derivative of the Helmholtz free energy function with respect to C^S is obtained from Eq. (A-4), and is given by

(A-7)

$$
\begin{aligned}
\frac{\partial}{\partial C^S}\left(\frac{\partial \hat{\psi}^S}{\partial C^S}\right) = {} & (\psi^S_{,2} + \psi^S_{,11} + 2I_1\psi^S_{,21} + I_1^2\psi^S_{,22})\,\mathbf{1}\otimes\mathbf{1} \\
& - (\psi^S_{,21} + I_1\psi^S_{,22})\,(\mathbf{1}\otimes C^S + C^S\otimes\mathbf{1}) \\
& + I_3(\psi^S_{,31} + I_1\psi^S_{,32})\left(\mathbf{1}\otimes C^{S-1} + C^{S-1}\otimes\mathbf{1}\right) \\
& + (\psi^S_{,41} + I_1\psi^S_{,42})\,(\mathbf{1}\otimes M_0 + M_0\otimes\mathbf{1}) \\
& + (\psi^S_{,51} + I_1\psi^S_{,52})\,[\mathbf{1}\otimes(M_0C^S + C^SM_0) + (M_0C^S + C^SM_0)\otimes\mathbf{1}] \\
& + \psi^S_{,22}C^S\otimes C^S \\
& - I_3\psi^S_{,32}\left(C^S\otimes C^{S-1} + C^{S-1}\otimes C^S\right) \\
& - \psi^S_{,42}(C^S\otimes M_0 + M_0\otimes C^S) \\
& - \psi^S_{,52}[C^S\otimes(M_0C^S + C^SM_0) + (M_0C^S + C^SM_0)\otimes C^S] \\
& + I_3(\psi^S_{,3} + I_3\psi^S_{,33})\left(C^{S-1}\otimes C^{S-1}\right) \\
& + I_3\psi^S_{,43}\left(C^{S-1}\otimes M_0 + M_0\otimes C^{S-1}\right) \\
& + I_3\psi^S_{,53}\left[C^{S-1}\otimes(M_0C^S + C^SM_0) + (M_0C^S + C^SM_0)\otimes C^{S-1}\right] \\
& + \psi^S_{,44}M_0\otimes M_0 \\
& + \psi^S_{,54}[M_0\otimes(M_0C^S + C^SM_0) + (M_0C^S + C^SM_0)\otimes M_0] \\
& + \psi^S_{,55}(M_0C^S + C^SM_0)\otimes(M_0C^S + C^SM_0) \\
& - \psi^S_{,2}I \\
& + I_3\psi^S_{,3}I_{C^{-1}} \\
& + \psi^S_{,5}(M_0I + IM_0)\,,
\end{aligned}
$$

where $\psi^{s}_{,ij}$, $i, j = 1, \ldots, 5$ denotes the second derivatives with respect to the invariants I_i, I_j, $[I]_{IJAB} = \frac{1}{2}(\delta_{IA}\delta_{JB} + \delta_{IB}\delta_{JA})$, and $[I_{C^{-1}}]_{IJAB} = -\frac{1}{2}\left(C^{s-1}_{IA}C^{s-1}_{JB} + C^{s-1}_{IB}C^{s-1}_{JA}\right)$.

APPENDIX B

Gradient and Divergence Forms in the Weight Residual Statement

This appendix provides the intermediate matrices associated with the gradient and divergence of the interpolation functions. Special attention is dedicated to the gradient of the solid volume fraction, which arises in the nonlinear penalty formulations when fluid and solid velocities are chosen as field variables. After a brief review of the notation and conventions, specialized expressions, valid for isoparametric elements of any polynomial order, are presented for two-dimensional (2-D) and three-dimensional (3-D) problems in Cartesian coordinates, as well as for torsionless axisymmetric problems in polar cylindrical coordinates.

B.1 Notation and Conventions

The comma convention, where a comma followed by indices stands for differentiation in space, is used throughout the appendix. The indices determine the coordinate component, the coordinate system and, in some cases, the configuration with which they are associated. For instance, upper case indices (*K, L, M*), lower case indices (*i, j*), and greek indices (μ, η, ζ) — varying from one to the number of spatial dimensions, n_{sd} — indicate material (X_K), spatial (x_i) and parent coordinates (ξ_μ), respectively. To improve clarity, the superscript identifying the phase is dropped from the coordinates. The usefulness of the comma convention is apparent in Eq. (B-1) and Fig. B.1, where components of the deformation gradient and the transformation matrices from reference to current, parent to current, and parent to reference coordinates are expressed in Cartesian coordinates,

$$F^s_{iK} = x_{i,K} = \frac{\partial x_i}{\partial X_K}, \qquad x_{i,\mu} = \frac{\partial x_i}{\partial \xi_\mu}, \qquad X_{K,\mu} = \frac{\partial X_K}{\partial \xi_\mu}. \tag{B-1}$$

For polar cylindrical coordinates, indices are replaced with the coordinates themselves. We use lower case letters (*r*, θ and *z*) for the radius, the angle and the elevation of a point in the current

configuration, while upper case letters (R, Θ and Z) are the corresponding coordinates in the reference configuration.

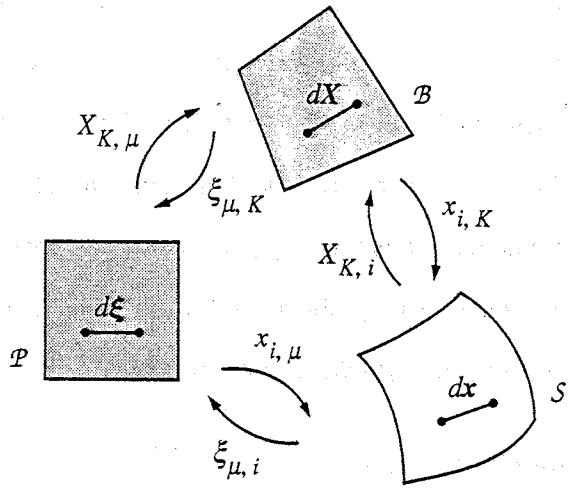

Figure B.1 Element in the parent coordinate system ($\mathcal{P}$, also called *natural* or *parametric* system), and in the reference ($\mathcal{B}$) and current ($\mathcal{S}$) configurations.

The summation convention is used throughout the appendix, with indices varying from one to n_{sd}. In what follows, v denotes a vector-valued function defined in a finite-dimensional subspace $\mathcal{V}_h$, while q denotes a scalar-valued function defined in a finite-dimensional subspace $\mathbb{R}_h$. Within each finite element, these functions are interpolated in terms of nodal values as

$$v = N^a v^a, \qquad q = N^a q^a, \tag{B-2}$$

where the superscript a specifies element node numbers, and its repetition implies summation from one to the number of nodes per element, n_{npe}. For the pressure fields, the index a refers to pressure nodes or coefficients, the repetition implying summation over their number per element, n_{pn} or n_{pc}. The same scalar functions N^a are used to interpolate each component of v, as implied by Eq. $(B\text{-}2)_1$. The finite elements are isoparametric with respect to the kinematic variables, with functions N^a being also used to interpolate the coordinates of a point within the element ($X = N^a X^a$ and $x = N^a x^a$).

In most of this appendix the terms *axisymmetry* and *axisymmetric* refer to a torsionless axisymmetric model in cylindrical coordinates. For this particular case, the expressions are obtained directly from the tensor forms of the finite element matrices, avoiding the distinction between covariant and contravariant coordinates and bases. The final expressions are written using the physical components, with no summation being implied by the repetition of the subscripts r, θ, and z, or R, Θ, and Z in a monomial. In contrast, the summation convention is always used for Cartesian coordinates, with the distinction between 2-D and 3-D expressions being made when necessary.

B.2 Condensed Representation of Tensors

The arrangement of the elements in matrix $\boldsymbol{B}_{\mathrm{L}}$, one of the intermediate matrices developed in this appendix, depends on the way the second Piola-Kirchhoff stress and Lagrangian strain tensors are represented in the FE implementation. It is typical to condense these symmetric tensors, together with the fourth-order elasticity tensor, in order to reduce the number of algebraic operations. This process affects the matrices in the next sections and requires a formal correspondence between tensor components and array elements that will be established below. The components of the second Piola-Kirchhoff stress tensor are packed in vectors of 6 and 4 components for 3-D and axisymmetric problems, respectively. An under-tilde is used to distinguish the condensed representation from the tensor symbol,

$$\boldsymbol{S} = \begin{bmatrix} S_{11} & S_{12} & S_{13} \\ S_{21} & S_{22} & S_{23} \\ S_{31} & S_{32} & S_{33} \end{bmatrix}, \qquad \underset{\sim}{S} = \begin{Bmatrix} S_{11} \\ S_{22} \\ S_{33} \\ S_{12} \\ S_{13} \\ S_{23} \end{Bmatrix}, \qquad \underset{\sim}{S} = \begin{Bmatrix} S_{RR} \\ S_{\Theta\Theta} \\ S_{ZZ} \\ S_{RZ} \end{Bmatrix}. \tag{B-3}$$

The same representation could have been adopted for the Lagrangian strain tensor $\boldsymbol{E}$. However, it is advantageous to define the condensed vector $\underset{\sim}{E}$ so that the vector product $\underset{\sim}{E}^{\mathrm{T}}\underset{\sim}{S}$

gives the same result of the double contraction $\boldsymbol{E} : \boldsymbol{S}$. This yields the following representations for the strain tensor:

$$\boldsymbol{E} = \begin{bmatrix} E_{11} & E_{12} & E_{13} \\ E_{21} & E_{22} & E_{23} \\ E_{31} & E_{32} & E_{33} \end{bmatrix}, \qquad \underline{E} = \begin{Bmatrix} E_{11} \\ E_{22} \\ E_{33} \\ 2E_{12} \\ 2E_{13} \\ 2E_{23} \end{Bmatrix}, \qquad \underline{E} = \begin{Bmatrix} E_{RR} \\ E_{\Theta\Theta} \\ E_{ZZ} \\ 2E_{RZ} \end{Bmatrix}. \tag{B-4}$$

Major and minor symmetries of the elasticity tensor are considered to convert this fourth-order tensor into a square matrix. For *linear materials under infinitesimal deformation*, this means rewriting the tensor relationship $S_{\mathrm{E}}^{\mathrm{s}} = \mathbf{C} : E^{\mathrm{s}}$ into the equivalent form $\underline{S}_{\mathrm{E}}^{\mathrm{s}} = \underline{\mathbf{C}}\,\underline{E}^{\mathrm{s}}$. For *hyper-elastic materials*, the constitutive law is expressed in terms of admissible increments of the second Piola-Kirchhoff stress and the Lagrangian strain tensors, $\delta S_{\mathrm{E}}^{\mathrm{s}} = 1/2\ \mathbf{C} : \delta C^{\mathrm{s}} = \mathbf{C} : \delta E^{\mathrm{s}}$ (see Eqs. (3-34) and (4-101)), yielding the relationships

for 3-D:

$$\begin{Bmatrix} \delta S_{11} \\ \delta S_{22} \\ \delta S_{33} \\ \delta S_{12} \\ \delta S_{13} \\ \delta S_{23} \end{Bmatrix} = \begin{bmatrix} C_{1111} & C_{1122} & C_{1133} & C_{1112} & C_{1113} & C_{1123} \\ & C_{2222} & C_{2233} & C_{2212} & C_{2213} & C_{2223} \\ & & C_{3333} & C_{3312} & C_{3313} & C_{3323} \\ & & & C_{1212} & C_{1213} & C_{1223} \\ & \text{Sym.} & & & C_{1313} & C_{1323} \\ & & & & & C_{2323} \end{bmatrix} \begin{Bmatrix} \delta E_{11} \\ \delta E_{22} \\ \delta E_{33} \\ 2\delta E_{12} \\ 2\delta E_{13} \\ 2\delta E_{23} \end{Bmatrix}; \tag{B-5}$$

and for axisymmetry:

$$\begin{Bmatrix} \delta S_{RR} \\ \delta S_{\Theta\Theta} \\ \delta S_{ZZ} \\ \delta S_{RZ} \end{Bmatrix} = \begin{bmatrix} C_{RRRR} & C_{RR\Theta\Theta} & C_{RRZZ} & C_{RRRZ} \\ & C_{\Theta\Theta\Theta\Theta} & C_{\Theta\Theta ZZ} & C_{\Theta\Theta RZ} \\ & \text{Sym.} & C_{ZZZZ} & C_{ZZRZ} \\ & & & C_{RZRZ} \end{bmatrix} \begin{Bmatrix} \delta E_{RR} \\ \delta E_{\Theta\Theta} \\ \delta E_{ZZ} \\ 2\delta E_{RZ} \end{Bmatrix}; \tag{B-6}$$

where C_{KLMN} are components of the elasticity tensor, with $K, L, M, N = 1,...,n_{sd}$ (see also Appendix D).

B.3 Gradient of a Scalar Field

The gradient of a scalar field is obtained by introducing the interpolation function and collecting nodal values, that is

$$\nabla q = \frac{\partial q}{\partial x} = q^a \frac{\partial N^a}{\partial x} . \tag{B-7}$$

In Cartesian coordinates, making use of the chain rule of differentiation, we obtain

$$\frac{\partial q}{\partial x_j} = q^a \frac{\partial N^a}{\partial x_j} = q^a \frac{\partial N^a}{\partial \xi_\mu} \frac{\partial \xi_\mu}{\partial x_j}, \tag{B-8}$$

or using the comma convention,

$$q_{,j} = q^a N^a_{,j} = q^a N^a_{,\mu} \xi_{\mu,j} , \tag{B-9}$$

where $\xi_{\mu,j} = x_{j,\mu}^{-1} = \left(x_j^b N^b_{,\mu} \right)^{-1}$ is obtained by numerical inversion, a procedure valid for elements based on any polynomial interpolation.

For axisymmetry, the gradient is given by

$$\nabla q = \begin{Bmatrix} q_{,r} \\ 0 \\ q_{,z} \end{Bmatrix} = \begin{Bmatrix} q^a N^a_{,r} \\ 0 \\ q^a N^a_{,z} \end{Bmatrix} , \tag{B-10}$$

where $N^a_{,j} = N^a_{,\mu} \xi_{\mu,j}$ with $j = r, z;\ \mu = 1, 2$.

B.4 Gradient of a Vector Field

The gradient of a vector is given by

$$\nabla v = \frac{\partial v}{\partial x} = \frac{\partial}{\partial x} (N^a v^a) . \tag{B-11}$$

In Cartesian coordinates the final expression is similar to Eq. (B-9),

$$v_{i,j} = v_i^a N_{,j}^a = v_i^a N_{,\mu}^a \xi_{\mu,j}. \tag{B-12}$$

The gradient for axisymmetry uses the operator $\nabla = \boldsymbol{e}_r \frac{\partial}{\partial r} + \boldsymbol{e}_\theta \frac{1}{r}\frac{\partial}{\partial \theta} + \boldsymbol{e}_z \frac{\partial}{\partial z}$ for cylindrical coordinates, with $\boldsymbol{e}_r$, $\boldsymbol{e}_\theta$, and $\boldsymbol{e}_z$ constituting an orthogonal basis, and is given by

$$[\nabla \boldsymbol{v}] = \begin{bmatrix} v_{r,r} & \bullet & v_{r,z} \\ \bullet & \dfrac{v_r}{r} & \bullet \\ v_{z,r} & \bullet & v_{z,z} \end{bmatrix} = \begin{bmatrix} v_r^a N_{,r}^a & \bullet & v_r^a N_{,z}^a \\ \bullet & \dfrac{N^a v_r^a}{N^b r^b} & \bullet \\ v_z^a N_{,r}^a & \bullet & v_z^a N_{,z}^a \end{bmatrix}, \tag{B-13}$$

where the dot stands for null elements, and v_r^a and v_z^a are physical components of the nodal velocity.

B.5 The Divergence of a Vector Field

For Cartesian coordinates, the divergence can be obtained from Eq. (B-12), yielding

$$\nabla \cdot \boldsymbol{v} = \operatorname{tr}(\nabla \boldsymbol{v}) = v_{i,i} = v_i^a N_{,i}^a, \tag{B-14}$$

and, for axisymmetry, from Eq. (B-13),

$$\nabla \cdot \boldsymbol{v} = v_r^a \left(N_{,r}^a + \frac{N^a}{r} \right) + v_z^a N_{,z}^a. \tag{B-15}$$

An intermediate vector $\boldsymbol{h}$ is defined in the $\boldsymbol{v}$-p formulation in order to factor out the nodal velocities from the divergence, $\boldsymbol{h}^{\mathrm{T}} \boldsymbol{v}^{\mathrm{s}} := \nabla \cdot (N^a \boldsymbol{v}^{\mathrm{s}\,a})$ as given by Eq. (4-76). This vector is immediately assembled from Eqs. (B-14) and (B-15), and has the following nonzero components in the axisymmetric case:

$$h_r^a = N_{,r}^a + \frac{N^a}{N^b r^b}, \qquad h_z^a = N_{,z}^a. \tag{B-16}$$

B.6 The Deformation Gradient F^S

In Cartesian coordinates, the expression of the deformation gradient is analogous to Eq. (B-12), except that the derivatives are taken with respect to the reference configuration

$$F^S_{iK} = x_{i,K} = x_i^a N^a_{,K} = x_i^a N^a_{,\mu} \xi_{\mu,K}, \tag{B-17}$$

where $\xi_{\mu,K} = X_{K,\mu}^{-1} = \left(X_K^b N^b_{,\mu} \right)^{-1}$ is obtained numerically. In the axisymmetric case, the matrix of the deformation gradient is given by

$$\boldsymbol{F}^S = \nabla_X \boldsymbol{x} = \begin{bmatrix} r_{,R} & \cdot & r_{,Z} \\ \cdot & \dfrac{r}{R} & \cdot \\ z_{,R} & \cdot & z_{,Z} \end{bmatrix} = \begin{bmatrix} r^a N^a_{,R} & \cdot & r^a N^a_{,Z} \\ \cdot & \dfrac{N^a r^a}{N^b R^b} & \cdot \\ z^a N^a_{,R} & \cdot & z^a N^a_{,Z} \end{bmatrix}, \tag{B-18}$$

where $N^a_{,K} = N^a_{,\mu} \xi_{\mu,K}$, with $K = R, Z; \ \mu = 1, 2$.

B.7 The Matrices $\boldsymbol{B}_L$ and $\boldsymbol{B}$

The intermediate matrix $\boldsymbol{B}_L$ arises in nonlinear elasticity and should be understood as part of the effort to replace a tensor double contraction with a matrix product (Eq. (4-105)). This aspect is hidden in the following definition

$$\boldsymbol{B}_L \, \delta \boldsymbol{u}^S := \left[\boldsymbol{F}^{S^T} \nabla_X (\delta \boldsymbol{u}^S) \right]^{sym}, \tag{B-19}$$

where $\boldsymbol{B}_L = \left[[\boldsymbol{B}_L]^1, [\boldsymbol{B}_L]^2, \ldots, [\boldsymbol{B}_L]^{n_{npe}} \right]$, with $[\boldsymbol{B}_L]^a$ being the sub-matrix associated with node a. Since the symmetric tensors with which $[\boldsymbol{B}_L]^a$ is multiplied in the large deformation stiffness matrix and in the elasticity vector are condensed in matrix form, we must rearrange its components in a similar way, that is in columns of condensed vectors. Following the same strategy used to condense the Lagrangian strain tensor $\boldsymbol{E}$ in Section B.2, each column of the sub-matrix is built according to the formats

$$\{\boldsymbol{B}_{\mathrm{L}}\}_i^a = \left[B_{11},\ B_{22},\ B_{33},\ (B_{12}+B_{21}),\ (B_{13}+B_{31}),\ (B_{23}+B_{32})\right]^T \quad \text{for 3-D, and}$$
$$\{\boldsymbol{B}_{\mathrm{L}}\}_i^a = \left[B_{11},\ B_{22},\ (B_{12}+B_{21})\right]^T \qquad \text{for 2-D.} \tag{B-20}$$

After factoring out the nodal components $\delta \boldsymbol{u}^s$ in Eq. (B-19), we obtain for 3-D and 2-D

$$\{\boldsymbol{B}_{\mathrm{L}}\}_i^a = \begin{bmatrix} F^s_{i1}N^a_{,1} \\ F^s_{i2}N^a_{,2} \\ F^s_{i3}N^a_{,3} \\ F^s_{i1}N^a_{,2}+F^s_{i2}N^a_{,1} \\ F^s_{i1}N^a_{,3}+F^s_{i3}N^a_{,1} \\ F^s_{i2}N^a_{,3}+F^s_{i3}N^a_{,2} \end{bmatrix}, \qquad \{\boldsymbol{B}_{\mathrm{L}}\}_i^a = \begin{bmatrix} F^s_{i1}N^a_{,1} \\ F^s_{i2}N^a_{,2} \\ F^s_{i1}N^a_{,2}+F^s_{i2}N^a_{,1} \end{bmatrix}, \tag{B-21}$$

where the partial derivatives of N^a refer to the reference configuration. For axisymmetry, the columns are arranged in the format $\{\boldsymbol{B}_{\mathrm{L}}\}_i^a = \left[B_{RR},\ B_{\Theta\Theta},\ B_{ZZ},\ (B_{RZ}+B_{ZR})\right]^T$, yielding

$$\{\boldsymbol{B}_{\mathrm{L}}\}_r^a = \begin{bmatrix} F^s_{rR}N^a_{,R} \\ F^s_{\theta\Theta}\dfrac{N^a}{R} \\ F^s_{rZ}N^a_{,Z} \\ F^s_{rR}N^a_{,Z}+F^s_{rZ}N^a_{,R} \end{bmatrix}, \qquad \{\boldsymbol{B}_{\mathrm{L}}\}_z^a = \begin{bmatrix} F^s_{zR}N^a_{,R} \\ \bullet \\ F^s_{zZ}N^a_{,Z} \\ F^s_{zR}N^a_{,Z}+F^s_{zZ}N^a_{,R} \end{bmatrix}. \tag{B-22}$$

Eqs. (B-21) and (B-22) are much shorter than the expressions presented by Bathe in terms of nodal displacements [7].

In the linear theory the assumption of infinitesimal deformation is equivalent to $\boldsymbol{F}^s \approx \mathbf{1}$, and matrix $\boldsymbol{B}_{\mathrm{L}}$ simplifies to the familiar matrix $\boldsymbol{B}$ used with linear finite elements. For 3-D and 2-D Cartesian coordinates, respectively, results

$$[\boldsymbol{B}]^a = \begin{bmatrix} N^a_{,1} & \bullet & \bullet \\ \bullet & N^a_{,2} & \bullet \\ \bullet & \bullet & N^a_{,3} \\ N^a_{,2} & N^a_{,1} & \bullet \\ N^a_{,3} & \bullet & N^a_{,1} \\ \bullet & N^a_{,3} & N^a_{,2} \end{bmatrix}, \qquad [\boldsymbol{B}]^a = \begin{bmatrix} N^a_{,1} & \bullet \\ \bullet & N^a_{,2} \\ N^a_{,2} & N^a_{,1} \end{bmatrix}, \tag{B-23}$$

where partial derivatives are computed with respect to the reference configuration. In the axisymmetric case, we have

$$[\boldsymbol{B}]^a = \begin{bmatrix} N^a_{,R} & \bullet \\ \dfrac{N^a}{N^b R^b} & \bullet \\ \bullet & N^a_{,Z} \\ N^a_{,Z} & N^a_{,R} \end{bmatrix}, \tag{B-24}$$

where the columns refer to the degrees of freedom r and z, respectively.

B.8 Gradient of the Solid Volume Fraction

The penalty and mixed-penalty formulations require the gradient of the solid volume fraction, which depends upon the Jacobian determinant J^s. That gradient arises from the following divergence terms in the weighted residual statements (Eq. (4-31)):

$$\begin{aligned} \nabla \cdot (\phi^{\mathrm{s}} \boldsymbol{v}^{\mathrm{s}}) &= \phi^{\mathrm{s}} \nabla \cdot \boldsymbol{v}^{\mathrm{s}} + \boldsymbol{v}^{\mathrm{s}} \cdot \nabla \phi^{\mathrm{s}} = \phi^{\mathrm{s}} \nabla \cdot \boldsymbol{v}^{\mathrm{s}} + \boldsymbol{v}^{\mathrm{s}} \cdot \left(\nabla_{\boldsymbol{X}} \phi^{\mathrm{s}} \boldsymbol{F}^{\mathrm{s}-1} \right), \\ \nabla \cdot (\phi^{\mathrm{f}} \boldsymbol{v}^{\mathrm{f}}) &= \phi^{\mathrm{f}} \nabla \cdot \boldsymbol{v}^{\mathrm{f}} + \boldsymbol{v}^{\mathrm{f}} \cdot \nabla \phi^{\mathrm{f}} = \phi^{\mathrm{f}} \nabla \cdot \boldsymbol{v}^{\mathrm{f}} - \boldsymbol{v}^{\mathrm{f}} \cdot \left(\nabla_{\boldsymbol{X}} \phi^{\mathrm{s}} \boldsymbol{F}^{\mathrm{s}-1} \right), \end{aligned} \tag{B-25}$$

where the fact that the biphasic mixture is saturated is considered in the last equation. The above divergences are used to define the following intermediate vector $\boldsymbol{h}^{\alpha}$ in Chapter 4:

$$h^{\alpha T} v^{\alpha} := \nabla \cdot (\phi^{\alpha} v^{\alpha}), \tag{B-26}$$

with no summation implied by the superscript α. Using the relationship $\phi^s = J^{s-1} \phi_0^s$, the gradient of the volume fraction can be written as

$$\nabla_X \phi^s = -\frac{\phi_0^s}{J^{s2}} \nabla_X J^s = -\frac{\phi_0^s}{J^s} F^{s-T} : \nabla_X F^s, \tag{B-27}$$

and the problem is now reduced to the computation of $\nabla_X F^s$. We will return to Eqs. (B-25) and (B-27) later when dealing with axisymmetry.

B.8.1 Cartesian Coordinates

For Cartesian coordinates, it is convenient to proceed with index notation and rewrite $\nabla_X F^s$ as

$$(F^s_{iK})_{,L} = [x_{i,\mu}\, \xi_{\mu,K}]_{,L} = x_{i,\mu\eta}\, \xi_{\mu,K}\, \xi_{\eta,L} + x_{i,\mu}\, \xi_{\mu,KL}, \tag{B-28}$$

where $x_{i,\mu\eta} = x_i^a N^a_{,\mu\eta}$ and the expression for $\xi_{\mu,KL}$ can be shortened by using the definition of the cofactor matrix

$$\begin{aligned} \xi_{\mu,KL} &= (X_{K,\mu}^{-1})_{,L} \\ &= \left[\frac{1}{J} \mathrm{Cof}(X_{K,\mu})\right]_{,L} \\ &= -\frac{J_{,L}}{J} X_{K,\mu}^{-1} + \frac{1}{J} [\mathrm{Cof}(X_{K,\mu})]_{,\eta}\, \xi_{\eta,L} \\ &= -\frac{J_{,L}}{J} \xi_{\mu,K} + \frac{1}{J} [\mathrm{Cof}(X_{K,\mu})]_{,\eta}\, \xi_{\eta,L}. \end{aligned} \tag{B-29}$$

where J is the Jacobian of the isoparametric map from parent to material coordinates, $J = \det(F) = \det(X_{K,\mu})$, and its gradient with respect to material coordinates is given by

$$\nabla_X J = J\, F^{-T} : \nabla_X F, \tag{B-30}$$

or, in index notation,

$$J_{,L} = J\,\xi_{\eta,M}\,X_{M,\eta\zeta}\xi_{\zeta,L}\,. \tag{B-31}$$

The gradient of the Cofactor matrix is introduced next. Denoting K_1, K_2 (, K_3) and μ_1, μ_2 (, μ_3) the circular permutations of the indices K and μ, varying from 1 to n_{sd}, it follows

for 3-D:

$$[\mathrm{Cof}(X_{K_1,\mu_1})]_{,\eta} = X_{K_2,\mu_2\eta}X_{K_3,\mu_3} + X_{K_2,\mu_2}X_{K_3,\mu_3\eta} - (X_{K_2,\mu_3\eta}X_{K_3,\mu_2} + X_{K_2,\mu_3}X_{K_3,\mu_2\eta}), \tag{B-32}$$

from: $\mathrm{Cof}(X_{K_1,\mu_1}) = X_{K_2,\mu_2}X_{K_3,\mu_3} - X_{K_2,\mu_3}X_{K_3,\mu_2}$;

and, for 2-D:

$$[\mathrm{Cof}(X_{K_1,\mu_1})]_{,\eta} = (-1)^{K_1+\mu_1}X_{K_2,\mu_2\eta}, \tag{B-33}$$

from: $\mathrm{Cof}(X_{K_1,\mu_1}) = (-1)^{K_1+\mu_1}X_{K_2,\mu_2}$.

The above equations can now be used to write the expression of the vectors $\boldsymbol{h}^{\mathrm{s}}$ and $\boldsymbol{h}^{\mathrm{f}}$. Introducing Eq. (B-28) into Eq. (B-27), and that result into Eq. (B-25)$_1$ yields

$$(\phi^{\mathrm{s}}v_j^{\mathrm{s}})_{,j} = \frac{\phi_0^{\mathrm{s}}}{J^{\mathrm{s}}}[v_{j,j}^{\mathrm{s}} - v_j^{\mathrm{s}}(x_{i,\mu\eta}\,\xi_{\mu,K}\,\xi_{\eta,L} + x_{i,\mu}\,\xi_{\mu,KL})\,X_{K,i}X_{L,j}]\,, \tag{B-34}$$

where

$$\xi_{\mu,KL} = -\,X_{M,\eta\zeta}\,\xi_{\zeta,L}\,\xi_{\eta,M}\,\xi_{\mu,K} + \frac{1}{J}[\mathrm{Cof}(X_{K,\mu})]_{,\eta}\,\xi_{\eta,L}, \tag{B-35}$$

Finally, making use of Eqs. (B-25), (B-26), and (B-34), we obtain the generic components of $\boldsymbol{h}^{\mathrm{s}}$ and $\boldsymbol{h}^{\mathrm{f}}$:

$$\begin{aligned}\{h^{\mathrm{s}}\}_j^a &= \frac{\phi_0^{\mathrm{s}}}{J^{\mathrm{s}}}[N_{,j}^a - N^a(x_{i,\mu\eta}\,\xi_{\mu,K}\,\xi_{\eta,L} + x_{i,\mu}\,\xi_{\mu,KL})\,X_{K,i}X_{L,j}]\,,\\ \{h^{\mathrm{f}}\}_j^a &= N_{,j}^a - \{h^{\mathrm{s}}\}_j^a.\end{aligned} \tag{B-36}$$

B.8.2 Axisymmetric Case

For axisymmetry, the derivation must resume with the expression of the gradient $\nabla_X \boldsymbol{F}^s$. Using the operator $\nabla = \boldsymbol{e}_r \frac{\partial}{\partial r} + \boldsymbol{e}_\theta \frac{1}{r}\frac{\partial}{\partial \theta} + \boldsymbol{e}_z \frac{\partial}{\partial z}$ for cylindrical coordinates, we obtain the following expression for this third-order tensor:

$$\nabla_X \boldsymbol{F}^s = \begin{bmatrix} r_{,RR} & \bullet & r_{,ZR} \\ \bullet & \left(\frac{r}{R}\right)_{,R} & \bullet \\ z_{,RR} & \bullet & z_{,ZR} \end{bmatrix} + \begin{bmatrix} \bullet & \left(\frac{r}{R}\right)_{,R} & \bullet \\ \left(\frac{r}{R}\right)_{,R} & \bullet & \frac{r_{,Z}}{R} \\ \bullet & \frac{z_{,R}}{R} & \bullet \end{bmatrix} + \begin{bmatrix} r_{,RZ} & \bullet & r_{,ZZ} \\ \bullet & \frac{r_{,Z}}{R} & \bullet \\ z_{,RZ} & \bullet & z_{,ZZ} \end{bmatrix} \qquad \text{(B-37)}$$

$$\boldsymbol{e}_i \otimes \boldsymbol{e}_K \otimes \boldsymbol{e}_R \qquad \boldsymbol{e}_i \otimes \boldsymbol{e}_K \otimes \boldsymbol{e}_\Theta \qquad \boldsymbol{e}_i \otimes \boldsymbol{e}_K \otimes \boldsymbol{e}_Z,$$

where the indices $i = r, \theta, z$ and $K = R, \Theta, Z$ are determined by the numbers of the row and column in the above matrices. The components of the gradient $\nabla_X J^s = J^s \boldsymbol{F}^{s-T} : \nabla_X \boldsymbol{F}^s$ are given by

$$\begin{aligned} J^s_{,R} &= J^s\left[r_{,RR}R_{,r} + r_{,ZR}Z_{,r} + z_{,RR}R_{,z} + z_{,ZR}Z_{,z} + \frac{R}{r}\left(\frac{r}{R}\right)_{,R}\right], \\ J^s_{,\Theta} &= 0, \\ J^s_{,Z} &= J^s\left[r_{,RZ}R_{,r} + r_{,ZZ}Z_{,r} + z_{,RZ}R_{,z} + z_{,ZZ}Z_{,z} + \frac{r_{,Z}}{r}\right], \end{aligned} \qquad \text{(B-38)}$$

where $r_{,KL} = r_{,\mu\eta}\,\xi_{\mu,K}\,\xi_{\eta,L} + r_{,\mu}\,\xi_{\mu,KL}$ and $z_{,KL} = z_{,\mu\eta}\,\xi_{\mu,K}\,\xi_{\eta,L} + z_{,\mu}\,\xi_{\mu,KL}$ with $K, L = R, Z$ and $\mu, \eta = 1, 2$.

Finally the components of $\boldsymbol{h}^s$ and $\boldsymbol{h}^f$ are obtained by introducing Eq. (B-38) into Eq. (B-27), and that result into Eq. (B-25), yielding:

$$\begin{aligned} \{h^s\}^a_r &= \frac{\phi^s_0}{J^s}\left[N^a_{,r} + N^a\left(\frac{1}{r} - \frac{1}{J^s}\left(J^s_{,R}R_{,r} - J^s_{,Z}Z_{,r}\right)\right)\right], \\ \{h^s\}^a_z &= \frac{\phi^s_0}{J^s}\left[N^a_{,z} - \frac{N^a}{J^s}\left(J^s_{,R}R_{,z} + J^s_{,Z}Z_{,z}\right)\right], \end{aligned} \qquad \text{(B-39)}$$

and

$$\{h^{\mathrm{f}}\}_r^a = N_{,r}^a + \frac{N^a}{r} - \{h^{\mathrm{s}}\}_r^a,$$
$$\{h^{\mathrm{f}}\}_z^a = N_{,z}^a - \{h^{\mathrm{s}}\}_z^a. \tag{B-40}$$

APPENDIX C

Finite Element Matrices

This appendix examines FE techniques that take advantage of the similarity between operations with solid- and fluid-phase degrees of freedom in the penalty formulations. The FE matrices implemented for 3-D and axisymmetric problems were obtained following simple guidelines. First, the original expressions in index notation were manipulated to identify zeros and redundant terms. As a result, costly numerical computations were avoided by matrix partitioning and rearrangement of element DOFs. Second, tensor symmetry was explored to pack components in condensed matrices, as seen in Appendix B. And finally some matrices were decomposed into products of intermediate matrices that were created to minimize the number of operations.

This appendix uses the simplified index notation for Cartesian coordinate systems, with lower indices referring to coordinate components and upper ones referring to node numbers. Table C.1 summarizes the indices whose repetition implies summation in their range of variation (see also Section B.1).

Table C.1 Indices and ranges

Index	Refer to	Range
a, b	Kinematic node	$1,...,n_{npe}$
c, d	Pressure coefficient (MP)	$1,...,n_{pc}$
c, d	Pressure node (v-p)	$1,...,n_{pn}$
i, j	Direction (current configuration)	$1,...,n_{sd}$
K, L	Direction (reference configuration)	$1,...,n_{sd}$

C.1 Order of the Degrees of Freedom in Matrices and Vectors

To take advantage of the presence of null sub-matrices, displacement and velocity vectors are partitioned into sub-vectors containing solid- and fluid-phase degrees of freedom. In each sub-

vector, as illustrated below for velocities, DOFs are first grouped according to their directions and then, within a group, ordered by node number:

$$v^{\mathrm{e}} = \left\{ \begin{array}{c} v^{\mathrm{se}} \\ v^{\mathrm{fe}} \end{array} \right\}, \qquad v^{\alpha \mathrm{e}} = \left\{ \begin{array}{c} v_1^{\alpha} \\ \vdots \\ v_{n_{sd}}^{\alpha} \end{array} \right\}, \qquad v_i^{\alpha} = \left\{ \begin{array}{c} v_i^{\alpha 1} \\ \vdots \\ v_i^{\alpha\, n_{npe}} \end{array} \right\}, \tag{C-1}$$

$$\alpha = \mathrm{s,f}; \qquad i = 1, \ldots, n_{sd}.$$

The order described represents a rearrangement of the usual 'node-then-degree-of-freedom' order and leads to significant savings when the permeability tensor is isotropic. The same arrangement is used for the solid-phase DOFs in the *v-p* formulation, with nodal pressures replacing nodal fluid velocities, even though the benefit in this case is smaller.

C.2 Nonlinear Elasticity Vector

The elements of the nonlinear elasticity vector are obtained using Eq. (4-105):

$$\{g^{\mathrm{se}}\}_i^a = \int_{\Omega_0^e} \{\boldsymbol{B}_{\mathrm{L}}^{\mathrm{T}}\}_i^a \, \underset{\sim}{S}_{\mathrm{E}}^s \, d\Omega_0 \quad , \tag{C-2}$$

where $\{\boldsymbol{B}_{\mathrm{L}}\}_i^a$ are the columns of matrix $\boldsymbol{B}_{\mathrm{L}}$, which is specialized in Appendix B. The arrangement of these columns must be consistent with the order of the solid velocity DOFs, yielding the following partitioning:

$$\boldsymbol{B}_{\mathrm{L}} = \left[\boldsymbol{B}_{\mathrm{L}_1} \cdots \boldsymbol{B}_{\mathrm{L}_{n_{sd}}} \right], \qquad \text{where } \boldsymbol{B}_{\mathrm{L}_i} = \left[\{\boldsymbol{B}_{\mathrm{L}}\}_i^1 \cdots \{\boldsymbol{B}_{\mathrm{L}}\}_i^{n_{npe}} \right]. \tag{C-3}$$

C.3 Tangent Stiffness Matrix

In Section 4.7 the tangent stiffness matrix is presented as a sum of two matrices: the large deformation and the geometric stiffness matrices, $\boldsymbol{K}^{\mathrm{se}} = \boldsymbol{K}_{\mathrm{L}}^{\mathrm{se}} + \boldsymbol{K}_{\mathrm{G}}^{\mathrm{se}}$. We follow the procedure pre-

sented by Bathe in reference [7] in order to decompose the integrand of $\boldsymbol{K}_{\mathrm{L}}^{\mathrm{se}}$ into a product of three matrices:

$$\boldsymbol{K}_{\mathrm{L}}^{\mathrm{se}} = \int_{\Omega_0^{\mathrm{e}}} \boldsymbol{B}_{\mathrm{L}}^{\mathrm{T}} \underset{\sim}{\mathbf{C}} \boldsymbol{B}_{\mathrm{L}} d\Omega_0 , \tag{C-4}$$

yielding, for a generic element,

$$[K_{\mathrm{L}}^{\mathrm{se}}]_{ij}^{ab} = \int_{\Omega_0^{\mathrm{e}}} \{\boldsymbol{B}_{\mathrm{L}}^{\mathrm{T}}\}_i^a \, \underset{\sim}{\mathbf{C}} \, \{\boldsymbol{B}_{\mathrm{L}}\}_j^b \, d\Omega_0 . \tag{C-5}$$

Matrix $\boldsymbol{B}_{\mathrm{L}}$ is the same intermediate matrix used in the previous section, and the arrangement of the elements of matrix $\underset{\sim}{\mathbf{C}}$ is described in Section B.2.

An interesting consequence of the DOF ordering considered in this work is that the sparsity of the geometric matrix, $\boldsymbol{K}_{\mathrm{G}}$, disappears; this matrix is now formed by non-zero sub-matrices along its diagonal. Nevertheless, this requires that we abandon the decomposition presented by Bathe in favor of a new one. To do so, interpolation functions are introduced in the integrand of the second term in Eq. (4-103), that is $\mathrm{tr}\left((\nabla_X \boldsymbol{w}^{\mathrm{s}})^{\mathrm{sym}} \, \tilde{\boldsymbol{S}}_{\mathrm{E}}^{\mathrm{s}} \, [\nabla_X (\delta \boldsymbol{u}^{\mathrm{s}})]^{\mathrm{T\,sym}} \right)$; and the nodal values of $\boldsymbol{w}^{\mathrm{s}}$ and $\delta \boldsymbol{u}^{\mathrm{s}}$ are factored out of the expression. The remaining terms inside the integral are then arranged in sub-matrices, yielding

$$\boldsymbol{K}_{\mathrm{G}}^{\mathrm{e}} = \begin{bmatrix} \boldsymbol{k}_{\mathrm{G}} & \cdot & \cdot \\ \cdot & \boldsymbol{k}_{\mathrm{G}} & \cdot \\ \cdot & \cdot & \boldsymbol{k}_{\mathrm{G}} \end{bmatrix}, \qquad \boldsymbol{K}_{\mathrm{G}}^{\mathrm{e}} = \begin{bmatrix} \boldsymbol{k}_{\mathrm{G}}^{(r)} & \cdot \\ \cdot & \boldsymbol{k}_{\mathrm{G}}^{(z)} \end{bmatrix}, \tag{C-6}$$

for 3-D and axisymmetric problems, respectively. In Eq. (C-6), dots represent null sub-matrices, and the elements of the sub-matrices $\boldsymbol{k}_{\mathrm{G}}$ are given by

$$[\boldsymbol{k}_{\mathrm{G}}]^{ab} = \int_{\Omega_0^{\mathrm{e}}} N^a_{,K} S_{KL} N^b_{,L} d\Omega_0 \qquad \text{with } K, L = 1, \ldots, n_{sd}, \tag{C-7}$$

and

$$[k_G^{(r)}]^{ab} = \int_{\Omega_0^e} \left(N^a_{,K} S_{KL} N^b_{,L} + \frac{N^a N^b}{R^2} S_{\Theta\Theta} \right) d\Omega_0,$$
$$[k_G^{(z)}]^{ab} = \int_{\Omega_0^e} N^a_{,K} S_{KL} N^b_{,L} d\Omega_0, \qquad \text{with} \quad K, L = R, Z. \tag{C-8}$$

The computational advantage obtained by avoiding a sparse matrix reinforces the decision to keep a unique order of the DOFs at element level. However, the main justification for this ordering comes with the capacity matrices examined next.

C.4 Capacity Matrices for the Penalty Formulations

The capacity matrix of the mixed-penalty formulation is provided by Eq. (4-38):

$$Y^e_{MP} = \beta Y^e_1 + Y^e_2, \tag{C-9}$$

Matrix Y^e_1 (Eq. (4-39)) requires the computation of two other matrices. The first matrix has the partition

$$A^e = \left[A^s \; A^f \right] = \left[\left[A^s_1 \; \ldots \; A^s_{n_{sd}} \right] \left[A^f_1 \; \ldots \; A^f_{n_{sd}} \right] \right]. \tag{C-10}$$

The elements of sub-matrix A^α_i, α = s,f, are provided by Eq. (4-32):

$$[A^\alpha]^{ca}_i = \int_{\Omega_0^e} \mathcal{N}^c \{h^\alpha\}^a_i J^s d\Omega_0, \tag{C-11}$$

with $\{h^\alpha\}^a_i$ being an element of the intermediate vector $\boldsymbol{h}^\alpha$ developed in Appendix B. The second matrix, $\boldsymbol{H}^e$, has its components determined using Eq. (4-34):

$$[H^e]^{cd} = \int_{\Omega_0^e} \mathcal{N}^c \mathcal{N}^d J^s d\Omega_0. \tag{C-12}$$

For an isotropic permeability tensor (or equivalently, an isotropic drag tensor $\boldsymbol{\zeta} = \zeta \mathbf{1}$), matrix Y^e_2 defined in Eq. (4-33) can be partitioned for 3-D and axisymmetric problems as

$$Y_2^e = \begin{bmatrix} y_2 & \bullet & \bullet & -y_2 & \bullet & \bullet \\ & y_2 & \bullet & \bullet & -y_2 & \bullet \\ & & y_2 & \bullet & \bullet & -y_2 \\ & & & y_2 & \bullet & \bullet \\ & \text{Sym.} & & & y_2 & \bullet \\ & & & & & y_2 \end{bmatrix}, \qquad Y_2^e = \begin{bmatrix} y_2 & \bullet & -y_2 & \bullet \\ & y_2 & \bullet & -y_2 \\ & & y_2 & \bullet \\ \text{Sym.} & & & y_2 \end{bmatrix}, \tag{C-13}$$

respectively, with the elements of sub-matrix y_2 given by

$$[y_2]^{ab} = \int_{\Omega_0^e} N^a \zeta N^b J^s d\Omega_0 . \tag{C-14}$$

C.5 Capacity Matrix for the *v-p* Formulation

From Eq. (4-78)$_3$, the "generalized" capacity matrix is given by

$$Y_{vp}^e = \begin{bmatrix} \mathbf{0} & -A_{vp}^{e\,T} \\ -A_{vp}^e & -H_{vp}^e \end{bmatrix}. \tag{C-15}$$

The elements of matrix A_{vp}^e are computed using Eq. (4-77):

$$[A_{vp}^e]_i^{ca} = \int_{\Omega_0^e} \mathcal{N}^c \{h\}_i^a J^s d\Omega_0 , \tag{C-16}$$

where vector $\boldsymbol{h}$ is given in Section B.5. The elements of matrix $\boldsymbol{H}_{vp}^e$ for an isotropic permeability are readily derived from Eq. (4-74):

$$[H_{vp}^e]^{cd} = \int_{\Omega_0^e} \kappa \nabla \mathcal{N}^c \cdot \nabla \mathcal{N}^d J^s d\Omega_0 . \tag{C-17}$$

The equations in this appendix, together with the ones in Appendix B, correspond to the matrices implemented in the biphasic finite element program.

APPENDIX D

Restrictions Imposed on the Exponential Helmholtz Free Energy Function

This appendix examines basic aspects for the preliminary acceptance of the exponential Helmholtz free energy function studied in Chapter 7. These aspects include the existence of a natural state, the stress-strain relations under infinitesimal deformation, and the extension-tension (E-T) condition for stretches in the principal directions of the material.

D.1 Existence of a Natural State

A natural state corresponds to an unstressed reference configuration. Incorporating this condition into the elastic Cauchy stress tensor for transverse isotropy, Eq. (3-33), yields

$$\begin{aligned} \psi^s_{,1} + 2\psi^s_{,2} + \psi^s_{,3} &= 0, \\ \psi^s_{,4} + 2\psi^s_{,5} &= 0. \end{aligned} \tag{D-1}$$

For the exponential function defined by Eqs. (7-1) and (7-2), the above equations produce the conditions

$$\begin{aligned} n &= \alpha_1 + 2\alpha_2, \\ \alpha_4 &= -2\alpha_7, \end{aligned} \tag{D-2}$$

which reduce the number of parameters in the exponential function from nine to seven.

D.2 Stress-Strain Relations under Infinitesimal Deformations

For infinitesimal strains, the stress-strain relation can be expressed as:

$$\underset{\sim}{\sigma}^s_E = \underset{\sim}{\mathbf{C}}\ \underset{\sim}{\epsilon}. \tag{D-3}$$

where $\underset{\sim}{\sigma}^s_E = \left[\sigma_{11}, \sigma_{22}, \sigma_{33}, \sigma_{12}, \sigma_{13}, \sigma_{23}\right]^T$ and $\underset{\sim}{\epsilon} = \left[\varepsilon_{11}, \varepsilon_{22}, \varepsilon_{33}, 2\varepsilon_{12}, 2\varepsilon_{13}, 2\varepsilon_{23}\right]^T$ are condensed vectors of the stress tensor and the infinitesimal strain tensor, respectively; and $\underset{\sim}{\mathbf{C}}$ is the condensed matrix of the elasticity tensor. When the preferred direction coincides with the direction X_1, the matrix $\underset{\sim}{\mathbf{C}}$ for transverse isotropy has the general form

$$\underset{\sim}{C} = \begin{bmatrix} C_{1111} & C_{1122} & C_{1122} & 0 & 0 & 0 \\ C_{1122} & C_{2222} & C_{2233} & 0 & 0 & 0 \\ C_{1122} & C_{2233} & C_{2222} & 0 & 0 & 0 \\ 0 & 0 & 0 & C_{1212} & 0 & 0 \\ 0 & 0 & 0 & 0 & C_{1212} & 0 \\ 0 & 0 & 0 & 0 & 0 & C_{2323} \end{bmatrix}, \tag{D-4}$$

with $C_{2323} = (C_{2222} - C_{2233})/2$. The inverse of $\underset{\sim}{C}$ is the compliance matrix, which can be expressed using engineering coefficients as

$$\underset{\sim}{C}^{-1} = \begin{bmatrix} \frac{1}{E_1} & -\frac{\nu_{21}}{E_2} & -\frac{\nu_{21}}{E_2} & 0 & 0 & 0 \\ -\frac{\nu_{12}}{E_1} & \frac{1}{E_2} & -\frac{\nu_{32}}{E_2} & 0 & 0 & 0 \\ -\frac{\nu_{12}}{E_1} & -\frac{\nu_{23}}{E_2} & \frac{1}{E_2} & 0 & 0 & 0 \\ 0 & 0 & 0 & \frac{1}{G_{12}} & 0 & 0 \\ 0 & 0 & 0 & 0 & \frac{1}{G_{12}} & 0 \\ 0 & 0 & 0 & 0 & 0 & \frac{E_2}{2(1+\nu_{23})} \end{bmatrix}, \tag{D-5}$$

where E_1 and E_2 are the Young's moduli in the preferred direction and directions perpendicular to it, respectively; G_{12} is the shear modulus in planes containing the preferred direction; ν_{12} is the Poisson's ratio for the transverse strain in the X_2 direction when the body is stressed in the X_1 direction; and ν_{23} is the Poisson's ratio in the planes of isotropy. Other Poisson's ratios in Eq. (D-5) are determined from the symmetry of the compliance matrix, that is $\nu_{21}/E_2 = \nu_{12}/E_1$.

One way to obtain the relationships between the coefficients of $\underset{\sim}{C}$ and the parameters of the exponential function is through the linearization of the elastic Cauchy stress tensor, Eq. (3-33). The linearization provides:

$$\alpha_1 = \frac{C_{2323}}{\alpha_0} - n, \qquad \alpha_2 = -\frac{C_{2323}}{2\alpha_0} + n,$$

$$\alpha_3 = \frac{1}{2}\left(\frac{C_{2222}}{4\alpha_0} - n\right), \qquad \alpha_4 = -2\alpha_7,$$

$$\alpha_5 = \frac{1}{8\alpha_0}\left[(C_{1111} - C_{2222}) + 2(C_{2233} - C_{1122}) + 4(C_{2323} - C_{1212})\right], \tag{D-6}$$

$$\alpha_6 = \frac{C_{1122} - C_{2233}}{4\alpha_0}, \qquad \alpha_7 = \frac{C_{1212} - C_{2323}}{2\alpha_0}.$$

Except for α_0 and n, the remaining parameters can be associated with linear material properties. In this context, α_5, α_6 and α_7 specify the material anisotropy of the exponential function under infinitesimal deformation; these parameters are zero for isotropic materials.

The requirement that the matrix $\mathbf{C}$ is positive definite leads to the following conditions [63]:

$$(C_{1111}, C_{2222}, C_{1212}, C_{2323}) > 0, \tag{D-7}$$

$$C_{2222}^2 - C_{2233}^2 > 0, \tag{D-8}$$

$$2C_{1122}^2 < C_{1111}(C_{2222} + C_{2233}), \tag{D-9}$$

which, through Eq. (D-6), can also be expressed in terms of the parameters of the exponential function.

D.3 Restrictions Imposed by the Extension-Tension (E-T) Condition

In Fig. D.1 a unit cube is stretched along its principal directions *m*, *t* and *u*, with *m* being the preferred direction of the material. The principal elastic stresses on the deformed cube are

$$\sigma^s_{Em} = \frac{2\rho^s_0 \lambda_m}{\lambda_t \lambda_u}\left[\psi^s_{,1} + \psi^s_{,2}(\lambda_t^2 + \lambda_u^2) + \psi^s_{,3}\lambda_t^2\lambda_u^2 + \psi^s_{,4} + 2\psi^s_{,5}\lambda_m^2\right],$$

$$\sigma^s_{Et} = \frac{2\rho^s_0 \lambda_t}{\lambda_u \lambda_m}\left[\psi^s_{,1} + \psi^s_{,2}(\lambda_u^2 + \lambda_m^2) + \psi^s_{,3}\lambda_u^2\lambda_m^2\right], \qquad \text{(D-10)}$$

$$\sigma^s_{Eu} = \frac{2\rho^s_0 \lambda_u}{\lambda_m \lambda_t}\left[\psi^s_{,1} + \psi^s_{,2}(\lambda_m^2 + \lambda_t^2) + \psi^s_{,3}\lambda_m^2\lambda_t^2\right],$$

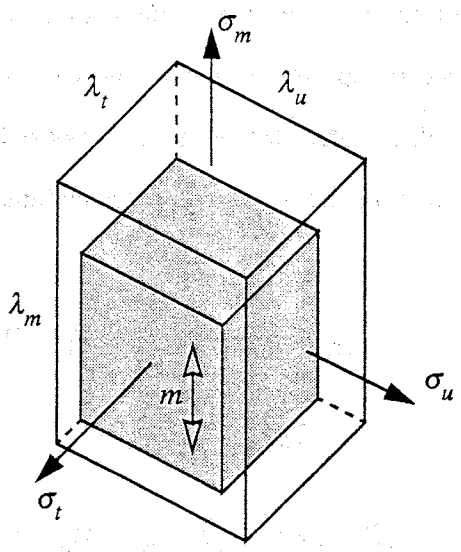

Figure D.1 Unit cube stretched along its principal directions. The preferred direction *m*, indicated by a double arrow, coincides with a principal direction.

where σ^s_{Em} is the stress in the plane normal to the preferred direction, σ^s_{Et} and σ^s_{Eu} are the stresses in two orthogonal planes containing the preferred direction, and λ_m, λ_t and λ_u are the corresponding stretches. The above equations can be used with the Extension-Tension (E-T) condition (Section 3.5) to establish restrictions on the exponential function. Two situations are of particular interest in the case of transversely isotropic materials:

Stretch Prescribed along the Preferred Direction

Introducing $\lambda_m = \lambda$, and $\lambda_t = \lambda_u = 1$ into Eq. (D-10), and making use of Eq. (7-3), yields the principal stress in the preferred direction:

$$\sigma^{s}_{Em} = 2\alpha_0\left(2\alpha_a + \frac{n}{\lambda^2}\right)\frac{(\lambda^2-1)}{\lambda^{2n-1}}\, e^{[n+\alpha_a(\lambda^2-1)](\lambda^2-1)}, \tag{D-11}$$

and the confining principal stresses:

$$\sigma^{s}_{Et} = \sigma^{s}_{Eu} = 2\alpha_0\alpha_b\frac{(\lambda^2-1)}{\lambda^{2n+1}}\, e^{[n+\alpha_a(\lambda^2-1)](\lambda^2-1)}, \tag{D-12}$$

where $\alpha_a = \alpha_3 + \alpha_5 + \alpha_6$ and $\alpha_b = \alpha_2 + 2\alpha_3 + \alpha_6$.

Stretch Prescribed Perpendicularly to the Preferred Direction

For $\lambda_u = \lambda$ and $\lambda_m = \lambda_t = 1$, the principal stress in the direction u is

$$\sigma^{s}_{Eu} = 2\alpha_0\left(2\alpha_3 + \frac{n}{\lambda^2}\right)\frac{(\lambda^2-1)}{\lambda^{2n-1}}\, e^{[n+\alpha_3(\lambda^2-1)](\lambda^2-1)}, \tag{D-13}$$

and the principal confining stresses are

$$\sigma^{s}_{Em} = 2\alpha_0\alpha_b\frac{(\lambda^2-1)}{\lambda^{2n+1}}\, e^{[n+\alpha_3(\lambda^2-1)](\lambda^2-1)}, \tag{D-14}$$

$$\sigma^{s}_{Et} = 2\alpha_0(\alpha_2 + 2\alpha_3)\frac{(\lambda^2-1)}{\lambda^{2n+1}}\, e^{[n+\alpha_3(\lambda^2-1)](\lambda^2-1)}. \tag{D-15}$$

The imposition of the (E-T) condition upon Eqs. (D-11) and (D-13), together with the assumption of a positive α_0, produces the inequalities

$$\alpha_3 + \alpha_5 + \alpha_6 + \frac{n}{2\lambda^2} > 0, \tag{D-16}$$

$$\alpha_3 + \frac{n}{2\lambda^2} > 0. \tag{D-17}$$

If the (E-T) condition is complemented with the requirement that a longitudinal elongation is accompanied by tensile transverse stresses (a requirement not always valid for collapsible materials such as foams), the following inequalities result from Eqs. (D-12) and (D-15)

$$\alpha_2 + 2\alpha_3 + \alpha_6 > 0\,, \tag{D-18}$$

$$\alpha_2 + 2\alpha_3 > 0\,. \tag{D-19}$$

where, again, a positive α_0 has been assumed.

APPENDIX E

A Variant of the Mixed-Penalty Formulation

In the mixed-penalty (MP) formulation, the need to compute the gradient of the porosity, and thus the second-order derivatives of the interpolation functions, can be eliminated by replacing the fluid velocity unknown. The outline of the resulting formulation that uses solid velocity and a new "relative" velocity as unknowns is presented in this appendix. We refer to Chapter 4 for a complete description of the equations and terms used in this appendix.

The elimination of the gradient of the porosity from the finite element equations starts with the continuity equation. Using the relationship $\phi^s = 1 - \phi^f$, the penalty form of the continuity condition, Eq. (4-1), becomes:

$$\nabla \cdot [v^s + \phi^f (v^f - v^s)] + \frac{p}{\beta} = 0 . \tag{E-1}$$

A new velocity v^R is then defined based upon the relative velocity of the fluid

$$v^R = \frac{1}{\phi^f}(v^f - v^s) , \tag{E-2}$$

so that Eq. (E-1) now reads

$$\nabla \cdot (v^s + v^R) + \frac{p}{\beta} = 0 , \tag{E-3}$$

The replacement of the fluid velocity by v^R requires rewriting the linear momentum equation for the fluid, and redefining boundary conditions. Making use of Eq. (E-2) in the momentum equation for the fluid in Table 3.2, yields

$$\nabla p + \zeta v^R = 0 . \tag{E-4}$$

As for boundary condition, the following equation replaces the condition for fluid velocity used in Chapter 4:

$$v^{R}(x,t) = \overset{.R}{g}, \qquad \text{for} \quad x \in \Gamma_{g^{R}}, \tag{E-5}$$

where $\overset{.R}{g}$ denotes prescribed values on $\Gamma_{g^{R}} \subset \Gamma$.

To obtain the weak form, the momentum equation for the mixture, Eq. (4-53), the momentum equation for the fluid phase, Eq. (E-4), the new form of the continuity equation, Eq. (E-3), and boundary conditions given by Eqs. (4-57) and (4-58) and are introduced into the weighted residual statement, yielding

$$\begin{aligned}\int_{\Omega} \{ w^{s} \cdot [\nabla \cdot (\sigma_{E}^{s} - p1)] - w^{R} \cdot [\nabla p + \zeta v^{R}] + q\left[\nabla \cdot (v^{s} + v^{R}) + \frac{p}{\beta}\right] \} d\Omega \\ + \int_{\Gamma_{t^{s}}} w^{s} \cdot (\bar{t} - \sigma n)\, d\Gamma - \int_{\Gamma_{t^{R}}} w^{R} \cdot n\,(\bar{p} - p)\, d\Gamma = 0,\end{aligned} \tag{E-6}$$

where the boundary $\Gamma_{t^{R}}$ is defined such that $\overline{\Gamma_{t^{R}} \cup \Gamma_{g^{R}}} = \Gamma$ and $\Gamma_{t^{R}} \cap \Gamma_{g^{R}} = \varnothing$. The weighting function w^{R} must satisfy the homogenous form of the boundary condition for the trial solutions v^{R}. The weak form is then obtained by applying the divergence theorem to Eq. (E-6):

$$\begin{aligned}\int_{\Omega} \{ \mathrm{tr}((\nabla w^{s})^{T} \sigma_{E}^{s}) - \nabla \cdot (w^{s} + w^{R})\, p + w^{R} \cdot \zeta v^{R} - q\left[\nabla \cdot (v^{s} + v^{R}) + \frac{p}{\beta}\right] \} d\Omega \\ = \int_{\Gamma_{t^{s}}} w^{s} \cdot \bar{t}\, d\Gamma - \int_{\Gamma_{Q}} w^{R} \cdot n\, \bar{p} d\Gamma.\end{aligned} \tag{E-7}$$

In contrast to Eq. (4-15), developed using fluid velocity, the above equation does not have the volume fraction gradients, so its discretization leads to standard finite element matrices that require only the first derivative of the interpolation functions.